NUMERICAL AND ANALYTICAL MODELS OF SELF-FORCE EFFECTS IN KERR EXTREME-MASS-RATIO INSPIRALS

Zachary Nasipak

A dissertation submitted to the faculty at the University of North Carolina at Chapel Hill in partial fulfillment of the requirements for the degree of Doctor of Philosophy in the Department of Physics and Astronomy.

Chapel Hill
2020

Approved by:

Charles R. Evans

Joaquín Drut

Jonathan Engel

Adrienne Erickcek

Reyco Henning

Thomas Osburn

ABSTRACT

Zachary Nasipak: Numerical and analytical models of self-force effects in Kerr extreme-mass-ratio inspirals
(Under the direction of Charles R. Evans)

Ground-based detectors now regularly observe the merger of stellar-mass compact objects and their gravitational waves. Building on this success, ESA, in partnership with NASA, will launch the space-based LISA observatory to detect milli-Hertz gravitational wave signals. Extreme-mass-ratio inspirals (EMRIs)—binaries composed of a stellar-mass compact object orbiting a massive black hole—are ideal gravitational wave sources for LISA. Because of their unique properties, EMRIs can provide new insights concerning the growth of massive black holes (and their host galaxies) and enable the most precise tests of general relativity. To achieve this science, LISA will rely on accurate EMRI models to search for and analyze gravitational wave signals. The most accurate EMRI models rely on a mechanism known as the gravitational self-force to calculate an EMRI inspiral and the resulting gravitational waveform. For EMRIs with rotating (Kerr) massive black holes, current gravitational self-force calculations are too computationally demanding to be incorporated into full EMRI models. For my dissertation, I built a developmental scalar self-force code to devise and implement new numerical and analytical techniques for calculating self-force effects in Kerr spacetime. I introduce spectral techniques for numerically evaluating Kerr geodesics and the sources of scalar perturbations. I discuss how these methods can be extended to gravitational self-force calculations. With this code, I produced the first calculations of the scalar self-force along resonant and non-resonant inclined, eccentric orbits in Kerr spacetime. With these new resonant calculations I provided one of the first tests of the integrability conjecture, which holds for these scalar self-force results. I also uncovered the existence of a physical effect in EMRI waveforms, now referred to as quasinormal bursts. Quasinormal bursts are periodic high-frequency oscillations in EMRI waveforms which may aid in the characterization of EMRI gravitational wave sources.

ACKNOWLEDGEMENTS

Thank you to my advisor Prof. Charles R. Evans for his patience, wisdom, and mentorship. His enthusiasm for our work and this field of physics is contagious and inspiring. He has made me a better researcher and physicist. Without him, this work would not have been possible.

Thank you to Prof. Thomas Osburn for his guidance and collaboration. His continuous encouragement has been invaluable.

Thank you to my friends and colleagues for their support. The communities I have found in North Carolina and through my research have been essential to my success. This community is what makes me truly feel like a physicist.

Thank you to my wife Rebecca, my mother and father, Debra and James, my sister Jessica, my mother- and father-in-law, Dick and Mary, and my dear friend Bryan for their unwavering love and support. Thank you for enduring my moments of stress, self-doubt, and frustration over my research and instead reminding me of the intrigue, joy, and thrill I find in my work.

Thank you to all of you. These words only describe a fraction of my gratitude.

This work was financially supported in part by the National Science Foundation grants PHY-1506182 and PHY-1806447, the North Carolina Space Grant, and the University of North Carolina at Chapel Hill.

TABLE OF CONTENTS

LIST OF TABLES

LIST OF FIGURES

LIST OF ABBREVIATIONS AND SYMBOLS

BHPT	black hole perturbation theory
DCT	discrete cosine transform
DFT	discrete Fourier transform
EHS	extended homogeneous solutions
EMRI	extreme-mass-ratio inspiral
FFT	fast Fourier transform
GSF	gravitational self-force
LIGO	Laser Interferometer Gravitational-wave Observatory
LISA	Laser Interferometer Space Antenna
MBH	massive black hole
MiSaTaQuWa	Mino, Sasaki, Tanaka, Quinn, and Wald
MST	Mano, Suzuki, and Takasugi
NP	Newman-Penrose
NR	numerical relativity
PN	post-Newtonian
QNB	quasinormal burst
QNM	quasinormal mode
SSF	scalar self-force
SSI	spectral source integration
μ	mass of a small object
M	mass of a large black hole
ϵ	mass ratio μ/M

q	scalar charge
$M_\odot$	mass of the Sun
$M_\oplus$	mass of the Earth
G	Newton's gravitational constant
c	speed of light
α, $\beta, \gamma, \ldots$	spacetime coordinate indices running from 0 to 3
i, j, $k, \ldots$	spatial coordinate indices running from 1 to 3
x^α	spacetime coordinates, e.g., (x^0, x^1, x^2, x^3) or (t, x, y, z) or (t, r, θ, φ)
$\mathbf{x}$	spatial coordinates, e.g., (x^1, x^2, x^3) or (x, y, z) or (r, θ, φ)
s, τ	proper distance and proper time
u^α	four-velocity of a particle
∂_μ	partial derivative operator $\partial/\partial x^\mu$
$g_{\mu\nu}$, $g^{\mu\nu}$	background spacetime metric, inverse of the background metric
$\eta_{\mu\nu}$	Minkowski metric, i.e., $\mathrm{diag} = (-1, 1, 1, 1)$
∇_μ	covariant derivative operator defined with respect to $g_{\mu\nu}$
$\Gamma^\alpha_{\mu\nu}$	Christoffel symbols defined with respect to $g_{\mu\nu}$
$G_{\mu\nu}$	Einstein tensor defined with respect to a metric $g_{\mu\nu}$
$T_{\mu\nu}$	stress-energy tensor
$R_{\mu\nu}$	Ricci tensor defined with respect to a metric $g_{\mu\nu}$
R	Ricci scalar defined with respect to a metric $g_{\mu\nu}$
$R^\alpha{}_{\beta\mu\nu}$	Riemann curvature tensor defined with respect to a metric $g_{\mu\nu}$
$\mathbf{g}_{\mu\nu}$	perturbed metric, i.e., $g_{\mu\nu} + h_{\mu\nu}$
$\mathbf{G}$, $\mathbf{T}$, $\mathbf{\Gamma}, \ldots$	bold faced symbols are defined with respect to the perturbed metric $\mathbf{g}_{\mu\nu}$

$h_{\mu\nu}$	metric perturbation
$h^{(1)}_{\mu\nu}$, $h^{(2)}_{\mu\nu}$	first-order and second-order metric perturbations
$\bar{h}_{\mu\nu}$	trace-reversed metric perturbation $h^{(1)}_{\mu\nu} - \frac{1}{2} g_{\mu\nu} h^{(1)\,\alpha}_{\alpha}$
$F^{\alpha}_{\mathrm{GSF}}$	gravitational self-force
$F^{\alpha}_{\mathrm{GSF},1}$, $F^{\alpha}_{\mathrm{GSF},2}$	first-order and second-order gravitational self-force
ϕ_{EMRI}	phase of an EMRI inspiral
κ	expansion coefficients for the EMRI phase
$h^{\mathrm{tail}}_{\mu\nu}$	tail contribution to the first-order metric perturbation
$h^{\mathrm{R}}_{\mu\nu}$, $h^{\mathrm{S}}_{\mu\nu}$	Detweiler-Whiting regular and singular metric perturbations
Φ	scalar potential field of a scalar point charge q
ρ_{scalar}	the scalar (point) charge density
Φ^{ret}, Φ^{adv}	the retarded (causal) scalar field, the advanced scalar field solution
Φ^{R}, Φ^{S}	the regular and singular components of the retarded scalar field
F_{α}	scalar self-force
$F^{\mathrm{ret},l}_{\alpha}$, $F^{\mathrm{S},l}_{\alpha}$	the multipole contributions of the retarded and singular scalar fields to the scalar self-force
Y_{lm}	scalar spherical harmonics
$F^{\mathrm{cons}}_{\alpha}, F^{\mathrm{diss}}_{\alpha}$	conservative and dissipative contributions to the scalar self-force
(t, r, θ, φ)	Boyer-Lindquist coordinates
x^{α}_{p}	wordline of a point particle $(t_p, r_p, \theta_p, \varphi_p)$
$\mathcal{E}$, $\mathcal{L}_z$	the specific energy and the z-component of the specific angular momentum
$\xi^{\alpha}_{(t)}$, $\xi^{\alpha}_{(\varphi)}$	time and azimuthal Killing vectors
$\mathcal{Q}$	Carter constant
$K_{\mu\nu}$	Killing tensor associated with the Carter constant

$\mathtt{l}^{\alpha}$, $\mathtt{n}^{\alpha}$, $\mathtt{m}^{\alpha}$	basis vectors of an arbitrary null tetrad
l^{α}, n^{α}, m^{α}	basis vectors of the Kinnersley null tetrad
V_{tr}, $V_{t\theta}$	coordinate time potentials of the geodesic equations
$V_{\varphi r}$, $V_{\varphi\theta}$	azimuthal potentials of the geodesic equations
V_r, V_θ	radial and polar potentials of the geodesic equations
p, e, x_{inc}	semi-latus rectum, orbital eccentricity, and projection of the orbital inclination
ι	alternative parameterization of geodesic inclination
λ, λ_0	(Carter-)Mino time and the initial Mino time offset
$\lambda_0^{(r)}$, $\lambda_0^{(\theta)}$	radial and polar initial Mino time offsets
Γ, Υ_r, Υ_θ, Υ_θ	time, radial, polar, and azimuthal frequencies with respect to Mino time
Ω_r, Ω_θ, Ω_θ	fundamental radial, polar, and azimuthal frequencies with respect to coordinate time
ω_{mkn}	frequency spectrum $m\Omega_\varphi + k\Omega_\theta + n\Omega_r$
$\hat{x}^{\mu}_{p}(\lambda)$	a fiducial geodesic, i.e., a geodesic with fiducial initial conditions $\hat{x}^{\mu}_{p}(0) = (0, r_{\mathrm{min}}, \theta_{\mathrm{min}}, 0)$
$\Delta\hat{x}^{(r)}(\Upsilon_r\lambda)$	fiducial geodesic functions with periodicity $\Delta\hat{x}^{(r)}(2\pi + \Upsilon_r\lambda) = \Delta\hat{x}^{(r)}(\Upsilon_r\lambda)$, $(x = t, r, \theta, \varphi)$
$\Delta\hat{x}^{(\theta)}(\Upsilon_\theta\lambda)$	fiducial geodesic functions with periodicity $\Delta\hat{x}^{(\theta)}(2\pi + \Upsilon_\theta\lambda) = \Delta\hat{x}^{(\theta)}(\Upsilon_\theta\lambda)$, $(x = t, r, \theta, \varphi)$
β_r, β_θ	integers that define an $r\theta$-resonance, i.e., $\Upsilon_r/\Upsilon_\theta = \beta_r/\beta_\theta$
Υ, Ω	resonant Mino time frequency, resonant coordinate time frequency
ω_{mN}	reduced resonant frequency spectrum $m\Omega_\varphi + N\Omega$
$\bar{x}^{\mu}_{p}(\lambda; \lambda_0)$	a resonant geodesic that is dependent on the initial Mino time offset λ_0
ψ, χ	Darwin-like variables
q_r, q_θ	angle variables
q_{r0}, $q_{\theta 0}$	initial orbital phases
$\bar{q}$, $\bar{q}_0$	resonant angle variable, initial resonant phase

A^{α}_{EM}	electromagnetic four-potential
j^{μ}	(electric) current density
$A^{\alpha}_{\mathrm{ret}}$, $A^{\alpha}_{\mathrm{adv}}$	the retarded (causal) and advanced four-potentials
G_{+}, G_{-}	retarded and advanced Green's functions
$F_{\mu\nu}$	the field-strength (Faraday) tensor $\partial_{\mu}A^{\mathrm{EM}}_{\nu} - \partial_{\nu}A^{\mathrm{EM}}_{\mu}$
$\epsilon_{\alpha\beta\mu}$, $\epsilon_{\alpha\beta\mu\nu}$	the Levi-Cevita symbol
$F^{\alpha}_{\mathrm{ESF}}$	electromagnetic self-force
A^{α}_{S}, A^{α}_{R}	singular and regular electromagnetic four-potentials
G_{S}, G_{R}	singular Green's function and regular two-point function
H	symmetric two-point function
$F^{\alpha(\mathrm{diss})}_{\mathrm{ESF}}$, $F^{\alpha(\mathrm{cons})}_{\mathrm{ESF}}$	dissipative and conservative components of the electromagnetic self-force
$F^{\alpha(\mathrm{diss})}_{\mathrm{GSF}}$, $F^{\alpha(\mathrm{cons})}_{\mathrm{GSF}}$	dissipative and conservative components of the (first-order) gravitational self-force
$\langle \dot{E} \rangle^{\mathcal{H},\infty,\mathrm{tot}}$	energy flux through the horizon, through infinity, and the total energy flux
$\langle \dot{L}_z \rangle^{\mathcal{H},\infty,\mathrm{tot}}$	z-component of the angular momentum flux through the horizon, through infinity, and the total (z-component of the) angular momentum flux
$\langle \dot{Q} \rangle^{\mathrm{tot}}$	global averaged time-rate-of-change of the Carter constant
$\langle \cdot \rangle$	average with respect to coordinate time
$\langle \cdot \rangle_{\lambda}$	average with respect to Mino time
$\mathcal{W}$, $\mathcal{T}$	rate of local work done on a particle, local torque acting on a particle due to the self-force
$\mathcal{K}$	local time-rate-of-change of the Carter constant due to the self-force
A_{α}, B_{α}, $D_{\alpha,n}$	regularization parameters
$C_{\alpha\beta\gamma\delta}$	the conformal Weyl tensor
ψ_0, ψ_4	the Weyl scalars with spin-weights $s=+2$ and $s=-2$, respectively
Ψ_s	field of spin-weight s

${}_sR_{\hat{l}m\omega}$	spin-weighted radial Teukolsky function
${}_sS^{a\omega}_{\hat{l}m}$	spin-weighted angular Teukolsky function
${}_sS^{a\omega}_{\hat{l}m}(\theta)e^{im\varphi}$	spin-weighted spheroidal harmonic with spheroidicity $\sigma = -a^2\omega^2$
${}_s\lambda^{a\omega}_{\hat{l}m}$	separation constant or spin-weighted spheroidal eigenvalue
$C^{\pm}_{s\hat{l}m\omega}$	Teukolsky amplitudes
Ψ^{Hertz}	Hertz potential
$R_{\hat{l}mkn}$	scalar radial Teukolsky function
$S_{\hat{l}mkn}$	scalar angular Teukolsky function
$X_{\hat{l}mkn}$	scalar Sasaki-Nakamura radial function
$\lambda_{\hat{l}mkn}$	scalar spheroidal eigenvalue
$C^{\pm}_{\hat{l}mkn}$	scalar normalization coefficients
$b^{\hat{l}}_{lmkn}$	spherical-spheroidal coupling coefficients
$\phi^{\pm}_{lm}$	extended homogeneous (scalar) functions
$F(c_1, c_2, c_3; x)$	Gauss hypergeometric function
$\Psi(c_1, c_2; x)$	irregular confluent hypergeometric function
ν	renormalized angular momentum
$M(c_1, c_2; x)$	regular confluent hypergeometric function
$\hat{F}_\alpha$	scalar self-force sourced by a particle following a fiducial geodesic $\hat{x}^\mu_p$
$\bar{F}^{\mathrm{res}}_\alpha$	resonant scalar self-force sourced by a particle following a resonant geodesic $\bar{x}^\mu_p$

CHAPTER 1: Introduction

Science progresses best when observations force us to alter our preconceptions.

— Vera Rubin

Section 1.1: A new era of astronomy

The recent emergence of gravitational wave astronomy has ushered in a new age of observational science. For centuries astronomy relied on light—the electromagnetic waves emitted by charged particles—to map and understand the universe. Now, ultra-precise gravitational observatories, such as LIGO [4] and Virgo [8], regularly measure gravitational waves—small ripples in the fabric of space and time. The primary sources of these gravitational waves are energetic binaries composed of stellar-mass compact objects, such as black holes and neutron stars. As these gravitationally-bound compact objects orbit one another, their motion warps space and time, producing gravitational waves that carry away energy and momentum. Over time, the objects sink into more tightly bound orbits, inspiraling towards one another as they reach orbital velocities near the speed of light. Eventually the compact objects will merge, releasing a dramatic burst of gravitational radiation and forming a new black hole.

Theoretical models of these compact object binaries are essential to detecting their gravitational waves. Despite the immense amount of energy released by compact mergers, gravitational wave signals are incredibly faint and dominated by external noise. Gravitational models aid detectors in filtering gravitational wave signals from noisy measurements and extracting the characteristics of their sources. Gravitational wave observations, assisted by these models, have provided novel strong-field tests of general relativity and revealed new insights into the nature of binary black hole and neutron star systems, affirming and altering our preconceptions of the universe. Building on this success, the European Space Agency (ESA), with the support of NASA, is constructing the Laser Interferometer Space Antenna (LISA) [5], a space-based gravitational wave detector that will launch in 2034. The focus of this dissertation is to develop new methods for modeling optimal LISA sources—known as extreme-mass-ratio inspirals (EMRIs)—to aid the detection and characterization of gravitational waves by LISA.

1.1.1: History of gravitational waves and gravitational wave astronomy

Gravitational waves are oscillations in the curvature of spacetime, predicted by general relativity and produced by the motion of mass and energy. The existence of gravitational waves was originally proposed by Einstein in 1916 [95], though he doubted that gravitational waves, even if they were real, could ever be observed [96]. Other researchers were similarly skeptical and for decades relativists debated their existence. Eddington [94] suggested that gravitational waves were merely a coordinate effect in general relativity and, thus, not physically observable. Even Einstein, in his work with Rosen, famously denied that gravitational radiation was measurable [98]. Tides shifted at the 1957 Chapel Hill Conference on the Role of Gravitation in Physics [45], in part due to Feynman's renowned "sticky-bead" argument [196]. Inspired by the work of Pirani [196], Feynman argued that a passing gravitational wave would cause sticky beads on a rod to oscillate towards and away from one another, generating heat due to the friction between the beads and the rod. Because this heat can be measured, so can gravitational waves. This reasoning would eventually convince many researchers that the energy carried by gravitational radiation could, theoretically, be transferred to an experimental apparatus, enabling the measurement of passing gravitational waves.

While relativists became increasingly convinced of the detectability of gravitational waves, it would still take decades for researchers to observe the physical effects of gravitational radiation. The first observational evidence came after Hulse and Taylor [136], in 1975, discovered a rapidly-rotating, radiating neutron star—known as a pulsar—bound in orbit with another neutron star. The Hulse-Taylor binary pulsar, referred to as PSR B1913+16, emits "pulsing" radio signals with precise arrival times. By recording the arrival times of these pulses, Hulse and Taylor calculated various properties of the binary, such as its eccentricity, inclination, and orbital period [136]. Due to the compact nature of the binary, researchers realized that PSR B1913+16 radiated enough energy through gravitational waves that its orbital period would decay by about 76 microseconds each year [208]. Taylor and Weisberg [208], after tracking the orbital period of the binary over seven years, found that the orbit was decaying at exactly this predicted rate, thus providing indirect evidence for the existence of gravitational waves. Repeated observations of PSR B1913+16 over the last several decades have continued to support these results, making the Hulse-Taylor binary the longest-serving astrophysical laboratory for gravitational wave science [244].

The success of the Hulse-Taylor measurements spurred on efforts to directly detect gravitational wave signals. Gravitational waves, however, are challenging to measure because they are incredibly weak. (In fact gravity is generally very weak compared to the other fundamental forces of nature. Spacetime does not bend easily.) As gravitational waves pass through objects, they will stretch and compress the objects in the transverse directions, but only to one part in 10^{21} [4]. Therefore kilometer-sized gravitational wave detectors must be able to measure changes in distance that are 10 thousand times smaller than the width of a proton. This required the construction of a new class of ultra-precise ground-based observatories: namely, the Laser Interferometer Gravitational-wave Observatory (LIGO) [4], the largest and most expensive experiment ever funded by the National Science Foundation, and its European counterpart Virgo [8]. While the construction of LIGO was completed in 1999, it would take 16 years of empty searches for LIGO to finally measure gravitational waves.

1.1.2: The birth and future of gravitational wave detections

On September 4, 2015, LIGO recorded its first detection as the gravitational waves emitted by two merging black holes—located nearly 1.3 billion lightyears away—finally passed through the Earth [11]. The measurement of this gravitational signal, named GW150914, was a groundbreaking moment for astronomy. With GW150914, researchers not only affirmed the existence of black holes and their gravitational waves, but also deduced the properties of its source, leading to novel measurements of the masses and spins of stellar-mass black holes [11]. Since this first detection, there has been a proliferation of gravitational wave observations. LIGO, assisted by Virgo, detected at least ten more gravitational wave events during its O1 and O2 observing runs [22], with tens of more potential detections found during its most recent O3 observations [4].

Theoretical models have played a vital role in detecting these gravitational waves and characterizing their sources. Despite the incredible precision of current detectors, gravitational measurements are still dominated by numerous sources of noise (e.g., thermal, seismic, quantum, laser, electronic) [4, 11]. Accurate models of gravitational waves, known as waveform templates, aid detectors by guiding searches for signals, typically through a method known as *matched filtering* [11, 152]. Waveform templates are also essential for *parameter estimation*: approximations of gravitational wave source characteristics, such as the masses, spins, distances, and locations of merging black holes.

Together, gravitational wave models and detections are reshaping our understanding of the universe. Observations of compact object mergers have led to the discovery of a new class of heavy stellar-mass black holes [11, 12, 16, 17, 19, 18], provided evidence for the existence of uncharacteristically massive neutron star binaries [23], and placed constraints on the astrophysical environments of compact objects [10]. Detections have also set new limits on our understanding of gravity and the universe by enabling strong-field tests of general relativity [13] and new measurements of the Hubble constant [14].

The advent of gravitational wave astronomy has also precipitated novel *multi-messenger* observations of the universe. Astronomers, armed with the location of recent gravitational wave sources, are now providing follow-up observations of gravitational events with traditional telescopes. By capturing the electromagnetic radiation that accompanies some gravitational wave events, observers are measuring astrophysical systems through multiple windows. This field of multi-messenger astrophysics has already provided the first observation of a kilonova explosion due to the merger of two neutron stars [20, 15], confirmed the primary site of the r-process for creation of heavy elements [13], and constrained the neutron star equation of state [21].

These new scientific advances will continue as gravitational wave detections and multi-messenger follow-ups continue in the years to come. Detection rates have already increased within the last year due to the recent sensitivity enhancements of LIGO and Virgo. Though the current observing runs have been cut short due to the COVID-19 pandemic, the recent inauguration of the new ground-based observatory KAGRA [3] in Japan and the continuing development of LIGO-India [219] promise a fruitful future for ground-based gravitational wave science.

These ground-based detectors will be complemented by the space-based LISA mission [25, 6, 9, 28], which was recently approved by ESA for its L3 mission. LISA will be sensitive to gravitational waves with frequencies of $10^{-4} - 10^{-1}$ Hz. Because this range of frequencies is invisible to ground-based detectors, LISA will detect tens of thousands of new gravitational wave sources, from white dwarf binaries in the local Milky Way to merging massive black holes in the distant and early universe [28]. While white dwarf and massive black hole binaries evolve in a similar manner to the stellar-mass compact object binaries observed by LIGO and Virgo, their unique astrophysical environments will allow LISA to study the birth and growth of massive black holes, galaxies, and the universe [28]. Another promising candidate for LISA will be stellar-mass compact objects inspiraling into massive black holes, also known as extreme-mass-ratio inspirals (EMRIs). Unlike the similar-mass binaries observed by ground-based observatories, EMRIs will produce long-lived and intricate gravitational wave signals, making them an exciting new source for observing the universe with gravitational wave astronomy.

1.1.3: Extreme-mass-ratio inspirals

EMRIs are compact object binaries composed of a stellar-mass compact object with mass $\mu \simeq 1 - 60 M_\odot$ in orbit around a massive black hole (MBH) with mass $M \simeq 10^4 - 10^7 M_\odot$.[1] They are characterized by their small mass-ratio $\epsilon \equiv \mu/M \sim 10^{-7} - 10^{-4}$. They primarily reside in galactic cores, where MBHs can capture stellar-mass compact objects that form in the surrounding stellar cusp [27]. Once captured, the stellar

---

[1] They are also closely connected to intermediate-mass-ratio inspirals (IMRIs), which consist of stellar-mass black holes inspiraling into an intermediate-mass black hole with mass $M \sim 10^3 - 10^4 M_\odot$, and are potential LIGO sources. The recent detection by LIGO and Virgo of an asymmetric mass-ratio stellar-mass black hole binary [211] is a promising sign that IMRIs may be observed in future observing runs by ground-based detectors.

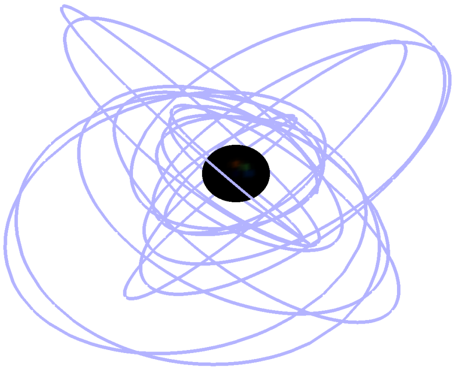

Figure 1.1: Several orbits for an EMRI. The lines trace the path of a small compact object as it orbits around a rotating MBH. On short timescales, this path is well described by a geodesic.

compact object undergoes a gradual inspiral around the MBH, completing approximately $\epsilon^{-1} \sim 10^4 - 10^7$ orbits while it radiates gravitational waves that are visible to LISA [26]. Several orbits of a typical EMRI are shown in Fig. 1.1. Due to their long duration, EMRI signals will have cumulative signal-to-noise ratios of several tens to several hundreds, allowing for high-precision measurements that exceed the capabilities of optical telescopes or current gravitational wave detectors [47].

For example, LISA will measure the spins and masses of MBHs in EMRIs to a fractional precision of $\sim 10^{-5}$, providing precise data for understanding the MBH mass function and the astrophysical channels that lead to MBH growth [26, 27, 47]. With LISA, astronomers will also learn about the astrophysical environments and stellar populations of galactic nuclei—along with the evolutionary histories of MBHs and their host galaxies—by identifying the processes that drive EMRI formation [47, 27]. EMRIs composed of white dwarfs or surrounded by accretion disks may even produce electromagnetic counterparts, enabling multi-messenger observations of EMRI mergers [27, 47]. Cosmologists will also be able to calculate the Hubble constant by measuring the redshift of EMRI sources to a fractional error $< 10\%$, out to redshifts $z \sim 4.5$ [47]. Furthermore, as an EMRI evolves, its GW signal will effectively 'map' the spacetime of the MBH, allowing LISA to measure fractional deviations in the quadrupole moment of the MBH (which describes the degree to which the MBH deviates from being a perfect sphere) on the order $\sim 10^{-4}$ [32, 26, 27]. Because the quadrupole moment of a black hole is precisely determined by the rotation of the black hole, these measurements will provide an unprecedented test of general relativity and a probe for alternate theories of gravity. LISA, like current ground-based detectors, will rely on simulated waveforms to guide gravitational wave observations and allow detailed parameter fits that extract the characteristics of these sources (e.g., masses, spins) [27]. Accurate models of EMRIs are, therefore, vital to unlocking the scientific potential of LISA observations.

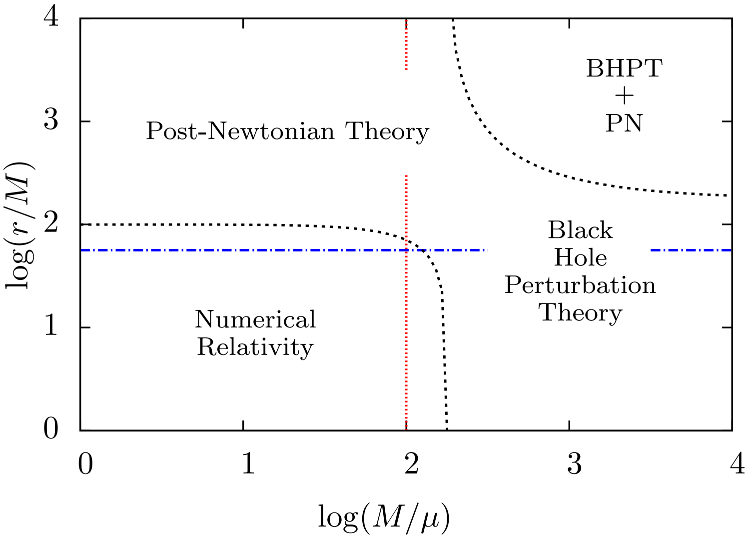

Figure 1.2: The domains of validity for various approximation techniques for solving the two-body problem in general relativity. Here, μ and M refer to the masses of the two bodies and r refers to their separation. Post-Newtonian (PN) theory is most accurate for systems with large separations $r \gg M$, numerical relativity (NR) for systems with similar mass and length scales $\mu \sim M \sim r$, and black hole perturbation theory (BHPT) for systems with large mass ratios $\mu \ll M$.

Section 1.2: The two-body problem

Modeling the motion and evolution of two interacting objects is known as the *two-body problem* in physics. While this problem sounds deceptively simple, methods for solving the two-body problem can significantly vary depending on the types of interactions that guide the bodies' motions. One of the most famous two-body problems is the case of two astrophysical bodies interacting according to Newton's law of gravitation. This, of course, is referred to as the Kepler problem. As is well known, the Kepler problem possesses exact solutions, known as *Keplerian orbits*, for the motion of the binary. Given the initial positions and velocities of the two astrophysical bodies, one can exactly solve for their Keplerian orbital motion. For most of the planets in our solar system, Keplerian orbits provide a reasonable approximation of their motion around the Sun (on short timescales).

Compact object binaries, on the other hand, are not well-approximated by Newtonian gravity. They interact according to Einstein's field equations of general relativity. Unfortunately, the two-body problem in general relativity has no exact, closed-form solutions. This is due to the non-linearity of Einstein's equations and the fact that the relativistic gravitational field is dynamical. Researchers must rely, instead, on approximation frameworks to model the motion of compact object binaries. Post-Newtonian (PN) theory, numerical relativity (NR), and black hole perturbation theory (BHPT) form the three leading approximation methods for modeling compact binaries. The PN and BHPT formalisms make use of iterative schemes to solve Einstein's field equations, while NR recasts the field equations so that they can be solved via numerical routines on a computer. Each approximation method is best suited for different physical regimes, as shown in Fig. 1.2. Widely-separated, slow-moving binaries are best approximated by PN theory; similar-mass, close binaries by NR; and disparate-mass binaries by BHPT. The EMRI two-body problem, therefore, is naturally approached by the methods of BHPT.

To better understand these methods, I first provide a brief review of the general two-body problem in general relativity to establish the notation and conventions that will be used in this dissertation. Following this review, I will outline how the PN and NR frameworks have been used to model compact object binaries in aid of recent gravitational wave detections. Building on this discussion I will present the BHPT formalism and how it has been used to model EMRIs. I will then conclude by summarizing some of the outstanding questions and unresolved issues in BHPT research.

1.2.1: Brief review of gravity and general relativity

In this section I give a brief overview of the basic principles and equations of general relativity to provide some background for the introductory reader and to set notation for the expert. (For a more in depth review of general relativity, I refer the reader to Ref. [63].) To make this discussion more concrete, consider the two-body problem of an astronaut and the Earth. Since the Earth is much more massive than the astronaut, the Earth is effectively stationary while the astronaut orbits around it. In Newtonian gravity, the Earth possesses a gravitational potential $U_\oplus$, which satisfies Poisson's equation

$$\nabla^2 U_\oplus \equiv \left(\frac{\partial^2}{\partial x^2} + \frac{\partial^2}{\partial y^2} + \frac{\partial^2}{\partial z^2}\right) U_\oplus = 4\pi G \rho_\oplus, \tag{1.1}$$

where ∇ is the standard gradient operator, G is Newton's gravitational constant, and $\rho_\oplus$ is the (mass) density of the Earth. Outside of the Earth, $U_\oplus$ takes the form

$$U_\oplus(\mathbf{x}) = -\frac{GM_\oplus}{|\mathbf{x} - \mathbf{x}_\oplus|}, \tag{1.2}$$

where $M_\oplus$ is the gravitational mass of the Earth and $\mathbf{x}_\oplus$ is the position of the Earth's center of mass. The astronaut, due to their own gravitational mass μ, interacts with the Earth's gravitational field, $-\nabla U_\oplus$, via Newton's universal law of gravitation

$$\mathbf{F}_{\mathrm{ast}} = -\mu \nabla U_\oplus = -\frac{G\mu M_\oplus}{\mathrm{r}^3}\mathbf{r}, \tag{1.3}$$

where $\mathbf{F}_{\rm ast}$ is the gravitational force experienced by the astronaut, $\mathrm{r} \equiv |\mathbf{r}| \equiv |\mathbf{x}_{\rm ast} - \mathbf{x}_{\oplus}|$, and $\mathbf{x}_{\rm ast}$ is the position of the astronaut. The astronaut's motion around the Earth is then given by Newton's second law, $\mathbf{F}_{\rm ast} = \mu' \mathbf{a}_{\rm ast}$, where $\mathbf{a}_{\rm ast}$ is the astronaut's acceleration and μ' is its *inertial* mass. An unique property of gravity is that an object's intertial mass is equivalent to its gravitational mass, i.e., $\mu' = \mu$. The equivalence of the inertial and gravitational masses is known as the *weak equivalence principle.*[2]. Consequently, the astronaut's acceleration only depends on the Earth's gravitational field,

$$\mathbf{a}_{\rm ast} \equiv \frac{d^2\mathbf{x}_{\oplus}}{dt^2} = -\nabla U_{\oplus} = -\frac{GM_{\oplus}}{\mathrm{r}^3}\mathbf{r}. \tag{1.4}$$

Furthermore, any object, regardless of its mass or composition, experiences the exact same acceleration due to the Earth's gravitational field.

While this result may appear innocuous, imagine if the astronaut lets go of a hammer (without giving it any additional velocity) as they orbit the Earth. Because the astronaut and the hammer have the exact same acceleration, the hammer will appear to remain at rest in the astronaut's reference frame. Because everything immediately around the astronaut (i.e., the hammer) is effectively stationary, the astronaut cannot measure the presence of any external forces. (This type of reference frame—in which there are no external, non-gravitational forces—is known as a *locally inertial frame.*) An interesting consequence is that, even though the astronaut is supposedly orbiting the Earth due to a gravitational force, the astronaut cannot actually measure this force of gravity. Therefore, they can claim that *there is no gravity* in their locally inertial frame. This is an example of the *Einstein equivalence principle*:

> *No measurement carried out in a suitably small laboratory moving freely in a gravitational field can reveal the existence of gravity locally, within the confines of the laboratory,*

as succinctly stated by Poisson and Will [181]. The Einstein equivalence principle provides the foundation for general relativity. If freely-moving observers cannot measure the existence of gravity, then gravitational fields and gravitational forces do not exist. Instead, in general relativity, the gravitational "field" and "force" that one measures are instead the result of the curvature of spacetime produced by the nearby presence of mass and energy. On small-enough scales spacetime appears flat (just like how, on small scales, the Earth appears to be flat), and an observer can construct a locally inertial frame where they do not measure any effects due to gravity, just like the astronaut with their hammer. But on larger scales, the curvature of spacetime will curve the paths of freely moving observers. For example, the astronaut orbits the Earth, because the Earth curves spacetime, and the astronaut follows a curved path through this curved space.

---

[2] Newtonian gravity does not provide an explanation as to why this occurs.

Mathematically, the structure of curved spacetime is represented by a differentiable manifold, $\mathcal{M}$, which is described by a *metric tensor* $g_{\mu\nu}$, where Greek indices range from 0 to 3. The metric is real and symmetric ($g_{\mu\nu} = g_{\nu\mu}$), and measures (four-dimensional) lengths in spacetime. For example, the proper distance s is given by the infinitesimal line element

$$ds^2 = g_{\mu\nu} dx^\mu dx^\nu = \sum_{\mu=0}^{3} \sum_{\nu=0}^{3} g_{\mu\nu} dx^\mu dx^\nu, \tag{1.5}$$

where the second equality defines the Einstein summation convention, in which repeated indices are summed over. I will use this convention throughout the rest of this work. Equation (1.5) is the non-Euclidian generalization of the Pythagorean theorem.

Therefore, in general relativity the metric describes the "gravitational field" and small objects move along the extremal paths, or *geodesics*, through the curved "gravitational" space defined by the metric. If the astronaut follows a geodesic around the Earth, then their (four-)position $x^\mu_{\rm ast}$ is given by the geodesic equation

$$u^\alpha \nabla_\alpha u^\beta = 0, \tag{1.6}$$

where $u^\alpha \equiv dx^\alpha_{\rm ast}/d\tau$ is the astronaut's four-velocity, τ is the proper time ($d\tau^2 = -ds^2$), and ∇_α is the *covariant derivative*, which is defined with respect to the metric $g_{\alpha\beta}$. The covariant derivative is the curved-space generalization of the standard partial differential operator $\partial_\mu \equiv \partial/\partial x^\mu$. It is connected to the partial differential operator by the Christoffel symbols (more generally known as the connection coefficients) $\Gamma^\mu_{\alpha\beta}$,

$$\Gamma^\mu_{\alpha\beta} = \frac{1}{2} g^{\mu\nu} (\partial_\alpha g_{\nu\beta} + \partial_\beta g_{\nu\alpha} - \partial_\nu g_{\alpha\beta}). \tag{1.7}$$

and operates on vectors and other low-order tensors in the following manner,

$$\nabla_\mu v^\alpha = \partial_\mu v^\alpha + \Gamma^\alpha_{\mu\nu} v^\nu, \qquad \nabla_\mu V^{\alpha\beta} = \partial_\mu V^{\alpha\beta} + \Gamma^\alpha_{\mu\nu} V^{\nu\beta} + \Gamma^\beta_{\mu\nu} V^{\alpha\nu}, \tag{1.8}$$

$$\nabla_\mu w_\alpha = \partial_\mu w_\alpha - \Gamma^\nu_{\mu\alpha} w_\nu, \qquad \nabla_\mu W_{\alpha\beta} = \partial_\mu W_{\alpha\beta} - \Gamma^\nu_{\mu\alpha} W_{\nu\beta} - \Gamma^\nu_{\mu\beta} W_{\alpha\nu}. \tag{1.9}$$

Consequently, the geodesic equations for the astronaut can also be written in the more detailed form

$$\frac{d^2 x^\alpha_{\rm ast}}{d\tau^2} + \Gamma^\alpha_{\mu\nu} \frac{dx^\mu_{\rm ast}}{d\tau} \frac{dx^\nu_{\rm ast}}{d\tau} = 0. \tag{1.10}$$

In flat spacetime, the metric is given by the Minkowski metric $\eta_{\mu\nu} = \mathrm{diag}(-1, 1, 1, 1)$, so that $\Gamma^\alpha_{\mu\nu} = 0$. The geodesic equation, therefore, reduces to the equation for a straight line $d^2\mathbf{x}_{\rm ast}/dt^2 = 0$, just as expected. In curved spacetime the Christoffel symbols do not vanish globally. A particle's path, will therefore, deviate from a straight line due to the presence of spacetime curvature.

Geodesics, however, only describe the paths of small objects, or *test bodies*. Extended, massive bodies, like stars or white dwarfs, are described by a stress-energy tensor $T_{\mu\nu}$, which evolves due to the curved-space generalization of the conservation of energy and momentum

$$\nabla_\nu T^{\mu\nu} = \partial_\nu T^{\mu\nu} + \Gamma^\mu_{\nu\alpha} T^{\alpha\nu} + \Gamma^\nu_{\nu\alpha} T^{\mu\alpha} = 0. \tag{1.11}$$

These conservation-like equations, much like the geodesic equations, are influenced by spacetime curvature through their dependence on the metric. Equation (1.11), therefore, describes how a stress-energy source, such as a white dwarf, evolves through curved spacetime. The metric, in turn, evolves according Einstein's field equations

$$G_{\mu\nu}[g] \equiv R_{\mu\nu}[g] - \frac{1}{2} g_{\mu\nu} R[g] = \frac{8\pi G}{c^4} T_{\mu\nu}, \tag{1.12}$$

where c is the speed of light, $G_{\mu\nu}$ is the Einstein tensor (which depends on $g_{\mu\nu}$), $R \equiv R^\alpha{}_\alpha$ is the Ricci scalar, $R_{\alpha\beta} \equiv R^\mu{}_{\alpha\mu\beta}$ is the Ricci tensor, and

$$R^\alpha{}_{\beta\gamma\delta} \equiv \partial_\delta \Gamma^\alpha_{\beta\gamma} - \partial_\gamma \Gamma^\alpha_{\beta\delta} + \Gamma^\alpha_{\mu\gamma} \Gamma^\mu_{\beta\delta} - \Gamma^\alpha_{\mu\delta} \Gamma^\mu_{\beta\gamma}, \tag{1.13}$$

is the Riemann curvature tensor. Equation 1.12 represents a set of 10 coupled, nonlinear partial differential equations for the 10 independent components of $g_{\mu\nu}$. This is in contrast to Newtonian gravity, which has a single field equation, Eq. (1.1), for the single component of the gravitational potential field, U. Therefore, there are few known analytical solutions to Eq. 1.12. For black hole spacetimes, the field equations slightly simplify to the vacuum field equation, $R_{\mu\nu} = 0$, and thus are more amenable to solution. Leveraging this vacuum condition and multiple symmetries, researchers have found analytic, closed-form solutions for isolated black holes, such as the spherically-symmetric Schwarzschild spacetime of a non-spinning black hole and the axisymmetric Kerr spacetime of a rotating black hole. For general two-body system, however, there is no known way to exactly calculate $g_{\mu\nu}$. Hence, researchers must turn towards approximate methods for solving Eqs. (1.11) and (1.12).

1.2.2: Post-Newtonian theory and numerical relativity

PN theory has been one of the longest-serving approximation tools for general relativity [96, 150, 97, 102]. In the PN formalism, one assumes that a gravitational system is weakly bound and slowly moving, compared to the speed of light c. Then one can expand Einstein's field equations and the stress-energy constraint in powers of $1/c$, and iteratively solve for the equations of motion for a gravitational system. This formalism was employed by Einstein to derive the famous quadrupole formula [96] soon after formulating his theory of general relativity. Lorentz and Droste [150]; Einstein, Infeld, and Hoffman [97]; and Fock [102] would later develop the first-order (1PN) corrections to the equations of motion. At higher-orders, calculations at first diverge, because the PN approximation only makes assumption about spacetime near the source, in the region known as the *near zone*. These divergences are tamed by introducing additional, sophisticated expansions near the boundaries in the *wave zone* and finding solutions that match in the regions where the near and wave zones overlap. Through various methods, PN researchers have calculated the equations of motion to 4PN order [77, 46, 78, 155, 104, 103], with 5PN results now emerging [51]. (For an in depth review on PN theory, I refer the reader to Refs. [52, 181].)

In NR, Einstein's field equations are recast in the form of an initial value problem so that they are more amenable to solution via numerical integration. Using a 3+1 decomposition, the field equations are separated into slices, or *foliations*, of three-dimensional space, with each slice acting as a different snapshot in time. First the initial data are solved on the first time slice. Data are then pushed from one time slice to another by numerically solving Einstein's field equations using finite-differencing or spectral algorithms. Though some of the first NR simulations were attempted by Hahn and Lindquist in 1964 [120], it took over four decades for numerical relativists to successfully simulate the merger of two inspiraling, equal-mass black holes [190, 61, 29]. While NR simulations are still computationally intensive, highly-developed codes, such as the Einstein Toolkit [2] and SpEC [7], are well advanced, making NR simulations and routines much more accessible to researchers. (For more discussion on NR, I refer the reader to Refs. [24, 116, 44, 99].)

Full inspiral waveforms of stellar-mass compact binaries are now constructed by combining PN results with NR simulations. PN theory provides a powerful approximation for computing the early inspiral of the compact objects, while NR captures their behavior as they merge and ring down spacetime to form a new black hole. By calibrating phenomenological and physically-motivated effective-one-body models against PN and NR calculations, researchers have generated libraries of gravitational waveform templates for LIGO and Virgo [11]. Thus, PN theory and NR have been the two leading approximations for studying black hole binaries in the era of gravitational wave astronomy. Unfortunately, neither approximation method is well suited for modeling the strong-field dynamics of EMRIs. PN theory eventually breaks down in an EMRI due to the large orbital velocity of the stellar-mass compact object,[3] while NR has a difficult time numerically handling the disparate length scales set by the small compact object and the MBH. EMRIs are, therefore, more naturally understood using BHPT.

---

[3] As shown in Fig. 1.2, there exists an overlap region where the PN and BHPT approximations are equally valid. This occurs when two bodies have disparate masses but are also widely separated.

1.2.3: Black hole perturbation theory and the gravitational self-force

BHPT is best suited for astrophysical systems with a small mass μ orbiting a much more massive black hole with mass M, (e.g., an EMRI or IMRI). The equations of motion for the system are generated by expanding the metric tensor for the entire spacetime $\mathbf{g}_{\mu\nu}$ in powers of the mass ratio $\epsilon \equiv \mu/M$,

$$\mathbf{g}_{\mu\nu} = g_{\mu\nu} + \epsilon h^{(1)}_{\mu\nu} + \epsilon^2 h^{(2)}_{\mu\nu} + O(\epsilon^3), \tag{1.14}$$

where $g_{\mu\nu}$ is the 'background' spacetime defined by the MBH (e.g., Schwarzschild, Kerr metrics), $h^{(1)}_{\mu\nu}$ is the first-order metric perturbation due to the presence of the small mass, $h^{(2)}_{\mu\nu}$ is the second-order perturbation, and so on. Similar to PN theory, the field equations, stress-energy constraint, and gauge conditions are expanded in powers of ϵ and iteratively solved to find field equations for the metric perturbations $h^{(n)}_{\mu\nu}$ and equations of motion for the small mass.

In the limit $\epsilon \to 0$, all of the $h^{(n)}_{\mu\nu}$ terms vanish and the stellar-mass compact object follows a geodesic in the 'background' spacetime defined by the MBH (e.g., Schwarzschild, Kerr metrics). At higher orders, this small body has its own radiative field (metric perturbation) that carries away gravitational waves. For example, the first-order metric perturbation is given by the linearized Einstein equation,

$$\nabla^\alpha \nabla_\alpha \bar{h}_{\mu\nu} + g_{\mu\nu} \nabla_\alpha \nabla_\beta \bar{h}^{\alpha\beta} - \nabla_\alpha \nabla_\mu \bar{h}^\alpha{}_\nu - \nabla_\alpha \nabla_\nu \bar{h}^\alpha{}_\mu + 2R_{\alpha\mu\beta\nu} \bar{h}^{\alpha\beta} = -16\pi T_{\mu\nu}, \tag{1.15}$$

where $\bar{h}_{\mu\nu} \equiv h^{(1)}_{\mu\nu} - \frac{1}{2} g_{\mu\nu} h^{(1)}{}_\mu{}^\mu$ and $T_{\mu\nu}$ is the stress-energy tensor for the small perturbing object. The body interacts with this perturbing field, giving rise to a *gravitational self-force* (GSF) that drives its motion according to

$$\mu u^\alpha \nabla_\alpha u^\beta = \epsilon F^\beta_{\mathrm{GSF},1} + \epsilon^2 F^\beta_{\mathrm{GSF},2} + O(\epsilon^3), \tag{1.16}$$

where u^α is the four-velocity of the small mass, $F^\beta_{\mathrm{GSF},1}$ is the first-order gravitational self-force (which depends on $h^{(1)}_{\mu\nu}$), $F^\beta_{\mathrm{GSF},2}$ is the second-order gravitational self-force (which depends on $h^{(1)}_{\mu\nu}$ and $h^{(2)}_{\mu\nu}$), and higher-order terms are neglected. While, in theory, additional self-force terms can be included, for practical purposes in modeling EMRIs only the first few orders are necessary [125, 180]. Hinderer and Flanagan [125] found that the phase of an EMRI waveform, via a two-timescale expansion, can also be expressed as a series in ϵ,

$$\phi_{\mathrm{EMRI}} = \kappa_{-1} \epsilon^{-1} + \kappa_{-1/2} \epsilon^{-1/2} + \kappa_0 \epsilon^0 + O(\epsilon^{1/2}), \tag{1.17}$$

where the *adiabatic* term κ_{-1} depends on the orbit-averaged first-order gravitational self-force, the *post-1/2 adiabatic* term $\kappa_{-1/2}$ depends on the effect of special orbital resonances, and the *post-1 adiabatic* term κ_0

depends on the instantaneous value of the first-order gravitational self-force and the orbit-averaged second-order gravitational self-force. To maximize the precision of LISA gravitational wave measurements, models will need to be phase accurate within ~ 0.1 radians over the entire inspiral, requiring calculations of both the first-order and the orbit-averaged second-order gravitational self-force.

An implicit assumption in Eq. (1.16) is that, in some suitable limit, the small perturbing body can be treated as a "point-like" particle with a well-defined worldline $x_p^\mu(\tau)$ and four-velocity $u^\alpha = dx_p^\alpha/d\tau$. However, a point-particle source in Eq. (1.15) results in a retarded metric perturbation, $h_{\mu\nu}^{(1)}$, that will diverge at the location of the particle. Because the self-force acts on the particle exactly at this point, a naive calculation of the self-force using this singular field gives an unphysical result. Therefore, to obtain the regular metric perturbation that is solely responsible for the self-force one must either abandon the point-particle approximation or find a suitable procedure for "regularizing" the divergent field.

Mino, Sasaki, and Tanaka [166] provided a (non-divergent) expression for the gravitational self-force by treating the small body as an extended object and employing the method of *matched asymptotic expansions.* (See Sec. 3.3 for an extended discussion of this method.) Far from the small body, the mass μ can be treated as a point particle with a timelike worldline $x_p^\mu(\tau)$, so that at first-order Eq. (1.16) is given by

$$\mu u^\mu \nabla_\mu u^\alpha = \epsilon F^\alpha_{\mathrm{GSF},1} = -\frac{\epsilon}{2}\left(g^{\alpha\beta} + u^\alpha u^\beta\right) u^\mu u^\nu \left(2\nabla_\mu h^{\mathrm{tail}}_{\nu\beta} - \nabla_\beta h^{\mathrm{tail}}_{\mu\nu}\right), \tag{1.18}$$

where $h^{\mathrm{tail}}_{\mu\nu}$ is the tail contribution of the first-order metric perturbation $h^{(1)}_{\mu\nu}$. (I define $h^{\mathrm{tail}}_{\mu\nu}$ more precisely later in Eq. (3.61).) While $h^{(1)}_{\mu\nu}$ is still divergent, $h^{\mathrm{tail}}_{\mu\nu}$ is regular at the location of the particle. The results of Mino, Sasaki, and Tagoshi were quickly confirmed by Quinn and Wald [192]. Therefore, Eq. (1.18) is commonly referred to as the (first-order) MiSaTaQuWa equations of motion.

Detweiler and Whiting [82] provided an elegant modification to the MiSaTaQuWa equations by decomposing $h^{(1)}_{\mu\nu}$ into a regular contribution $h^{\mathrm{R}}_{\mu\nu}$, which satisfies the homogeneous form of Eq. (1.15), and a singular contribution $h^{\mathrm{S}}_{\mu\nu}$, which satisfies the sourced form of Eq. (1.15) (but with acausal boundary conditions). They found that the regular field and tail field are closely related, and that $h^{\mathrm{R}}_{\mu\nu}$ can simply replace $h^{\mathrm{tail}}_{\mu\nu}$ in Eq. (1.18),

$$F^\alpha_{\mathrm{GSF},1} = -\frac{1}{2}\left(g^{\alpha\beta} + u^\alpha u^\beta\right) u^\mu u^\nu \left(2\nabla_\mu h^{\mathrm{R}}_{\nu\beta} - \nabla_\beta h^{\mathrm{R}}_{\mu\nu}\right). \tag{1.19}$$

In the Detweiler-Whiting formalism, the particle's self-forced motion in the background $g_{\mu\nu}$ can be equivalently expressed as geodesic motion in the *effective background* $g_{\mu\nu} + h^{\mathrm{R}}_{\mu\nu}$, providing a clever reinterpretation of the self-force problem. (For a more in depth review of BHPT, I refer the reader to Refs. [30, 180, 41].)

In practice, it is challenging to self-consistently evolve Eq. (1.18). The motion of the small body—

captured by $T_{\mu\nu}$ in Eq. (1.15)—sources the metric perturbation, which, in turn, produces a self-force that reacts back on the small body and changes its motion (Eq. (1.18)). Either new approximations must be introduced to separate this interdependence, or Eqs. (1.15) and (1.18) must be solved "all-at-once," akin to NR.

The *two-timescale* expansion provides an approximate framework for evolving an EMRI. This method expands the equations of motion for an EMRI in terms of two fundamental time periods: the orbital timescale $T_{\mathrm{orb}} \sim M$ (i.e., the time it takes the small mass to complete an orbit around the MBH) and the adiabatic or radiation-reaction timescale $T_{\mathrm{rr}} \sim M\epsilon^{-1}$ (i.e., the time it takes the small mass to inspiral into the MBH) [125]. This expansion naturally separates how the short-term orbital motion gives rise to gravitational waves (and a gravitational self-force), and how the long-term radiation of gravitational waves drives the stellar-mass compact object on a decaying inspiral into the MBH. While the two-timescale expansion is a promising formalism for modeling EMRIs, the general form of this expansion is still in development and breaks down at large distances, near the horizon of the MBH, and during resonances [41].

Consequently, EMRI waveforms are typically modeled with a method closely-related to the two-timescale expansion, known as *osculating geodesics* [187, 112]. On orbital timescales the small body's motion is well approximated by a bound geodesic and can be parameterized in terms of orbital 'constants,' such as the semi-latus rectum, orbital eccentricity, and orbital inclination. (See Chapter 2 for further discussion of geodesics and bound motion.) In the osculating geodesics approach, these constants are allowed to evolve due to the effects of the gravitational self-force. This motivates an additional approximation: to calculate the self-force, one assumes that the *entire* past motion of the stellar-mass compact object s described by a geodesic, then calculates the first-order gravitational self-force produced by this geodesic motion. Because the gravitational self-force mostly depends on the small body's geodesic-like motion on orbital timescales, this approximation is relatively accurate and only produces an $O(\epsilon)$ error in the self-force. (Therefore, this assumption is equivalent to neglecting the second-order self-force.) To model the long-term evolution of an EMRI, an osculating geodesics code (1) assigns the small body to a geodesic, (2) calculates the resulting gravitational self-force produced by this geodesic motion, and then (3) uses this gravitational self-force result to effectively 'push' the small mass to a new geodesic. The process is then repeated, driving the body from one geodesic to another until it is eventually pushed onto a plunging orbit into the MBH. The EMRI's waveform is then constructed by 'stitching' together the gravitational wave signals produced along each geodesic in the evolution.

Long-term, self-forced inspiral calculations of Schwarzschild EMRIs via osculating geodesics are well advanced [235, 177, 239, 226], tracking the accumulated orbital or gravitational wave phase to accuracies better than $\phi_{\mathrm{EMRI}} \simeq 0.1$ due to all first-order-in-the-mass-ratio effects at post-1-adiabatic order. [125] These

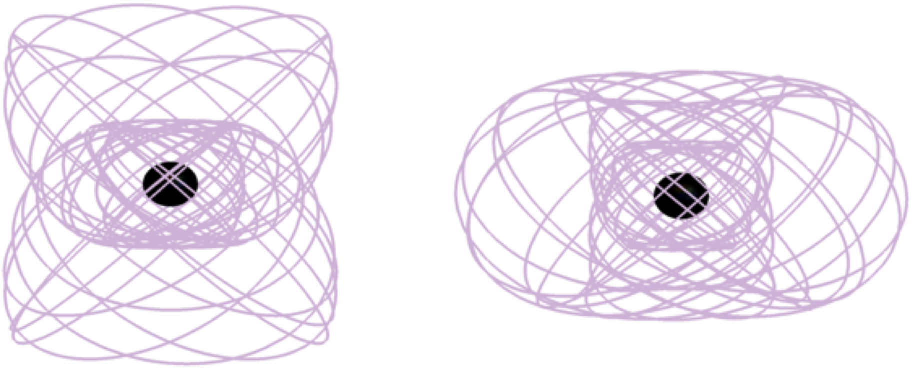

Figure 1.3: Two trajectories for stellar-mass compact objects with the exact same $r\theta$-resonant frequencies. These two compact objects, however, entered resonance with different initial positions and velocities, resulting in these two different trajectories.

calculations, however, lack only the orbit-averaged dissipative part of the second-order self-force. Progress is still being made on understanding and calculating the second-order gravitational self-force [183, 182, 186, 243, 161, 184, 170, 188]. In the case of Kerr EMRIs, steady developments have been made in gravitational self-force calculations for circular and bound equatorial orbits [206, 138, 225, 222, 160, 110, 33], with progress recently reported [224] in calculating the gravitational self-force on generic Kerr orbits. In principle this latest self-force result could serve as the basis for long-term inspiral models of astrophysically relevant EMRIs, but prospects are dimmed at present by high computational costs of these gravitational self-force calculations.

The exploration of orbital resonances and their impact on EMRI gravitational waves has also been limited. Researchers expect that the vast majority of EMRIs observed by LISA will experience at least one strong $r\theta$-resonance [200]. These resonances occur when the frequencies associated with the librating radial and polar motion of an EMRI's smaller body form a rational-number ratio. (The lower the integers in the numerator and denominator of the rational number, the stronger the resonance.) During these resonances, EMRIs will evolve either slower or faster than the non-resonant prediction, depending on their phase when they enter the resonance. Resonant moments thus drive significant 'kicks' in the amount of energy and angular momentum that EMRIs radiate through gravitational waves [100, 200]. The structure of the resonant motion and the nature of the kick is quite sensitive to the orbital phase, varying significantly as a function of the initial position and velocity at which the small mass enters resonance, as shown in Fig. 1.3. This sensitivity to initial conditions during resonant kicks can enhance errors in EMRI waveform models by a factor of $\epsilon^{-1/2}$ and thus contribute to $\kappa_{-1/2}$ in Eq. (1.17). Previous research on these resonant effects have relied on approximate adiabatic flux codes and weak-field PN results [100, 200, 48]. To date, the relationship between $r\theta$-resonances and the behavior of the full gravitational self-force remains unexplored. The focus of this work is to test new techniques for calculating the self-force in Kerr spacetime and to provide the first numerical calculations of the self-force during $r\theta$-resonances.

Section 1.3: A developmental scalar model

Waveform templates produced from self-force calculations will be useful in aiding signal detection of EMRIs and will be essential for parameter estimation of LISA sources [27]. Calculations of the gravitational self-force in Kerr spacetime, however, still require significant refinement and development in order to contribute to full inspiral models of EMRIs. In the past, the scalar field self-force analogue [191] has frequently been used as a simplified model to develop new insights and tools for use in the gravitational case. In the scalar model, the stellar-mass compact object is given a scalar charge. Consequently, the object possesses a perturbing scalar field and radiates scalar waves, which interact with the charge to produce a *scalar self-force* (SSF). The SSF has been computed in Schwarzschild spacetime [56, 245, 57, 31, 81, 84, 118, 227, 228, 66, 60, 62, 242, 85, 229, 241] and in Kerr spacetime using frequency-domain [236, 237, 234] and time-domain calculations [214]. For my dissertation, I consider a scalar model and produce the first scalar self-force calculations for generic (inclined, eccentric) orbits to develop new methods for tackling the gravitational self-force problem in Kerr spacetime.

1.3.1: Summary of scalar self-force formalism

The SSF model I consider assumes a point particle of mass μ and scalar-charge q in bound motion about a Kerr black hole of mass M and spin parameter a. Perturbations in the gravitational field and the associated gravitational self-force are neglected. Instead the particle's motion generates a scalar field Φ, whose local behavior acts back on the scalar charge to produce the SSF. Absent the SSF, the motion of the particle is a geodesic in the Kerr spacetime. The scalar field satisfies the curved-space Klein-Gordon equation (i.e., the spin-0 Teukolsky equation [209])

$$g^{\alpha\beta}\nabla_\alpha\nabla_\beta\Phi = -4\pi\rho_{\mathrm{scalar}}, \tag{1.20}$$

where ρ_{scalar} is the scalar (point) charge density, $g^{\alpha\beta}$ is the (inverse) Kerr metric, and ∇_α is the covariant derivative with respect to the Kerr metric. Causal boundary conditions are selected, making the resulting solution the retarded field Φ^{ret}. The particle's timelike worldline is $x_p^\alpha(\tau)$ and its four-velocity is $u^\alpha = dx_p^\alpha/d\tau$, where τ is proper time. Formally, the SSF will make the motion non-geodesic and the SSF will in principle depend upon the entire past inspiral. However, if q is sufficiently small and the SSF weak, the inspiral will be adiabatic, mimicking the gravitational self-force case with EMRIs. Making this assumption here, I take the past worldline as some (arbitrary) bound geodesic and calculate the SSF along that fixed motion, the result being the (approximate) *geodesic self-force.*

The retarded field diverges at the point charge, necessitating a regularization procedure [191] to compute the SSF. Detweiler and Whiting [82], much like in the gravitational case, gave one particular separation of the retarded field into regular and singular pieces $\Phi^{\mathrm{ret}} = \Phi^{\mathrm{R}} + \Phi^{\mathrm{S}}$, where Φ^{S} satisfies the same inhomogeneous wave equation (1.20) as Φ^{ret} but with (different) boundary conditions, such that Φ^{R} not only satisfies the source-free wave equation but is the part of the field solely responsible for the SSF

$$u^{\beta}\nabla_{\beta}(\mu u_{\alpha}) = F_{\alpha} = \lim_{x\to x_p} q\nabla_{\alpha}\Phi^{\mathrm{R}}. \tag{1.21}$$

Because the SSF is not orthogonal to the four-velocity [191], all four components of F_{α} must be determined. Substitution of Φ^{ret} or Φ^{S} in Eq. (1.21) in place of Φ^{R} produces corresponding forces, $F^{\mathrm{ret}}_{\alpha}$ and F^{S}, both of which are divergent on the particle worldline. Thus even though one might write

$$F_{\alpha} = F^{\mathrm{ret}}_{\alpha} - F^{\mathrm{S}}_{\alpha}, \tag{1.22}$$

the expression is not immediately useful given the divergences. Instead, one practical procedure is mode-sum regularization [37, 39], wherein the retarded, singular, and regular fields (as well as their associated forces) are decomposed into angular harmonic multipoles (typically using scalar spherical harmonics Y_{lm}). The individual mode amplitudes are finite and if the subtraction in (1.22) is taken before summing (over l), the finite SSF is recovered

$$F_{\alpha} = \sum_{l=0}^{+\infty}\left(F^{\mathrm{ret},l}_{\alpha} - F^{\mathrm{S},l}_{\alpha}\right). \tag{1.23}$$

The singular part $F^{\mathrm{S},l}_{\alpha}$ can be obtained by local analytic expansion in an l-dependent series with l-independent regularization parameters. The lower-order parameters are known [39]. The structure of higher-order terms is also understood [81] and analytic expressions have been given for certain restricted motions on Schwarzschild [121, 123] and Kerr [122] backgrounds.

With an assumed fixed background geodesic, the SSF can be further decomposed into dissipative ($F^{\mathrm{diss}}_{\alpha}$) and conservative ($F^{\mathrm{cons}}_{\alpha}$) pieces [162, 125]

$$F_{\alpha} = F^{\mathrm{diss}}_{\alpha} + F^{\mathrm{cons}}_{\alpha}. \tag{1.24}$$

The dissipative part $F^{\mathrm{diss}}_{\alpha}$ is responsible for the secular orbital decay producing the inspiral, while $F^{\mathrm{cons}}_{\alpha}$ serves to perturb the orbital parameters. The dissipative self-force does not require regularization, as it is derived from the difference between retarded and advanced fields, $\Phi^{\text{diss}} = \frac{1}{2}(\Phi^{\text{ret}} - \Phi^{\text{adv}})$. The regularization procedure is still necessary to determine F_α^{cons}.

Calculating the SSF is, therefore summarized by the following five-step process:

1. calculate the background geodesic motion of the scalar charge,
2. solve for the retarded scalar field, Φ^{ret}, produced by the moving charge,
3. evaluate the retarded multipole contributions to the SSF, $F_\alpha^{\text{ret},l}$,
4. separate $F_\alpha^{\text{ret},l}$ into its conservative and dissipative components, and
5. regularize the conservative contributions via the mode-sum regularization of Eq. (1.23).

1.3.2: Summary of dissertation work

For my dissertation work, I built a *Mathematica* code that generalizes previous frequency-domain SSF calculations to arbitrary eccentric, inclined geodesics in Kerr spacetime [172]. The code serves as a test bed for developing more advanced physical and numerical techniques to aid downstream work in making generic Kerr gravitational self-force calculations more practical. It also allows for the rapid exploration of physical parameter spaces that are less accessable to gravitational self-force codes.

In building this code, I adapted spectral source integration to the Kerr generic-orbit, scalar-source problem, significantly optimizing computation of the self-force calculations by several orders of magnitude compared to traditional numerical methods [172]. Spectral integration routines were also designed to calculate Kerr geodesics numerically and I have implemented these spectral integrators in the open-source KerrGeodesics *Mathematica* package in the Black Hole Perturbation Toolkit [1]. Through this work, I also discovered methods for optimizing the numerical implementation of the Mano-Suzuki-Takasugi (MST) function expansion formalism [154].

Upon completing this code, I produced the first calculations of the SSF due to a scalar source on an inclined, eccentric geodesic [172]. My results validated previous SSF calculations in the Kerr spacetime, and shared similar features to the recent Kerr gravitational self-force calculations produced by van de Meent [224]. I followed this work by then exploring the SSF sourced by $r\theta$-resonances. Prior to this investigation, strong-field self-force calculations had not yet been performed in this area of parameter space. My resonant SSF results, therefore, provide the first insights into the behavior of self-forces during $r\theta$-resonances. One important outcome from this exploration was the discovery that the orbit-averaged conservative self-force is negligible along resonances, supporting the "integrability conjecture" proposed by Flanagan and Hinderer [100].

With my SSF code, I also uncovered the existence of high-frequency ringing that repeatedly appears in the measurable waveforms of highly-eccentric and rapidly-rotating EMRIs. These excitations were first observed in the self-force itself by Thornburg in time-domain SSF simulations of highly-eccentric Kerr orbits, which were discussed in a series of talks [212, 213, 215] by Thornburg and reported in a paper by Thornburg and Wardell [214]. I confirmed these oscillations in the SSF with my frequency-domain SSF code and then found that these periodic high-frequency oscillations also appear in the asymptotically-accessible signals of EMRIs. These oscillations, named *quasinormal bursts* (QNBs), can be mapped to the quasinormal mode spectrum of Kerr MBHs and arise in an EMRI when the close periapsis passage of the stellar-mass compact object 'rings' the MBH. The presence of QNB features in EMRI waveforms, though faint, may aid in the characterization of EMRI GW sources. These results have already sparked follow-up research by other authors on this phenomena [197, 216, 74].

Section 1.4: Dissertation overview

The rest of my dissertation is outlined as follows. In Chapter 2, I begin with the zeroth-order approximation of EMRI motion: geodesics. I review current techniques for analyzing geodesics in Kerr spacetime, then present several methods for numerically solving Kerr geodesics. In Chapter 3, I review the basic principles of radiation, radiation-reaction, and self-forces and how they are used to evaluate the evolution of a two-body system, such as EMRIs. In Chapter 4, I present the analytical framework for calculating gravitational perturbations of Kerr black holes and the resulting gravitational self-force. In Chapter 5, I introduce an analogous but more tractable scalar perturbation model that I implemented for my dissertation. I first discuss how gravitational self-force calculations can be extended from this scalar model and then outline the methods that I use to numerically calculate the scalar self-force in Kerr spacetime. In Chapter 6, I present novel scalar self-force results for a small scalar-charged particle orbiting a Kerr black hole. I also confirm the accuracy of my code and these results with a series of validation tests. In Chapter 7, I discuss how the exploration of the scalar self-force led to the discovery of quasinormal bursts in EMRI waveforms and consider how their presence in EMRI waveforms may impact observations by LISA. In Chapter 8, I report the first (scalar) self-force results for a perturbing particle encountering an $r\theta$-resonant orbit around a Kerr black hole and discuss new findings on the behavior of the conservative self-force during resonances. I conclude with a summary of my dissertation work in Chapter 9. Throughout this work, unless stated otherwise, I use units such that $G = c = 1$, the metric signature $(-+++)$, and the sign conventions set by Misner, Thorne, and Wheeler [168].

CHAPTER 2: Bound orbits in Kerr spacetime

Section 2.1: Chapter overview

For a small mass orbiting a much more massive rotating black hole, its zeroth-order motion can be given by a bound timelike geodesic in Kerr spacetime. Unlike geodesics in Schwarzschild spacetime, bound geodesics around Kerr black holes can librate both radially and in the polar direction at different frequencies due to the axisymmetry of Kerr spacetime, as shown in Fig. 2.1. Generally, the periods of a body's radial and polar motion are incommensurate. In these cases, geodesics are *ergodic*: given an infinite amount of time, a geodesic passes through every point in a finite, bounded region of space. For certain orbital configurations, however, these radial and polar periods will form a rational number ratio. These geodesics are referred to as $r\theta$-resonances. They are distinctly not ergodic and have a different structure from non-resonant geodesics. This is highlighted in the second panel in Fig. 2.1.

To better understand these different behaviors, and to establish notation, I review the analytic framework for studying bound geodesics in the Kerr spacetime, primarily following the work of Refs. [64, 168, 205, 91, 93, 101], though I have consolidated and adapted notation for consistency. I also discuss various prescriptions for parameterizing geodesics and how those parameterizations must be handled when describing $r\theta$-resonances. I then conclude this chapter by presenting original methods for calculating Kerr geodesics numerically.

Section 2.2: Separation of the geodesic equations and chosen parameters

Consider a point particle with mass μ on a bound geodesic $x_p^\mu(\tau)$ in a Kerr background. Its geodesic is parameterized in terms of proper time τ and the background, described by the metric $g_{\alpha\beta}$, is parametrized by the black hole spin a and mass M. Adopting Boyer-Lindquist coordinates (t, r, θ, φ), the Kerr line element reads

$$ds^2 = -\left(1 - \frac{2Mr}{\Sigma}\right) dt^2 + \frac{\Sigma}{\Delta} dr^2 - \frac{4Mar\sin^2\theta}{\Sigma} dt d\varphi + \Sigma d\theta^2 + \frac{\sin^2\theta}{\Sigma}(\varpi^4 - a^2\Delta\sin^2\theta) d\varphi^2, \tag{2.1}$$

where

$$\Sigma \equiv r^2 + a^2\cos^2\theta, \qquad \Delta \equiv r^2 - 2Mr + a^2, \qquad \varpi \equiv \sqrt{r^2 + a^2}.$$

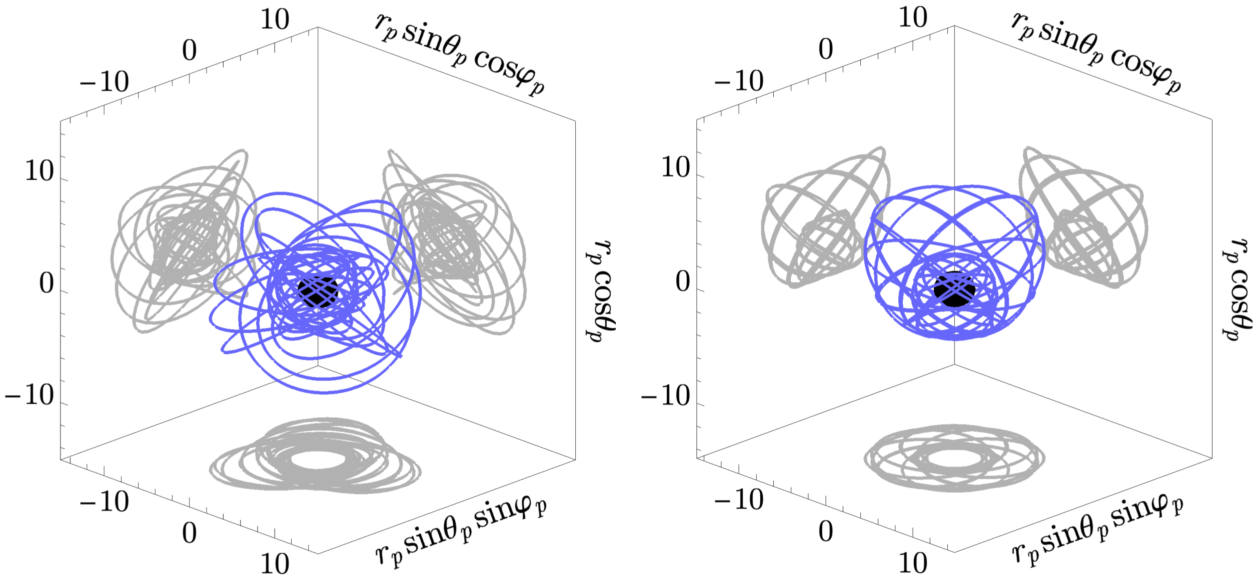

Figure 2.1: Inclined, eccentric geodesics around a Kerr black hole with spin $a/M = 0.9$ and $M = 1$. The plot on the left is a non-resonant geodesic with orbital parameters $(p, e, x_{\mathrm{inc}}) = (4.700, 0.5, \cos\pi/4)$. The motion is fairly complicated, with no obvious periodicity. The plot on the right, in contrast, is a 1:2 $r\theta$-resonant geodesic with orbital parameters $(p, e, x_{\mathrm{inc}}) \approx (4.607, 0.5, \cos\pi/4)$, where the semi-latus rectum p is truncated at four significant digits. The value of p is specifically chosen so that the periods of the particle's radial and polar motion form the ratio 1:2, one radial period for every two polar periods. The blue solid lines trace out the geodesics' three-dimensional evolution through Boyer-Lindquist coordinate space (r, θ, φ). The grey solid lines show various two-dimensional projections of the three-dimensional orbit.

In the limit that $a \to 0$ the Kerr metric in Boyer-Lindquist coordinates reduces to the Schwarzschild metric in Schwarzschild coordinates, i.e.,

$$ds^2 = -f_{\mathrm{Schw}}(r)dt^2 + f^{-1}_{\mathrm{Schw}}(r)dr^2 + r^2 d\theta^2 + r^2 \sin^2\theta d\varphi^2, \tag{2.2}$$

where

$$f_{\mathrm{Schw}}(r) \equiv \left.\frac{\Delta}{\varpi^2}\right|_{a=0} = 1 - \frac{2M}{r}, \tag{2.3}$$

and where I have used the same notation for Schwarzschild coordinates as Boyer-Lindquist coordinates (i.e., (t, r, θ, φ)), because these coordinate systems agree for $a = 0$.

Geodesic motion in Kerr spacetime is completely integrable, leading to three constants of motion—the specific energy $\mathcal{E}$, the z-component of the specific angular momentum $\mathcal{L}_z$, and the (scaled) Carter constant $\mathcal{Q}$ [64]—all of which can be related to the Killing symmetries that satisfy Killing's equation (and its tensorial generalization)

$$\nabla_\mu \xi_\nu + \nabla_\mu \xi_\nu = 0, \qquad \nabla_\mu K_{\alpha\beta} + \nabla_\alpha K_{\beta\mu} + \nabla_\beta K_{\mu\alpha} = 0. \tag{2.4}$$

The energy and angular momentum correspond to the Killing vectors $\xi^\mu_{(t)}$ and $\xi^\mu_{(\varphi)}$,

$$\mathcal{E} \equiv -\xi^\mu_{(t)} u_\mu = -u_t, \tag{2.5}$$

$$\mathcal{L}_z \equiv \xi^\mu_{(\varphi)} u_\mu = u_\varphi, \tag{2.6}$$

while the Carter constant is associated with the Killing tensor $K^{\mu\nu}$ [233],

$$\mathcal{Q} \equiv K^{\mu\nu} u_\mu u_\nu - (\mathcal{L}_z - a\mathcal{E})^2. \tag{2.7}$$

The Killing tensor can be expressed in terms of the Kinnersley null tetrad,

$$K^{\mu\nu} = 2\Sigma\, m^{(\mu} m^{*\nu)} - a^2 \cos^2\theta g^{\mu\nu}, \tag{2.8}$$

$$= 2\Sigma\, l^{(\mu} n^{\nu)} + r^2 g^{\mu\nu}, \tag{2.9}$$

where the Kinnersley null tetrad basis vectors are given by

$$l^\mu \doteq \frac{1}{\Delta}(\varpi^2, \Delta, 0, a), \qquad n^\mu \doteq \frac{1}{2\Sigma}(\varpi^2, -\Delta, 0, a), \tag{2.10}$$

$$m^\mu \doteq \frac{1}{\sqrt{2}(r + ia\cos\theta)}(ia\sin\theta, 0, 1, i\csc\theta), \tag{2.11}$$

and $m^{*\mu}$ is the complex conjugate of m^μ. The origin and utility of the Kinnersley tetrad is further discussed in Sec. 4.4.3.

The geodesic equations then take the form

$$\Sigma_p \frac{dt_p}{d\tau} = V_{tr}(r_p) + V_{t\theta}(\theta_p), \tag{2.12}$$

$$\Sigma_p \frac{dr_p}{d\tau} = \pm\sqrt{V_r(r_p)}, \tag{2.13}$$

$$\Sigma_p \frac{d\theta_p}{d\tau} = \pm\sqrt{V_\theta(\theta_p)}, \tag{2.14}$$

$$\Sigma_p \frac{d\varphi_p}{d\tau} = V_{\varphi r}(r_p) + V_{\varphi\theta}(\theta_p), \tag{2.15}$$

where the radial and polar potentials are given by

$$V_r(r) \equiv \left(\mathcal{E}\varpi^2 - a\mathcal{L}_z\right)^2 - \Delta\left(r^2 + (\mathcal{L}_z - a\mathcal{E})^2 + \mathcal{Q}\right), \tag{2.16}$$

$$V_\theta(\theta) \equiv \mathcal{Q} - \mathcal{L}_z^2 \cot^2\theta - a^2(1 - \mathcal{E}^2)\cos^2\theta, \tag{2.17}$$

while the time and azimuthal potentials are separated into their radial and polar dependencies

$$V_{tr}(r) \equiv \mathcal{E}\frac{\varpi^4}{\Delta} + a\mathcal{L}_z\left(1 - \frac{\varpi^2}{\Delta}\right), \qquad V_{t\theta}(\theta) \equiv -a^2\mathcal{E}\sin^2\theta, \tag{2.18}$$

$$V_{\varphi r}(r) \equiv a\mathcal{E}\left(\frac{\varpi^2}{\Delta} - 1\right) - \frac{a^2\mathcal{L}_z}{\Delta}, \qquad V_{\varphi\theta}(\theta) \equiv \mathcal{L}_z\csc^2\theta. \tag{2.19}$$

The subscript p means that a function is evaluated on the worldline.

Rather than parameterizing a geodesic in terms of $\mathcal{E}$, $\mathcal{L}_z$, and $\mathcal{Q}$, it is often preferable to choose constants of motion that are more closely tied to the geometry of the orbit, such as its size, shape, and orientation. The radial potential in Eq. (2.16) is a quartic polynomial in r and has four roots: $r_1 \geq r_2 \geq r_3 \geq r_4$. For a bound, stable orbit the two largest roots are finite and represent the extrema of the radial motion, such that $r_{\mathrm{max}} \equiv r_1$ and $r_{\mathrm{min}} \equiv r_2$. Analogous to Keplerian orbits, these extrema can be used to define the semi-latus rectum p and orbital eccentricity e,

$$r_{\mathrm{max}} \equiv \frac{pM}{1-e}, \qquad r_{\mathrm{min}} \equiv \frac{pM}{1+e}. \tag{2.20}$$

On the other hand, the polar potential in Eq. (2.17) can be re-expressed as a quadratic polynomial in $z^2 \equiv \cos^2\theta$,[1] with roots

$$z_{\pm}^2 \equiv \frac{\mathcal{L}_z^2 + \mathcal{Q} + \beta \pm \sqrt{(\mathcal{L}_z^2 + \mathcal{Q} + \beta)^2 - 4\mathcal{Q}\beta}}{2\beta}, \tag{2.21}$$

where $\beta \equiv a^2(1 - \mathcal{E}^2)$. In the case of a Schwarzschild black hole, this reduces to a single (degenerate) root

$$z_-^2 \equiv \frac{Q}{\mathcal{L}_z^2 + Q}. \tag{2.22}$$

For bound, stable orbits z_-^2 corresponds to the extrema of the polar motion, $\cos\theta_{\mathrm{min}} \equiv z_-$ and $\cos\theta_{\mathrm{max}} \equiv -z_-$. These extrema then define the projection of the orbital inclination,

$$x_{\mathrm{inc}} \equiv \pm\sqrt{1 - z_-^2} = \pm\cos\left(\frac{\pi}{2} - \theta_{\mathrm{min}}\right), \tag{2.23}$$

where a positive value specifies a prograde orbit and a negative value specifies a retrograde orbit. Other authors use an alternative inclination parameter that is defined from $\mathcal{L}_z$ and $\mathcal{Q}$ [134]

$$\cos\iota \equiv \sqrt{\frac{\mathcal{L}_z^2}{\mathcal{L}_z^2 + \mathcal{Q}}}. \tag{2.24}$$

---

[1] Note that this definition of z matches the definition used in Refs. [222, 224], but differs from the definition used in Refs. [92, 93], $z \equiv \cos^2\theta$.

In Schwarzschild spacetime $x_{\rm inc}$ and $\cos\iota$ are identical, which can be shown by combining Eqs. (2.22) and (2.23). I will make use of both parameters in this work. Once p, e, and $x_{\rm inc}$ are specified for an orbit, it is straightforward to determine $\mathcal{E}$, $\mathcal{L}_z$, and $\mathcal{Q}$ [205, 92].

The presence of Σ_p on the lefthand-side of Eq. (2.12)-(2.15) couples the radial and polar motion. Introducing the (Carter-)Mino time parameter λ [64, 168, 162, 91], defined by

$$d\lambda \equiv \Sigma_p^{-1} d\tau, \tag{2.25}$$

separates the radial and polar motions

$$\frac{dr_p}{d\lambda} = \pm\sqrt{V_r(r_p)}, \qquad\qquad \frac{d\theta_p}{d\lambda} = \pm\sqrt{V_\theta(\theta_p)}, \tag{2.26}$$

yielding solutions that are functions of Mino time rather than proper time, i.e., $r_p(\lambda)$. One can then solve Eqs. (2.12)-(2.15) using spectral integration methods [130, 172], analytic special functions [92, 108], or a "hybrid" scheme combining both approaches (Sec. 2.7.2). I will review methods for numerically solving Eqs. (2.12)-(2.15) in Sec. 2.7.

Section 2.3: Frequencies of generic bound motion

For inclined eccentric bound geodesics, the particle librates in r and θ with radial and polar Mino time periods

$$\Lambda_r \equiv 2\int_{r_{\rm min}}^{r_{\rm max}} \frac{dr}{\sqrt{V_r(r)}}, \qquad\qquad \Lambda_\theta \equiv 2\int_{\theta_{\rm min}}^{\pi-\theta_{\rm min}} \frac{d\theta}{\sqrt{V_\theta(\theta)}}, \tag{2.27}$$

and corresponding Mino time frequencies

$$\Upsilon_r = \frac{2\pi}{\Lambda_r} \qquad \Upsilon_\theta = \frac{2\pi}{\Lambda_\theta}. \tag{2.28}$$

In Kerr spacetime, Υ_θ is always greater than Υ_r for bound geodesics. The time and azimuthal coordinates, which depend on the radial and polar motions, accumulate at the average rates in λ

$$\Gamma = \frac{1}{\Lambda_r}\int_0^{\Lambda_r} d\lambda\, V_{tr} + \frac{1}{\Lambda_\theta}\int_0^{\Lambda_\theta} d\lambda\, V_{t\theta}, \tag{2.29}$$

$$\Upsilon_\varphi = \frac{1}{\Lambda_r}\int_0^{\Lambda_r} d\lambda\, V_{\varphi r} + \frac{1}{\Lambda_\theta}\int_0^{\Lambda_\theta} d\lambda\, V_{\varphi\theta}, \tag{2.30}$$

respectively. Together, these form the complete set of Mino time frequencies $\Upsilon_\alpha = (\Gamma, \Upsilon_r, \Upsilon_\theta, \Upsilon_\varphi)$. They are related to the fundamental coordinate time frequencies

$$\Omega_r = \frac{\Upsilon_r}{\Gamma}, \qquad \Omega_\theta = \frac{\Upsilon_\theta}{\Gamma}, \qquad \Omega_\theta = \frac{\Upsilon_\varphi}{\Gamma}, \tag{2.31}$$

which define the discrete frequency spectrum for a non-resonant geodesic

$$\omega_{mkn} \equiv m\Omega_\varphi + k\Omega_\theta + n\Omega_r. \tag{2.32}$$

Note that these coordinate frequencies do not uniquely define a geodesic due to the existence of isofrequency pairings [238], though it has been well-argued that geodesics are uniquely defined by their Mino time frequencies, Υ_α [220].

Section 2.4: Mino time representation of geodesic solutions

To understand the impact of initial conditions on geodesics, first consider an inclined, eccentric geodesic $\hat{x}_p^\mu$ with the initial conditions

$$\hat{x}_p^\mu(\lambda = 0) = (0, r_{\text{min}}, \theta_{\text{min}}, 0), \qquad\qquad \hat{u}^r(\lambda = 0) = \hat{u}^\theta(\lambda = 0) = 0. \tag{2.33}$$

Following the nomenclature of Ref. [91], I refer to a geodesic with these initial conditions as a *fiducial geodesic*. Integrating Eqs. (2.12)-(2.15) and enforcing these fiducial conditions, one finds solutions of the form

$$\hat{t}_p(\lambda) = \Gamma\lambda + \Delta\hat{t}^{(r)}(\Upsilon_r\lambda) + \Delta\hat{t}^{(\theta)}(\Upsilon_\theta\lambda), \tag{2.34}$$

$$\hat{r}_p(\lambda) = r_{\text{min}} + \Delta\hat{r}^{(r)}(\Upsilon_r\lambda), \tag{2.35}$$

$$\hat{\theta}_p(\lambda) = \theta_{\text{min}} + \Delta\hat{\theta}^{(\theta)}(\Upsilon_\theta\lambda), \tag{2.36}$$

$$\hat{\varphi}_p(\lambda) = \Upsilon_\varphi\lambda + \Delta\hat{\varphi}^{(r)}(\Upsilon_r\lambda) + \Delta\hat{\varphi}^{(\theta)}(\Upsilon_\theta\lambda), \tag{2.37}$$

where the $\Delta\hat{x}$ terms are oscillatory, periodic functions. Here I use $\Delta\hat{x}$ to represent $\Delta\hat{t}$, $\Delta\hat{r}$, $\Delta\hat{\theta}$, and $\Delta\hat{\varphi}$. These periodic functions have the properties

$$\Delta\hat{x}^{(r)}(2\pi + \Upsilon_r\lambda) = \Delta\hat{x}^{(r)}(\Upsilon_r\lambda), \qquad\qquad \Delta\hat{x}^{(r)}(0) = 0, \tag{2.38}$$

$$\Delta\hat{x}^{(\theta)}(2\pi + \Upsilon_\theta\lambda) = \Delta\hat{x}^{(\theta)}(\Upsilon_\theta\lambda), \qquad\qquad \Delta\hat{x}^{(\theta)}(0) = 0, \tag{2.39}$$

While the $\Delta\hat{x}$ functions share the same periodic behavior, $\Delta\hat{t}$ and $\Delta\hat{\varphi}$ are anti-symmetric (odd) functions, while $\Delta\hat{r}^{(r)}$ and $\Delta\hat{\theta}^{(\theta)}$ are symmetric (even) functions. Exact definitions of these geodesic functions are provided in Refs. [91, 108]. I will discuss different methods for constructing these functions in Sec. 2.7.

Next, I consider a generic inclined eccentric geodesic x_p^μ with arbitrary initial conditions

$$x_p^\mu(\lambda = 0) = (t_0, r_0, \theta_0, \varphi_0), \qquad u^r(\lambda = 0) = u_0^r, \qquad u^\theta(\lambda = 0) = u_0^\theta. \tag{2.40}$$

Retaining the notation that fiducial geodesic functions are represented with a hat (e.g., $\hat{x}_p^\mu$), the arbitrary geodesic can be expressed in terms of the fiducial solutions

$$t_p(\lambda; t_0, \lambda_0^{(r)}, \lambda_0^{(\theta)}) = t_0 + \Gamma\lambda + \Delta\hat{t}(\Upsilon_r\lambda + \Upsilon_r\lambda_0^{(r)}, \Upsilon_\theta\lambda + \Upsilon_\theta\lambda_0^{(\theta)}) - \Delta\hat{t}(\Upsilon_r\lambda_0^{(r)}, \Upsilon_\theta\lambda_0^{(\theta)}), \tag{2.41}$$

$$r_p(\lambda; \lambda_0^{(r)}) = r_{\min} + \Delta\hat{r}^{(r)}(\Upsilon_r\lambda + \Upsilon_r\lambda_0^{(r)}), \tag{2.42}$$

$$\theta_p(\lambda; \lambda_0^{(\theta)}) = \theta_{\min} + \Delta\hat{\theta}^{(\theta)}(\Upsilon_\theta\lambda + \Upsilon_\theta\lambda_0^{(\theta)}), \tag{2.43}$$

$$\varphi_p(\lambda; \varphi_0, \lambda_0^{(r)}, \lambda_0^{(\theta)}) = \varphi_0 + \Upsilon_\varphi\lambda + \Delta\hat{\varphi}(\Upsilon_r\lambda + \Upsilon_r\lambda_0^{(r)}, \Upsilon_\theta\lambda + \Upsilon_\theta\lambda_0^{(\theta)}) - \Delta\hat{\varphi}(\Upsilon_r\lambda_0^{(r)}, \Upsilon_\theta\lambda_0^{(\theta)}), \tag{2.44}$$

where

$$\Delta\hat{t}(\Upsilon_r\lambda, \Upsilon_\theta\tilde{\lambda}) \equiv \Delta\hat{t}^{(r)}(\Upsilon_r\lambda) + \Delta\hat{t}^{(\theta)}(\Upsilon_\theta\tilde{\lambda}), \tag{2.45}$$

$$\Delta\hat{\varphi}(\Upsilon_r\lambda, \Upsilon_\theta\tilde{\lambda}) \equiv \Delta\hat{\varphi}^{(r)}(\Upsilon_r\lambda) + \Delta\hat{\varphi}^{(\theta)}(\Upsilon_\theta\tilde{\lambda}), \tag{2.46}$$

are the sums of the radial and polar dependencies of the time and azimuthal components, and the initial orbital offsets $\lambda_0^{(r/\theta)}$ are defined such that

$$\begin{aligned} \Delta\hat{r}^{(r)}(\Upsilon_r\lambda_0^{(r)}) &= r_0 - r_{\min}, \qquad \mathrm{sgn}\left(\sin\Upsilon_r\lambda_0^{(r)}\right) = \mathrm{sgn}\left(u_0^r\right), \\ \Delta\hat{\theta}^{(\theta)}(\Upsilon_\theta\lambda_0^{(\theta)}) &= \theta_0 - \theta_{\min}, \qquad \mathrm{sgn}\left(\sin\Upsilon_\theta\lambda_0^{(\theta)}\right) = \mathrm{sgn}\left(u_0^\theta\right). \end{aligned}$$

Here, sgn represents the sign function. The fiducial case is recovered by setting $t_0 = \varphi_0 = \lambda_0^{(r)} = \lambda_0^{(\theta)} = 0$.

All bound geodesics can be described by Eqs. (2.41)-(2.44), though any geodesic that passes through a simultaneous minimum in the radial and polar motion (i.e., $r_p = r_{\min}$ and $\theta_p = \theta_{\min}$) can be mapped to a fiducial geodesic with trivial offsets in t_0 and φ_0. As long as there exist integers k and n such that

$$\lambda_0^{(\theta)} - \lambda_0^{(r)} = n\Lambda_r - k\Lambda_\theta, \tag{2.47}$$

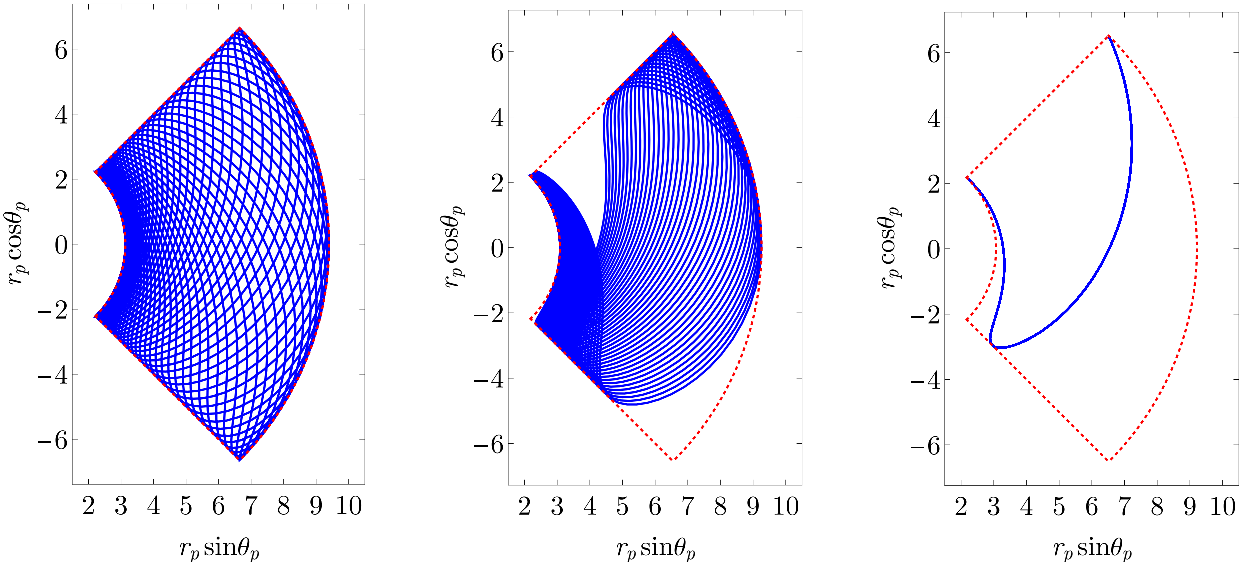

Figure 2.2: The projected radial and polar motion (solid blue lines) of three fiducial geodesics about a Kerr black hole with spin $a/M = 0.9$ and $M = 1$. All three plots share the orbital parameters $(e, x_{\mathrm{inc}}) = (0.5, \cos\pi/4)$ but differ in their semi-latus rectum, which from left to right are given by $p = 4.700$, $p = 4.630$, and $p \approx 4.607$. The last (right) plot has a semi-latus rectum chosen exactly to produce a 1:2 resonance. The dashed (red) lines outline the region $r_{\min} \leq r \leq r_{\max}$ and $\theta_{\min} \leq \theta \leq \pi - \theta_{\min}$. The motion for each geodesic is plotted from $\lambda = 0$ to $\lambda = 94$. The non-resonant orbits (the left and center plots) gradually sample the entire $r\theta$-space, while the resonant orbit (right plot) follows a closed track through the poloidal plane.

is satisfied, then a simultaneous turning point will occur. Because non-resonant, eccentric, inclined geodesics are ergodic, this simultaneous turning point always exists, and, therefore, non-resonant geodesics can be described by the fiducial expressions in Eqs. (2.34)-(2.37), without loss of generality.

Section 2.5: Resonant geodesics

A geodesic is called a $r\theta$-resonance when its radial and polar frequencies form a rational number ratio,

$$\frac{\Omega_r}{\Omega_\theta} \equiv \frac{\beta_r}{\beta_\theta}, \tag{2.48}$$

where β_r and β_θ are integers. Low-integer ratios (e.g., β_r:β_θ = 1:2, 2:3) are referred to as *strong* resonances, while high-integer ratios (e.g., 10:11, 1:20) are known as *weak* resonances. Because the radial and polar frequencies become commensurate during an $r\theta$-resonance, the discrete frequency spectrum of $r\theta$-resonant geodesics reduces to

$$\omega_{mN} \equiv m\Omega_\varphi + N\Omega, \tag{2.49}$$

where $\Omega \equiv \Omega_r/\beta_r = \Omega_\theta/\beta_\theta$ and $N \equiv k\beta_\theta + n\beta_r$.

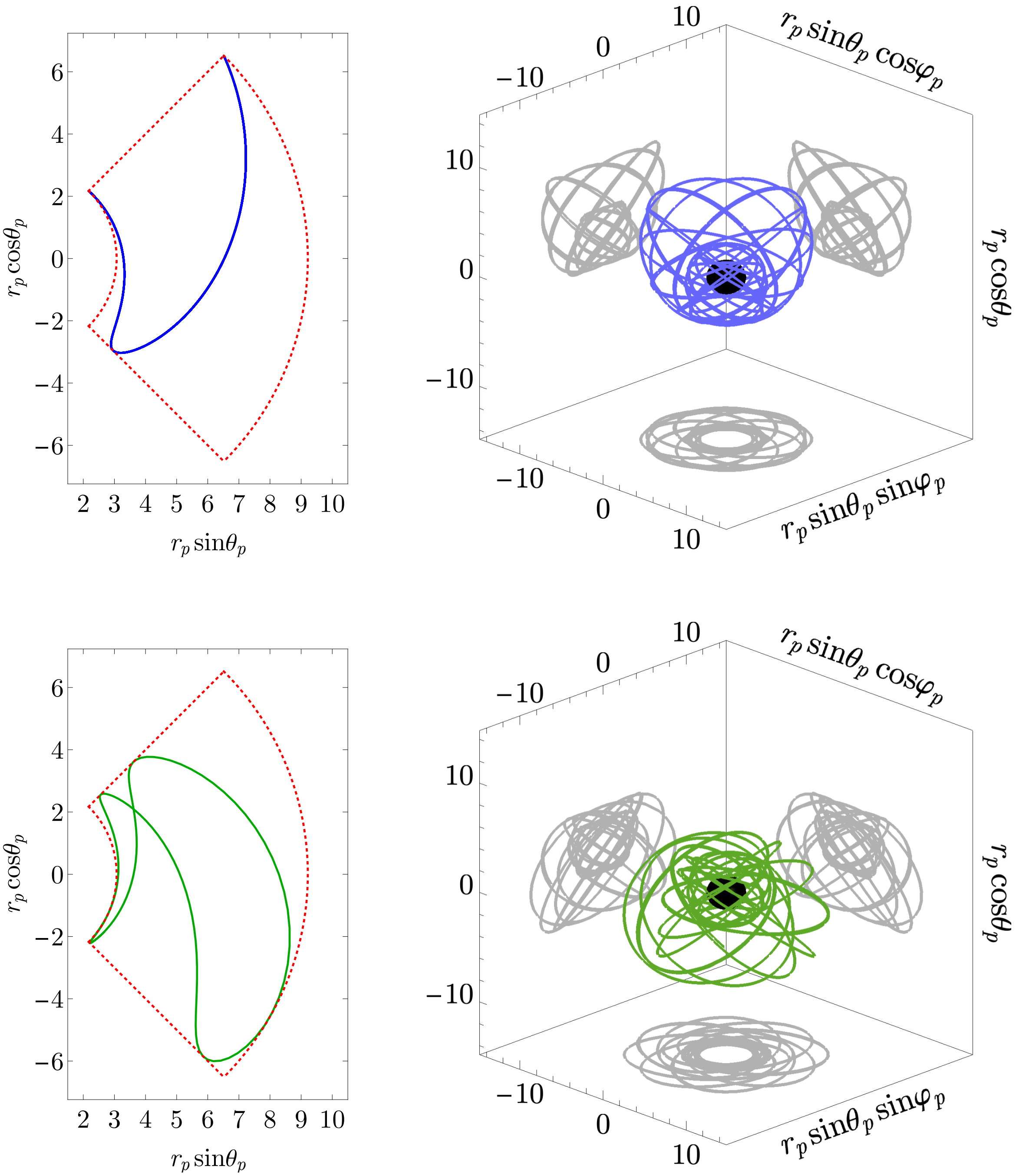

Figure 2.3: Projected motion for two 1:2 $r\theta$-resonant geodesics around a Kerr black hole with spin $a/M = 0.9$ and mass $M = 1$. The left plots, like Fig. 2.2, depict the radial and polar motion of both geodesics in the poloidal plane. The three-dimensional motion of these two geodesics are mapped separately in the right-most plots. Both of the top and bottom plots depict orbits that share the same orbital parameters $(p, e, x) \approx (4.607, 0.5, \cos\pi/4)$ and $r\theta$-resonant frequencies. While they both start at $r_p(0) = r_{\min}$, they differ in their initial polar positions and polar velocities. The solid (blue) lines in the top plots trace out a geodesic with the initial offset $\lambda_0^{(\theta)} = 0$ ($q_{\theta 0} = q_0 = 0$), while the solid (green) lines in the bottom plots represent a geodesic with the initial offset $\lambda_0^{(\theta)} = -3\Lambda_\theta/8$ ($q_{\theta 0} = \beta_\theta q_0 = -3\pi/4$). The motion for each plot is shown for $\lambda = 0$ to $\lambda = 47$.

Like non-resonant geodesics, resonant geodesics can also be described by Eqs. (2.41)-(2.44). However, as shown in Figures 2.1 and 2.2, resonant and non-resonant geodesics are recognizably different. While non-resonant geodesics are ergodic, $r\theta$-resonances follow restricted paths through the poloidal plane. Furthermore, these paths are sensitive to the initial conditions $\lambda_0^{(r)}$ and $\lambda_0^{(\theta)}$, as shown in Fig. 2.3. For a resonance, the radial and polar motions oscillate with the shared Mino time frequency and period

$$\Upsilon \equiv \frac{\Upsilon_r}{\beta_r} = \frac{\Upsilon_\theta}{\beta_\theta}, \qquad \Lambda \equiv \beta_r \Lambda_r = \beta_\theta \Lambda_\theta. \tag{2.50}$$

For a simultaneous turning point to occur during a resonance, Eq. (2.47) reduces to the more stringent restriction that $\lambda_0^{(\theta)} - \lambda_0^{(r)} = N'\Lambda$, for some integer N'. This relationship does not hold true for most choices of $\lambda_0^{(r)}$ and $\lambda_0^{(\theta)}$. Resonances, therefore, cannot always be mapped to a fiducial geodesic.

One can still simplify the geodesic equations for $r\theta$-resonances by defining the initial resonant offset $\lambda_0 \equiv \lambda_0^{(\theta)} - \lambda_0^{(r)}$. Any two $r\theta$-resonances that share the same value of λ_0 (module Λ) can be mapped onto one another. Taking advantage of this mapping, one can simplify the description of geodesic orbits by setting $\lambda_0^{(r)}$ or $\lambda_0^{(\theta)}$ to 0. In this work, I choose $\lambda_0^{(r)} = 0$ so that $\lambda_0 = \lambda_0^{(\theta)}$. Resonant orbits can then be described by

$$t_p(\lambda; \lambda_0) = \Gamma\lambda + \Delta\hat{t}(\beta_r\Upsilon\lambda, \beta_\theta\Upsilon\lambda + \beta_\theta\Upsilon\lambda_0) - \Delta\hat{t}(0, \beta_\theta\Upsilon\lambda_0) \tag{2.51}$$

$$r_p(\lambda; \lambda_0) = r_{\min} + \Delta\hat{r}^{(r)}(\beta_r\Upsilon\lambda), \tag{2.52}$$

$$\theta_p(\lambda; \lambda_0) = \theta_{\min} + \Delta\hat{\theta}^{(\theta)}(\beta_\theta\Upsilon\lambda + \beta_\theta\Upsilon\lambda_0), \tag{2.53}$$

$$\varphi_p(\lambda; \lambda_0) = \Upsilon_\varphi\lambda + \Delta\hat{\varphi}(\beta_r\Upsilon\lambda, \beta_\theta\Upsilon\lambda + \beta_\theta\Upsilon\lambda_0) - \Delta\hat{\varphi}(0, \beta_\theta\Upsilon\lambda_0), \tag{2.54}$$

without loss of generality. By varying the value of the initial resonant phase in the range $0 \leq \lambda_0 < \Lambda$, one can generate unique paths through the poloidal plane that are characterized by the same orbital parameters and frequencies but that have different initial positions, as demonstrated in Fig. 2.3.

Section 2.6: Alternative parameterizations

While the Mino time parameterization is particularly useful for separating the radial and polar motions, other parameterizations may be more elegant, such as the angle variable parameterization, or numerically practical, such as the Darwin [79] variable parameterization. These two parameterizations have also been used by a number of other authors [125, 93, 222, 224], and I will make use of both parameterizations in this work. In the following section, I introduce both of these alternative choices for parameterizing geodesic motion.

2.6.1: Angle variable representation

Motion in Kerr spacetime is completely integrable and therefore can be represented within the action-angle formalism. This formalism forms the basis for the two-timescale description of EMRI dynamics [125]. While in this work I am not focused on evolving EMRIs with a two-timescale expansion, the angle variables still provide natural parameterizations for functions that depend on the librating radial and polar motion of the particle. Other authors have also made use of this angle variable parameterization for presenting gravitational self-force results [224] and I adopt a similar parameterization in this work.

For non-resonant motion, I define the angle variables

$$q_r \equiv \Upsilon_r \lambda, \qquad\qquad q_\theta \equiv \Upsilon_\theta \lambda, \tag{2.55}$$

and the initial orbital phases

$$q_{t0} \equiv t_0, \qquad q_{r0} \equiv \Upsilon_r \lambda_0^{(r)}, \qquad q_{\theta 0} \equiv \Upsilon_\theta \lambda_0^{(\theta)}, \qquad q_{\varphi 0} \equiv \varphi_0. \tag{2.56}$$

Functions that are periodic with respect to the Mino time periods, Λ_r and Λ_θ, can then be parameterized in terms of the corresponding angle variables, q_r and q_θ, e.g.,

$$\Delta\hat{r}^{(r)}(\Upsilon_r\lambda + \Upsilon_r\lambda_0^{(r)}) \to \Delta\hat{r}^{(r)}(q_r + q_{r0}), \qquad\qquad \Delta\hat{\theta}^{(\theta)}(\Upsilon_\theta\lambda + \Upsilon_\theta\lambda_0^{(\theta)}) \to \Delta\hat{\theta}^{(\theta)}(q_\theta + q_{\theta 0}), \tag{2.57}$$

$$\Delta\hat{t}(\Upsilon_r\lambda + \Upsilon_r\lambda_0^{(r)}, \Upsilon_\theta\lambda + \Upsilon_\theta\lambda_0^{(\theta)}) \to \Delta\hat{t}(q_r + q_{r0}, q_\theta + q_{\theta 0}), \tag{2.58}$$

$$\Delta\hat{\varphi}(\Upsilon_r\lambda + \Upsilon_r\lambda_0^{(r)}, \Upsilon_\theta\lambda + \Upsilon_\theta\lambda_0^{(\theta)}) \to \Delta\hat{\varphi}(q_r + q_{r0}, q_\theta + q_{\theta 0}). \tag{2.59}$$

By parameterizing geodesic functions in terms of the angle variables, they now map to an invariant two-torus, which I will refer to as $\mathcal{T}^2_{r\theta}$. This torus forms a section of configuration space for the radial and polar motion of a particle on a generic geodesic. The geodesic flow on $\mathcal{T}^2_{r\theta}$ then describes the evolution of the particle through this configuration space, as discussed in Ref. [54]. Possible paths traced by this flow are shown in Fig. 2.4. Starting these paths at different points on the torus is equivalent to choosing different initial conditions for the particle's geodesic motion. Given an infinite amount of Mino time, a particle following a non-resonant geodesic will sample each point in $\mathcal{T}^2_{r\theta}$.

For $r\theta$-resonant geodesics, the particle evolves through $\mathcal{T}^2_{r\theta}$ on closed tracks, as seen in Fig. 2.5. Choosing different initial positions on the torus can generate unique paths on $\mathcal{T}^2_{r\theta}$ that never intersect. To sample all of the points in $\mathcal{T}^2_{r\theta}$, one cannot follow the geodesic flow of a single geodesic orbit. One must consider an infinite number of resonant orbits that share the same frequencies Υ_α but different initial offsets λ_0.

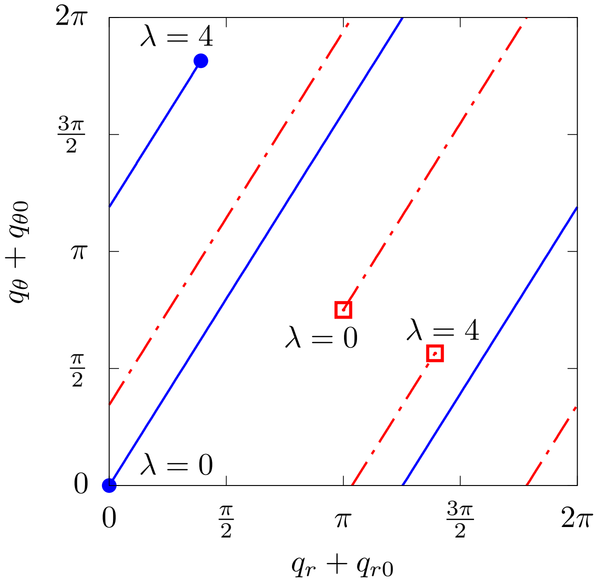

Figure 2.4: A geodesic with orbital parameters $(a/M, p, e, x) = (0.9, 6, 0.5, \cos\pi/4)$ mapped to the two-torus $\mathcal{T}^2_{r\theta}$ spanned by $q_r + q_{r0}$ and $q_\theta + q_{\theta 0}$. The solid (blue) line follows the path of a geodesic with fiducial initial conditions $(t_0, q_{r0}, q_{\theta 0}, \varphi_0) = (0, 0, 0, 0)$ on the Mino time interval $\lambda \in [0, 4]$. The dashed (red) line follows the path of an geodesic with initial conditions $(t_0, q_{r0}, q_{\theta 0}, \varphi_0) = (0, \pi, \pi/2, 0)$ on the Mino time interval $\lambda \in [0, 4]$. Both orbits have radial and polar frequencies, $\Upsilon_r \simeq 1.879$ and $\Upsilon_\theta \simeq 2.997$, and thus their tracks have slope $\simeq 1.595$.

To better distinguish between different resonant geodesic orbits, or paths on the torus, I define an alternate set of angle variables for resonances: the resonant angle variable $\bar{q}$ and the initial resonant phase $\bar{q}_0$,

$$\bar{q} \equiv \Upsilon\lambda = \frac{q_r}{\beta_r} = \frac{q_\theta}{\beta_\theta}, \qquad \bar{q}_0 \equiv \Upsilon\lambda_0 = \frac{q_{\theta 0}}{\beta_\theta} - \frac{q_{r0}}{\beta_r}, \tag{2.60}$$

which better emphasize the coupled nature of the radial and polar periods and the sensitivity of resonant orbits to the initial phase λ_0.[2] Functions that are parameterized in terms of these resonant variables provide alternative maps to $\mathcal{T}^2_{r\theta}$, which is illustrated in Fig. 2.5. Through this new mapping, particles evolve on flows of constant $\bar{q}_0$ in $\mathcal{T}^2_{r\theta}$.

I will denote functions that are re-parameterized in terms of these resonant variables with a bar, so that

$$\Delta\hat{r}^{(r)}(\Upsilon_r\lambda) \qquad \rightarrow \qquad \Delta\bar{r}^{(r)}(\bar{q}) \equiv \Delta\hat{r}^{(r)}(\beta_r\bar{q}), \tag{2.61}$$

$$\hat{\theta}^{(\theta)}(\Upsilon_\theta\lambda + \Upsilon_\theta\lambda_0^{(\theta)}) \qquad \rightarrow \qquad \Delta\bar{\theta}^{(\theta)}(\bar{q} + \bar{q}_0) \equiv \Delta\hat{\theta}^{(\theta)}(\beta_\theta\bar{q} + \beta_\theta\bar{q}_0), \tag{2.62}$$

$$\Delta\hat{t}(\Upsilon_r\lambda, \Upsilon_\theta\lambda + \Upsilon_\theta\lambda_0) \qquad \rightarrow \qquad \Delta\bar{t}(\bar{q}, \bar{q} + \bar{q}_0) \equiv \Delta\hat{t}(\beta_r\bar{q}, \beta_\theta\bar{q} + \beta_\theta\bar{q}_0), \tag{2.63}$$

$$\Delta\hat{\varphi}(\Upsilon_r\lambda, \Upsilon_\theta\lambda + \Upsilon_\theta\lambda_0) \qquad \rightarrow \qquad \Delta\bar{\varphi}(\bar{q}, \bar{q} + \bar{q}_0) \equiv \Delta\hat{\varphi}(\beta_r\bar{q}, \beta_\theta\bar{q} + \beta_\theta\bar{q}_0). \tag{2.64}$$

---

[2] Note that $\bar{q}_0$ is similar to the resonant phase parameter $q_\perp$ defined in Ref. [220].

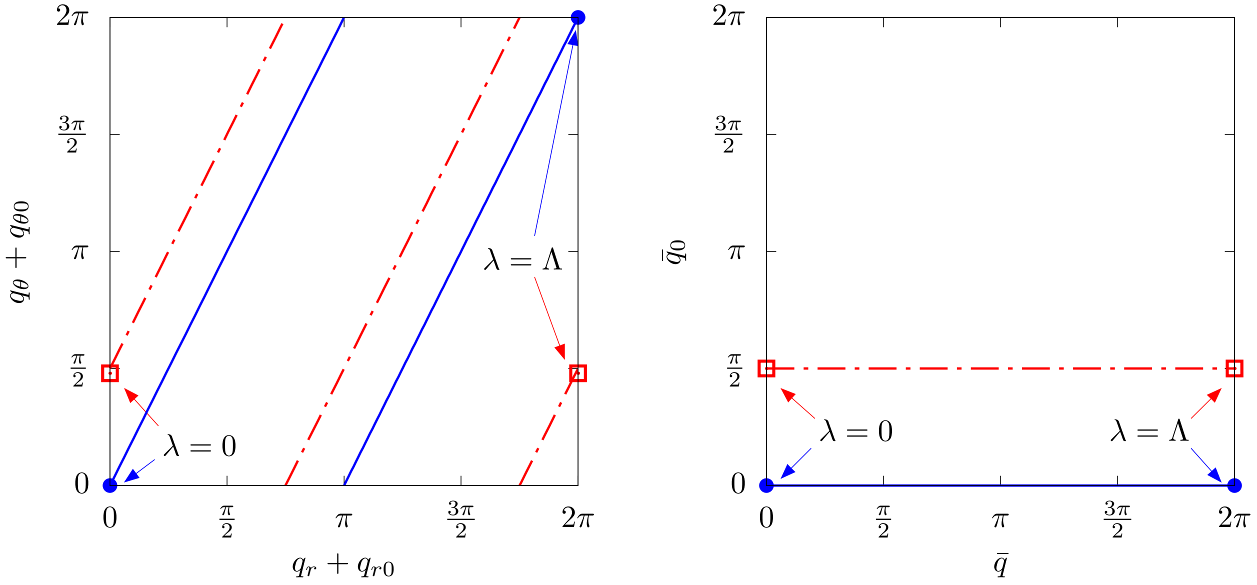

Figure 2.5: The left panel plots geodesics with orbital parameters $(a/M, p, e, x) = (0.9, 4.607, 0.5, \cos\pi/4)$ on the two-torus $\mathcal{T}^2_{r\theta}$ spanned by $q_r + q_{r0}$ and $q_\theta + q_{\theta 0}$, like in Fig. 2.4. The orbital parameters are chosen to generate a 1:2 $r\theta$-resonance, i.e., $\Upsilon_r/\Upsilon_\theta = 1/2$. The solid (blue) line follows the path of a geodesic with the initial resonant phase $q_0 = 0$ on the Mino time interval $\lambda \in [0, \Lambda]$, where $\Lambda = 4.494$ is the resonant Mino time period. The dashed (red) line follows the path of a geodesic with the initial resonant phase $\bar{q}_0 = \pi/2$ ($\theta_p(\lambda = 0) = \pi - \theta_{\min}$) on the Mino time interval $\lambda \in [0, \Lambda]$. One can see that each orbit samples a unique but limited track of points on the two-torus. The right panel plots the same orbits shown on the left, but now these orbits are mapped to the two-torus using the resonant angle variables $\bar{q}$ and $\bar{q}_0$. Each unique orbit forms a different horizontal line on the plot.

These angle variable descriptions will be particularly useful for calculating and visualizing the scalar self-force in later chapters.

2.6.2: Darwin variable parameterization

Rather than using angle variables based on an action-angle formalism, one can instead introduce the Darwin-like [79] angular coordinates ψ and χ [205, 92]

$$\check{r}_p(\psi) = \frac{pM}{1 + e\cos\psi}, \qquad \cos\check{\theta}_p(\chi) = z_- \cos\chi. \tag{2.65}$$

Equations (2.26) and (2.65) may be combined to find differential equations relating ψ and χ to λ, or vice versa with functions $\lambda = \lambda^{(r)}(\psi)$ and $\lambda = \lambda^{(\theta)}(\chi)$ satisfying

$$\frac{d\lambda^{(r)}}{d\psi} = \frac{a(1-e^2)\left[(p-p_4) + e(p - p_4\cos\psi)\right]^{-1/2}}{M\beta^{1/2}\left[(p-p_3) - e(p + p_3\cos\psi)\right]^{1/2}} \equiv P^{(r)}(\psi), \tag{2.66}$$

$$\frac{d\lambda^{(\theta)}}{d\chi} = \left[\beta(z_+^2 - z_-^2\cos^2\chi)\right]^{-1/2} \equiv P^{(\theta)}(\chi). \tag{2.67}$$

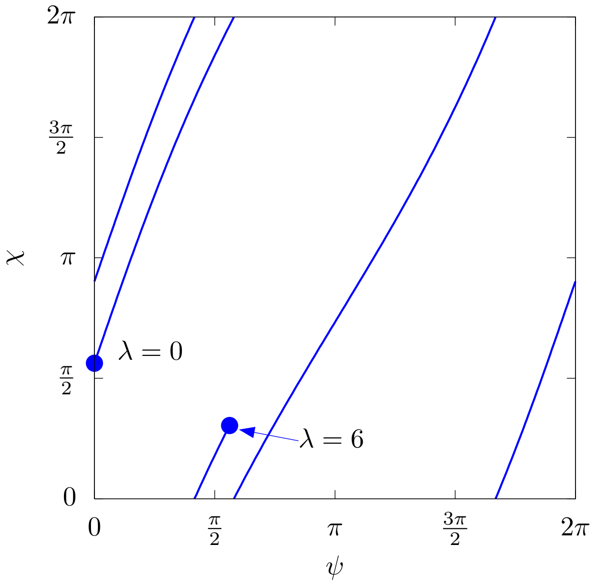

Figure 2.6: A geodesic with orbital parameters $(a/M, p, e, \iota) = (0.95, 5, 0.6, 1.04954)$ mapped to the two-torus $\mathcal{T}^2_{r\theta}$ now spanned by the rotational coordinates ψ and χ. The solid (blue) line traces an orbit that begins at Mino time $\lambda = 0$ with initial position $(r_p, \theta_p) = (r_{\min}, 1.7409)$ and is terminated at $\lambda = 6$. This orbit follows from choosing $\lambda_0^{(r)} = 0$ and $\lambda_0^{(\theta)} = 0.587813$ in Eqs. (2.68) and (2.69). Note by choosing these coordinates for the radial and polar section of configuration space, geodesic flow along the torus no longer follows straight lines.

The definitions of ψ and χ in (2.65) are made to improve the behavior of the differential equations for the geodesics at what would otherwise be turning points for r and θ. The solutions for $\lambda^{(r)}$ and $\lambda^{(\theta)}$ can be expressed as integrals

$$\lambda = \lambda^{(r)}(\psi) = \int_0^{\psi} P^{(r)}(\psi')\, d\psi' + \lambda_0^{(r)}, \tag{2.68}$$

$$\lambda = \lambda^{(\theta)}(\chi) = \int_0^{\chi} P^{(\theta)}(\chi')\, d\chi' + \lambda_0^{(\theta)}, \tag{2.69}$$

where $\lambda_0^{(r)}$ and $\lambda_0^{(\theta)}$ are integration constants, with $\lambda_0^{(r)} - \lambda_0^{(\theta)} \neq 0$ providing initial conditions for orbits that do not simultaneously pass through $r = r_{\min}$ and $\theta = \theta_{\max}$. The effect of choosing a non-zero value for $\lambda_0^{(\theta)}$, for example, is demonstrated in Fig. 2.6. The periods of motion in r and θ measured in Mino time are then given by

$$\Lambda_r = \lambda^{(r)}(2\pi) - \lambda_0^{(r)}, \qquad \Lambda_\theta = \lambda^{(\theta)}(2\pi) - \lambda_0^{(\theta)}. \tag{2.70}$$

The integrals in Eqs. (2.68) and (2.69) may be re-expressed in terms of elliptic integrals [92, 108] and thereby regarded as solved.

While these Darwin-like parameters provide simple parameterizations of the radial and polar motion, these variables do not possess a simple, linear relation during resonances, as opposed to the angle variables. This becomes particularly clear in Fig. 2.6, which maps geodesics to $\mathcal{T}^2_{r\theta}$ with the Darwin variables. With ψ and χ as coordinates for the two-torus, the geodesic flow no longer has constant slope, but oscillates due to the nontrivial interdependence of ψ, χ, and λ. While these are still valid parameters to use during resonances, I will rely on the Mino time or angle variable parameterizations when exploring the impact of resonances on perturbations in Kerr spacetime. The Darwin parameters, on the other hand, provide a convenient parameterization for numerically integrating the geodesic equations, and will be essential to the methods outlined in the next section.

Section 2.7: Solving Kerr geodesics numerically

As an alternative to using initial value integration, or special functions [92, 108], I present a spectral (Fourier) integration technique to find Kerr geodesics numerically. These methods are based on the spectral methods developed in Ref. [130] for calculations in Schwarzschild spacetime. The following work was first started by Osburn [175], then published by myself, Osburn, and Evans in Ref. [172]. I have subsequently incorporated the methods outlined below into the KerrGeodesics package of the Black Hole Perturbation Toolkit [1].

2.7.1: Spectral integration methods

First consider the dependence of λ on Darwin angles ψ and χ. The integration for $\lambda^{(r)}(\psi)$ is given as an example, but the same approach applies to $\lambda^{(\theta)}(\chi)$. The function $P^{(r)}(\psi)$, given by Eq. (2.66), can be written as a cosine series because it is smooth, even, and periodic

$$P^{(r)}(\psi) = \sum_{n=0}^{\infty} \tilde{\mathcal{P}}^{(r)}_n \cos(n\,\psi). \tag{2.71}$$

Because $P^{(r)}$ is C^∞, Eq. (2.71) converges exponentially with the number of harmonics, and for a given accuracy may be truncated at some $n = N_r - 1$.

Fourier series coefficients like $\tilde{\mathcal{P}}^{(r)}_n$ are derived from integrals, so computing many of these by, for example, adaptive stepsize integration is no improvement over simply integrating Eq. (2.66) itself. Instead, an efficient alternative is to use the discrete Fourier transform (DFT). To do so, one uses Eq. (2.66) to sample $P^{(r)}(\psi)$ at N_r evenly-spaced points ψ_j. The N_r sampled values, $P^{(r)}(\psi_j)$, are the DFT of N_r Fourier coefficients, $\mathcal{P}^{(r)}_n$. Up to a normalization factor, the DFT coefficients (with no tilde) converge exponentially to the Fourier series coefficients (with tilde) as the sample number N_r increases. Since $P^{(r)}$ is even, one can discretely sample the arc of half the radial motion and represent the function with the type-I discrete cosine transform (DCT-I)

$$\psi_\imath \equiv \frac{\imath\pi}{N_r - 1}, \qquad \imath \in 0, 1, \dots, N_r - 1, \tag{2.72}$$

$$\mathcal{P}_n^{(r)} = \frac{2}{N_r - 1}\left[\frac{1}{2}P^{(r)}(0) + \frac{1}{2}(-1)^n P^{(r)}(\pi) + \sum_{\imath=1}^{N_r-2} P^{(r)}(\psi_\imath)\cos(n\psi_\imath)\right], \tag{2.73}$$

$$P^{(r)}(\psi) = \frac{1}{2}\mathcal{P}_0^{(r)} + \frac{1}{2}\mathcal{P}_{N_r-1}^{(r)}\cos\left[(N_r - 1)\psi\right] + \sum_{n=1}^{N_r-2}\mathcal{P}_n^{(r)}\cos(n\psi)\,. \tag{2.74}$$

The DFT (or in this case DCT) may be computed numerically using a fast Fourier transform (FFT) algorithm, efficiently finding all of the Fourier coefficients $\mathcal{P}_n^{(r)}$. The angular sampling of $P^{(\theta)}(\chi)$ is made over N_θ equally-spaced points. The required radial and angular sample numbers are independent and subject only to desired numerical accuracy goals.

Returning to the radial motion example, once $P^{(r)}(\psi)$ is adequately represented, then $\lambda^{(r)}$ is found by substituting (2.74) into (2.68) and integrating term-by-term

$$\lambda^{(r)}(\psi; \lambda_0^{(r)}) = \frac{1}{2}\psi\,\mathcal{P}_0^{(r)} + \frac{1}{2}\mathcal{P}_{N_r-1}^{(r)}\frac{\sin\left[(N_r - 1)\psi\right]}{(N_r - 1)} + \sum_{n=1}^{N_r-2}\mathcal{P}_n^{(r)}\frac{\sin(n\psi)}{n} + \lambda_0^{(r)}, \tag{2.75}$$

thus obtaining an expression that can be evaluated at any ψ. A similar result is found for $\lambda^{(\theta)}$,

$$\lambda^{(\theta)}(\chi; \lambda_0^{(\theta)}) = \frac{1}{2}\chi\,\mathcal{P}_0^{(\theta)} + \frac{1}{2}\mathcal{P}_{N_\theta-1}^{(\theta)}\frac{\sin\left[(N_\theta - 1)\chi\right]}{(N_\theta - 1)} + \sum_{k=1}^{N_\theta-2}\mathcal{P}_k^{(\theta)}\frac{\sin(k\chi)}{n} + \lambda_0^{(\theta)}, \tag{2.76}$$

where

$$\mathcal{P}_k^{(\theta)} = \frac{2}{N_\theta - 1}\left[\frac{1}{2}P^{(\theta)}(0) + \frac{1}{2}(-1)^n P^{(\theta)}(\pi) + \sum_{\jmath=1}^{N_\theta-2} P^{(\theta)}(\chi_\jmath)\cos(n\chi_\jmath)]\right]. \tag{2.77}$$

The integration constants $\lambda_0^{(r)}$ and $\lambda_0^{(\theta)}$ are identical to the offsets defined in Eqs. (2.68) and (2.69). I, therefore, define the fiducial Mino time functions $\hat{\lambda}^{(r)}(\psi) \equiv \lambda^{(r)}(\psi; 0)$ and $\hat{\lambda}^{(\theta)}(\chi) \equiv \lambda^{(\theta)}(\chi; 0)$ for later convenience. The Mino time periods, Λ_r and Λ_θ, are related to the leading Fourier coefficients

$$\Lambda_r = \pi\mathcal{P}_0^{(r)}, \qquad \Lambda_\theta = \pi\mathcal{P}_0^{(\theta)}. \tag{2.78}$$

Taken all together, these solutions for $\lambda^{(r)}(\psi)$ and $\lambda^{(\theta)}(\chi)$ end up accurately relating motion in r and θ with λ. This approach models that found in Sec. II of Ref. [130].

Next consider the motion in t and φ. With Eqs. (2.12) and (2.15) re-expressed in terms of Mino time, the periodicity of Eqs. (2.18)-(2.19), and the ability to express those functions in terms of λ, suggests a Mino-time Fourier decomposition of V_{tr}, $V_{t\theta}$, $V_{\varphi r}$, and $V_{\varphi\theta}$ [92]

$$V_{\varphi r}(r_p(\lambda)) = \sum_{n=-\infty}^{+\infty} \wp_n^{(r)}\, e^{-in\Upsilon_r\lambda}, \qquad V_{\varphi\theta}(\theta_p(\lambda)) = \sum_{k=-\infty}^{+\infty} \wp_k^{(\theta)}\, e^{-ik\Upsilon_\theta\lambda}, \tag{2.79}$$

$$V_{tr}(r_p(\lambda)) = \sum_{n=-\infty}^{+\infty} \mathcal{T}_n^{(r)}\, e^{-in\Upsilon_r\lambda}, \qquad V_{t\theta}(\theta_p(\lambda)) = \sum_{k=-\infty}^{+\infty} \mathcal{T}_k^{(\theta)}\, e^{-ik\Upsilon_\theta\lambda}, \tag{2.80}$$

where, in keeping with the lefthand sides being real functions, the coefficients will satisfy crossing relations (e.g., $\mathcal{T}_{-n}^{(r)} = \mathcal{T}_n^{(r)*}$). As before, the series might be truncated (here with some upper and lower bounds on n and k). The Fourier coefficients are found from integrals over λ,

$$\mathcal{T}_n^{(r)} = \frac{1}{\Lambda_r}\int_0^{\Lambda_r} V_{tr}\, e^{in\Upsilon_r\lambda}\, d\lambda, \qquad \mathcal{T}_k^{(\theta)} = \frac{1}{\Lambda_\theta}\int_0^{\Lambda_\theta} V_{t\theta}\, e^{ik\Upsilon_\theta\lambda}\, d\lambda, \tag{2.81}$$

$$\wp_n^{(r)} = \frac{1}{\Lambda_r}\int_0^{\Lambda_r} V_{\varphi r}\, e^{in\Upsilon_r\lambda}\, d\lambda, \qquad \wp_k^{(\theta)} = \frac{1}{\Lambda_\theta}\int_0^{\Lambda_\theta} V_{\varphi\theta}\, e^{ik\Upsilon_\theta\lambda}\, d\lambda. \tag{2.82}$$

If one introduces sufficiently-fine, evenly-spaced divisions of the respective periods in λ, each of the Fourier coefficient integrals, like Eq. (2.81), could be accurately replaced with a finite sum. Unfortunately, the functions being integrated depend on r_p or θ_p (e.g., $T^{(r)}(r)$ above), which are known from the previous analysis as functions sampled on evenly-spaced grids in ψ or χ. To construct radial and polar functions that are evenly sampled in Mino time, one must first solve for ψ and χ as functions of λ. One straightforward method is to numerically invert Eqs. (2.75) and (2.76) via root-finding methods. This method grows increasingly inefficient, however, as the number of summands in Eqs. (2.75) and (2.76) grows. Instead, one can solve for ψ and χ as functions of λ using a discrete Fourier sum.

For example, $\psi(\lambda)$ can be constructed by integrating the reciprocal of Eq. (2.66),

$$\psi(\lambda; \lambda_0^{(r)}) = \int_{\lambda_0^{(r)}}^{\lambda} \frac{d\lambda'}{P^{(r)\prime}}. \tag{2.83}$$

Because $P^{(r)}$ and its reciprocal are periodic with respect to ψ, then $P^{(r)}$ and its reciprocal must also be periodic with respect to λ, based on the form of Eq. (2.75). The reciprocal of $P^{(r)}$ is then well-represented by the Fourier series

$$\left(P^{(r)}\right)^{-1} = \sum_{n=-\infty}^{\infty} p_n^{(r)} e^{-in\Upsilon_r\lambda}, \qquad p_n^{(r)} = \frac{1}{\Lambda_r}\int_0^{\Lambda_r} \left(P^{(r)}\right)^{-1} e^{in\Upsilon_r\lambda} d\lambda. \tag{2.84}$$

Of course, $P^{(r)}$ is only known as a function of ψ. With a change of coordinates the Fourier coefficients take the more amenable form,

$$p_n^{(r)}(\lambda_0^{(r)}) = \frac{1}{\Lambda_r}\int_0^{2\pi} e^{in\Upsilon_r\lambda^{(r)}(\psi;\lambda_0^{(r)})}\,d\psi, \tag{2.85}$$

where I have made the dependence on the offset $\lambda_0^{(r)}$ explicit. Recognizing, based on Eq. (2.75), that $p_n^{(r)}(\lambda_0^{(r)}) = p_n^{(r)}(0)e^{-in\Upsilon\lambda_0^{(r)}}$, I can proceed using just the fiducial values $\hat{p}_n^{(r)} \equiv p_n^{(r)}(0)$. As argued in Sec. III.B.3 of Ref. [130], exponentially-convergent approximations can still be made for this sort of smooth reparameterization, and the integral can be replaced with a finite sum on an evenly-spaced grid in ψ,

$$\psi_\imath \equiv \frac{2\imath\pi}{N_r}, \qquad \imath \in 0,1,\ldots,N_r-1, \tag{2.86}$$

$$\hat{p}_n^{(r)} \simeq \frac{\Upsilon_r}{N_r}\sum_{\imath=0}^{N_r-1} e^{in\Upsilon_r\hat{\lambda}^{(r)}(\psi_\imath)}. \tag{2.87}$$

The coefficients $\hat{p}_n^{(r)}$ turn out to be purely real, because $\hat{\lambda}^{(r)}(\psi)$ is odd, reducing Eq. (2.87) to a discrete cosine series

$$\hat{p}_n^{(r)} \simeq \frac{2\Upsilon_r}{N_r}\left[\frac{1}{2} + (-1)^n\frac{1}{2} + \sum_{\imath=1}^{N_r/2-1}\cos\left(n\Upsilon_r\hat{\lambda}^{(r)}(\psi_\imath)\right)\right]. \tag{2.88}$$

Because Eq. (2.87) is not evaluated on an evenly-spaced, periodic grid in λ, it does not represent a DCT sum (the argument of the cosine is nonlinear in ψ). Accordingly, the coefficients cannot be computed with the $\mathcal{O}(N\log N)$ FFT algorithm, but instead are evaluated directly, which is an $\mathcal{O}(N^2)$ process. As before, by combining Eqs. (2.83) and (2.84), and integrating term-by-term, one arrives at a discrete representation for $\psi(\lambda)$,

$$\psi(\lambda;\lambda_0^{(r)}) = \hat{\psi}\left(\lambda - \lambda_0^{(r)}\right), \tag{2.89}$$

$$\hat{\psi}(\lambda) \simeq \Upsilon_r\lambda + 2\sum_{n=1}^{N_r/2}\frac{\hat{p}_n^{(r)}}{n\Upsilon_r}\sin\left(n\Upsilon_r\lambda\right), \tag{2.90}$$

where I have used the fact that $\hat{p}_0^{(r)} = \Upsilon_r$ and $\hat{p}_n^{(r)}$ are real. The Mino time dependence of χ can be found through an analogous process. A hat (e.g., $\hat{\psi}$) implies fiducial initial conditions $\lambda_0^{(r)} = \lambda_0^{(\theta)} = 0$.

With new sampling in terms of λ, Eqs. (2.81)-(2.82) can then be replaced by exponentially-convergent sums

$$\lambda_j = \frac{\Lambda_{r/\theta}}{N_{r/\theta}}, \qquad j \in 0,1,\ldots,N_{r/\theta}-1, \tag{2.91}$$

$$\hat{\mathcal{T}}_n^{(r)} = \frac{\Upsilon_r}{N_r} \sum_{\imath=0}^{N_r-1} V_{tr} \left[\check{r}_p(\hat{\psi}(\lambda_\imath))\right] e^{in\Upsilon_r\lambda_\imath}, \qquad \hat{\mathcal{T}}_k^{(\theta)} = \frac{\Upsilon_\theta}{N_\theta} \sum_{\jmath=0}^{N_\theta-1} V_{t\theta} \left[\check{\theta}_p(\chi(\lambda_\jmath))\right] e^{ik\Upsilon_\theta\lambda_\jmath}, \tag{2.92}$$

$$\hat{\wp}_n^{(r)} = \frac{\Upsilon_r}{N_r} \sum_{\imath=0}^{N_r-1} V_{\varphi r} \left[\check{r}_p(\psi(\lambda_\imath))\right] e^{in\Upsilon_r\lambda_\imath}, \qquad \hat{\wp}_k^{(\theta)} = \frac{\Upsilon_\theta}{N_\theta} \sum_{\jmath=0}^{N_\theta-1} V_{\varphi\theta} \left[\check{\theta}_p(\chi(\lambda_\jmath))\right] e^{ik\Upsilon_\theta\lambda_\jmath}. \tag{2.93}$$

Once the Fourier coefficients are known, the average λ accumulation rates, Γ and Υ_φ, are found from the leading coefficients

$$\Gamma = \hat{\mathcal{T}}_0^{(r)} + \hat{\mathcal{T}}_0^{(\theta)}, \qquad \Upsilon_\varphi = \hat{\wp}_0^{(r)} + \hat{\wp}_0^{(\theta)}. \tag{2.94}$$

Alternatively, rather than resampling to produce to an evenly-spaced grid in λ, one can instead convert the integrals in Eqs. (2.81) and (2.82) and integrate over ψ or χ. For example,

$$\hat{\mathcal{T}}_n^{(r)} = \frac{1}{\Lambda_r} \int_0^{2\pi} T^{(r)}\, P^{(r)}\, e^{in\Upsilon_r\hat{\lambda}^{(r)}(\psi)}\, d\psi, \tag{2.95}$$

$$\hat{\mathcal{T}}_k^{(\theta)} = \frac{1}{\Lambda_\theta} \int_0^{2\pi} T^{(\theta)}\, P^{(\theta)}\, e^{ik\Upsilon_\theta\hat{\lambda}^{(\theta)}(\chi)}\, d\chi, \tag{2.96}$$

with similar expressions for $\hat{\wp}_n^{(r)}$ and $\hat{\wp}_k^{(\theta)}$. Once again, I assume fiducial initial conditions. Despite the transformations, all of these integrands are still C^∞ periodic functions of (now) ψ or χ. As discussed above, these integrals can be replaced with a finite, exponentially-convergent sum over an evenly-sampled grid in the new coordinate (either ψ or χ),

$$\psi_\imath \equiv \frac{2\imath\pi}{N_r}, \qquad \imath \in 0, 1, \ldots, N_r - 1, \tag{2.97}$$

$$\hat{\mathcal{T}}_n^{(r)} \simeq \frac{\Upsilon_r}{N_r} \sum_{\imath=0}^{N_r-1} T^{(r)}(\psi_\imath)\, P^{(r)}(\psi_\imath)\, e^{in\Upsilon_r\hat{\lambda}^{(r)}(\psi_\imath)}, \tag{2.98}$$

$$\chi_\jmath \equiv \frac{2\jmath\pi}{N_\theta}, \qquad \jmath \in 0, 1, \ldots, N_\theta - 1, \tag{2.99}$$

$$\hat{\mathcal{T}}_k^{(\theta)} \simeq \frac{\Upsilon_\theta}{N_\theta} \sum_{\jmath=0}^{N_\theta-1} T^{(\theta)}(\chi_\jmath)\, P^{(\theta)}(\chi_\jmath)\, e^{ik\Upsilon_\theta\hat{\lambda}^{(\theta)}(\chi_\jmath)}. \tag{2.100}$$

Similar expressions hold for $\hat{\wp}_n^{(r)}$ and $\hat{\wp}_k^{(\theta)}$. The remaining parts that determine the advance of t and φ in Eqs. (2.34) and (2.37), the periodic functions $\Delta\hat{t}_p$ and $\Delta\hat{\varphi}_p$, may be expressed as functions of λ by integrating Eqs. (2.79)-(2.80) term-by-term

$$\Delta\hat{t}^{(r)}(\Upsilon_r\lambda) \simeq 2\ \mathrm{Re}\left[\sum_{n=1}^{N_r/2} \frac{i\hat{\mathcal{T}}_n^{(r)}}{n\Upsilon_r}\, e^{-in\Upsilon_r\lambda}\right], \qquad \Delta\hat{t}^{(\theta)}(\Upsilon_\theta\lambda) \simeq 2\ \mathrm{Re}\left[\sum_{k=1}^{N_\theta/2} \frac{i\hat{\mathcal{T}}_k^{(\theta)}}{k\Upsilon_\theta}\, e^{-ik\Upsilon_\theta\lambda}\right], \tag{2.101}$$

$$\Delta\hat{\varphi}^{(r)}(\Upsilon_r\lambda) \simeq 2\ \mathrm{Re}\left[\sum_{n=1}^{N_r/2} \frac{i\hat{\wp}_n^{(r)}}{n\Upsilon_r}\, e^{-in\Upsilon_r\lambda}\right], \qquad \Delta\hat{\varphi}^{(\theta)}(\Upsilon_\theta\lambda) \simeq 2\ \mathrm{Re}\left[\sum_{k=1}^{N_\theta/2} \frac{i\hat{\wp}_k^{(\theta)}}{k\Upsilon_\theta}\, e^{-ik\Upsilon_\theta\lambda}\right]. \tag{2.102}$$

Here N_r and N_θ are assumed to be even and the restricted range of the sums reflects use of the crossing relations. Lastly, the periodic functions $\Delta\hat{r}$ and $\Delta\hat{\theta}$ in Eqs. (2.35) and (2.36) take the form

$$\Delta\hat{r}(\Upsilon_r\lambda) = \check{r}_p(\hat{\psi}(\lambda)) - r_{\min}, \qquad \Delta\hat{\theta}(\Upsilon_\theta\lambda) = \check{\theta}_p(\hat{\chi}(\lambda)) - \theta_{\min}, \tag{2.103}$$

and the the geodesic equations are considered solved.

2.7.2: Hybrid method

The spectral methods outlined above are best for numerical calculations performed at double precision. For higher precision calculations performed in *Mathematica*, the sampling density and number of Fourier coefficients can dramatically increase. With a number of the spectral calculations scaling as N^2, these additional terms will reduce the efficiency of spectral integration. It is advantageous to instead use *Mathematica*'s own built-in special functions library to evaluate the analytic expressions for the geodesic equations in terms of Elliptic and Jacobi functions [108]. The drawback, however, of using these special functions is that they take longer to evaluate than a Fourier sum with a modest number of terms, which particularly becomes an issue if one plans on repeatedly sampling these functions throughout the course of a calculation. Thereforem I introduce a "hybrid" approach, where one initially samples the geodesic functions using analytic special functions, then stores this data using either discrete cosine or discrete sine transforms. For orbits with lower eccentricities and inclinations, Fourier interpolations of these discrete transforms can be much faster to evaluate than *Mathematica*'s special functions.

It is relatively straightforward to construct discrete Fourier approximations of $\Delta\hat{t}$, $\Delta\hat{r}$, $\Delta\hat{\theta}$, and $\Delta\hat{\varphi}$, if one is given their analytic forms. First consider the radial and polar motion. The oscillatory components $\Delta\hat{r}$ and $\Delta\hat{\theta}$ are even functions of λ and well represented by the DCT-I

$$\lambda_j = \frac{\Lambda_{r/\theta}}{2(N_{r/\theta}-1)}, \qquad j \in 0, 1, \ldots, N_{r/\theta}-1, \tag{2.104}$$

$$\Delta\hat{r}(\Upsilon_r\lambda) = \frac{1}{2}\mathfrak{p}_0^{(r)} + \frac{1}{2}\mathfrak{p}_{N_r-1}^{(r)} \cos\left[(N_r-1)\Upsilon_r\lambda\right] + \sum_{n=1}^{N_r-2} \mathfrak{p}_n^{(r)} \cos(n\Upsilon_r\lambda), \tag{2.105}$$

$$\mathfrak{p}_n^{(r)} = \frac{2}{N_r-1}\left[\frac{1}{2}\Delta\hat{r}(0) + \frac{1}{2}(-1)^n\Delta\hat{r}(\pi) + \sum_{\imath=1}^{N_r-2} \Delta\hat{r}(\Upsilon_r\lambda_\imath)\cos(n\Upsilon_r\lambda_\imath)\right], \tag{2.106}$$

$$\Delta\hat{\theta}(\Upsilon_\theta\lambda) = \frac{1}{2}\mathfrak{p}_0^{(\theta)} + \frac{1}{2}\mathfrak{p}_{N_\theta-1}^{(\theta)} \cos\left[(N_\theta-1)\Upsilon_\theta\lambda\right] + \sum_{k=1}^{N_\theta-2} \mathfrak{p}_k^{(\theta)} \cos(k\Upsilon_\theta\lambda), \tag{2.107}$$

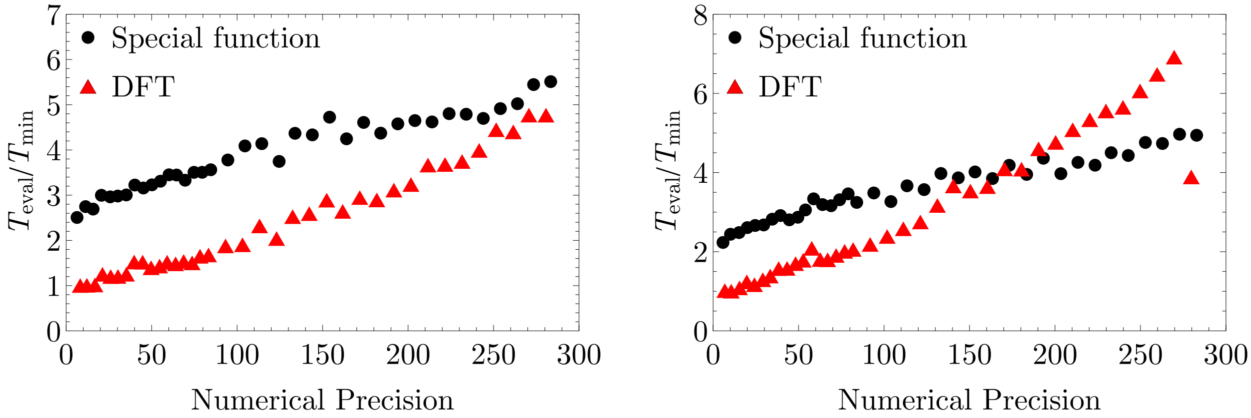

Figure 2.7: Plots of the time it takes to evaluate geodesic solutions with two different numerical algorithms. The plot on the left evaluates solutions $(t_p(\lambda), r_p(\lambda), \theta_p(\lambda), \varphi_p(\lambda))$ for a fiducial geodesic with orbital parameters $(a/M, p, e, x_{\rm inc}) = (0.9, 10, 0.4, 0.5)$. The right plot evaluates solutions for a fiducial geodesic with orbital parameters $(a/M, p, e, x_{\rm inc}) = (0.9, 10, 0.8, 0.5)$. The (black) dots refer to the time it takes to evaluate the geodesic solutions using the special function methods of Ref. [108]. The (red) triangles refer to the time it takes to evaluate the solutions using the DFT methods described in this section. All of the evaluation times $T_{\rm eval}$ are normalized by the shortest evaluation time $T_{\rm min}$.

$$\mathfrak{p}_k^{(\theta)} = \frac{2}{N_\theta - 1}\left[\frac{1}{2}\Delta\hat{\theta}(0) + \frac{1}{2}(-1)^k \Delta\hat{\theta}(\pi) + \sum_{\jmath=1}^{N_\theta - 2} \Delta\hat{\theta}(\Upsilon_\theta \lambda_\jmath)\cos(k\Upsilon_\theta\lambda_\jmath)\right]. \tag{2.108}$$

On the other hand, the oscillatory functions $\Delta\hat{t}$ and $\Delta\hat{\varphi}$ are odd, and well represented by the discrete sine transform of type I (DST-I). For example,

$$\lambda_j = \frac{\Lambda_{r/\theta}}{2(N_{r/\theta} - 1)}, \qquad j \in 0, 1, \dots, N_{r/\theta} - 1, \tag{2.109}$$

$$\Delta\hat{t}^{(r)}(\Upsilon_r\lambda) = \sum_{n=1}^{N_r - 1} \mathfrak{t}_n^{(r)} \sin(n\Upsilon_r\lambda), \qquad \mathfrak{t}_n^{(r)} = \frac{2}{N_r}\sum_{\imath=1}^{N_r-1} \Delta\hat{t}^{(r)}(\lambda_\imath)\sin(n\Upsilon_r\lambda_\imath), \tag{2.110}$$

$$\Delta\hat{t}^{(\theta)}(\Upsilon_\theta\lambda) = \sum_{k=1}^{N_\theta - 1} \mathfrak{t}_k^{(\theta)} \sin(k\Upsilon_\theta\lambda), \qquad \mathfrak{t}_k^{(\theta)} = \frac{2}{N_\theta}\sum_{\jmath=1}^{N_\theta-1} \Delta\hat{t}^{(\theta)}(\lambda_\jmath)\sin(k\Upsilon_\theta\lambda_\jmath), \tag{2.111}$$

and similarly for $\Delta\hat{\varphi}^{(r)}$ and $\Delta\hat{\varphi}^{(\theta)}$.

To demonstrate the advantage of using these discrete transforms, consider a fiducial geodesic with parameters $(a/M, p, e, x_{\rm inc}) = (0.9, 10, 0.4, 0.5)$. I first evaluate the geodesic functions $t_p(\lambda)$, $r_p(\lambda)$, $\theta_p(\lambda)$, and $\varphi_p(\lambda)$ at 256 different values of Mino time using *Mathematica*'s library of special functions. I repeat this process at various levels of numerical precision. The time it takes to perform these evaluations is given by the (black) dots in the left plot of Fig. 2.7. I then repeat these evaluations, but instead sample $t_p(\lambda)$, $r_p(\lambda)$, $\theta_p(\lambda)$, and $\varphi_p(\lambda)$ using their discrete Fourier representations, provided above. The time it takes to complete this second set of evaluations is given by the (red) triangles in the left plot of Fig. 2.7. Comparing these two processes, the discrete Fourier transforms evaluate more rapidly than the special functions, though it appears that at higher precisions the efficiency of the Fourier transforms over the special functions diminishes. This is because, at higher precisions, the Fourier series require a growing amount of summands and, consequently, take more time to evaluate.

This can also be seen if one considers a geodesic with a higher eccentricity, which will require more terms in the Fourier representations of the radial motion. In right plot of Fig. 2.7, I repeat the previous analysis for a new fiducial geodesic with orbital parameters $(a/M, p, e, x_{\mathrm{inc}}) = (0.9, 10, 0.8, 0.5)$. Once again, the (black) dots refer to the evaluation time using the *Mathematica* library of special functions, while the (red) dot triangles refer to the evaluation time using discrete Fourier transforms. When performing evaluations with numerical precisions $\gtrsim 175$, the special functions become more efficient to evaluate. Decreasing p and increasing x_{inc} also reduces the efficiency of this “hybrid” approach. Nonetheless, for moderate orbital parameters, the hybrid scheme is another useful tool for numerically storing and evaluating geodesic.

CHAPTER 3: Radiation, radiation-reaction, and self-forces

Section 3.1: Chapter overview

While geodesics provide an adequate approximation for the short-term motion of an EMRI, gravitational radiation must be taken into account to model an EMRI's long-term evolution. As discussed in Sec. 1.2.3, as an EMRI evolves, it radiates gravitational waves that act back on the small body, producing a gravitational self-force that perturbs the small body's motion and drives its gradual inspiral. For this dissertation work, I consider the analogous scalar self-force problem to develop and test new methods for modeling these radiation effects, specifically for EMRIs with Kerr primaries. However, before introducing this scalar model, it is important to first review the gravitational problem that motivates it.

Gravitational radiation—waves propagating through the ever-evolving metrical properties of space and time—is a complicated and, for many, unintuitive phenomenon. Even Einstein and his contemporaries were skeptical that gravitational waves were a measurable, physical effect. But radiation is an essential attribute of other dynamical fields. The radiation of light by electromagnetic fields has been studied and measured for over 150 years [159]. From this perspective, the appearance of gravitational radiation in the classical theory of general relativity is actually quite natural. Nonetheless, describing the gravitational radiation of two-body systems in general relativity remains a formidable task.

It is, therefore, instructive to turn towards classical electrodynamics, one of physics' most mature and successful classical field theories, to develop some intuition for radiative systems. By considering different electromagnetic examples, I will review the source of radiative behavior in classical fields and how this radiation affects the dynamics of radiative systems, particularly through the concepts of radiation-reaction and self-forces. Using the tools and intuition developed for electromagnetism, I will then discuss the role of gravitational radiation for EMRI dynamics, particularly through a mechanism known as the gravitational self-force. For more detailed discussions of radiation, radiation-reaction, and self-forces, particularly in the case of EMRIs, I refer the reader to Refs. [30, 180, 41].

Section 3.2: Electromagnetic radiation, radiation-reaction, and self-force

Classic examples of electromagnetic radiation include the Bremsstrahlung radiation produced by braking electrons approaching atomic nuclei or accelerating charged particles traveling in cyclotrons (leading to what is also known as cyclotron radiation). Assuming these charges are moving at non-relativistic speeds, the power P radiated by these systems is given by the Larmor formula (in units $c = 1$),

$$P = \frac{2}{3}|\ddot{\mathbf{d}}|^2, \tag{3.1}$$

where $\mathbf{d}$ is the electric dipole moment of the system and $\ddot{\mathbf{d}} \equiv d^2\mathbf{d}/dt^2$. Simplifying to the case of a single electron with charge e, position $\mathbf{x}_e$, and dipole moment $\mathbf{d} = e\mathbf{x}_e$,

$$P = \frac{2}{3}e^2|\mathbf{a}|^2, \tag{3.2}$$

where $\mathbf{a} = \ddot{\mathbf{x}}_e$ is the charge's acceleration. For students of electrodynamics, the simple take-away of the Larmor formula is that accelerating charges radiate, while inertial charges do not.

But this radiation also has a subtle secondary consequence that is often ignored in introductory studies. As the charge emits electromagnetic waves, these waves will carry energy and momentum away from the system. For energy to be conserved, this energy must come at the expense of the kinetic energy of the charge, thus altering its motion. This process, in which an object's motion is affected by its own radiation, is known as *radiation-reaction.* A famous consequence of radiation-reaction is that the two-body problem in classical electrodynamics is unstable.[1] An electron orbiting an atomic nucleus will radiate away its orbital energy and eventually "fall" into the nucleus.

But what if the electron, rather than orbiting an atomic nucleus, is orbiting a black hole? Do these same concepts of radiation and radiation-reaction apply in curved spacetime? As discussed in Sec. 1.2, according to general relativity and the equivalence principle, in the electron's local frame spacetime appears flat and the charge will not measure any acceleration due to gravity. If only external forces and fields source radiation, like in a globally flat spacetime, then the electron will not radiate. On the other hand, a distant observer will notice that the electron's motion deviates from a straight line and will deduce that the electron is accelerating. If Eq. (3.2) holds true in their reference frame, then the particle should be radiating. DeWitt and Brehme investigated this supposed conflict in 1960 [83] and found that the electron will in fact emit a type of "gravito-bremsstrahlung" radiation. While spacetime appears "flat" in the local neighborhood of the electron, the *global* electromagnetic field, much like a distant observer, "sees" the curvature of spacetime and its effect on the electron's motion.

To better understand this radiative behavior in curved spacetime, I will first review the source of electro-

---

[1] Of course, many atoms *are* stable and the instability predicted by the Larmor formula emphasizes the breakdown of classical mechanics in atomic models and the need for quantum mechanics at small scales. At large scales, however, this radiative behavior holds.

magnetic radiation in flat spacetime, and how one can calculate the resulting radiation-reaction effects and self-forces experienced by a charge due to its own radiation. I will then review how these results generalize to curved spacetime.

3.2.1: Electromagnetic radiation in flat-space

Consider an electron with charge e moving through a flat spacetime with Minkowski metric $\eta_{\mu\nu}$. The electron moves along its worldline $x_e^\mu(\tau)$ with four-velocity $u^\mu \equiv dx_e^\mu/d\tau$, where τ is its proper time. Its electromagnetic field is encoded in its four-potential $A^\mu_{\rm EM}$, which in Lorenz gauge ($\partial_\mu A^\mu_{\rm EM} = 0$) satisfies

$$\partial^\alpha \partial_\alpha A^\mu_{\rm EM} = -4\pi j^\mu, \tag{3.3}$$

where j^μ is the current density of the particle

$$j^\mu(x) = e \int u^\mu(\tau')\delta^{(4)}\left(x, x_e(\tau')\right) d\tau', \tag{3.4}$$

and $\delta^{(4)}\left(x, x'\right)$ is the invariant four-dimensional Dirac function. Note that in a generic spacetime with metric $\mathbf{g}_{\mu\nu}$, $\delta^{(4)}(x, x') = \left[-\det(\mathbf{g})\right]^{-1/2} \delta^{(4)}(x - x')$, where $\det(\mathbf{g})$ is the determinant of the metric $\mathbf{g}_{\mu\nu}$, and $\delta^{(4)}(x - x') = \delta(x^0 - x'^0)\delta(x^1 - x'^1)\delta(x^2 - x'^2)\delta(x^3 - x'^3)$. Importantly, $\delta^{(4)}\left(x, x'\right)$ differs from $\delta^{(4)}\left(x - x'\right)$ if $\det(\mathbf{g}) \neq -1$. In Minkowski spacetime $\det(\eta) = -1$. In its non-covariant form, Eq. (3.4) reduces to

$$j^\mu(t, \mathbf{x}) = e\frac{u^\mu}{u^0}\delta^{(3)}(\mathbf{x} - \mathbf{x}_e(t)), \tag{3.5}$$

where $x^\alpha = (t, \mathbf{x})$. While there are many solutions to Eq. (3.3), the physically relevant solution is found by integrating the source j^μ over the retarded Green's function $G^\alpha_{+\beta'}$, which, in Minkowski spacetime, satisfies the inhomogeneous wave equation

$$\partial^\alpha \partial_\alpha G^{\ \mu}_{+\ \nu'}(x, x') = -4\pi \delta^\mu_{\ \nu'} \delta^{(4)}(x, x'), \tag{3.6}$$

where $\delta^\mu_{\ \nu'}$ is the Kronecker delta. Once again relying on non-covariant notation, the retarded Green's function in Minkowski spacetime takes the form

$$G^{\ \mu}_{+\ \nu'}(x, x') = \delta^\mu_{\ \nu'} \frac{\delta(t - t'_+)}{|\mathbf{x} - \mathbf{x}'|}, \tag{3.7}$$

where $t_\pm \equiv t \mp |\mathbf{x} - \mathbf{x}'|$ is the retarded/advanced time coordinate. Consequently, when one evaluates the electromagnetic four-potential

$$A^\mu_{\text{ret}}(x) = \int G_{+}{}^{\mu}{}_{\nu'}(x,x') j^{\mu'}(x')\, d^4x', \tag{3.8}$$

$$= \left[\frac{eu^\alpha(t)}{\eta_{\alpha\beta}u^\beta(x^\alpha - x^\alpha_e(t))}\right]_{t=t_+}, \tag{3.9}$$

all functions of time are evaluated at the retarded time t_+. Thus, Eq. (3.9) reduces to the classical Liénard-Wiechert potential

$$A^0_{\text{ret}}(x^\alpha) \equiv \Phi_+(t,\mathbf{x}) = \left[\frac{e}{(1-\mathbf{v}\cdot\mathbf{n})\mathrm{r}}\right]_{t=t_+}, \tag{3.10}$$

$$A^i_{\text{ret}}(x^\alpha) \equiv \mathbf{A}_+(t,\mathbf{x}) = \left[\frac{e\mathbf{v}}{(1-\mathbf{v}\cdot\mathbf{n})\mathrm{r}}\right]_{t=t_+}, \tag{3.11}$$

where $\mathbf{v} \equiv d\mathbf{x}_e/dt$, $\mathbf{r} \equiv \mathbf{x} - \mathbf{x}_e$, $\mathrm{r} \equiv |\mathbf{r}|$, $\mathbf{n} \equiv \mathbf{r}/\mathrm{r}$, and Latin indices are spatial and run from 1 to 3.

The associated electromagnetic field is captured by the retarded field-strength tensor

$$F^{\alpha\beta}_{\text{ret}} = \partial^\alpha A^\beta_{\text{ret}} - \partial^\beta A^\alpha_{\text{ret}} = \left\{\frac{e}{u_\mu(x^\mu - x^\mu_e)}\frac{d}{d\tau}\left[\frac{(x^\alpha - x^\alpha_e)u^\beta - (x^\beta - x^\beta_e)u^\alpha}{u_\mu(x^\mu - x^\mu_e)}\right]\right\}_{t=t_+}, \tag{3.12}$$

which is related to the electric field $E^i = F^{0i}_{\text{ret}}$ and magnetic field $B_i = -\frac{1}{2}\epsilon_{ijk}F^{jk}_{\text{ret}}$, where ϵ_{ijk} is the standard Levi-Cevita symbol. If the charge is moving with a constant velocity $\mathbf{v}$, then one can Lorentz boost to a frame where $\mathbf{v} = 0$. In this frame, the particle produces a static Coulomb electric field

$$\mathbf{E}(t,\mathbf{x}) = -\nabla\Phi_+(t,\mathbf{x}) - \partial_t\mathbf{A}_+(t,\mathbf{x}) = \frac{e}{\mathrm{r}^2}\mathbf{n}, \tag{3.13}$$

and vanishing magnetic field

$$\mathbf{B}(t,\mathbf{x}) = \nabla\times\mathbf{A}_+(t,\mathbf{x}) = 0. \tag{3.14}$$

An inertial observer, therefore, will not measure any radiation from the system. Thus, if one can construct a global inertial frame where the particle and its field are not accelerating, then the system will not radiate.

When the particle does accelerate, its field experiences a delay as it responds to the change in the particle's motion. This 'delay,' which is encoded in the potential through the retarded time t_+, gives rise to an additional r^{-1} term that depends on the particle's acceleration $\dot{\mathbf{v}} \equiv d\mathbf{v}/dt$

$$\mathbf{E}(t,\mathbf{x}) = e\left[\frac{\mathbf{n}-\mathbf{v}}{\gamma^2(1-\mathbf{v}\cdot\mathbf{n})^3\mathrm{r}^2}\right]_{t=t_+} + e\left[\frac{\mathbf{n}\times[(\mathbf{n}-\mathbf{v})\times\dot{\mathbf{v}}]}{(1-\mathbf{v}\cdot\mathbf{n})^3\mathrm{r}}\right]_{t=t_+}, \tag{3.15}$$

$$\mathbf{B}(t, \mathbf{x}) = [\mathbf{n} \times \mathbf{E}]_{t=t_+}, \tag{3.16}$$

where the Lorentz factor $\gamma \equiv u^0$. A Lorentz boost can, once again, reduce the first term in Eq. 3.15 to the static r^{-2} Coulomb field. The r^{-1} term, however, does not vanish. Since this term does not exist in the static case, it must constitute the *radiative* contribution to the field, which is clear from the r^{-1} dependence. A similar result is found for the magnetic field of the charged particle based on Eq. 3.16. The radiative terms are direct consequences of the field's dependence on the retarded time. Hence, radiation results from a particle's electromagnetic field responding to changes in the particle's motion.

3.2.2: Electromagnetic self-force in flat-space

Now assume that the electron is accelerated by an external electromagnetic field $F^{\alpha\beta}_{\text{ext}}$, which interacts with the charge through the Lorentz force $F^{\alpha}_{\text{ext}} = eF^{\alpha\beta}_{\text{ext}} u_\beta$. As discussed at the beginning of this section, a distant observer will measure the radiative power of the accelerating electron and deduce that it must be losing energy. While this radiation can only be observed far away from the electron, the electron still reacts to these radiative losses and its accelerated motion will deviate from its Lorentz-forced trajectory. Because the electron is already interacting with the external electromagnetic field via the Lorentz force, this additional acceleration must be sourced by a type of *self-force* as the electron interacts with its own (radiative) field. The equation of motion for the electron can, then, be described by

$$\mu u^\alpha \nabla_\alpha u^\beta = F^{\beta}_{\text{ext}} + F^{\beta}_{\text{ESF}}, \tag{3.17}$$

where F^{μ}_{ESF} is the particle's own *electromagnetic self-force.* One might expect that F^{μ}_{ESF} should be similar in form to the Lorentz force, with the external field replaced by the particle's interaction with its own retarded electromagnetic field

$$F^{\mu}_{\text{ESF}} = F^{\mu}_{\text{ret}} = eF^{\mu\nu}_{\text{ret}} u_\nu, \tag{3.18}$$

where $F^{\text{ret}}_{\mu\nu} \equiv \partial_\mu A^{\text{ret}}_\nu - \partial_\nu A^{\text{ret}}_\mu$ and A^{μ}_{ret} is the charge's retarded four-potential, given by Eq. (3.9). The self-force, however, must be evaluated at the location of the particle x^α_e, where the retarded potential diverges to due to the r^{-2} and r^{-1} terms, given by Eqs. (3.15) and (3.16). Using the retarded field thus gives a physically meaningless result.

While these divergences may seem disconcerting, this problem is not new. Even the static Coulomb field diverges at the location of the electron. In classical electrostatics, this suggests that the electron possesses infinite electrostatic self-energy, which is clearly not true because the electron possesses a measurable and finite mass. This divergence is ultimately an artifact of approximating charges as point-particles and describing their structure with the Dirac-delta source term in Eqs. (3.3) and (3.4). One approach for curing these divergences is to give the electron some extended structure. This leads to the definition for the classical electron radius $r_e \equiv e^2/(mc^2)$. Adding additional structure, however, just adds another layer of approximation, since the internal composition of an electron is not actually known and in a classical, non-quantum description is inherently flawed. Even in quantum field theory, which more appropriately describes electromagnetic effects on scales $\sim O(r_e)$, the self-energy of the electron is only made finite through the delicate process of mass renormalization.

Consequently, these divergences are not related to the radiation field of the electron, but the mathematical framework used to model the particle's internal structure. For instance, the leading-order r^{-2} divergence is produced by the static field and should not contribute to the self-force, because static particles do not radiate. One can, therefore, separate the electron's electromagnetic potential into two different components: a singular field A^α_{S} tied to the fundamental, static structure of the particle and a regular field A^α_{R} that encodes its radiative nature and is solely responsible for the electromagnetic self-force.

Researchers typically make this separation using the mathematics of Green's functions. Green's functions not only serve as elementary mathematical objects for solving differential equations, but also, in the analysis of wave equations, communicate how waves and information propagate through spacetime. For instance, in flat spacetime the retarded Green's function $G_{+}{}^{\mu}{}_{\nu'}(x,x')$, given in Eq. (3.7), is only non-zero if the point x'^β lies on the past light-cone of the point x^α. This means that waves emanating from a point x'^β propagate into the future at the speed of light. The flat-space retarded Green's function essentially enforces Huygen's principle. As a consequence, the value of the retarded potential at the point x^α, i.e. $A^\mu_{\mathrm{ret}}(x)$, does not depend on the behavior of the electron at the current moment of time $t = x^0$, but on the time when its wordline x'^μ_e intersected the past light-cone of x^α. This is what defines the retarded time $t_+ = t - |\mathbf{x} - \mathbf{x}_e|$.

The first step in constructing the regular field is to identify the singular Green's function $G_{\mathrm{S}}{}^{\mu}{}_{\nu'}(x,x')$, which captures the non-radiative behavior of the divergent potential. Because the singular behavior of the retarded Green's function arises from the Dirac delta source term in Eq. (3.6), $G_{\mathrm{S}}{}^{\mu}{}_{\nu'}(x,x')$ must be a solution of the inhomogeneous wave equation, as well. Additionally, the singular Green's function should be symmetric, i.e., $G^{\mathrm{S}}_{\mu\nu'}(x,x') = G^{\mathrm{S}}_{\nu'\mu}(x',x)$, with no distinction between past and future, so that it has no impact on causal processes like radiation. Incorporating this symmetry requires the use of the advanced Green's function $G_{-}{}^{\mu}{}_{\nu'}(x,x')$, which also satisfies Eq. (3.6) and produces an advanced potential $A^\mu_{\mathrm{adv}}(x) = \int G_{-}{}^{\mu}{}_{\nu'}(x,x') j^{\nu'}(x') d^4x'$. In flat spacetime it takes the form

$$G_{-}{}^{\mu}{}_{\nu'}(x,x') = \delta^{\mu}{}_{\nu'} \frac{\delta(t - t'_{-})}{\mathrm{r}}. \tag{3.19}$$

While $G_{+\ \nu'}^{\ \mu}(x,x')$ connects the source position x'^{β} that intersects the past null rays emanating from the field point x^{α}, $G_{-\ \nu'}^{\ \mu}(x,x')$ connects points x'^{β} that intersect the future null rays of x^{α}. As a result, the A_{ret}^{μ} is interpreted as the causal solution that emits outgoing waves at infinity, while A_{adv}^{μ} gives the time-reversed scenario with ingoing waves from the distant past and from infinity. Thus, the two Green's functions are connected via the reciprocity relation $G_{\mu\nu'}^{-}(x,x') = G_{\nu'\mu}^{+}(x',x)$. A symmetric solution is then constructed from the average of these two Green's functions,

$$G_{\text{S}\ \nu'}^{\ \mu}(x,x') = \frac{1}{2}\left[G_{+\ \nu'}^{\ \mu}(x,x') + G_{-\ \nu'}^{\ \mu}(x,x')\right]. \tag{3.20}$$

This results in a singular Green's function that is not only symmetric, but also satisfies Eq. (3.6). One can then think of the resulting singular potential $A_{\text{S}}^{\mu}(x) = \int G_{\text{S}\ \nu'}^{\ \mu}(x,x')j^{\nu'}(x')d^4x'$ as the relativistic generalization of the Coulomb field [41]. The regular solution is formed by subtracting the singular structure from the retarded Green's function, giving the regular two-point function

$$G_{\text{R}\ \nu'}^{\ \mu}(x,x') = G_{+\ \nu'}^{\ \mu}(x,x') - G_{\text{S}\ \nu'}^{\ \mu}(x,x') = \frac{1}{2}\left[G_{+\ \nu'}^{\ \mu}(x,x') - G_{-\ \nu'}^{\ \mu}(x,x')\right]. \tag{3.21}$$

Note that $G_{\text{R}\ \nu'}^{\ \mu}(x,x')$ is typically not referred to as a Green's function, because it satisfies the source-free form of Eq. (3.6) and, therefore, is free of the divergences possessed by $G_{\pm\ \nu'}^{\ \mu}$.

Finally, the regular potential is constructed by replacing the retarded Green's function with $G_{\text{R}\ \nu'}^{\ \mu}$ in Eq. (3.8),

$$A_{\text{R}}^{\mu}(x) = \int G_{\text{R}\ \nu'}^{\ \mu}(x,x')j^{\nu'}(x')d^4x', \tag{3.22}$$

which provides a radiative solution to the homogeneous wave-equation $\partial^{\alpha}\partial_{\alpha}A_{\text{R}}^{\mu} = 0$. As shown by Dirac [86], this regular potential is exactly the potential one needs to construct the electromagnetic self-force. Not only is it regular at the location of the particle, but the total retarded field $A_{\text{R}}^{\mu} + A_{\text{S}}^{\mu}$ is still a valid solution of Eq. (3.3). As a further check, one can consider the case where there is no external field and the particle is static or moving with constant velocity. In this case, the retarded and advanced solutions are identical, so that $A_{\text{R}}^{\mu} = 0$, while A_{S}^{μ} is given by a static Coulomb field and captures the full singular structure of the retarded field. (For a more complete explanation of why A_{R}^{μ} is the radiative solution responsible for the self-force, I refer the reader to Dirac's original work [86].)

Interestingly, A_{R}^{μ} and the two-point function $G_{\text{R}\ \nu'}^{\ \mu}(x,x')$ (along with A_{S}^{μ} and $G_{\text{S}\ \nu'}^{\ \mu}(x,x')$) are acausal. The field's dependence on both the retarded and advanced times means that the behavior of the potential field at some point x^{α} depends on the behavior of the particle in both the past and the future. Causal structure is restored, however, when $A^\mu_{\rm R}$ and $G^\mu_{{\rm R}\,\nu'}$ (and $A^\mu_{\rm S}$ and $G^\mu_{{\rm S}\,\nu'}(x,x')$) are examined solely along the worldline of the particle, where the retarded and advanced times are equivalent. Therefore, $A^\mu_{\rm R}$ is not interpreted as a global, physical potential field, but as a contribution to the *effective* potential $A^\mu_{\rm eff} = A^\mu_{\rm ext} + A^\mu_{\rm R}$ that the particle measures in its local neighborhood. The force exerted by this effective potential is still simply the net Lorentz force, so that

$$\mu u^\alpha \nabla_\alpha u^\beta = eF^{\beta\nu}_{\rm eff} u_\nu = eF^{\beta\nu}_{\rm ext} u_\nu + eF^{\beta\nu}_{\rm R} u_\nu, \tag{3.23}$$

where $F^{\rm eff}_{\alpha\beta} = \partial_\alpha A^{\rm eff}_\beta - \partial_\beta A^{\rm eff}_\alpha$ and $F^{\rm R}_{\mu\nu} = \partial_\mu A^{\rm R}_\nu - \partial_\mu A^{\rm R}_\nu$. Comparing with Eq. (3.17), one finds that the electromagnetic self-force (in flat spacetime) takes the form

$$F^\alpha_{\rm ESF} = eF^{\alpha\nu}_{\rm R} u_\nu. \tag{3.24}$$

As shown by Dirac [86], and verified in more recent work [115, 180], Eq. (3.23) simplifies to the more commonly recognized Abraham-Lorentz-Dirac force law

$$\mu u^\alpha \nabla_\alpha u^\beta = F^\beta_{\rm ext} + \frac{2}{3} e^2 (\delta^\beta{}_\nu + u^\beta u_\nu) \frac{da^\nu}{d\tau}. \tag{3.25}$$

While the presence of a^β and its time derivative can lead to spurious physical solutions to the equations of motion, these problematic pathologies are avoided by recasting Eq. (3.25) in the reduced-order form

$$\mu u^\alpha \nabla_\alpha u^\beta = F^\beta_{\rm ext} + \frac{2}{3}\frac{e^2}{\mu} (\delta^\beta{}_\nu + u^\beta u_\nu) \frac{dF^\nu_{\rm ext}}{d\tau}, \tag{3.26}$$

which are valid as long as the radiation reaction effects are small compared to the external force.

To verify that this electromagnetic self-force is actually responsible for the radiation predicted by the Larmor formula, consider the non-relativistic form of Eq. (3.25),

$$\mu \mathbf{a} = \mathbf{F}_{\rm ext} + \frac{2}{3} e^2 \frac{d\mathbf{a}}{dt}, \tag{3.27}$$

where $a^\mu = (a^0, \mathbf{a})$ and $F^\mu_{\rm ext} = (F^0_{\rm ext}, \mathbf{F}_{\rm ext})$. The power P radiated by the electron's field will be balanced by the work done on the electron by its own self-force

$$\int P dt = -\frac{2}{3} e^2 \int \frac{d\mathbf{a}}{dt} \cdot d\mathbf{x}. \tag{3.28}$$

Performing integration by parts,

$$\int P dt = \frac{2}{3}e^2 \int \frac{d\mathbf{v}}{dt} \cdot \left(\frac{d\mathbf{v}}{dt}dt\right). \tag{3.29}$$

By equating both integrands, one sees that the electromagnetic self-force reproduces the (non-relativistic) Larmor formula

$$P = \frac{2}{3}e^2|\mathbf{a}|^2, \tag{3.30}$$

just as expected.

So why is the electromagnetic self-force so often ignored when calculating the motion of radiating charged particles? For many charged systems, radiation-reaction effects are quite small compared to the accelerations produced by the external field. For example, consider an electron that constantly accelerates with acceleration $a_{\rm ext}$ for some time interval $T_{\rm rad}$.[2] The energy radiated by the electron over this period is roughly given by

$$E_{\rm rad} \sim P T_{\rm rad} \sim \frac{2}{3}e^2 a_{\rm ext}^2 T_{\rm rad}, \tag{3.31}$$

where P is the power given by the Larmor formula. If one compares this to the change in the kinetic energy of the electron (neglecting radiation-reaction effects)

$$E_{\rm kinetic} \sim \mu a_{\rm ext}^2 T_{\rm rad}^2, \tag{3.32}$$

then $E_{\rm rad}/E_{\rm kinetic} \ll 1$ as long as

$$T_{\rm rad} \gg T_e \equiv \frac{2}{3}\frac{e^2}{\mu}. \tag{3.33}$$

For an electron, this characteristic timescale is given by $T_e = 6.3 \times 10^{-24}$ s and, therefore, is closely related to the light-crossing time of the classical electron radius (r_e/c). Consequently, in common radiative processes, such as Bremsstrahlung radiation, electromagnetic radiation-reaction and the electromagnetic self-force are negligible perturbative effects to the particle's motion. Of course, neglecting radiation-reaction effects only gives the leading-order behavior of the system. If one desires results with precisions $\sim O(T_e/T_{\rm rad})$, then radiation-reaction effects and self-forces must be included. In curved spacetime, these effects are more important to include, because, as I will show in the next section, no external force is needed for the particle to experience a self-force. Radiation and the self-force arise from spacetime curvature itself, accelerating the particle and altering its otherwise geodesic motion.

---

[2] This example originates from the last chapter of Jackson's book *Classical Electrodynamics*[141]

3.2.3: Electromagnetic self-force in curved-space

Now consider an electron in orbit around a compact object with metric $g_{\mu\nu}$. For generality, I will also assume that there may be some external electromagnetic field $F^{\mu\nu}_{\text{ext}}$ present. In curved spacetime, the electromagnetic four-potential A^{μ}_{EM} (in Lorenz gauge) is given by the curved-space wave equation

$$\nabla^{\alpha}\nabla_{\alpha}A^{\mu}_{\text{EM}} - R^{\mu}{}_{\nu}A^{\nu}_{\text{EM}} = -4\pi j^{\mu}, \tag{3.34}$$

where ∇_{α} is the covariant derivative and $R_{\mu\nu}$ is the Ricci tensor, both of which are defined with respect to the background metric $g_{\mu\nu}$. The covariant form of the current density j^{μ} is given in Eq. (3.4). Just as in Minkowski spacetime, the causal solution to Eq. (3.34) is given by the retarded potential

$$A^{\mu}_{\text{ret}}(x) = \int G^{\mu}_{+\,\nu'}(x,x')j^{\nu'}(x')\sqrt{-g(x')}\,d^4x' \tag{3.35}$$

where $g = \det(g_{\mu\nu})$ is the metric determinant and $G^{\mu}_{+\,\nu'}$ is still the retarded Green's function, which in curved spacetime satisfies the inhomogeneous equation

$$\nabla^{\alpha}\nabla_{\alpha}G^{\mu}_{+\,\nu'}(x,x') - R^{\mu}{}_{\beta}(x)G^{\beta}_{+\,\nu'} = -4\pi\delta^{\mu}{}_{\nu'}\delta^{(4)}(x,x'). \tag{3.36}$$

Note than in flat-space $g_{\mu\nu} = \eta_{\mu\nu}$, $\nabla_{\alpha} = \partial_{\alpha}$, and $R_{\mu\nu} = 0$, so that Eqs. (3.34), (3.35), and (3.36) simplify to Eqs. (3.3), (3.6), and (3.8), as expected. Also, even in curved spacetime, $R_{\mu\nu}$ vanishes in vacuum regions.

Recall that $G^{\beta}_{\pm\,\nu'}$ vanishes in Minkowski spacetime unless x^{α} and x'^{β} are connected by null rays. The retarded Green's function $G^{\mu}_{+\,\nu'}(x,x')$ only has support on the past light-cone of x^{α}. In curved spacetime, Green's functions take on a much more complicated structure due to the failure of Huygen's principle: waves scatter off of the surrounding curvature, causing them to propagate at all speeds less than and equal to the speed of light [180]. As a result, the retarded Green's function has support both on and *within* the past light-cone, producing a retarded potential that not only depends on the position of the electron at t_+ but at all times $t \leq t_+$. Similarly, the advanced potential depends on the position of the particle at all times $t \geq t_-$.

This additional structure complicates the construction of the singular Green's function. In Minkowski space, $G^{\mu'}_{\text{S}\,\nu'}$ is constructed solely from the average of the advanced and retarded Green's functions, as shown in Eq. (3.20). If, in curved spacetime, one constructed A^{μ}_{S} and A^{μ}_{R} using this same form of the singular Green's function, then both A^{μ}_{S} and A^{μ}_{R} would depend on the *entire history* of the particle's motion. While A^{μ}_{R} might be regular everywhere, its acausal structure, particularly along the wordline, leads to an unphysical solution for the self-force.

This problem is avoided, however, by adding an additional two-point function $H^{\mu}{}_{\nu'}(x,x')$ to the singular Green's function,

$$G^{\mu}_{\mathrm{S}\,\nu'}(x,x') = \frac{1}{2}\left[G^{\mu}_{+\,\nu'}(x,x') + G^{\mu}_{-\,\nu'}(x,x') - H^{\mu}{}_{\nu'}(x,x')\right]. \tag{3.37}$$

The new two-point function $H^{\mu}{}_{\nu'}(x,x')$ is chosen so that

(H1) $H^{\mu}{}_{\nu'}(x,x') = G^{\mu}_{-\,\nu}(x,x')$ for points x'^{α} that are in or on the future light-cone of point x^{β};

(H2) $H^{\mu}{}_{\nu'}(x,x') = G^{\mu}_{+\,\nu}(x,x')$ for points x'^{α} that are in or on the past light-cone of point x^{β};

(H3) $H^{\mu}{}_{\nu'}$ is symmetric, i.e. $H_{\mu\nu'}(x,x') = H_{\nu'\mu}(x',x)$; and

(H4) $H^{\mu}{}_{\nu'}$ is a homogeneous solution of Eq. (3.36).

Conditions (H1) and (H2) remove the dependence of the singular potential on the past and future history of the particle; (H3) ensures that $G^{\mu}_{\mathrm{S}\,\nu'}(x,x')$ is symmetric; and (H4) guarantees that $G^{\mu}_{\mathrm{S}\,\nu'}(x,x')$ is still a solution to Eq. (3.36). As before, the regular two-point function is then constructed by removing the singular structure from the retarded Green's function

$$G^{\mu}_{\mathrm{R}\,\nu'}(x,x') = G^{\mu}_{+\,\nu'}(x,x') - G^{\mu}_{\mathrm{S}\,\nu'}(x,x') \tag{3.38}$$

$$= \frac{1}{2}\left[G^{\mu}_{+\,\nu'}(x,x') - G^{\mu}_{-\,\nu'}(x,x') + H^{\mu}{}_{\nu'}(x,x')\right], \tag{3.39}$$

leading to the regular potential

$$A^{\mu}_{\mathrm{R}}(x) = \int G^{\mu}_{\mathrm{R}\,\nu'}(x,x') j^{\nu'}(x') \sqrt{-g(x')}\, d^4x'. \tag{3.40}$$

Once again A^{μ}_{R} provides a radiative solution of the source-free form of Eq. (3.34) that is both regular and causal along the particle's wordline. The particle experiences the net Lorentz force due to the effective electromagnetic field $F^{\mu\nu}_{\mathrm{eff}} = \nabla^{\mu} A^{\nu}_{\mathrm{eff}} - \nabla^{\nu} A^{\mu}_{\mathrm{eff}}$, where $A^{\mu}_{\mathrm{eff}} = A^{\mu}_{\mathrm{ext}} + A^{\mu}_{\mathrm{R}}$, leading to the same expression for the equations of motion as Eq. (3.23). As shown by DeWitt and Brehme [83] (with a correction by Hobbs [127]), and verified by Quinn and Wald [192], in curved spacetime Eq. (3.23) simplifies to

$$\mu u^{\alpha} \nabla_{\alpha} u^{\beta} = F^{\beta}_{\mathrm{ext}} + \frac{2}{3}\frac{e^2}{\mu}(\delta^{\beta}{}_{\nu} + u^{\beta} u_{\nu})\left(\frac{dF^{\nu}_{\mathrm{ext}}}{d\tau} + \frac{1}{2} R^{\nu}{}_{\lambda} u^{\lambda} + F^{\beta}_{\mathrm{tail}}\right), \tag{3.41}$$

where the additional *tail-term* is given by

$$F^{\mu}_{\text{tail}}(\tau) = 3\mu u_{\nu}(\tau) \int_{-\infty}^{\tau^{-}} \nabla^{[\mu} G_{+}{}^{\nu]}{}_{\lambda'}\left(x_e(\tau), x_e(\tau')\right) u^{\lambda'}(\tau')\, d\tau', \tag{3.42}$$

and τ^{-} means that one must cut-off integration right before reaching the location of the particle $x^{\alpha}_{e}(\tau)$. The electromagnetic self-force depends on the time-derivative of the external force, just as in flat spacetime, but there are additional terms that arise due to the presence of curvature. The tail-term, which involves an integral over the entire past history of the particle, accounts for the interaction of the electron's electromagnetic field with the surrounding curved spacetime. While in flat spacetime radiation results from the field responding to the particle's acceleration, in curved spacetime radiation can result from the field responding to spacetime curvature itself. Hence, even in the absence of an external field, the electron can still experience an electromagnetic self-force.

As a check, in flat spacetime $R^{\mu}{}_{\nu\alpha\beta} = 0$, while the retarded Green's function only has support on the past light-cone of the point x^{α}. Consequently, $F^{\mu}_{\text{tail}} = 0$, and one recovers the same expression for the electromagnetic self-force as in the previous section. While I will not verify it here, Quinn and Wald [193] also demonstrated that the work done by the electromagnetic self-force given in Eq. (3.41) does in fact balance the "gravito-bremsstrahlung" radiation produced by the electron, just as one would expect from conservation of energy and momentum.

Another interesting feature of the electromagnetic self-force in curved spacetime is that it can be separated into *dissipative* and *conservative* components, i.e., $F^{\alpha}_{\text{ESF}} = F^{\alpha(\text{diss})}_{\text{ESF}} + F^{\alpha(\text{cons})}_{\text{ESF}}$, where

$$F^{\alpha(\text{diss})}_{\text{ESF}} \equiv eF^{\alpha\nu}_{\text{diss}} u_{\nu}, \qquad\qquad F^{\alpha(\text{cons})}_{\text{ESF}} \equiv eF^{\alpha\nu}_{\text{cons}} u_{\nu}, \tag{3.43}$$

and, $F^{\alpha\nu}_{\text{diss}}$ and $F^{\alpha\nu}_{\text{cons}}$ are constructed from the four-potentials

$$A^{\mu}_{\text{diss}}(x) = \frac{1}{2}\int \left(G_{+}{}^{\mu}{}_{\nu'}(x,x') - G_{-}{}^{\mu}{}_{\nu'}(x,x')\right) j^{\nu'}(x')\sqrt{-g(x')}\, d^4x', \tag{3.44}$$

$$A^{\mu}_{\text{cons}}(x) = \frac{1}{2}\int H^{\mu}{}_{\nu'}(x,x') j^{\nu'}(x')\sqrt{-g(x')}\, d^4x', \tag{3.45}$$

via $F^{\text{diss}}_{\alpha\beta} = \partial_{\alpha}A^{\text{diss}}_{\beta} - \partial_{\beta}A^{\text{diss}}_{\alpha}$, $F^{\text{cons}}_{\alpha\beta} = \partial_{\alpha}A^{\text{cons}}_{\beta} - \partial_{\beta}A^{\text{cons}}_{\alpha}$.

For an electron on a bound orbit around the black hole, the dissipative component—due to the anti-symmetry of the integrand in Eq. (3.44)—provides the reaction to the dissipation of energy and drives the electron's decaying inspiral into the black hole. The conservative component, on the other hand, does not contribute to the decay of the electron's orbit; it conserves the bound orbit but perturbs its constants of motion. This is because ${H^{\mu}}_{\nu'}(x, x')$ is symmetric and, like the singular Green's function, does not distinguish between past and future and thus is not responsible for radiative losses. In flat spacetime, ${H^{\mu}}_{\nu'}(x, x') = 0$ and the electromagnetic self-force is purely dissipative.

Section 3.3: Gravitational radiation, radiation-reaction, and the self-force

Many of the principles and concepts developed in the previous electromagnetic examples also apply when considering gravitational radiation. In fact, an electron orbiting a black hole will not only produce electromagnetic radiation, but gravitational waves as well. The electron possesses some small mass-energy which perturbs the "background" spacetime produced by the Earth. If one thinks of this perturbation as the "gravitational field" of the electron, then the electron's perturbing field carries away radiation as the field responds to the electron's motion through the "background" curvature around the black hole.

For systems where spacetime curvature is relatively weak, the parallels between electromagnetic and gravitational radiation are particularly strong. Much like a charged particle that radiates as it orbits the Earth, the Earth will radiate gravitational waves as it orbits the Sun. In constrast to electromagnetic radiation, however, gravitational radiation does not depend on the change in the dipole moment of a system. (One can always find a "center-of-mass-like" frame in which the mass dipole moment is zero.) Instead a massive system radiates due to changes in its next multipole: the quadrupole. For non-relativistic systems, such as the Earth-Sun system, the power P_{GW} radiated through gravitational waves is [181]

$$P_{\text{GW}} = \frac{1}{5}\dddot{Q}^{ij}\dddot{Q}_{ij}, \tag{3.46}$$

where the system's reduced (Newtonian) quadrupole moment is given by

$$Q^{ij} = \int \rho_m \left(x^i x^j - \frac{1}{3}\delta^{ij}x^k x_k\right) d^3x, \tag{3.47}$$

and where ρ_m is the mass density of the system, and $\dddot{Q}^{ij} \equiv d^3Q^{ij}/dt^3$. In these equations, Latin indices are spatial and run from 1 to 3. For the simplified case of the Earth on a circular orbit around the Sun, the gravitational wave power reduces to

$$P_{\text{GW}}^{\text{circ}} \simeq \frac{32}{5}M_{\oplus}^2 r_{\text{orbit}} a_{\oplus}^3, \tag{3.48}$$

where $M_{\oplus}$ is the Earth's mass, r_{orbit} is the radius of its orbit, and $a_{\oplus} \simeq M_{\odot}/r_{\text{orbit}}^2$ is its Newtonian orbital acceleration. Equation (3.48) mirrors the behavior captured by the Larmor formula (3.2): accelerating masses radiate, while static sources do not.

The connection between electromagnetic and gravitational radiation becomes more complicated for relativistic systems and large spacetime curvature. In these systems, gravitational radiation not only has a significant impact on the dynamics of the system, but is much more challenging to quantify due to the nonlinearities of general relativity. Unlike electromagnetic fields, spacetime is self-interacting. Gravitational waves carry energy and momentum that can source new gravitational waves. I, therefore, restrict this discussion to the main focus of this work: EMRIs. For EMRIs, these non-linearities are tamed through the framework of BHPT, though applying perturbation theory rigorously and self-consistently in curved spacetime is still a challenging task. In the following section I discuss how researchers model the gravitational radiation in EMRIs using the concepts of radiation-reaction and self-forces discussed in the previous sections.

3.3.1: EMRI equations of motion

Consider the case of a small compact object with mass μ orbiting a MBH with mass M and spin a. (For simplicity, I assume the smaller object is not spinning.) The system is characterized in terms of its mass ratio $\epsilon \equiv \mu/M$. Far away from the small mass, the full spacetime metric $\mathbf{g}_{\mu\nu}$ can be separated into two components,

$$\mathbf{g}_{\mu\nu}(x,\epsilon) = g_{\mu\nu}(x) + h_{\mu\nu}(x,\epsilon) = g_{\mu\nu}(x) + \sum_{n=1}^{\infty} \epsilon^n h^{(n)}_{\mu\nu}(x), \tag{3.49}$$

where $g_{\mu\nu}$ is the background metric defined by the MBH and $h_{\mu\nu}$ is the metric perturbation due to the presence of the small body. In the previous sections, much of the analysis was simplified by assuming that the perturbing body is well-approximated by a point particle. One does not know a priori if the same assumption provides a suitable approximation for a compact object. The task then is to find well-defined equations of motion for the small body.

Both the small compact object and the MBH contribute to the full spacetime metric $\mathbf{g}_{\mu\nu}$, which is defined by Einstein's field equations,

$$\mathbf{G}_{\mu\nu}[\mathbf{g}] = 8\pi \mathbf{T}_{\mu\nu}, \tag{3.50}$$

where the stress-energy $\mathbf{T}_{\mu\nu}$ depends on the structure of the small body and thus encodes its evolution. The equations of motion then follow from the constraint on the stress-energy $\boldsymbol{\nabla}_\mu \mathbf{T}^{\mu\nu} = 0$, where $\boldsymbol{\nabla}_\mu$ is the covariant derivative with respect to $\mathbf{g}_{\mu\nu}$. In the absence of the mass μ, $\mathbf{T}_{\mu\nu} = 0$, and one recovers the vacuum field equations for an isolated black hole. For higher-orders, the field equations for $h_{\mu\nu}$ and the equations of motion for the small body must be derived by perturbatively solving Einstein's equations.

Using the expansion in Eq. (3.49), one can similarly expand the full Einstein tensor $\mathbf{G}_{\mu\nu}$,

$$\mathbf{G}_{\mu\nu}[\mathbf{g}] = G_{\mu\nu}[g] + \epsilon\delta G_{\mu\nu}[h^{(1)}] + \epsilon^2 \left(\delta^2 G_{\mu\nu}[h^{(1)}] + \delta G_{\mu\nu}[h^{(2)}]\right) + O(\epsilon^3), \tag{3.51}$$

where $G_{\mu\nu}[g] = 0$ is the background Einstein operator, $\delta G_{\mu\nu}$ is the linearized Einstein operator, $\delta^2 G_{\mu\nu}$ is the second-order operator, and all operators on the righthand side of Eq. (3.51) are defined with respect to the background metric $g_{\mu\nu}$. One can similarly expand the full stress-energy tensor

$$\mathbf{T}^{\mu\nu}(x,\epsilon) = T^{\mu\nu}(x,\epsilon) = \sum_{n=1}^{\infty} \epsilon^n T^{\mu\nu}_{(n)}(x), \tag{3.52}$$

where $T_{\mu\nu}$ is the stress-energy of the perturbations. Note that the "background," or zero-order, stress-energy tensor is zero. Only the perturbations contribute to $\mathbf{T}_{\mu\nu}$. Using Eq. (3.52) the stress-energy constraint is expanded in a similar fashion,

$$\boldsymbol{\nabla}_\mu \mathbf{T}^{\mu\nu} \equiv \mathbf{D}^\nu[\mathbf{T}] = \epsilon D^\nu[T_{(1)}] + \epsilon^2 \left(D^\nu[T_{(2)}] + \delta D^\nu[h_{(1)}, T_{(1)}]\right) + O(\epsilon^3), \tag{3.53}$$

where $D^\nu[T_{(1)}] \equiv \nabla_\mu T^{\mu\nu}_{(1)}$, ∇_μ is the covariant derivative with respect to $g_{\mu\nu}$, and all other operators on the righthand side of Eq. (3.53) are defined with respect to the background $g_{\mu\nu}$.

Combining Eqs. (3.51)-(3.53), one arrives at an iterative scheme for finding the equations of motion for the evolution of the system (left column) and the field equations for the metric perturbations $h^{(n)}_{\mu\nu}$ that correct the motion (right column)

$$\begin{aligned}
T^{\mu\nu}_{(0)} &= 0 & \Longrightarrow \quad & G_{\mu\nu}[g] = 0, && (3.54)\\
\nabla_\mu T^{\mu\nu}_{(1)} &= 0 & \Longrightarrow \quad & \delta G_{\mu\nu}[h^{(1)}] = 8\pi T^{(1)}_{\mu\nu}, && (3.55)\\
\nabla_\mu T^{\mu\nu}_{(2)} &= -\delta D^\nu[h_{(1)}, T_{(1)}] & \Longrightarrow \quad & \delta G_{\mu\nu}[h^{(2)}] = 8\pi T^{(2)}_{\mu\nu} - \delta^2 G_{\mu\nu}[h^{(1)}], && (3.56)\\
& & \vdots \quad & && (3.57)
\end{aligned}$$

While this provides a formal framework for analyzing the perturbations there are still many limitations to this approach. (See Ref. [180] for a more in depth discussion of these limitations.) First of all, in order to actually solve each equation, one must first determine the forms of the stress-energy terms. One possible approach is to naively approximate the small mass as a point particle. This does not pose an issue at first-order (i.e., Eq. (3.55)), though once again it leads to metric perturbations that diverge at the location of the particle, necessitating some type of regularization procedure to calculate any resulting self-forces. At second-order (i.e., Eq. (3.56)) this approximation breaks down because $\delta^2 G_{\mu\nu}[h^{(1)}]$ contains products of $h^{(1)}_{\mu\nu}$ and its derivatives. Thus the righthand side of the field equations, found in (3.56), essentially acts as a source term containing products of delta functions and their derivatives. Ultimately this is tied to the fact that point particles (along with strings) are not valid distributional sources in the full nonlinearity of general relativity [114]. More rigorous expansion methods are needed to evaluate Eqs. (3.55)-(3.57).

Mino, Sasaki, and Tanaka [142, 166, 165] were the first to evaluate Eqs. (3.55)-(3.57) and derive the equations of motion for an EMRI by employing a series of different methods, including the method of *matched asymptotic expansions* [142, 166, 165]. The method of matched asymptotic expansions relies on two expansions of the full spacetime: one that is valid in the *far zone* from the small mass, given by Eq. (3.49), and one that is valid in the *near-zone* of the small mass,

$$\begin{aligned} \mathrm{g}_{\mu\nu}(\tilde{x};\epsilon) &= g^{(\mathrm{body})}_{\mu\nu}(\tilde{x}) + h^{(\mathrm{body})}_{\mu\nu}(\tilde{x},\epsilon), \\ h^{(\mathrm{body})}_{\mu\nu}(\tilde{x},\epsilon) &= \sum_{n=1}^{\infty} \epsilon^n h^{(\mathrm{body},n)}_{\mu\nu}(\tilde{x}). \end{aligned} \tag{3.58}$$

Outside of the two objects, $\mathbf{T}_{\mu\nu} = 0$, and both expansions satisfy the vacuum Einstein equations ($\mathbf{R}_{\mu\nu} = 0$) in their respective domains of validity. They can also be matched in some suitable “buffer” region where they are both valid. Because $\mathbf{T}_{\mu\nu} = 0$, the equations of motion arise, not from stress-energy conservation, but by imposing the gauge conditions [165, 180]. (In their work, Mino, Sasaki, and Tanaka used Lorenz gauge.) Soon after, Quinn and Wald [192] devised a similar but more axiomatic approach that confirmed the results of Mino, Sasaki, and Tanaka. In their derivation, they produced a family of metrics connected by a shared parameter. From this family they could construct near and far zone metrics analogous to (3.49) and (3.58), without having to make any assumptions about the structure of the small compact object (unlike Mino, Sasaki, and Tanaka, who assumed the small compact object was a Schwarzschild black hole.)

This work by Mino, Sasaki, Tanaka, Quinn, and Wald demonstrated that, far from the small compact object, the small body can be treated as a point particle with a worldline $x^\alpha_p(\tau)$ and four-velocity u^α. Its equations of motion are then given by the famous *MiSaTaQuWa formula*

$$\mu u^\beta \nabla_\beta u^\alpha = F^\alpha_{\mathrm{GSF},1} + O(\epsilon^2) \equiv \mu \nabla^{\alpha\mu\nu} h^{\mathrm{tail}}_{\mu\nu} + O(\epsilon^2), \tag{3.59}$$

where

$$\nabla^{\mu\alpha\beta} \equiv -\frac{1}{2}(2g^{\mu\alpha}u^\beta u^\gamma - g^{\mu\gamma}u^\alpha u^\beta + u^\mu u^\alpha u^\beta u^\gamma)\nabla_\gamma, \tag{3.60}$$

and $h^{\mathrm{tail}}_{\mu\nu}$, like (3.42) in the electromagnetic case, is the tail field found by integrating the derivative of the retarded Green's function over the entire past history of the particle

$$\nabla_\alpha h^{\rm tail}_{\mu\nu} = 4\mu \int_{-\infty}^{\tau^-} \nabla_\alpha \left(G_{+\mu\nu\mu'\nu'}\left(x_p(\tau), x_p(\tau')\right) - \frac{1}{2} g_{\mu\nu} G_{+\ \rho\mu'\nu'}^{\ \rho}\left(x_p(\tau), x_p(\tau')\right)\right) u^{\mu'} u^{\nu'} d\tau'. \tag{3.61}$$

Here, $G_{+\mu\nu\mu'\nu'}$ is the retarded Green's function for the linearized Einstein equation (3.55).

Another important consequence of the MiSaTaQuWa derivations is that the stress-energy tensor $\mathbf{T}_{\mu\nu}$ of Eq. (3.50) is accurately approximated by a point-particle distribution at first-order. Because, in this work, I am concerned with leading-order self-force effects, rather than exploring the more involved method of matched asymptotic expansions, I will assume this point-particle approximation to outline a derivation of the field equations for the metric perturbation and the resulting self-force in the following sections.

3.3.2: Point-particle approximation

Because one can treat the small mass μ as a point particle (to first-order in ϵ), the derivation of the gravitational self-force follows similarly to the previous electromagnetic examples. I assume the particle has a timelike wordline x_p^μ. Its stress-energy is given by

$$\mathbf{T}^{\alpha\beta} = \epsilon T^{\alpha\beta} + O(\epsilon^2) = \epsilon\mu \int \frac{dx_p^\alpha}{d\boldsymbol{\tau}} \frac{dx_p^\beta}{d\boldsymbol{\tau}} \delta^{(4)}(x, x_p(\boldsymbol{\tau})) d\boldsymbol{\tau} + O(\epsilon^2), \tag{3.62}$$

where $\boldsymbol{\tau}$ is the proper time of the particle in the perturbed spacetime, i.e. $d\boldsymbol{\tau} = \sqrt{-\mathbf{g}_{\mu\nu} dx_p^\mu dx_p^\nu} = \sqrt{-(g_{\mu\nu} + \epsilon h^{(1)}_{\mu\nu}) dx_p^\mu dx_p^\nu}$. The equations of motion are then determined by

$$\boldsymbol{\nabla}_\mu \mathbf{T}^{\mu\nu} = 0 = \mu \int \boldsymbol{\nabla}_\mu \left(\frac{dx_p^\alpha}{d\boldsymbol{\tau}} \frac{dx_p^\beta}{d\boldsymbol{\tau}} \delta^{(4)}(x, x_p(\boldsymbol{\tau})) \right) d\boldsymbol{\tau} \tag{3.63}$$

At leading order $\boldsymbol{\tau}$ is equivalent to the proper time of the particle with respect to the background spacetime $d\tau = \sqrt{-g_{\mu\nu} dx_p^\mu d_p^\nu}$ and its four-velocity is defined by $u^\alpha = dx_p^\alpha / d\tau$. Thus the equations of motion at leading order reduce to

$$\begin{aligned} \nabla_\mu T^{\mu\nu} = O(\epsilon) &= \partial_\mu T^{\mu\nu} + \Gamma^\mu_{\mu\alpha} T^{\alpha\nu} + \Gamma^\nu_{\mu\alpha} T^{\alpha\mu}, && (3.64) \\ &= \mu \int \frac{u^\mu u^\nu}{\sqrt{-g}} \partial_\mu \delta^{(4)}(x - x_p) d\tau + \mu \int (\Gamma^\nu_{\mu\alpha} u^\mu + \Gamma^\mu_{\mu\alpha} u^\nu) u^\alpha \delta^{(4)}(x, x_p) d\tau, && (3.65) \\ &= -\mu \int \frac{u^\nu}{\sqrt{-g}} \frac{d}{d\tau} \delta^{(4)}(x - x_p) d\tau + \mu \int (\Gamma^\nu_{\mu\alpha} u^\mu + \Gamma^\mu_{\mu\alpha} u^\nu) u^\alpha \delta^{(4)}(x, x_p) d\tau, && (3.66) \end{aligned}$$

where the sign arises because the derivative now acts on $x_p^\mu(\tau)$ rather than x^α in the Dirac delta. Continuing with the simplification of this constraint equation,

$$\begin{aligned}
&= \mu \int \left[\frac{d}{d\tau}\left(\frac{u^\nu}{\sqrt{-g}}\right) + (\Gamma^\nu_{\mu\alpha}u^\mu + \Gamma^\mu_{\mu\alpha}u^\nu)\frac{u^\alpha}{\sqrt{-g}}\right]\delta^{(4)}(x-x_p)d\tau, && (3.67)\\
&= \mu \int \left[\frac{1}{\sqrt{-g}}\frac{du^\nu}{d\tau} - \frac{u^\nu}{-g}\frac{d}{d\tau}\sqrt{-g} + (\Gamma^\nu_{\mu\alpha}u^\mu + \Gamma^\mu_{\mu\alpha}u^\nu)\frac{u^\alpha}{\sqrt{-g}}\right]\delta^{(4)}(x-x_p)d\tau, && (3.68)
\end{aligned}$$

where I have used the relation $\Gamma^\mu_{\mu\alpha} = \partial_\alpha \ln\sqrt{-g}$,

$$\begin{aligned}
&= \mu \int \left[\frac{1}{\sqrt{-g}}\frac{du^\nu}{d\tau} - \frac{u^\nu}{\sqrt{-g}}u^\alpha\Gamma^\mu_{\mu\alpha} + (\Gamma^\nu_{\mu\alpha}u^\mu + \Gamma^\mu_{\mu\alpha}u^\nu)\frac{u^\alpha}{\sqrt{-g}}\right]\delta^{(4)}(x-x_p)d\tau, && (3.69)\\
&= \mu \int \left[\frac{du^\nu}{d\tau} + \Gamma^\nu_{\mu\alpha}u^\mu u^\alpha\right]\delta^{(4)}(x,x_p)d\tau, && (3.70)
\end{aligned}$$

and thus the stress-energy constraint implies that the point particle, as expected, will follow a geodesic $u^\beta\nabla_\beta u^\alpha = du^\alpha/d\tau + \Gamma^\alpha_{\mu\nu}u^\mu u^\nu = 0$.

The goal then, much like in the electromagnetic cases considered above, is to (1) find field equations for the metric perturbation $h^{(1)}_{\mu\nu}$, (2) identify the regular part of the perturbation, $h^{\mathrm{R}}_{\mu\nu}$, that contributes to the system's radiation, and (3) to determine how the perturbation produces a self-force, $F^\alpha_{\mathrm{GSF},1}$, that acts back on the particle's motion. Because I am only concerned with the first-order metric perturbation $h^{(1)}_{\mu\nu}$, I will drop the superscript and denote it as $h_{\mu\nu}$ from here on.

Beginning with the first step, the metric perturbation is determined by the linearized Einstein operator in Eq. (3.55). To find the form of this equation, first consider the Christoffel symbols $\boldsymbol{\Gamma}^\alpha_{\mu\nu}$ defined with respect to $\mathbf{g}_{\mu\nu}$,

$$\boldsymbol{\Gamma}^\alpha_{\mu\nu}[\mathbf{g}] = \boldsymbol{\Gamma}^\alpha_{\mu\nu}[g+h] = \Gamma^\alpha_{\mu\nu}[g] + \epsilon\delta\Gamma^\alpha_{\mu\nu}[g,h], \tag{3.71}$$

where $\Gamma^\alpha_{\mu\nu}$ is defined with respect to $g_{\mu\nu}$, and $\delta\Gamma^\alpha_{\mu\nu}$ is a functional of $g_{\mu\nu}$ and $h_{\mu\nu}$. The perturbation to the Christoffel symbols takes the form

$$\begin{aligned}
\delta\Gamma^\alpha_{\mu\nu} &= \epsilon^{-1}\left(\boldsymbol{\Gamma}^\alpha_{\mu\nu} - \Gamma^\alpha_{\mu\nu}\right), && (3.72)\\
&= \frac{1}{2}\epsilon^{-1}\mathbf{g}^{\alpha\beta}(\partial_\mu\mathbf{g}_{\alpha\nu} + \partial_\nu\mathbf{g}_{\alpha\mu} - \partial_\alpha\mathbf{g}_{\mu\nu}) - \frac{1}{2}\epsilon^{-1}g^{\alpha\beta}(\partial_\mu g_{\alpha\nu} + \partial_\nu g_{\alpha\mu} - \partial_\alpha g_{\mu\nu}), && (3.73)\\
&= \frac{1}{2}g^{\alpha\beta}(\partial_\mu h_{\alpha\nu} + \partial_\nu h_{\alpha\mu} - \partial_\alpha h_{\mu\nu}) - \frac{1}{2}h^{\alpha\beta}(\partial_\mu g_{\alpha\nu} + \partial_\nu g_{\alpha\mu} - \partial_\alpha g_{\mu\nu}) + O(\epsilon), && (3.74)
\end{aligned}$$

where the metric inverse $\mathbf{g}^{\mu\nu} = g^{\mu\nu} - \epsilon h^{\mu\nu}$ so that

$$\mathbf{g}^{\mu\nu}\mathbf{g}_{\mu\nu} = (g^{\mu\nu} - \epsilon h^{\mu\nu})(g_{\mu\nu} + \epsilon h_{\mu\nu}) = g^{\mu\nu}g_{\mu\nu} + O(\epsilon^2) = 1 + O(\epsilon^2). \tag{3.75}$$

Note that, to leading order, the indices of the metric perturbation are raised or lowered with the background metric and its inverse, e.g., $g^{\alpha\beta}h_{\alpha\mu} = h^{\alpha}{}_{\mu} + O(\epsilon)$. Equation (3.74) can be further simplified by recognizing that the covariant derivative of the metric perturbation is given by

$$\begin{aligned} \nabla_\alpha h_{\mu\nu} &= \partial_\alpha h_{\mu\nu} - \Gamma^{\beta}_{\alpha\mu} h_{\beta\nu} - \Gamma^{\beta}_{\alpha\nu} h_{\beta\mu}, && (3.76)\\ &= \partial_\alpha h_{\mu\nu} - \frac{1}{2}h^{\gamma}{}_{\nu}(\partial_\mu g_{\gamma\alpha} + \partial_\alpha g_{\gamma\mu} - \partial_\gamma g_{\alpha\mu}) - \frac{1}{2}h^{\gamma}{}_{\mu}(\partial_\nu g_{\gamma\alpha} + \partial_\alpha g_{\gamma\nu} - \partial_\gamma g_{\alpha\nu}). && (3.77) \end{aligned}$$

Thus the perturbation to the Christoffel symbols reduces to

$$\delta\Gamma^{\alpha}_{\mu\nu} = \frac{1}{2}g^{\alpha\beta}(\nabla_\mu h_{\beta\nu} + \nabla_\nu h_{\beta\mu} - \nabla_\alpha h_{\mu\nu}) + O(\epsilon^2). \tag{3.78}$$

The Riemann tensor $\mathbf{R}^{\alpha}{}_{\beta\mu\nu}$ can be expanded in a similar fashion

$$\mathbf{R}^{\alpha}{}_{\beta\mu\nu} = R^{\alpha}{}_{\beta\mu\nu} + \epsilon\delta R^{\alpha}{}_{\beta\mu\nu}. \tag{3.79}$$

The perturbation to the Riemann tensor is then found by expanding $\mathbf{R}^{\alpha}{}_{\beta\mu\nu}$

$$\begin{aligned} \delta R^{\alpha}{}_{\beta\mu\nu} &= \epsilon^{-1}\left(\mathbf{R}^{\alpha}{}_{\beta\mu\nu} - R^{\alpha}{}_{\beta\mu\nu}\right), && (3.80)\\ &= \epsilon^{-1}\Big(\partial_\mu \boldsymbol{\Gamma}^{\alpha}_{\beta\nu} - \partial_\nu \boldsymbol{\Gamma}^{\alpha}_{\beta\mu} + \boldsymbol{\Gamma}^{\alpha}_{\mu\gamma}\boldsymbol{\Gamma}^{\gamma}_{\beta\nu} - \boldsymbol{\Gamma}^{\alpha}_{\nu\gamma}\boldsymbol{\Gamma}^{\gamma}_{\beta\mu} - \partial_\mu \Gamma^{\alpha}_{\beta\nu} + \partial_\nu \Gamma^{\alpha}_{\beta\mu} - \Gamma^{\alpha}_{\mu\gamma}\Gamma^{\gamma}_{\beta\nu} + \Gamma^{\alpha}_{\nu\gamma}\Gamma^{\gamma}_{\beta\mu}\Big), && (3.81)\\ &= \partial_\mu \delta\Gamma^{\alpha}_{\beta\nu} - \partial_\nu \delta\Gamma^{\alpha}_{\beta\mu} + \Gamma^{\alpha}_{\mu\gamma}\delta\Gamma^{\gamma}_{\beta\nu} + \delta\Gamma^{\alpha}_{\mu\gamma}\Gamma^{\gamma}_{\beta\nu} - \Gamma^{\alpha}_{\nu\gamma}\delta\Gamma^{\gamma}_{\beta\mu} - \delta\Gamma^{\alpha}_{\nu\gamma}\Gamma^{\gamma}_{\beta\mu} + O(\epsilon), && (3.82)\\ &= \nabla_\mu \delta\Gamma^{\alpha}_{\beta\nu} - \nabla_\nu \delta\Gamma^{\alpha}_{\beta\mu} + O(\epsilon). && (3.83) \end{aligned}$$

Inserting Eq. (3.78), this further expands to

$$\delta R^{\alpha}{}_{\beta\mu\nu} = \frac{1}{2}\left(\nabla_\mu\nabla_\nu h^{\alpha}{}_{\beta} + \nabla_\mu\nabla_\beta h^{\alpha}{}_{\nu} - \nabla_\mu\nabla^\alpha h_{\beta\nu} - \nabla_\nu\nabla_\mu h^{\alpha}{}_{\beta} - \nabla_\nu\nabla_\beta h^{\alpha}{}_{\mu} + \nabla_\nu\nabla^\alpha h_{\beta\mu}\right). \tag{3.84}$$

It is then straightforward to construct the perturbation to the Ricci tensor

$$\begin{aligned} \delta R_{\mu\nu} &= \epsilon^{-1}\left(\mathbf{R}_{\mu\nu} - R_{\mu\nu}\right) = \epsilon^{-1}\left(\mathbf{R}^{\alpha}{}_{\mu\alpha\nu} - R^{\alpha}{}_{\mu\alpha\nu}\right) = \delta R^{\alpha}{}_{\mu\alpha\nu}, && (3.85)\\ &= -\frac{1}{2}\nabla^\alpha\nabla_\alpha h_{\mu\nu} - \frac{1}{2}\nabla_\mu\nabla_\nu h^{\alpha}{}_{\alpha} + \frac{1}{2}\nabla_\alpha\nabla_\mu h^{\alpha}{}_{\nu} + \frac{1}{2}\nabla_\alpha\nabla_\nu h^{\alpha}{}_{\mu}. && (3.86) \end{aligned}$$

Einstein's field equations, when expanded in terms of $g_{\mu\nu}$ and $h_{\mu\nu}$ then take the form

$$R_{\mu\nu} + \epsilon\delta R_{\mu\nu} - \frac{1}{2}\epsilon g_{\mu\nu}\delta R + \frac{1}{2}\left(g_{\mu\nu} + \epsilon h_{\mu\nu}\right)R = 8\pi\epsilon T_{\mu\nu} + O(\epsilon^2). \tag{3.87}$$

For a background metric that satisfies the vacuum field equations $R_{\mu\nu} = R = 0$, we then have

$$\delta R_{\mu\nu} - \frac{1}{2} g_{\mu\nu} \delta R = 8\pi T_{\mu\nu} + O(\epsilon). \tag{3.88}$$

Defining the trace-reversed metric perturbation $\bar{h}_{\mu\nu} = h_{\mu\nu} - \frac{1}{2} g_{\mu\nu} h^{\alpha}{}_{\alpha}$, the linearized field equations take the form,

$$-16\pi T_{\mu\nu} = \nabla^{\alpha}\nabla_{\alpha}\bar{h}_{\mu\nu} - \nabla_{\alpha}\nabla_{\mu}\bar{h}^{\alpha}{}_{\nu} - \nabla_{\alpha}\nabla_{\nu}\bar{h}^{\alpha}{}_{\mu} + g_{\mu\nu}\nabla_{\alpha}\nabla_{\beta}\bar{h}^{\alpha\beta}. \tag{3.89}$$

For later convenience, one can make use of the identity

$$\nabla_{\mu}\nabla_{\nu}\bar{h}^{\alpha\beta} - \nabla_{\nu}\nabla_{\mu}\bar{h}^{\alpha\beta} = R^{\alpha}{}_{\gamma\mu\nu}\bar{h}^{\gamma\beta} + R^{\beta}{}_{\gamma\mu\nu}\bar{h}^{\gamma\alpha}, \tag{3.90}$$

to re-organize the order of the covariant derivatives

$$\begin{aligned} \nabla^{\alpha}\nabla_{\alpha}\bar{h}_{\mu\nu} + g_{\mu\nu}\nabla_{\alpha}\nabla_{\beta}\bar{h}^{\alpha\beta} - \nabla_{\alpha}\nabla_{\mu}\bar{h}^{\alpha}{}_{\nu} - R_{\gamma\mu}\bar{h}^{\gamma}{}_{\nu} - R_{\nu\gamma\alpha\mu}\bar{h}^{\gamma\alpha} & \\ - \nabla_{\alpha}\nabla_{\nu}\bar{h}^{\alpha}{}_{\mu} - R_{\gamma\nu}\bar{h}^{\gamma}{}_{\mu} - R_{\mu\gamma\alpha\nu}\bar{h}^{\gamma\alpha} &= -16\pi T_{\mu\nu}. \end{aligned} \tag{3.91}$$

Taking into account the interchange and skew symmetries of the Riemann tensor, the symmetry of $\bar{h}_{\alpha\beta}$, and the fact that $g_{\mu\nu}$ represents a vacuum solution to Einstein's equations ($R_{\mu\nu} = 0$), the linearized Einstein equations reduce to one of their most well-known forms

$$\nabla^{\alpha}\nabla_{\alpha}\bar{h}_{\mu\nu} + g_{\mu\nu}\nabla_{\alpha}\nabla_{\beta}\bar{h}^{\alpha\beta} - \nabla_{\alpha}\nabla_{\mu}\bar{h}^{\alpha}{}_{\nu} - \nabla_{\alpha}\nabla_{\nu}\bar{h}^{\alpha}{}_{\mu} + 2R_{\alpha\mu\beta\nu}\bar{h}^{\alpha\beta} = -16\pi T_{\mu\nu}. \tag{3.92}$$

Imposing the Lorenz gauge condition $\nabla_{\nu}\bar{h}^{\mu\nu} = 0$ simplifies Eq. (3.92) to the curved-space wave equation

$$\nabla^{\alpha}\nabla_{\alpha}\bar{h}_{\mu\nu} + 2R_{\alpha\mu\beta\nu}\bar{h}^{\alpha\beta} = -16\pi T_{\mu\nu}. \tag{3.93}$$

This is the field equation for the first-order perturbation in the metric.

To find the correction to the particle's motion, one must return to the full stress-energy constraint,

$$\boldsymbol{\nabla}_{\boldsymbol{\mu}}\mathbf{T}^{\mu\nu} = 0. \tag{3.94}$$

Because $\mathbf{T}^{\mu\nu}$ is still given by a point-particle source, based on the derivation at the beginning of this section (see Eqs. (3.64)-(3.70)), Eq. (3.94) enforces geodesic motion in the full, perturbed spacetime background $\mathbf{g}_{\mu\nu}$

(ignoring radiation-reaction effects beyond first-order),

$$\mu \mathbf{u}^{\alpha} \boldsymbol{\nabla}_{\alpha} \mathbf{u}^{\beta} = \frac{d^2 x_p^{\alpha}}{d\boldsymbol{\tau}^2} + \boldsymbol{\Gamma}^{\alpha}_{\mu\nu} \frac{dx_p^{\mu}}{d\boldsymbol{\tau}} \frac{dx_p^{\nu}}{d\boldsymbol{\tau}} = 0, \tag{3.95}$$

where $\mathbf{u}^{\alpha} = dx_p^{\alpha}/d\boldsymbol{\tau}$ is the particle's four-velocity in the full spacetime $\mathbf{g}_{\mu\nu}$.

A "fictitious" gravitational force arises if, rather than working in $\mathbf{g}_{\mu\nu}$, one continues to work in the mathematically simpler background $g_{\mu\nu}$ [30, 180]. The geodesic equation, then takes the form

$$\mu u^{\alpha} \nabla_{\alpha} u^{\beta} = \frac{d^2 x_p^{\alpha}}{d\tau^2} + \Gamma^{\alpha}_{\mu\nu} \frac{dx_p^{\mu}}{d\tau} \frac{dx_p^{\nu}}{d\tau} \equiv F^{\beta}_{\text{grav}}, \tag{3.96}$$

where $u^{\alpha} = dx_p/d\tau$, τ is now an affine parameter of the background metric g_{μ}, and the covariant derivative ∇_{α} is defined with respect to $g_{\mu\nu}$. The resulting gravitational force F^{β}_{grav} is then given by the difference of Eqs. (3.95) and (3.96)

$$F^{\alpha}_{\text{grav}} = -\mu\epsilon\, \delta\Gamma^{\alpha}_{\mu\nu} u^{\mu} u^{\nu} - \mu \left(\frac{d\boldsymbol{\tau}}{d\tau}\right)^2 \frac{d^2\tau}{d\boldsymbol{\tau}^2} u^{\alpha} + O(\epsilon^2), \tag{3.97}$$

$$= -\mu \frac{\epsilon}{2} g^{\alpha\beta} \left(2\nabla_{\mu} h_{\beta\nu} - \nabla_{\beta} h_{\mu\nu}\right) u^{\mu} u^{\nu} - \mu \left(\frac{d\boldsymbol{\tau}}{d\tau}\right)^2 \frac{d^2\tau}{d\boldsymbol{\tau}^2} u^{\alpha} + O(\epsilon^2), \tag{3.98}$$

The second term accounts for the failure of τ as an affine parameter for a geodesic in $\mathbf{g}_{\mu\nu}$,

$$\left(\frac{d\boldsymbol{\tau}}{d\tau}\right)^2 \frac{d^2\tau}{d\boldsymbol{\tau}^2} = \left(\frac{d\tau}{d\boldsymbol{\tau}}\right) \frac{d^2\boldsymbol{\tau}}{d\tau^2} = \frac{d}{d\tau} \ln \sqrt{1 - \epsilon h_{\mu\nu} u^{\mu} u^{\nu}}, \tag{3.99}$$

which can be expanded in powers of the mass ratio,

$$\frac{d}{d\tau} \ln \sqrt{1 - \epsilon h_{\mu\nu} u^{\mu} u^{\nu}} = -\frac{\epsilon}{2} u^{\alpha} u^{\mu} u^{\nu} \nabla_{\alpha} h_{\mu\nu} - \epsilon h_{\mu\nu} u^{\alpha} u^{\mu} \nabla_{\alpha} u^{\nu} + O(\epsilon^2). \tag{3.100}$$

Comparing to Eq. (3.98), the second term is also of $O(\epsilon^2)$ and can be neglected. Consequently

$$u_{\alpha} F^{\alpha}_{\text{grav}} = -\mu \frac{\epsilon}{2} (2\nabla_{\mu} h_{\beta\nu} - \nabla_{\beta} h_{\mu\nu}) u^{\mu} u^{\nu} u^{\beta} - \mu \left(\frac{d\boldsymbol{\tau}}{d\tau}\right)^2 \frac{d^2\tau}{d\boldsymbol{\tau}^2}, \tag{3.101}$$

$$= -\mu \frac{\epsilon}{2} \nabla_{\mu} h_{\beta\nu} u^{\mu} u^{\nu} u^{\beta} - \mu \left(\frac{d\boldsymbol{\tau}}{d\tau}\right)^2 \frac{d^2\tau}{d\boldsymbol{\tau}^2}, \tag{3.102}$$

$$= -\mu \frac{\epsilon}{2} \nabla_{\mu} h_{\beta\nu} u^{\mu} u^{\nu} u^{\beta} + \mu \frac{\epsilon}{2} \nabla_{\alpha} h_{\mu\nu} u^{\alpha} u^{\mu} u^{\nu}, \tag{3.103}$$

$$= 0, \tag{3.104}$$

ensuring that the gravitational force is orthogonal to the particle's four-velocity. Thus the expression for

$F^\alpha_{\rm grav}$ simplifies to

$$F^\alpha_{\rm grav} = -\frac{\mu\epsilon}{2}\left(g^{\alpha\beta} + u^\alpha u^\beta\right)(2\nabla_\mu h_{\beta\nu} - \nabla_\beta h_{\mu\nu})u^\mu u^\nu + O(\epsilon^2), \tag{3.105}$$

$$= \mu\epsilon\nabla^{\alpha\mu\nu}h_{\mu\nu} + O(\epsilon^2), \tag{3.106}$$

where $\nabla^{\alpha\mu\nu}$ is defined in Eq. (3.60). Comparing to Eq. (3.59), one can see that this has an equivalent form to the the MiSaTaQuWa result, but it does not specify which part of the metric perturbation contributes to the particle's self-force. Just as in the previous electromagnetic cases, $F^\alpha_{\rm grav}$ diverges at the location of the particle if one naively uses the retarded solution to the metric perturbation. One must perform a similar regularization procedure by decomposing the retarded field into singular and regular parts, the latter of which will be solely responsible for the gravitational self-force.

3.3.3: The retarded, singular, and regular metric perturbations

For simplicity, consider Eq. (3.93), which is Eq. (3.55) (or (3.92)) in Lorenz gauge. Following the procedures laid out in Sec. 3.2.3, the retarded (trace-reversed) metric perturbation is constructed from the retarded Green's function $G_{+\ \ \mu'\nu'}^{\alpha\beta}$

$$\bar{h}^{\alpha\beta}_{\rm ret}(x) = 4\int G_{+\ \ \mu'\nu'}^{\alpha\beta}(x,x')T^{\mu'\nu'}(x')\sqrt{-g(x')}\,d^4x', \tag{3.107}$$

where

$$\nabla^\gamma\nabla_\gamma G_{+\ \ \mu'\nu'}^{\alpha\beta}(x,x') + 2R_{\mu\ \nu}^{\ \alpha\ \beta}(x)G_{+\ \ \mu'\nu'}^{\mu\nu}(x,x') = -4\pi\delta^\alpha_{\ \mu'}\delta^\beta_{\ \nu'}\delta^{(4)}(x,x'). \tag{3.108}$$

The gravitational retarded Green's function, $G_{+\ \ \mu'\nu'}^{\alpha\beta}$, and its advanced counterpart, $G_{-\ \ \mu'\nu'}^{\alpha\beta}$, share the same local causal structure as the electromagnetic $G^\mu_{\pm\ \nu'}(x,x')$ in Sec. 3.2.3. Thus, following the work of Dirac, DeWitt, and Brehme, one can construct a singular Green's function

$$G_{\rm S\ \ \mu'\nu'}^{\alpha\beta}(x,x') \equiv \frac{1}{2}\left[G_{+\ \ \mu'\nu'}^{\alpha\beta}(x,x') + G_{-\ \ \mu'\nu'}^{\alpha\beta}(x,x') - H^{\alpha\beta}_{\ \ \ \mu'\nu'}(x,x')\right] \tag{3.109}$$

where $H^{\alpha\beta}_{\ \ \ \mu'\nu'}$ satisfies conditions analogous to (H1)-(H4), just like $H^\mu_{\ \nu'}$ in Sec. 3.2.3. The regular gravitational two-point function is then given by

$$G_{\rm R\ \ \mu'\nu'}^{\alpha\beta}(x,x') \equiv G_{+\ \ \mu'\nu'}^{\alpha\beta}(x,x') - G_{\rm S\ \ \mu'\nu'}^{\alpha\beta}(x,x'), \tag{3.110}$$

$$= \frac{1}{2}\left[G_{+\ \ \mu'\nu'}^{\alpha\beta}(x,x') - G_{-\ \ \mu'\nu'}^{\alpha\beta}(x,x') + H^{\alpha\beta}_{\ \ \ \mu'\nu'}(x,x')\right], \tag{3.111}$$

resulting in a regular (trace-reversed) metric perturbation that is a homogeneous solution to Eq. (3.93)

$$\bar{h}^{\alpha\beta}_{\mathrm{R}}(x) = 4\int G^{\alpha\beta}_{\mathrm{R}\ \mu'\nu'}(x,x')T^{\mu'\nu'}(x')\sqrt{-g(x')}\,d^4x', \tag{3.112}$$

Detweiler and Whiting [82] demonstrated that $\bar{h}^{\alpha\beta}_{\mathrm{R}}$ is related to the MiSaTaQuWa tail field by [180]

$$\nabla_\alpha h^{\mathrm{tail}}_{\mu\nu} = \nabla_\alpha h^{\mathrm{R}}_{\mu\nu} + 2\mu\left(u_\mu R_{\nu\alpha\beta\gamma} + u_\nu R_{\mu\alpha\beta\gamma} + 2u_\alpha R_{\mu\beta\nu\gamma}\right)u^\beta u^\gamma, \tag{3.113}$$

so that

$$\mu u^\beta \nabla_\beta u^\alpha = F^\alpha_{\mathrm{GSF},1} = \mu\nabla^{\alpha\mu\nu}h^{\mathrm{R}}_{\mu\nu}, \tag{3.114}$$

to first-order. Thus, like in the electromagnetic cases, one can interpret the particle as moving on a geodesic in an *effective* gravitational field $g_{\mu\nu} + h^{\mathrm{R}}_{\mu\nu}$. While this effective field only retains causal structure along the particle's wordline, it provides an elegant interpretation of the first-order gravitational self-force problem.

Note that, just like the electromagnetic self-force in curved spacetime, the regular field and the gravitational self-force can be further decomposed into dissipative and conservative components

$$F^{\alpha(\mathrm{diss})}_{\mathrm{GSF}} \equiv \mu\nabla^{\alpha\mu\nu}h^{\mathrm{diss}}_{\mu\nu}, \qquad F^{\alpha(\mathrm{cons})}_{\mathrm{GSF}} \equiv \mu\nabla^{\alpha\mu\nu}h^{\mathrm{cons}}_{\mu\nu}, \tag{3.115}$$

where

$$\bar{h}^{\alpha\beta}_{\mathrm{diss}}(x) = 2\int \left(G^{\alpha\beta}_{+\ \mu'\nu'}(x,x') - G^{\alpha\beta}_{-\ \mu'\nu'}(x,x')\right)T^{\mu'\nu'}(x')\sqrt{-g(x')}\,d^4x', \tag{3.116}$$

$$\bar{h}^{\alpha\beta}_{\mathrm{cons}}(x) = 2\int H^{\alpha\beta}_{\ \ \mu'\nu'}(x,x')T^{\mu'\nu'}(x')\sqrt{-g(x')}\,d^4x'. \tag{3.117}$$

The conservative gravitational self-force perturbs the "constants" of motion of the bound particle (e.g., $\mathcal{E}$, $\mathcal{L}_z$, and $\mathcal{Q}$ from Chapter 2), while the dissipative self-force sources its adiabatic inspiral and the eventual merger of the two bodies.

3.3.4: Gauge ambiguity

A notable feature of the gravitational (and electromagnetic) self-force is that it is a *gauge-dependent* quantity. Performing the gauge transformation $x^\mu \to \tilde{x}^\mu = x^\mu - \epsilon\xi^\mu$ alters the form of the metric perturbation and its regular contribution

$$\tilde{h}^{\mathrm{R}}_{\mu\nu} - h^{\mathrm{R}}_{\mu\nu} = (\nabla_\nu\xi_\mu + \nabla_\mu\xi_\nu), \tag{3.118}$$

where $\tilde{h}_{\mu\nu}$ is the metric perturbation in the new coordinates $\tilde{x}^\mu$. Using the fact that $(\nabla_\nu\nabla_\mu - \nabla_\mu\nabla_\nu)\xi_\alpha = \xi_\lambda R^\lambda{}_{\alpha\nu\mu}$, one finds that the gravitational self-force in this new gauge $\tilde{F}^\alpha_{\mathrm{GSF}}$ differs from the original value F^α_{GSF} according to

$$\tilde{F}^\alpha_{\mathrm{GSF}} - F^\alpha_{\mathrm{GSF}} = -(g^{\alpha\beta} + u^\alpha u^\beta)u^\nu\nabla_\nu(u^\mu\nabla_\mu\xi_\beta) - R^\alpha_{\beta\gamma\delta}u^\beta\xi^\gamma u^\delta + O(\epsilon^2). \tag{3.119}$$

This gauge ambiguity means that it is important to identify gauge-invariant quantities, such as the gravitational wave fluxes or the asymptotic gravitational signal, to give self-force results physical meaning.

3.3.5: Gravitational wave fluxes

While up to this point I have focused on the local self-force effects that arise from gravitational radiation, it is also useful to calculate the fluxes of energy and angular momentum that are radiated away due to gravitational wave emission. Not only are these fluxes gauge-invariant, but they can also be related to the gravitational self-force through *flux-balance* laws [113, 193, 162, 202, 135]. The total energy flux $\langle\dot{E}\rangle^{\mathrm{tot}}$ must balance the rate of work $\mathcal{W}$ done on the mass μ by the gravitational self-force, while the angular momentum flux $\langle\dot{L}_z\rangle^{\mathrm{tot}}$ must balance the torque $\mathcal{T}$ applied by the self-force

$$\langle\dot{E}\rangle^{\mathrm{tot}} = -\mathcal{W}, \qquad \langle\dot{L}_z\rangle^{\mathrm{tot}} = -\mathcal{T}, \tag{3.120}$$

where E^{tot} and L_z^{tot} are the total radiated energy and z-component of the angular momentum, $\dot{E} \equiv dE/dt$ and $\dot{L}_z \equiv dL_z/dt$, and the brackets $\langle\cdot\rangle$ denote averages over coordinate time t. The fluxes, therefore, drive the leading-order evolution of an EMRI, as given in Eq. (1.17). These flux-balance laws also provide an important tool for validating and comparing gauge-dependent self-force results.

In general, the average local work and torque are calculated by considering the time rate of change of the specific energy and angular momentum of the small body,

$$\mathcal{W} = \left\langle \mu\frac{d\mathcal{E}}{dt} \right\rangle \qquad \mathcal{T} = \left\langle \mu\frac{d\mathcal{L}_z}{dt} \right\rangle. \tag{3.121}$$

As demonstrated by Drasco and Hughes [92], Eq. (3.121) can also be expressed in terms of Mino time λ (see Sec. 2.2) via the relations

$$\left\langle \mu\frac{d\mathcal{E}}{dt} \right\rangle = \frac{1}{\Gamma}\left\langle \mu\frac{d\mathcal{E}}{d\lambda} \right\rangle_\lambda, \qquad \left\langle \mu\frac{d\mathcal{L}_z}{dt} \right\rangle = \frac{1}{\Gamma}\left\langle \mu\frac{d\mathcal{L}_z}{d\lambda} \right\rangle_\lambda, \tag{3.122}$$

where $\langle\cdot\rangle_\lambda$ denotes an average over Mino time. The work done by the self-force can then be found by taking the total Mino time derivative of $\mathcal{E}$,

$$\begin{aligned} \frac{d\mathcal{E}}{d\lambda} &= \Sigma \frac{d\mathcal{E}}{d\tau} && (3.123) \\ &= \Sigma u^\alpha \nabla_\alpha \left(g_{\mu\nu} \xi^\mu_{(t)} u^\nu \right), && (3.124) \\ &= \Sigma g_{\mu\nu} \left(u^\nu u^\alpha \nabla_\alpha \xi^\mu_{(t)} + \xi^\mu_{(t)} u^\alpha \nabla_\alpha u^\nu \right), && (3.125) \\ &= \Sigma g_{\mu\nu} \xi^\mu_{(t)} u^\alpha \nabla_\alpha u^\nu, && (3.126) \end{aligned}$$

where $u^\nu u^\alpha \nabla_\alpha \xi^\mu_{(t)}$ vanishes due to $\xi^\mu_{(t)}$ satisfying Killing's equation (Eq. (2.4)). Defining the four-acceleration a^μ and perpendicular self-force $f^\mu = \mu a^\mu \equiv (g^{\mu\nu} + u^\mu u^\nu) F^{\mathrm{SF}}_\nu$—where F^{SF}_ν represents the scalar, electromagnetic, or gravitational self-force—then

$$\mu \frac{d\mathcal{E}}{d\lambda} = -\Sigma f_t. \tag{3.127}$$

Therefore,

$$\left\langle \mu \frac{d\mathcal{E}}{dt} \right\rangle = -\frac{1}{\Gamma} \left\langle \Sigma f_t \right\rangle_\lambda = -\frac{1}{\Gamma} \left\langle \Sigma F^{\mathrm{SF}}_t \right\rangle_\lambda, \tag{3.128}$$

Note that for the electromagnetic and gravitational cases, the self-force is orthogonal to the four-velocity and the second equality is trivial. However, for the scalar case $u^\alpha F_\alpha = -d\mu/d\tau$, where the rest mass of the scalar particle varies with time, though even in the scalar case the average variation of the rest-mass vanishes, i.e.,

$$\left\langle \Sigma f_t \right\rangle_\lambda = \left\langle \Sigma (F_t + u_t u^\alpha F_\alpha) \right\rangle_\lambda = \left\langle \Sigma F_t \right\rangle_\lambda + \mathcal{E} \left\langle \frac{d\mu}{d\lambda} \right\rangle_\lambda = \left\langle \Sigma F_t \right\rangle_\lambda. \tag{3.129}$$

Following these same steps for $\mathcal{L}_z$, one finds

$$\left\langle \mu \frac{d\mathcal{L}_z}{dt} \right\rangle = \frac{1}{\Gamma} \left\langle \Sigma F^{\mathrm{SF}}_\varphi \right\rangle_\lambda. \tag{3.130}$$

The average work and torque can then be rewritten either as averages of the self-force over time or (in the case of non-resonant sources) as averages over the two-torus,

$$\begin{aligned} \mathcal{W} &= -\lim_{T\to\infty} \frac{1}{T} \int_0^T \frac{F^{\mathrm{SF(diss)}}_t}{u^t} dt = -\frac{1}{\Gamma} \int_0^{2\pi} \frac{dq_r}{2\pi} \int_0^{2\pi} \frac{dq_\theta}{2\pi} \Sigma_p F^{\mathrm{SF(diss)}}_t, && (3.131) \\ \mathcal{T} &= \lim_{T\to\infty} \frac{1}{T} \int_0^T \frac{F^{\mathrm{SF(diss)}}_\varphi}{u^t} dt = \frac{1}{\Gamma} \int_0^{2\pi} \frac{dq_r}{2\pi} \int_0^{2\pi} \frac{dq_\theta}{2\pi} \Sigma_p F^{\mathrm{SF(diss)}}_\varphi, && (3.132) \end{aligned}$$

where only the dissipative component contributes, because $F^{\mathrm{SF(cons)}}_t$ and $F^{\mathrm{SF(cons)}}_\varphi$ are time-antisymmetric.

(This behavior will be further discussed in Sec. 5.2.6.) Therefore the conservative pieces cancel when averaging, which is an essential aspect of deriving a gauge invariant result.

The total radiated energy and angular momentum can be calculated from the energy and angular momentum flux vectors [179]

$$\varepsilon^\alpha \equiv -g^{\alpha\beta}T_{\beta\mu}\xi^\mu_{(t)}, \qquad \ell^\alpha \equiv g^{\alpha\beta}T_{\beta\mu}\xi^\mu_{(\varphi)}, \tag{3.133}$$

where $T^{\mu\nu}$ is the stress-energy of the field that is carrying away energy and angular momentum. Recall that $\xi^\alpha_{(t)}$ and $\xi^\alpha_{(\varphi)}$ are the time and azimuthal Killing vectors. In the wave zone of an isolated source, $T_{\mu\nu} = T^{\mathrm{GW}}_{\mu\nu}$, where $T^{\mathrm{GW}}_{\mu\nu}$ is the effective stress-energy tensor that describes the gravitational waves. The gravitational wave flux through some surface S, $\dot{E} \equiv dE^S/dt$ and $\dot{L}^S_z \equiv dL^S_z/dt$, can then be found by projecting the flux vectors onto the surface's normal vector n^α_S and then integrating over the surface,

$$\dot{E}^S = -\oint_S T^{\mathrm{GW}}_{t\nu} n^\nu_S \, dS, \qquad \dot{L}^S_z = \oint_S T^{\mathrm{GW}}_{\varphi\nu} n^\nu_S \, dS. \tag{3.134}$$

For an observer measuring gravitational radiation at $r \to \infty$, $n^\mu dS \to \delta^\mu_r r^2 d\Omega$, where $d\Omega$ is the standard differential solid angle. The measured fluxes are then given by

$$\dot{E}^\infty = -\lim_{r\to\infty} r^2 \oint T^{\mathrm{GW}}_{tr}\, d\Omega, \qquad \dot{L}^\infty_z = \lim_{r\to\infty} r^2 \oint T^{\mathrm{GW}}_{\varphi r}\, d\Omega, \tag{3.135}$$

At infinity, the stress-energy tensor of the gravitational waves can be related to the metric perturbation through the Isaacson stress-energy tensor [137],

$$\left\langle T^{\mathrm{GW}}_{\alpha\beta}(r\to\infty)\right\rangle = \frac{1}{16\pi}\left\langle \partial_\alpha h_+ \partial_\beta h_+ + \partial_\alpha h_\times \partial_\beta h_\times \right\rangle, \tag{3.136}$$

where the polarization amplitudes h_+ and $h_\times$ are defined by the projection of $h_{\mu\nu}$ onto the two-polarization tensors $e^+_{\alpha\beta}$ and $e^\times_{\alpha\beta}$ so that the asymptotic behavior of the metric perturbation is [137, 93, 152]

$$h_{\alpha\beta}(r\to\infty) \simeq h_+ e^+_{\alpha\beta} + h_\times e^\times_{\alpha\beta}. \tag{3.137}$$

(See Chapter 1 of Ref. [152] for further discussion.) Upon calculating the metric perturbation $h_{\mu\nu}$, one can use Eqs. (3.135), (3.136), and (3.137) to find the time-averaged energy and angular momentum fluxes at infinity, $\langle \dot{E}\rangle^\infty$ and $\langle \dot{L}_z\rangle^\infty$, respectively. Unlike the gravitational self-force, these fluxes are gauge-invariant.

The radiation at infinity does not, however, account for the total flux of energy and angular momentum. Gravitational waves will not only radiate to infinity, but radiation will also be absorbed by the MBH. There is currently no known expression for $T_{\mu\nu}$ that describes gravitational radiation through the black hole's horizon, making it much more difficult to develop an equivalent expression for the flux of energy and angular momentum absorbed by the black hole. Poisson [178] found integral forms for the horizon fluxes that are similar to (3.135), but they require a specific gauge choice for solving the metric perturbation. As I will discuss, in Chapter 4, there are simpler methods for calculating the fluxes at both infinity and the horizon that avoid solving for the full metric perturbation $h_{\mu\nu}$.

Section 3.4: Relation to scalar radiation, radiation-reaction, and self-force

In this chapter, I discussed the impact of radiation on the dynamics of EMRIs. The EMRI and its dynamics are understood perturbatively through an expansion in the system's mass ratio ϵ. At first-order, the stellar-mass compact object of mass μ can be treated as a point particle following a worldline x_p^α in the background spacetime $g_{\alpha\beta}$ defined by the MBH. (In this work, I focus on perturbations of a background Kerr metric with black hole spin a and black hole mass M.) The motion of the stellar-mass body in this background spacetime is given by the MiSaTaQuWa equation of motion (3.114), which is driven by a gravitational self-force that arises from the small body interacting with its own (first-order) metric perturbation $h_{\mu\nu}$.

For my dissertation research, rather than calculating the gravitational self-force experienced by an EMRI, I instead consider an analogous scalar problem by giving the small body μ a scalar charge q (where $q^2 \ll \mu M$). As I will outline in further detail in Chapter 5, the formalisms presented in this chapter (e.g., radiation-reaction, self-forces, singular and regular Green's functions, tail fields, fluxes) directly transfer to the scalar case. The scalar-charged body possesses a scalar field Φ that interacts with the surrounding spacetime curvature, resulting in a *scalar self-force* that perturbs the motion of the small-body. The retarded scalar field—much like the retarded electromagnetic field and metric perturbation considered in this chapter—is formally divergent at the location of the charge. Therefore, one must identify the regular field Φ^{R} that is responsible for the scalar self-force that acts back on the perturbing scalar charge. The strong overlap between the scalar and gravitational cases makes the scalar model a powerful tool for developing new computational techniques that can be extended to the gravitational problem. Therefore, in the proceeding chapter (Chapter 4) I outline current state-of-the-art methods for calculating the gravitational self-force in Kerr spacetime. Then in Chapter 5 I demonstrate how these methods are mirrored by solving the scalar self-force problem and discuss how results in the scalar problem extend to the gravitational case.

CHAPTER 4: Gravitational perturbations of black holes

Section 4.1: Chapter overview

In this chapter, I outline current state-of-the-art procedures for calculating the gravitational self-force in Kerr spacetime. This review not only motivates the methods that I use to investigate the closely-related scalar self-force problem in the next chapter (Chapter 5), but also lays a foundation for future work as I generalize results from my scalar model to the gravitational case.

Recall from the last chapter that a key result of the MiSaTaQuWa derivations [166, 192], and the subsequent work of Detweiler and Whiting [82], is that the gravitational self-force does not depend on the full retarded metric perturbation, which is formally divergent, but just a regular component of it, $h^{\mathrm{R}}_{\mu\nu}$. Consequently, in order to calculate the gravitational self-force, one must be able to construct this regular contribution. This, however, is not a straightforward task. The global forms of the regular two-point function (3.38) and singular Green's function (3.37) are unknown. Additionally, the regular field is acausal and unphysical far from the particle. Thus it is unclear what boundary conditions would produce the correct regular solutions. Calculating $h^{\mathrm{R}}_{\mu\nu}$ and the resulting gravitational self-force requires a suitable *regularization procedure* to circumvent these issues.

In the following sections I review two of the leading regularization methods for calculating the gravitational self-force: *mode-sum regularization* and the *effective source* or *puncture* method. For my dissertation, I use mode-sum regularization, which requires the construction of the retarded field in order to calculate the self-force. Therefore, I will then survey important methods for constructing the retarded metric perturbations so that these perturbations are amenable to mode-sum regularization. I will first focus on constructing solutions in Schwarzschild spacetime ($a = 0$) before reviewing calculations of the gravitational self-force in Kerr spacetime.

Section 4.2: Regularization procedures for constructing the gravitational self-force

There are two main approaches for regularizing perturbations in order to calculate the self-force. Both methods rely on the fact that, though the singular field is also acausal away from the particle, one only needs to obtain its behavior in a normal neighborhood near the particle to form the regular field. While the global structure of the singular Green's function is not known, one can use the Hadamard expansion of the Green's function [119] to construct local analytic expansions of the singular field in the neighborhood of the small mass. In the first approach one first calculates the metric perturbation then subtracts the singular expansion to "regularize" the result, while in the second approach one subtracts the singular expansion's implied source from the source term before calculating an approximation to the regular metric perturbation. I will begin by discussing the first approach, which is commonly applied via *mode-sum regularization*, then conclude by outlining the second approach, which is commonly called the *effective source* or *puncture* method.

4.2.1: Mode-sum regularization

Mode-sum regularization takes advantage of the fact that, while $h^{\rm ret}_{\mu\nu}$ and $h^{\rm S}_{\mu\nu}$ are divergent at the location of the small mass, their multipole contributions are finite if they are decomposed onto a Legendre l-mode basis, i.e.

$$h^{\rm ret}_{\mu\nu}(t,r,\theta,\varphi) = \sum_{l=0}^{\infty} h^{{\rm ret},l}_{\mu\nu}(t,r,\theta,\varphi) \equiv \sum_{l=0}^{\infty}\sum_{m=-l}^{l} h^{{\rm ret},lm}_{\mu\nu}(t,r)Y_{lm}(\theta,\varphi), \tag{4.1}$$

$$h^{\rm S}_{\mu\nu}(t,r,\theta,\varphi) = \sum_{l=0}^{\infty} h^{{\rm S},l}_{\mu\nu}(t,r,\theta,\varphi) \equiv \sum_{l=0}^{\infty}\sum_{m=-l}^{l} h^{{\rm S},lm}_{\mu\nu}(t,r)Y_{lm}(\theta,\varphi), \tag{4.2}$$

where Y_{lm} is the standard scalar spherical harmonic. Note that it is traditional to expand components of vectors and tensors with scalar spherical harmonics. Similarly, one can define analogous self-force quantities and their multipole contributions

$$F^{\alpha({\rm ret})}_{\rm GSF} \equiv \lim_{x\to x_p} \mu\nabla^{\alpha\mu\nu}h^{\rm ret}_{\mu\nu} = \sum_{l=0}^{\infty} F^{\alpha({\rm ret}),l}_{\rm GSF}, \qquad F^{\alpha({\rm S})}_{\rm GSF} \equiv \lim_{x\to x_p} \mu\nabla^{\alpha\mu\nu}h^{\rm S}_{\mu\nu} = \sum_{l=0}^{\infty} F^{\alpha({\rm S}),l}_{\rm GSF}. \tag{4.3}$$

By subtracting the regular and singular multipoles one can then construct the gravitational self-force on a mode-by-mode basis,

$$F^{\alpha}_{{\rm GSF},1} = \lim_{x\to x_p} \sum_{l=0}^{\infty} \left(F^{\alpha({\rm ret}),l}_{\rm GSF} - F^{\alpha({\rm S}),l}_{\rm GSF} \right). \tag{4.4}$$

The singular contributions $F^{\alpha({\rm S}),l}_{\rm GSF}$ are obtained as a local analytic expansion near the location of the particle. As discussed in Chapter 3, the structure of the singular Green's function is now well understood, even if its global form is not exactly known [82, 180]. Through a Hadamard expansion of the Green's function, one can obtain an analytic expression for the singular self-force contributions $F^{\alpha({\rm S}),l}_{\rm GSF}$ [37, 39, 81, 121, 122] in the form of a series

$$F^{\alpha({\rm S}),l}_{\rm GSF} = A^{\alpha}\left(l+1/2\right) + B^{\alpha} + \frac{C^{\alpha}}{l+1/2} + \sum_{n=1}^{\infty} \frac{D^{\alpha,n}}{\prod_{k=1}^{n}(2l+1+2k)(2l+1-2k)}, \tag{4.5}$$

where the higher-order terms fall-off as $\sim l^{-4}$. While generating analytic expansions of the singular force is tedious, only the first few terms of this expansion are needed to eliminate the leading divergences of the singular field. The higher-order parameters have the convenient property that

$$\sum_{l=0}^{\infty}\left[\prod_{k=1}^{n}(2l+1+2k)(2l+1-2k)\right]^{-1}=0, \tag{4.6}$$

for $n>1$, while for geodesic sources in Kerr spacetime, $C^{\alpha}=0$ in Lorenz gauge [39, 30]. As a result, only the first two regularization parameters are necessary to formally correct for the divergent result

$$F^{\alpha}_{\mathrm{GSF},1}=\lim_{x\to x_p}\sum_{l=0}^{\infty}\left(F^{\alpha(\mathrm{ret}),l}_{\mathrm{GSF}}-A^{\alpha}\,(l+1/2)-B^{\alpha}\right). \tag{4.7}$$

In practice, however, one can not sum over an infinite number of modes when calculating the self-force. When truncating the sum in Eq. (4.7), the self-force only convergences as l^{-2}. Thus, higher-order regularization parameters, while not formally necessary, are still helpful for improving the convergence of gravitational self-force calculations. To date, A^{α} and B^{α} are known for generic geodesic sources in the Kerr spacetime [39], while higher-order parameters are known for equatorial geodesic sources [122]. Additional numerical considerations and techniques for applying mode-sum regularization are discussed later in Sec. 5.3.5.

Note that the mode-sum regularization only works if one calculates the Legendre l-mode contributions of the retarded field, which is particularly cumbersome to achieve in Kerr spacetime (see Sec. 4.4). Furthermore, the mode-sum regularization does not apply at second-order, because the multipole contributions to the second-order retarded metric perturbation are not necessarily finite [41].

4.2.2: Effective source

The effective source method, rather than generating regularization parameters that approximate the singular contribution to the "retarded self-force," relies on a puncture field, $h^{\mathcal{P}}_{\mu\nu}$, that approximates the singular structure of the retarded field [199, 34, 35, 227]. Like the previous procedure, subtracting the puncture from the retarded field then provides the residual perturbation, $h^{\mathcal{R}}_{\mu\nu}$, which is regular. If the puncture is a sufficiently accurate approximation of the singular field near the particle, then $h^{\mathcal{R}}_{\mu\nu}$ provides a local approximation of the regular field and, therefore, contains all of the information that is necessary to calculate the gravitational self-force, i.e.,

$$F^{\alpha}_{\mathrm{GSF},1}=\lim_{x\to x_p}\mu\nabla^{\alpha\mu\nu}h^{\mathcal{R}}_{\mu\nu}. \tag{4.8}$$

The residual field is constructed by solving the inhomogeneous linearized Einstein equation

$$\delta G_{\mu\nu}[h^{\mathcal{R}}] = 8\pi T_{\mu\nu} - \delta G_{\mu\nu}[h^{\mathcal{P}}] \equiv S^{\text{eff}}_{\mu\nu}. \tag{4.9}$$

with an effective source $S^{\text{eff}}_{\mu\nu}$. Unlike the regular field, which is an acausal solution to the homogeneous linearized Einstein equation (3.55), the residual field retains its causal structure far away from the particle, while the effective source encodes the behavior of the regular field near the particle. This makes the residual field more amenable to numerical calculations.

Of course, this method relies on a puncture that sufficiently captures the divergences of the singular field. The puncture must lead to a singular source term that cancels with the Dirac delta terms of the original source so that the resulting residual field is at least C^1 (once differentiable) at the location of the particle. These punctures are obtained as a local analytic expansion in the neighborhood of the particle [34, 35, 227] in a similar manner to the regularization parameters derived for the mode-sum method. Like the regularization parameters, only the first few orders in this expansion are needed to tame the divergences of the source. One strong advantage of the puncture method is that this regularization procedure also generalizes to second-order calculations, making it a promising approach for future computations of the higher-order self-force terms [41]. At the moment, however, puncture expansions have only been calculated for particular self-force problems and sources at first order [228, 88, 90, 89, 240, 243, 214], unlike the regularization parameters of the mode-sum method, whose analytic forms are now widely known for generic sources in Kerr spacetime. Ultimately, mode-sum regularization is one the most mature frameworks for calculating the self-force, and is extensively discussed in the literature. Thus, for the purposes of this work, I make use of mode-sum regularization. In the following sections, I outline how one can construct the retarded contributions that one regularizes to obtain the self-force.

Section 4.3: Calculating the retarded metric perturbations in Schwarzschild spacetime

In the limit $a \to 0$, the Kerr spacetime reduces to the spherically-symmetric Schwarzschild spacetime. For Schwarzschild, the full spacetime manifold $\mathcal{M}_{\text{Schw}}$ can be decomposed into two submanifolds, $\mathcal{M}_{\text{Schw}} = \mathcal{M}^2 \times S^2$, where $\mathcal{M}^2$ forms the "time-radial plane" and S^2 is the two-sphere. The metric is then conveniently represented by

$$ds^2 = g_{ab}dx^a dx^b + r^2\Omega_{AB}d\theta^A d\theta^B, \tag{4.10}$$

where g_{ab} is the two-metric for $\mathcal{M}^2$, Ω_{AB} is the metric on the two-sphere, and the coordinates x^a and θ^A span $\mathcal{M}^2$ and S^2, respectively. Lowercase Latin indices (e.g., a, b) run over 0 and 1, while uppercase indices (e.g.,

A, B) run over 2 and 3. In Schwarzschild coordinates, $x^a \doteq (t, r)$, $\theta^A \doteq (\theta, \varphi)$, $g_{ab} \doteq \mathrm{diag}(-f_{\mathrm{Schw}}, f_{\mathrm{Schw}}^{-1})$, and $\Omega_{AB} \doteq \mathrm{diag}(1, \sin^2\theta)$.

One can leverage these symmetries to separate the dependence of $h_{\mu\nu}$ on x^a and on θ^A. For scalar functions, this is traditionally done by decomposition on a scalar-spherical-harmonics basis. For the metric perturbation, this decomposition is instead performed with *tensor* spherical harmonics. Tensor spherical harmonics, as their name implies, are a tensorial generalization of the much more well known scalar spherical harmonics $Y^{lm}(\theta, \varphi)$ and are constructed from the Y^{lm} and their (first and second) derivatives. Following the notation and definitions of Martel and Poisson [158], the decomposition of $h_{\mu\nu}$ on a tensor-spherical-harmonics basis takes the form

$$h_{ab} = \sum_{lm} h^{lm}_{ab}(t, r) Y^{lm}(\theta, \varphi), \tag{4.11}$$

$$h_{aB} = \sum_{lm} (j^{lm}_a(t, r) Y^{lm}_B(\theta, \varphi) + h^{lm}_a X^{lm}_B(\theta, \varphi)), \tag{4.12}$$

$$h_{AB} = \sum_{lm} (r^2 K^{lm}(t, r) Y^{lm}(\theta, \varphi)\Omega_{AB} + r^2 G^{lm}(t, r) Y^{lm}_{AB}(\theta, \varphi) + h^{lm}_2(t, r) X^{lm}_{AB}(\theta, \varphi)), \tag{4.13}$$

where the even-parity vector harmonics Y^{lm}_A, the odd-parity vector harmonics X^{lm}_A, the even-parity tensor harmonics $\Omega_{AB}Y^{lm}$ and Y^{lm}_{AB}, and the odd-parity tensor harmonics X^{lm}_{AB} are all defined in Ref. [158]. Making use of this decomposition, Eq. (3.92) reduces to 10 coupled partial differential equations that only depend on the coordinates x^a.

4.3.1: Lorenz and Regge-Wheeler gauges

This system of equations can be further reduced by imposing a gauge condition. Lorenz gauge ($\nabla_\beta \bar{h}^{\alpha\beta} = 0$) is one convenient gauge choice. In Lorenz gauge, the field equations (Eq. (3.93)) form a linear, hyperbolic set of partial differential equations, and thus have a well-posed initial-value problem. By transforming to the frequency domain, the field equations can be recast as two sets of ordinary differential equations—six coupled field equations plus four coupled constraint equations due to the Lorenz gauge condition—which can be solved via traditional finite-differencing schemes. Additionally, as discussed in Chapter 3, Lorenz gauge has been a popular gauge for understanding electromagnetic fields and the electromagnetic self-force. Furthermore, the MiSaTaQuWa equations were first derived in Lorenz gauge and the analytic regularization parameters used in mode-sum regularization are known in Lorenz gauge [39]. As a result, there is an extensive literature of mathematical approaches for solving perturbations in this gauge, and, to date, gravitational self-force calculations in Schwarzschild spacetime have predominantly been performed using the Lorenz gauge condition [36, 42, 43, 176].

There are still other useful gauge choices. One alternative is Regge-Wheeler(-Zerilli) gauge [194, 247]. While, in general, the metric amplitudes are gauge-dependent, certain combinations of the amplitudes produce gauge-invariant quantities

$$\tilde{h}_{ab} \equiv h_{ab} - \nabla_a \varepsilon_a - \nabla_b \varepsilon_b, \tag{4.14}$$

$$\tilde{K} \equiv K + \frac{1}{2} l(l+1) G - \frac{2}{r} r^a \varepsilon_a, \tag{4.15}$$

$$\tilde{h}_a \equiv h_a - \frac{1}{2} \nabla_a h_2 + \frac{1}{r} r_a h_2, \tag{4.16}$$

where $\varepsilon_a \equiv j_a - \frac{1}{2} r^2 \nabla_a G$, $r_a \equiv \partial r / \partial x^a$, and the harmonic indices have been dropped to simplify notation. In Regge-Wheeler gauge, one uses the residual gauge freedom to choose $j_a^{lm} = G^{lm} = h_2 = 0$ [194, 247]. As a result, in Regge-Wheeler gauge the metric perturbations are *equivalent* to these gauge-invariant quantities, i.e., $\tilde{h}_{ab} = h_{ab}$, $\tilde{K} = K$, and $\tilde{h}_a = h_a$. If one constructs the metric amplitudes in any other gauge, it is then straightforward to calculate the metric amplitudes in Regge Wheeler gauge. Transforming from Regge-Wheeler gauge perturbations to Lorenz gauge, however, is much more challenging and has only been done for odd-parity perturbations [129], though procedures for transforming the even-parity perturbations have been proposed [201].

4.3.2: Master functions and equations

Rather than solving for the metric amplitudes h_{ab}^{lm}, h_a^{lm}, and K^{lm} directly, one can instead solve for two scalar "master functions" which encode all of the information about the metric perturbation. As first shown by Zerilli in the frequency-domain [247], then generalized to the time-domain by Moncrief [169], the even-parity amplitudes h_{ab}^{lm} and K^{lm} can be reconstructed by performing different operations (i.e, derivatives and integrals) on an even-parity master function, Ψ_{even}^{lm}, while Cunningham, Price, and Moncrief found that the odd-parity perturbations h_a could be constructed from an analogous master function, Ψ_{odd}^{lm} [156].

Martel and Poisson [158] combined these results to provide a gauge-invariant framework (in $\mathcal{M}^2$) for constructing the master functions and their associated master equations. To summarize their results, the even-parity perturbation amplitudes are encoded in the Zerilli-Moncrief master function [247, 169]

$$\Psi_{\text{even}}^{lm} \equiv \frac{2r}{l(l+1)} \left[\tilde{K}^{lm} + \frac{2}{\tilde{\Lambda}} \left(r^a r^b \tilde{h}_{ab}^{lm} - r r^a \nabla_a \tilde{K}^{lm} \right) \right], \tag{4.17}$$

where $r_a \equiv \partial r / \partial x^a$ and $\tilde{\Lambda} \equiv (l-1)(l+2) + 6M/r$. The master function is given by the Zerilli master equation

$$\left(\Box - V_{\text{even}}\right)\Psi_{\text{even}} = S_{\text{even}}, \tag{4.18}$$

where $\Box \equiv g^{ab}\nabla_a\nabla_b = -\partial_t^2 + f_{\text{Schw}}\partial_r(f_{\text{Schw}}\partial_r)$ is the wave operator in Schwarzschild coordinates, the potential takes the form

$$V_{\text{even}} = \frac{1}{\tilde{\Lambda}^2}\left[(l-1)^2(l+2)^2\left(\frac{(l-1)(l+2)+2}{r^2} + \frac{6M}{r}\right) + \frac{36M^2}{r^4}\left((l-1)(l+2) + \frac{2M}{r}\right)\right], \tag{4.19}$$

and the source term S_{even} is given in Eq. (4.27) of Ref. [158]. Likewise, the odd-parity perturbations are given by the Cunningham-Price-Moncrief master function [75, 158]

$$\Psi^{lm}_{\text{odd}} \equiv \frac{2r}{(l-1)(l+2)}\varepsilon^{ab}\left(\nabla_a \tilde{h}^{lm}_{ab} - \frac{2}{r}r_a \tilde{h}^{lm}_{b}\right), \tag{4.20}$$

where ε_{ab} is the Levi-Civita tensor on the submanifold $\mathcal{M}^2$. The behavior of Ψ^{lm}_{odd} is determined by the Regge-Wheeler master equation

$$\left(\Box - V_{\text{odd}}\right)\Psi_{\text{odd}} = S_{\text{odd}}, \tag{4.21}$$

with potential

$$V_{\text{odd}} \equiv \frac{l(l+1)}{r^2} = \frac{6M}{r^3}. \tag{4.22}$$

The source term S_{odd} is given by Eq. (5.16) of Ref. [158]. The Cunningham-Price-Moncrief master function is closely related to the original master function proposed by Regge and Wheeler [194],

$$\Psi^{lm}_{\text{RW}} \equiv \frac{1}{r}r^a \tilde{h}^{lm}_{a}, \tag{4.23}$$

which also satisfies the Regge-Wheeler equation but with a different source term. While these two master equations, Eqs. (4.18) and (4.21), are much simpler to solve than the 10 field equations, they do not directly yield the metric perturbations. One must subsequently reconstruct the metric amplitudes from the master functions. Current procedures can reconstruct the metric in Regge-Wheeler gauge but not Lorenz gauge [157, 128]. To calculate Lorenz gauge perturbations, one must either transform the reconstructed metric from Regge-Wheeler to Lorenz gauge [129] or solve for the metric amplitudes directly from the Lorenz gauge field equations [176].

While the metric amplitudes are necessary for gravitational self-force calculations, they are not necessary for calculating the asymptotic behavior of the gravitational radiation field [158]. For example, the time-averaged energy and angular momentum flux due to gravitational wave emission, $\langle \dot{E} \rangle$ and $\langle \dot{L} \rangle$ (which were first introduced in Sec. 3.3.5), can be calculated directly from the master functions [217, 158],

$$\langle \dot{E} \rangle = \frac{1}{64\pi} \sum_{lm} \frac{(l+2)!}{(l-2)!} \left\langle \left| \dot{\Psi}^{lm,+}_{\text{even}} \right|^2 + \left| \dot{\Psi}^{lm,-}_{\text{even}} \right|^2 + \left| \dot{\Psi}^{lm,+}_{\text{odd}} \right|^2 + \left| \dot{\Psi}^{lm,-}_{\text{odd}} \right|^2 \right\rangle, \tag{4.24}$$

$$\langle \dot{L} \rangle = \frac{1}{64\pi} \sum_{lm} im \frac{(l+2)!}{(l-2)!} \left\langle \dot{\Psi}^{lm,+}_{\text{even}} \Psi^{*lm,+}_{\text{even}} + \dot{\Psi}^{lm,+}_{\text{odd}} \Psi^{*lm,+}_{\text{odd}} + \dot{\Psi}^{lm,-}_{\text{even}} \Psi^{*lm,-}_{\text{even}} + \dot{\Psi}^{lm,-}_{\text{odd}} \Psi^{*lm,-}_{\text{odd}} \right\rangle, \tag{4.25}$$

where $\langle G \rangle$ denotes a long time-average of $G(t)$, the superscript "+" means functions are evaluated on the outer boundary $r \to +\infty$, while the superscript "−" means functions are evaluated on the inner boundary $r \to r_+$, where r_+ represents the radius of the massive black hole's horizon. (In Schwarzschild spacetime, $r_+ = 2M$.) Conveniently, no metric reconstruction procedure is needed to calculate these gauge-invariant quantities. This makes this master function approach, where one solves only two ordinary differential equations, instead of 10, quite powerful. In the following section I will discuss how a similar set of scalar functions and equations also exist in Kerr spacetime.

Section 4.4: Calculating the retarded metric perturbations in Kerr spacetime

Due to the axisymmetry of Kerr spacetime, separability of the linear Einstein equations is much more difficult to achieve. It does not appear that the Kerr manifold can be separated in an equivalently useful way into two two-dimensional submanifolds like in Schwarzschild spacetime. Consequently, a tensor-spherical-harmonic decomposition will not separate the angular dependence of the metric perturbation from its dependence on the time and radial coordinates. One can make use of the time and azimuthal symmetries of Kerr to Fourier expand the perturbation in t and φ, i.e.,

$$\bar{h}_{\mu\nu}(t, r, \theta, \varphi) = \sum_{m=0}^{\infty} \int d\omega \, \bar{h}^{m\omega}_{\mu\nu}(r, \theta) e^{im\varphi} e^{-i\omega t}. \tag{4.26}$$

Then Eq. (3.93) simplifies to sets of coupled (elliptic) partial differential equations that depend on r and θ and can be solved upon specifying suitable boundary data. While this decomposition reduces the dimensionality of the problem, the coupling between r and θ remains. Furthermore, there is still the problem of integrating the delta source term, which lacks the natural angular harmonic basis for constructing finite multipoles of the retarded field. This requires Lorenz gauge perturbations to be calculated through an effective source scheme. To date, there is no known method for separating the radial and polar coupling in the Lorenz-gauge gravitational field in Kerr spacetime, though promising work by Dolan [87] has shown how this can be done in the case of electromagnetic perturbations. Despite this lack of separability, there has been preliminary work on calculating the metric perturbations from the Lorenz-gauge field equations, with some authors solving the full linearized Einstein equations through a 3+1 decomposition [228], akin to numerical relativity; others using the azimuthal symmetry to reduce the problem to a 2+1 decomposition [88, 90, 89, 214]; and yet others developing an azimuthal and frequency domain decomposition [240, 243], such as Eq. (4.26). Even with these developments, a full calculation of the metric perturbations in Lorenz gauge in Kerr spacetime has not yet been made.

Alternatively, much like in Schwarzschild spacetime, it can be convenient to work in a different class of gauges from Lorenz gauge. One particularly useful set are the radiation gauges. This class includes the ingoing and outgoing radiation gauges, which are defined by the gauge conditions

$$l^\mu h_{\mu\nu} = 0, \qquad h^\alpha{}_\alpha = 0, \qquad \text{(ingoing)} \tag{4.27}$$

$$n^\mu h_{\mu\nu} = 0, \qquad h^\alpha{}_\alpha = 0, \qquad \text{(outgoing)} \tag{4.28}$$

where l^μ is the outgoing null vector and n^μ is the ingoing null vector of the Kinnersley tetrad.[1] Unfortunately, much like Lorenz gauge, the field equations do not easily separate as they do in Schwarzschild spacetime. In these radiation gauges, however, it is possible to calculate $h_{\mu\nu}$ by (re)constructing the metric perturbations from a set of two "master" functions: the Weyl scalars ψ_0 and ψ_4, which obey the Teukolsky equation [209]. Unlike the linearized Einstein equations, the Teukolsky equation is separable, provided one transforms ψ_0 and ψ_4 to the frequency domain, then decomposes their transforms onto a basis of (frequency-dependent) spin-weighted *spheroidal* harmonics [53, 209]. This greatly simplifies the numerical calculation of the Weyl scalars.

The Weyl scalar ψ_0 and ψ_4 possess *most* of the perturbation information, but not all of it. The additional metric information must be completed from the global perturbations of the Kerr mass and angular momentum, M and $J \equiv aM$ [231, 223]. This two-step process of metric reconstruction and metric completion is now well understood in radiation gauge and has been used to calculate the outgoing-radiation-gauge gravitational self-force in Kerr spacetime [222, 224]. I, therefore, review the origin of the Weyl scalars and the Teukolsky equation, and how to solve for them. I then outline how their solutions can be used to reconstruct and complete the metric perturbations in radiation gauge.

4.4.1: Newman-Penrose formalism

The Newman-Penrose (NP) formalism [173] leverages spinor calculus to examine the structure of different spacetimes in general relativity. This requires first choosing a special vector basis known as a null tetrad,

---

[1] In outgoing radiation gauge the metric perturbation, which encodes the system's radiation, is orthogonal to the lines of ingoing radiation n^ν so that there is only outgoing radiation.

which is represented by $e^{\alpha}_{(\mathtt{a})} \equiv (\mathtt{l}^{\alpha}, \mathtt{n}^{\alpha}, \mathtt{m}^{\alpha}, \mathtt{m}^{*\alpha})$, which are constrained by $\mathtt{l}^{\alpha}\mathtt{n}_{\alpha} = -\mathtt{m}^{\alpha}\mathtt{m}^{*}_{\alpha} = -1$ and all other inner products vanishing. An asterisk denotes complex conjugation. Note that tetrad components are labeled by Latin indices with typewriter font (e.g., $(\mathtt{a})$, $(\mathtt{b})$), while spacetime coordinates are labeled by Greek indices. Tetrad components can be raised or lowered by

$$\eta_{(\mathtt{a})(\mathtt{b})} = \eta^{(\mathtt{a})(\mathtt{b})} = \begin{pmatrix} 0 & -1 & 0 & 0 \\ -1 & 0 & 0 & 0 \\ 0 & 0 & 0 & 1 \\ 0 & 0 & 1 & 0 \end{pmatrix}, \tag{4.29}$$

while the vector and tensor indices are raised and lowered with the metric $g_{\alpha\beta} = e_{(\mathtt{a})\alpha} e_{(\mathtt{b})\beta} \eta^{(\mathtt{a})(\mathtt{b})}$ and its inverse $g^{\alpha\beta} = e^{\alpha}_{(\mathtt{a})} e^{\beta}_{(\mathtt{b})} \eta^{(\mathtt{a})(\mathtt{b})}$. One can then define a corresponding set of directional covariant derivatives

$$\hat{D} \equiv \nabla_{e^{\alpha}_{(\mathtt{l})}} = \mathtt{l}^{\alpha}\nabla_{\alpha}, \qquad \hat{\Delta} \equiv \nabla_{e^{\alpha}_{(\mathtt{n})}} = \mathtt{n}^{\alpha}\nabla_{\alpha}, \qquad \hat{\delta} \equiv \nabla_{e^{\alpha}_{(\mathtt{m})}} = \mathtt{m}^{\alpha}\nabla_{\alpha}, \qquad \hat{\delta}^{*} \equiv \nabla_{e^{\alpha}_{(\mathtt{m}^{*})}} = \mathtt{m}^{*\alpha}\nabla_{\alpha}. \tag{4.30}$$

The action of these directional derivatives on the tetrad elements themselves is then encoded in 12 spin coefficients

$$\kappa_{\mathrm{NP}} \equiv -\mathtt{m}^{\alpha}\hat{D}\mathtt{l}_{\alpha}, \qquad \tau_{\mathrm{NP}} \equiv -\mathtt{m}^{\alpha}\hat{\Delta}\mathtt{l}_{\alpha}, \qquad \sigma_{\mathrm{NP}} \equiv -\mathtt{m}^{\alpha}\hat{\delta}\mathtt{l}_{\alpha}, \qquad \rho_{\mathrm{NP}} \equiv -\mathtt{m}^{\alpha}\hat{\delta}^{*}\mathtt{l}_{\alpha}, \tag{4.31}$$

$$\pi_{\mathrm{NP}} \equiv \mathtt{m}^{*\alpha}\hat{D}\mathtt{n}_{\alpha}, \qquad \nu_{\mathrm{NP}} \equiv \mathtt{m}^{*\alpha}\hat{\Delta}\mathtt{n}_{\alpha}, \qquad \mu_{\mathrm{NP}} \equiv \mathtt{m}^{*\alpha}\hat{\delta}\mathtt{n}_{\alpha}, \qquad \lambda_{\mathrm{NP}} \equiv \mathtt{m}^{*\alpha}\hat{\delta}^{*}\mathtt{n}_{\alpha}, \tag{4.32}$$

$$\epsilon_{\mathrm{NP}} \equiv \frac{1}{2}\left(\mathtt{m}^{*\alpha}\hat{D}\mathtt{m}_{\alpha} - \mathtt{n}^{\alpha}\hat{D}\mathtt{l}_{\alpha}\right), \qquad \gamma_{\mathrm{NP}} \equiv \frac{1}{2}\left(\mathtt{m}^{*\alpha}\hat{\Delta}\mathtt{m}_{\alpha} - \mathtt{n}^{\alpha}\hat{\Delta}\mathtt{l}_{\alpha}\right), \tag{4.33}$$

$$\beta_{\mathrm{NP}} \equiv \frac{1}{2}\left(\mathtt{m}^{*\alpha}\hat{\delta}\mathtt{m}_{\alpha} - \mathtt{n}^{\alpha}\hat{\delta}\mathtt{l}_{\alpha}\right), \qquad \alpha_{\mathrm{NP}} \equiv \frac{1}{2}\left(\mathtt{m}^{*\alpha}\hat{\delta}^{*}\mathtt{m}_{\alpha} - \mathtt{n}^{\alpha}\hat{\delta}^{*}\mathtt{l}_{\alpha}\right). \tag{4.34}$$

Because $\nabla_{e^{(\mathtt{a})}_{\mu}} e^{(\mathtt{b})}_{\nu} = \Gamma^{\alpha}_{\mu\nu} e^{(\mathtt{b})}_{\alpha}$, the spin coefficients represent the tetrad projections of the connection coefficients.

The next step is to project the curvature tensors that describe spacetime structure onto this tetrad. Spacetime structure is generally encoded in the Riemann tensor, which can be separated into its trace components and trace-free components. The trace-free part of the Riemann tensor is the (conformal) Weyl tensor [168],

$$C_{\alpha\beta\gamma\delta} = R_{\alpha\beta\gamma\delta} - \frac{1}{2}\left(g_{\alpha\gamma}R_{\beta\delta} + g_{\beta\delta}R_{\alpha\gamma} - g_{\beta\gamma}R_{\alpha\delta} - g_{\alpha\delta}R_{\beta\gamma}\right) + \frac{1}{6}(g_{\alpha\gamma}g_{\beta\delta} - g_{\beta\gamma}g_{\alpha\delta})R, \tag{4.35}$$

while the trace part depends on the Ricci tensor. In vacuum spacetimes, the Riemann tensor and Weyl tensor are equivalent. Hence, the Weyl tensor contains all of the information about the intrinsic tidal gravitational field. By contracting the Weyl tensor with the null tetrad, Newman and Penrose [173] identified five complex Weyl scalars that encode the 10 independent components of the Weyl tensor

$$\begin{gathered}\psi_0 \equiv C_{\alpha\beta\gamma\delta}\mathtt{l}^{\alpha}\mathtt{m}^{\beta}\mathtt{l}^{\gamma}\mathtt{m}^{\delta}, \qquad \psi_1 \equiv C_{\alpha\beta\gamma\delta}\mathtt{l}^{\alpha}\mathtt{n}^{\beta}\mathtt{l}^{\gamma}\mathtt{m}^{\delta}, \\ \psi_2 \equiv C_{\alpha\beta\gamma\delta}\mathtt{l}^{\alpha}\mathtt{n}^{\beta}\left(\mathtt{l}^{\gamma}\mathtt{n}^{\delta} - \mathtt{m}^{\gamma}\mathtt{m}^{*\delta}\right), \\ \psi_3 \equiv C_{\alpha\beta\gamma\delta}\mathtt{l}^{\alpha}\mathtt{n}^{\beta}\mathtt{m}^{*\gamma}\mathtt{n}^{\delta}, \qquad \psi_4 \equiv C_{\alpha\beta\gamma\delta}\mathtt{n}^{\alpha}\mathtt{m}^{*\beta}\mathtt{n}^{\gamma}\mathtt{m}^{*\delta}.\end{gathered} \tag{4.36}$$

Similarly by contracting the Ricci tensor, they identified four real Ricci scalars

$$\Phi_{00}^{\mathrm{NP}} \equiv \frac{1}{2}R_{\alpha\beta}\mathtt{l}^{\alpha}\mathtt{l}^{\beta}, \qquad \Phi_{11}^{\mathrm{NP}} \equiv \frac{1}{2}R_{\alpha\beta}\left(\mathtt{l}^{\alpha}\mathtt{n}^{\beta} + \mathtt{m}^{\alpha}\mathtt{m}^{*\beta}\right), \qquad \Phi_{22}^{\mathrm{NP}} \equiv \frac{1}{2}R_{\alpha\beta}\mathtt{n}^{\alpha}\mathtt{n}^{\beta}, \qquad \Lambda^{\mathrm{NP}} \equiv \frac{1}{24}R, \tag{4.37}$$

and three complex Ricci scalars

$$\Phi_{01}^{\mathrm{NP}} \equiv \frac{1}{2}R_{\alpha\beta}\mathtt{l}^{\alpha}\mathtt{m}^{\beta}, \qquad \Phi_{02}^{\mathrm{NP}} \equiv \frac{1}{2}R_{\alpha\beta}\mathtt{m}^{\alpha}\mathtt{m}^{\beta}, \qquad \Phi_{12}^{\mathrm{NP}} \equiv \frac{1}{2}R_{\alpha\beta}\mathtt{m}^{\alpha}\mathtt{n}^{\beta}. \tag{4.38}$$

that encode the 10 independent components of the Ricci tensor [173]. Using the Ricci and Bianchi identities, i.e.,

$$(\nabla_{\alpha}\nabla_{\beta} - \nabla_{\beta}\nabla_{\alpha})e_{(\mathtt{a})\mu} = e_{(\mathtt{a})\nu}R^{\nu}{}_{\mu\alpha\beta}, \qquad \nabla_{\mu}R_{\alpha\beta\gamma\delta} + \nabla_{\gamma}R_{\alpha\beta\delta\mu} + \nabla_{\delta}R_{\alpha\beta\mu\gamma} = 0, \tag{4.39}$$

one can construct the NP field equations, leading to a (large) set of coupled differential equations for the Weyl and Ricci scalars. The full form of the NP field equations can be found in Refs. [173, 106]. Note that I have defined the spin coefficients, Weyl scalars, and Ricci scalars to have the opposite signs of the definitions provided by Newman and Penrose and later used by Teukolsky. This is because they used a metric signature $(+ - - -)$. By introducing this additional negative sign, but keeping the metric signature $(- + + +)$, the original forms of the NP equations, and the Teukolsky equations discussed in the proceeding sections, remain unchanged.

4.4.2: The Teukolsky equation: general framework

Teukolsky [209, 210] used the NP field equations to examine perturbations in the Kerr spacetime. Teukolsky introduced perturbations by splitting all quantities into their background components (B superscript) and perturbed components (P superscript), e.g. $\psi_0 = \psi_0^{\mathrm{B}} + \psi_0^{\mathrm{P}}, \kappa_{\mathrm{NP}} = \kappa_{\mathrm{NP}}^{\mathrm{B}} + \kappa_{\mathrm{NP}}^{\mathrm{P}}, \hat{D} = \hat{D}^{\mathrm{B}} + \hat{D}^{\mathrm{P}}$. He then used the fact that the Kerr and Schwarzschild geometries are of Petrov-Pirani type D, meaning that the equation

$$\tilde{\mathbf{C}}_{\alpha\beta\gamma[\delta}k_{\mu]}k^{\beta}k^{\gamma} = 0 \tag{4.40}$$

admits two independent solutions for k^α. (There can be up to four solutions; type D spacetimes only have two and, therefore, are referred to as doubly degenerate.) Here, $\tilde{\mathbf{C}}_{\alpha\beta\gamma\delta} \equiv C_{\alpha\beta\gamma\delta} + \frac{i}{2}\epsilon_{\alpha\beta\mu\nu}C^{\mu\nu}{}_{\gamma\delta}$ is the self-dual Weyl tensor and $\epsilon_{\alpha\beta\mu\nu}$ is the standard Levi-Cevita symbol. The solutions k^α are referred to as the principal null directions. Thus if one chooses $\mathtt{l}^\alpha$ and $\mathtt{n}^\alpha$ to lie along the principal null directions, then by the Goldberg-Sachs theorem and the vacuum condition $R_{\alpha\beta} = 0$, many of the background quantities vanish [173, 209]

$$\psi_0^{\mathrm{B}} = \psi_1^{\mathrm{B}} = \psi_3^{\mathrm{B}} = \psi_4^{\mathrm{B}} = \kappa_{\mathrm{NP}}^{\mathrm{B}} = \sigma_{\mathrm{NP}}^{\mathrm{B}} = \nu_{\mathrm{NP}}^{\mathrm{B}} = \lambda_{\mathrm{NP}}^{\mathrm{B}} = 0. \tag{4.41}$$

This results in sets of coupled differential equations for ψ_0^{P}, ψ_2, and ψ_4^{P}. The Bianchi identities determine the form of ψ_2

$$\hat{D}\psi_2 = 3\rho_{\mathrm{NP}}\psi_2, \qquad \hat{\delta}\psi_2 = 3\tau_{\mathrm{NP}}\psi_2, \qquad \hat{\Delta}\psi_2 = -3\mu_{\mathrm{NP}}\psi_2, \qquad \hat{\delta}^*\psi_2 = -3\pi_{\mathrm{NP}}\psi_2. \tag{4.42}$$

Teukolsky [209] found, by taking different combinations of the remaining NP field equations, that the equations for ψ_4^{P} and ψ_0^{P} conveniently separate,

$$\big[(\hat{D} - 3\epsilon_{\mathrm{NP}} + \epsilon_{\mathrm{NP}}^* - 4\rho_{\mathrm{NP}} - \rho_{\mathrm{NP}}^*)(\hat{\Delta} - 4\gamma_{\mathrm{NP}} + \mu_{\mathrm{NP}}) \tag{4.43}$$

$$- (\hat{\delta} + \pi_{\mathrm{NP}}^* - \alpha_{\mathrm{NP}}^* - 3\beta_{\mathrm{NP}} - 4\tau_{\mathrm{NP}})(\hat{\delta}^* + \pi_{\mathrm{NP}} - 4\alpha_{\mathrm{NP}}) - 3\psi_2\big]\psi_0 = 4\pi T_0, \tag{4.44}$$

$$\big[(\hat{\Delta} + 3\gamma_{\mathrm{NP}} - \gamma_{\mathrm{NP}}^* + 4\mu_{\mathrm{NP}} + \mu_{\mathrm{NP}}^*)(\hat{D} + 4\epsilon_{\mathrm{NP}} - \rho_{\mathrm{NP}}) \tag{4.45}$$

$$- (\hat{\delta}^* - \tau_{\mathrm{NP}}^* + \beta_{\mathrm{NP}}^* + 3\alpha_{\mathrm{NP}} + 4\pi_{\mathrm{NP}})(\hat{\delta} - \tau_{\mathrm{NP}} + 4\beta_{\mathrm{NP}}) - 3\psi_2\big]\psi_4 = 4\pi T_4, \tag{4.46}$$

where I have dropped the perturbation superscript since $\psi_0 = \psi_0^{\mathrm{P}}$ and $\psi_4 = \psi_4^{\mathrm{P}}$. The source terms T_0 and T_4 are given by

$$\Big(\hat{\delta} + \pi_{\mathrm{NP}}^* - \alpha_{\mathrm{NP}}^* - 3\beta_{\mathrm{NP}} - 4\tau_{\mathrm{NP}}\Big)\Big[\Big(\hat{D} - 2\epsilon_{\mathrm{NP}} - 2\rho_{\mathrm{NP}}^*\Big)T_{\mathtt{lm}} - \Big(\hat{\delta} + \pi_{\mathrm{NP}}^* - 2\alpha_{\mathrm{NP}}^* - 2\beta_{\mathrm{NP}}\Big)T_{\mathtt{ll}}\Big] \tag{4.47}$$

$$+ \Big(\hat{D} - 3\epsilon_{\mathrm{NP}} + \epsilon_{\mathrm{NP}}^* - 4\rho_{\mathrm{NP}} - \rho_{\mathrm{NP}}^*\Big)\Big[\Big(\hat{\delta} + 2\pi_{\mathrm{NP}}^* - 2\beta_{\mathrm{NP}}\Big)T_{\mathtt{lm}} - \Big(\hat{D} - 2\epsilon_{\mathrm{NP}} + 2\epsilon_{\mathrm{NP}}^* - \rho_{\mathrm{NP}}^*\Big)T_{\mathtt{mm}}\Big] = T_0,$$

$$\Big(\hat{\Delta} + 3\gamma_{\mathrm{NP}} - \gamma_{\mathrm{NP}}^* + 4\mu_{\mathrm{NP}} + \mu_{\mathrm{NP}}^*\Big)\Big[\Big(\hat{\delta}^* - 2\tau_{\mathrm{NP}}^* + 2\alpha_{\mathrm{NP}}\Big)T_{\mathtt{n}\bar{\mathtt{m}}} - \Big(\hat{\Delta} + 2\gamma_{\mathrm{NP}} - 2\gamma_{\mathrm{NP}}^* + \mu_{\mathrm{NP}}^*\Big)T_{\bar{\mathtt{m}}\bar{\mathtt{m}}}\Big] \tag{4.48}$$

$$+ \Big(\hat{\delta}^* - \tau_{\mathrm{NP}}^* + \beta_{\mathrm{NP}}^* + 3\alpha_{\mathrm{NP}} + 4\pi_{\mathrm{NP}}\Big)\Big[\Big(\hat{\Delta} + 2\gamma_{\mathrm{NP}} + 2\mu_{\mathrm{NP}}^*\Big)T_{\mathtt{n}\bar{\mathtt{m}}} - \Big(\hat{\delta}^* - \tau_{\mathrm{NP}}^* + 2\beta_{\mathrm{NP}}^* + 2\alpha_{\mathrm{NP}}\Big)T_{\mathtt{nn}}\Big] = T_4.$$

The separation of the field equations for ψ_0 and ψ_4 drastically reduces the calculation of these gravitational perturbations. In the next section, I will review how these equations reduce to even more amenable forms when specialized to the case of Boyer-Lindquist coordinates.

4.4.3: The Teukolsky equation: Boyer-Lindquist coordinates

The principal null congruences of the Kerr spacetime in Boyer-Lindquist coordinates are given by [168]

$$k_{\pm}^{\alpha} = \frac{1}{\Delta}\left(r^2 + a^2, \pm\Delta, 0, a\right), \tag{4.49}$$

where the ± refer to outgoing/ingoing null rays, respectively. Thus, $\mathtt{l}^{\alpha}$ and $\mathtt{n}^{\alpha}$ must be chosen to lie along these congruences, i.e., they must be proportional to $k_{\pm}^{\alpha}$. The residual freedom can be used to set certain spin coefficients to zero. Kinnersley [147] demonstrated that by performing particular null rotations (that preserve the inner products of the null tetrad vectors) one can restrict $\epsilon_{\mathrm{NP}} = 0$. This leads to the *Kinnersley tetrad* (Case *II.A* of "Type D Vacuum Metric" in Ref. [147])[2]

$$\mathtt{l}^{\alpha} \doteq l^{\alpha} = k_{+}^{\alpha}, \tag{4.50}$$

$$\mathtt{n}^{\alpha} \doteq n^{\alpha} = \frac{1}{2\Sigma}k_{-}^{\alpha}, \tag{4.51}$$

$$\mathtt{m}^{\alpha} \doteq m^{\alpha} = \frac{1}{\sqrt{2}\,(r + ia\cos\theta)}\left(ia\sin\theta, 0, 1, i\csc\theta\right), \tag{4.52}$$

The associated one-forms are then given by

$$\mathtt{l}_{\alpha} \doteq l_{\alpha} = \frac{1}{\Delta}\left(-\Delta, \Sigma, 0, a\Delta\sin^2\theta\right), \tag{4.53}$$

$$\mathtt{n}_{\alpha} \doteq n_{\alpha} = \frac{\Delta}{2\Sigma}\left(-1, -\frac{\Sigma}{\Delta}, 0, a\sin^2\theta\right), \tag{4.54}$$

$$\mathtt{m}_{\alpha} \doteq m_{\alpha} = \frac{1}{\sqrt{2}\,(r + ia\cos\theta)}\left(-ia\sin\theta, 0, \Sigma, i(r^2 + a^2)\sin\theta\right). \tag{4.55}$$

From these one can verify that $l^{\alpha}n_{\alpha} = n^{\alpha}l_{\alpha} = -1$, $m^{*\alpha}m_{\alpha} = m^{\alpha}m_{\alpha}^{*} = 1$, and all other inner products vanish (are null).

Using these tetrad components, one can insert Eqs. (4.50)-(4.55) into Eqs. (4.31)-(4.33) to find the spin coefficients in Boyer-Lindquist coordinates

$$\rho_{\mathrm{NP}} \equiv \rho = -\frac{1}{r - ia\cos\theta}, \qquad \tau_{\mathrm{NP}} = -\frac{ia\rho\rho^{*}\sin\theta}{\sqrt{2}}, \qquad \beta_{\mathrm{NP}} = -\frac{\rho^{*}\cot\theta}{2\sqrt{2}} \tag{4.56}$$

$$\mu_{\mathrm{NP}} = \frac{\rho^2\rho^{*}\Delta}{2}, \qquad \pi_{\mathrm{NP}} = \frac{ia\rho^2\sin\theta}{\sqrt{2}}, \qquad \gamma_{\mathrm{NP}} = \mu_{\mathrm{NP}} + \frac{\rho\rho^{*}(r - M)}{2}, \qquad \alpha_{\mathrm{NP}} = \pi_{\mathrm{NP}} - \beta_{\mathrm{NP}}^{*}, \tag{4.57}$$

---

[2] Kinnersley originally published this tetard in Kerr coordinates $x'^{\mu} = (u, r_K, x, y)$, which are related to the Boyer-Lindquist coordinates through the differential relations $du = dt - \frac{r^2+a^2}{\Delta}dr$, $dr_K = dr$, $dx = d\theta$, $dy = d\varphi - \frac{a}{\Delta}dr$.

while $\kappa_{\rm NP} = \sigma_{\rm NP} = \nu_{\rm NP} = \lambda_{\rm NP} = \epsilon_{\rm NP} = 0$, and the operators are given by

$$\hat{D} = \frac{1}{\Delta}\left[\left(r^2 + a^2\right)\nabla_t + \Delta\nabla_r + a\nabla_\varphi\right], \tag{4.58}$$

$$\hat{\Delta} = \frac{\rho\rho^*}{2}\left[\left(r^2 + a^2\right)\nabla_t - \Delta\nabla_r + a\nabla_\varphi\right], \tag{4.59}$$

$$\hat{\delta} = -\frac{\rho^*}{\sqrt{2}}\left[ia\sin\theta\nabla_t + \nabla_\theta + i\csc\theta\nabla_\varphi\right]. \tag{4.60}$$

The partial differential equations for ψ_2 then take the form

$$\hat{J}_-\psi_2 = 3\rho\psi_2, \qquad \hat{L}_0^*\psi_2 = 3ia\sin\theta\rho\psi_2, \tag{4.61}$$

$$\hat{J}_+\psi_2 = 3\rho\psi_2, \qquad \hat{L}_0\psi_2 = 3ia\sin\theta\rho\psi_2, \tag{4.62}$$

where the differential operators are given by

$$\hat{L}_s \equiv \partial_\theta - \frac{i}{\sin\theta}\partial_\varphi - ia\sin\theta\partial_t + s\cot\theta, \qquad \hat{J}_\pm \equiv \partial_r \mp \frac{1}{\Delta}\left(\left(r^2 + a^2\right)\partial_t + a\partial_\varphi\right). \tag{4.63}$$

Here $\hat{L}_s^*$ is the complex conjugate of $\hat{L}_s$. By recognizing that $\rho^{-n}\partial_r\rho^n = n\rho$, $\Delta^{-n}\partial_r\Delta^n = 2n(r-M)/\Delta$, and $\rho^{-n}\partial_\theta\rho^n = nia\rho\sin\theta$, where $n \in \mathbb{Z}$, the differential equations for ψ_2 reduce to

$$\rho^3\hat{J}_-\left(\rho^{-3}\psi_2\right) = 0, \qquad \rho^3\hat{L}_0^*\left(\rho^{-3}\psi_2\right) = 0, \tag{4.64}$$

$$\rho^3\hat{J}_+\left(\rho^{-3}\psi_2\right) = 0, \qquad \rho^3\hat{L}_0\left(\rho^{-3}\psi_2\right) = 0, \tag{4.65}$$

Therefore, $\rho^{-3}\psi_2 = \psi_2^0$, where ψ_2^0 is some constant that does not depend on r or θ. Kinnersley demonstrated that, based on the tetrad and coordinate choices made earlier, $\psi_2^0 = M$, so that $\psi_2 = M\rho^3$ [147]. The gravitational source terms then take the form

$$\begin{aligned} T_0 = {} & -\frac{\rho^4\rho^*}{\sqrt{2}}\hat{L}_{-1}^*\left[\rho^{-4}\rho^{*2}\hat{J}_-\left(\rho^{*-2}T_{(l)(m)}\right) - \frac{\rho^{-4}}{\sqrt{2}}\hat{L}_0^*\left(\rho^*T_{(l)(l)}\right)\right] \\ & \qquad - \rho^4\rho^*\hat{J}_-\left[\frac{\rho^{-4}\rho^{*2}}{\sqrt{2}}\hat{L}_{-1}^*\left(\rho^{*-2}T_{(l)(m)}\right) - \rho^{-4}\hat{J}_-\left(\rho^{*-1}T_{(m)(m)}\right)\right], \end{aligned} \tag{4.66}$$

$$\begin{aligned} T_4 = {} & -\frac{\rho^8\rho^*\Delta^2}{2}\hat{J}_+\left[\frac{\rho^{-4}}{2}\hat{J}_+\left(\rho^{-2}\rho^*T_{(m^*)(m^*)}\right) - \frac{\rho^{-4}\rho^{*2}\Delta^{-1}}{\sqrt{2}}\hat{L}_{-1}\left(\rho^{-2}\rho^{*-2}T_{(n)(m^*)}\right)\right] \\ & \qquad - \frac{\rho^8\rho^*}{\sqrt{2}}\hat{L}_{-1}\left[\frac{\rho^{-4}}{\sqrt{2}}\hat{L}_0\left(\rho^{-2}\rho^{*-1}T_{(n)(n)}\right) - \frac{\rho^{-4}\rho^{*2}\Delta^2}{2}\hat{J}_+\left(\rho^{-2}\rho^{*-2}\Delta^{-1}T_{(n)(m^*)}\right)\right], \end{aligned} \tag{4.67}$$

where $T_{(a)(b)}$ refer to the projections of the stress-energy tensor onto the tetrad, e.g. $T_{(l)(m)} \equiv T_{\alpha\beta}l^\alpha m^\alpha$.

In Boyer-Lindquist coordinates, the differential equation for ψ_4 (4.46) simplifies to

$$\begin{aligned}\left(\frac{(r^2+a^2)^2}{\Delta} - a^2\sin^2\theta\right)\partial_t^2\Psi_{-2} + \frac{4Mar}{\Delta}\partial_t\partial_\varphi\Psi_{-2} + \left(\frac{a^2}{\Delta} - \frac{1}{\sin^2\theta}\right)\partial_\varphi^2\Psi_{-2} \\ - \Delta^2\partial_r\left(\frac{1}{\Delta}\partial_r\Psi_{-2}\right) - \frac{1}{\sin\theta}\partial_\theta\left(\sin\theta\partial_\theta\Psi_{-2}\right) + 4\left(\frac{M(r^2-a^2)}{\Delta} - r - ia\cos\theta\right)\partial_t\Psi_{-2} \\ + 4\left(\frac{a(r-M)}{\Delta} + \frac{i\cos\theta}{\sin^2\theta}\right)\partial_\varphi\Psi_{-2} + \left(4\cot^2\theta + 2\right)\Psi_{-2} = 8\pi\Sigma\rho^{-4}T_4, \quad (4.68)\end{aligned}$$

where $\Psi_{-2} \equiv \rho^{-4}\psi_4$. Teukolsky also found a similar partial differential equation for ψ_0. Furthermore, by repeating these calculations for scalar, electromagnetic, and (massless) neutrino perturbations using the NP formalism, Teukolsky found a series of perturbation equations that all share similar forms to Eq. (4.68). By defining each field in terms of its spin-weight s, ($s = 0$ for a perturbing scalar field, $s = \pm\frac{1}{2}$ for a perturbing neutrino field, $s = \pm 1$ for a perturbing electromagnetic field, and $s = \pm 2$ for a perturbing gravitational field) Teukolsky found a single master equation that governs all of these perturbations [209],

$$\hat{\mathcal{O}}_s\Psi_s = 4\pi\Sigma T_s', \quad (4.69)$$

where the field operator $\hat{\mathcal{O}}_s$ is given by

$$\begin{aligned}\hat{\mathcal{O}}_s\Psi_s \equiv \left[\frac{\left(r^2+a^2\right)^2}{\Delta} - a^2\sin^2\theta\right]\partial_t^2\Psi + \frac{4Mar}{\Delta}\partial_t\partial_\varphi\Psi_s + \left[\frac{a^2}{\Delta} - \frac{1}{\sin^2\theta}\right]\partial_\varphi^2\Psi_s \\ - \Delta^{-s}\partial_r\left(\Delta^{s+1}\partial_r\Psi_s\right) - \frac{1}{\sin\theta}\partial_\theta\left(\sin\theta\partial_\theta\Psi_s\right) - 2s\left[\frac{a\left(r-M\right)}{\Delta} + \frac{i\cos\theta}{\sin^2\theta}\right]\partial_\varphi\Psi_s \\ - 2s\left[\frac{M\left(r^2-a^2\right)}{\Delta} - r - ia\cos\theta\right]\partial_t\Psi_s + (s^2\cot^2\theta - s)\Psi_s. \quad (4.70)\end{aligned}$$

This is known as the *Teukolsky master equation.* The form of Ψ_s and T_s' depends on the value of s. For $s = \pm 2$,

$$\Psi_{-2} = \rho^{-4}\psi_4, \qquad T_{-2}' = 2\rho^{-4}T_4 \qquad (s=-2), \quad (4.71)$$

$$\Psi_2 = \psi_0, \qquad T_2' = 2T_0 \qquad (s=2), \quad (4.72)$$

while the forms for $s = 0, \pm\frac{1}{2}, \pm 1$ can be found in Table 1 of Ref. [209]. One can verify by plugging in $s = -2$, that Eq. (4.69) is equivalent to Eq. (4.68). For scalar perturbations ($s = 0$), which I will consider later, $\Psi_0 = \Phi$ and $T_0' = \rho_{\mathrm{scalar}}$, where Φ is the scalar field of a particle with some scalar charge q and ρ_{scalar} is its scalar charge density.

4.4.4: Separating the Teukolsky equation

Another remarkable feature of the Teukolsky master equation is that it is amenable to solution via separation of variables in the frequency domain [53, 209],

$$\Psi_s = \int d\omega \sum_{\hat{l}=0}^{\infty}\sum_{m=\hat{l}}^{\infty} {}_sR_{\hat{l}m\omega}(r)\,{}_sS^{a\omega}_{\hat{l}m}(\theta)e^{im\varphi}e^{-i\omega t}, \tag{4.73}$$

$$-4\pi\Sigma T'_s = \int d\omega \sum_{\hat{l}=0}^{\infty}\sum_{m=\hat{l}}^{\infty} {}_sT_{\hat{l}m\omega}(r)\,{}_sS^{a\omega}_{\hat{l}m}(\theta)e^{im\varphi}e^{-i\omega t}, \tag{4.74}$$

where ${}_sS^{a\omega}_{\hat{l}m}(\theta)e^{im\varphi}$ are the *spin-weighted spheroidal harmonics* with spheroidicity $\sigma^2 = -a^2\omega^2$. Like the spin-weighted spherical harmonics, they form an orthonormal basis,

$$\int {}_sS^{a\omega}_{\hat{l}m}(\theta)e^{im\varphi}\,{}_sS^{*a\omega}_{\hat{l}'m'}(\theta)e^{-im'\varphi}d\Omega = \delta_{\hat{l}\hat{l}'}\delta_{mm'}. \tag{4.75}$$

With these decompositions, the radial and polar functions separate in Eq. (4.69),

$$\begin{aligned}\frac{\Delta^{-s}}{{}_sR_{\hat{l}m\omega}}\partial_r\left(\Delta^{s+1}\partial_r\,{}_sR_{\hat{l}m\omega}\right) - {}_sV^{(r)}_{a\omega}(r) - \frac{{}_sT_{\hat{l}m\omega}}{{}_sR_{\hat{l}m\omega}} &= \\ -\sum_{jk}\int d\Omega\left(\frac{1}{\sin\theta}\partial_\theta\left(\sin\theta\partial_\theta\,{}_sS^{a\omega}_{\hat{l}m}\right){}_sS^{*a\omega}_{jk}e^{i(m-k)\varphi} - {}_sV^{(\theta)}_{a\omega}(\theta)\,{}_sS^{a\omega}_{\hat{l}m}\,{}_sS^{*a\omega}_{jk}e^{i(m-k)\varphi}\right)&,\end{aligned} \tag{4.76}$$

where the potentials are given by

$${}_sV^{(r)}_{a\omega}(r) = -\frac{\left(r^2+a^2\right)^2\omega^2 - 4Mram\omega + a^2\omega^2}{\Delta} - 2is\frac{am(r-M)+\omega M\left(r^2-a^2\right)}{\Delta} - 2i\omega sr, \tag{4.77}$$

$${}_sV^{(\theta)}_{a\omega}(\theta) = a^2\omega^2\sin^2\theta + \frac{m^2}{\sin^2\theta} + \frac{2ms\cos\theta}{\sin^2\theta} + 2a\omega s\cos\theta + (s^2\cot^2\theta - s), \tag{4.78}$$

By equating both sides with the separation constant ${}_s\lambda^{a\omega}_{\hat{l}m} + 2ma\omega$, the radial and polar equations completely decouple into the angular Teukolsky equation for the spin-weighted spheroidal harmonics

$$\begin{aligned}\frac{1}{\sin\theta}\frac{d}{d\theta}\left(\sin\theta\frac{d\,{}_sS^{a\omega}_{\hat{l}m}}{d\theta}\right) + \Bigg[-a^2\omega^2\sin^2\theta - \frac{(m+s\cos\theta)^2}{\sin^2\theta}& \\ - 2sa\omega\cos\theta + s + 2ma\omega\Bigg]\,{}_sS^{a\omega}_{\hat{l}m} = -{}_s\lambda^{a\omega}_{\hat{l}m}\,{}_sS^{a\omega}_{\hat{l}m}&,\end{aligned} \tag{4.79}$$

and the radial Teukolsky equation for the radial Teukolsky function ${}_sR_{\hat{l}m\omega}$

$$\Delta^{-s}\frac{d}{dr}\left(\Delta^{s+1}\frac{d\,{}_sR_{\hat{l}m\omega}}{dr}\right) - {}_sV^{a\omega}_{\hat{l}m}(r)\,{}_sR_{\hat{l}m\omega} = {}_sT_{\hat{l}m\omega}, \tag{4.80}$$

where

$$ {}_sV^{a\omega}_{\hat{l}m}(r) \equiv {}_sV^{(r)}_{a\omega}(r) + 2am\omega + {}_s\lambda^{a\omega}_{\hat{l}m} = -\frac{K^2 - 2is\,(r-M)\,K}{\Delta} - 4is\omega r + {}_s\lambda^{a\omega}_{\hat{l}m}, \tag{4.81} $$

with $K \equiv \left(r^2 + a^2\right)\omega - ma$. The source term is found from Eq. (4.74),

$$ {}_sT_{\hat{l}m\omega}(r) = -2\int dt\, d\Omega\, \Sigma T'_s(t,r,\theta,\varphi)\, {}_sS^{*a\omega}_{\hat{l}m}(\theta) e^{-im\varphi} e^{i\omega t}. \tag{4.82} $$

The second-order homogeneous radial Teukolsky equation admits two independent homogeneous solutions, ${}_sR^{h,\pm}_{\hat{l}m\omega}$. Physical solutions are chosen based on causal boundary conditions, leading to the "inner" solutions (with "downgoing" waves) ${}_sR^{h,-}_{\hat{l}m\omega}$ and "outer" solutions (with "outgoing" waves) ${}_sR^{h,+}_{\hat{l}m\omega}$. The homogeneous solutions have respective asymptotic behaviors [209]

$$ \begin{aligned} &{}_sR^{h,-}_{\hat{l}m\omega}(r_* \to -\infty) \sim A_1 \Delta^{-s} e^{-i\gamma r_*}, && {}_sR^{h,-}_{\hat{l}m\omega}(r_* \to \infty) \sim A_2 r^{-1} e^{-i\omega r_*} + A_3 r^{-(2s+1)} e^{i\omega r_*}, \\ &{}_sR^{h,+}_{\hat{l}m\omega}(r_* \to -\infty) \sim B_1 \Delta^{-s} e^{-i\gamma r_*} + B_2 e^{i\gamma r_*}, && {}_sR^{h,+}_{\hat{l}m\omega}(r_* \to \infty) \sim B_3 r^{-(2s+1)} e^{i\omega r_*}, \end{aligned} \tag{4.83} $$

where the A and B coefficients are arbitrary constants, $\gamma \equiv \omega - m\omega_+$, $\omega_+ \equiv a/2Mr_+$, and the inner and outer horizons are given by $r_\pm \equiv M \pm \sqrt{M^2 - a^2}$ (roots of $\Delta = 0$). The tortoise coordinate r_* is defined by the differential relation

$$ \frac{dr_*}{dr} \equiv \frac{\varpi^2}{\Delta}. \tag{4.84} $$

Once homogeneous solutions of Eq. (4.80) are obtained, inhomogeneous solutions can be constructed via variation of parameters

$$ {}_sR_{\hat{l}m\omega}(r) = c^-_{s\hat{l}m\omega}(r) {}_sR^{h-}_{lm\omega}(r) + c^+_{s\hat{l}m\omega}(r) {}_sR^{h+}_{lm\omega}(r), \tag{4.85} $$

$$ c^-_{s\hat{l}m\omega}(r) = \int_r^\infty \frac{{}_sR^{h,+}_{\hat{l}m\omega}(r') {}_sT_{\hat{l}m\omega}(r')}{\Delta(r') W_{s\hat{l}m\omega}(r')} dr', \tag{4.86} $$

$$ c^+_{s\hat{l}m\omega}(r) = \int_{r_+}^r \frac{{}_sR^{h,-}_{\hat{l}m\omega}(r') {}_sT_{\hat{l}m\omega}(r')}{\Delta(r') W_{s\hat{l}m\omega}(r')} dr'. \tag{4.87} $$

where

$$ W_{s\hat{l}m\omega}(r) \equiv {}_sR^{h,-}_{lm\omega} \frac{d}{dr}\left({}_sR^{h,+}_{lm\omega}\right) - {}_sR^{h,+}_{lm\omega} \frac{d}{dr}\left({}_sR^{h,-}_{lm\omega}\right), \tag{4.88} $$

is the Wronskian. By evaluating the Wronskian at infinity using the asymptotic relations (4.83), one can express the Wronskian in terms of the asymptotic amplitudes in (4.83),

$$W_{s\hat{l}m\omega}(r) = \Delta^{-(s+1)} \lim_{r\to\infty} \Delta^{s+1} W_{s\hat{l}m\omega}(r) = 2i\omega A_3 B_3 \Delta^{-(s+1)}. \tag{4.89}$$

As discussed in Sec. 2.3 a source that is in bound geodesic motion results in a discrete frequency spectrum ω_{mkn}. Only these discrete frequency modes contribute to the time-domain reconstruction of the perturbing field Ψ_s, i.e.,

$$c^{\pm}_{s\hat{l}m\omega} = \sum_{k=-\infty}^{\infty} \sum_{n=-\infty}^{\infty} c^{\pm}_{s\hat{l}m\omega_{mkn}} \delta(\omega - \omega_{mkn}). \tag{4.90}$$

With only the variation parameters $c^{\pm}_{s\hat{l}mkn} \equiv c^{\pm}_{s\hat{l}m\omega_{mkn}}$ contributing, the decompositions of the field and the source reduce to mode sums

$$\Psi_s = \sum_{\hat{l}mkn} {}_sR_{\hat{l}mkn}(r) {}_sS_{\hat{l}mkn}(\theta) e^{im\varphi} e^{-i\omega_{mkn}t}, \tag{4.91}$$

$$-4\pi\Sigma T'_s = \sum_{\hat{l}mkn} {}_sT_{\hat{l}mkn}(r) {}_sS_{\hat{l}mkn}(\theta) e^{im\varphi} e^{-i\omega_{mkn}t}, \tag{4.92}$$

where ${}_sR_{\hat{l}mkn} \equiv {}_sR_{\hat{l}m\omega_{mkn}}$, ${}_sT_{\hat{l}mkn} \equiv {}_sT_{\hat{l}m\omega_{mkn}}$, ${}_sS_{\hat{l}mkn} \equiv {}_sS^{a\omega_{mkn}}_{\hat{l}m}$, and I use a shorthand notation for the sums,

$$\sum_{\hat{l}mkn} \equiv \sum_{\hat{l}=0}^{\infty} \sum_{m=\hat{l}}^{\infty} \sum_{k=-\infty}^{\infty} \sum_{n=-\infty}^{\infty}. \tag{4.93}$$

Furthermore, because ${}_sT_{\hat{l}mkn}$ only has support in the source region $r_{\text{min}} \leq r \leq r_{\text{max}}$, in the source-free regions, $r < r_{\text{min}}$ and $r > r_{\text{max}}$, the $c^{\pm}_{s\hat{l}mkn}$ reduce to constants

$$C^{+}_{s\hat{l}mkn} \equiv c^{+}_{s\hat{l}mkn}(r_{\text{min}}) = \int_{r_{\text{min}}}^{r_{\text{max}}} \frac{{}_sR^{h,+}_{\hat{l}mkn}(r') {}_sT_{\hat{l}mkn}(r')}{\Delta(r') W_{s\hat{l}mkn}(r')} dr', \tag{4.94}$$

$$C^{-}_{s\hat{l}mkn} \equiv c^{-}_{s\hat{l}mkn}(r_{\text{max}}) = \int_{r_{\text{min}}}^{r_{\text{max}}} \frac{{}_sR^{h,-}_{\hat{l}mkn}(r') {}_sT_{\hat{l}mkn}(r')}{\Delta(r') W_{s\hat{l}mkn}(r')} dr'. \tag{4.95}$$

As a result, the asymptotic behavior of the inhomogeneous radial solutions is described by outgoing waves at infinity and downgoing waves at the horizon

$${}_sR_{\hat{l}mkn}(r_* \to -\infty) \sim C^{-}_{s\hat{l}mkn} \Delta^{-s} e^{-i\gamma r_*}, \qquad {}_sR_{\hat{l}mkn}(r_* \to \infty) \sim C^{+}_{s\hat{l}mkn} r^{-(s+1)} e^{i\omega r_*}. \tag{4.96}$$

For the $s = \pm 2$ cases these coefficients are commonly referred to as *Teukolsky amplitudes*. For the ($s = 0$) scalar case I will refer to these coefficients as *normalization coefficients* or *normalization constants*.

In the limit that $a \to 0$, Eq. (4.79) reduces to the differential equation for the spin-weighted spherical harmonics, ${}_sY_{lm}$ with eigenvalue $\lambda^{a\omega=0}_{lm} = l(l+1) - s(s+1)$. Additionally, in the Schwarzschild limit, the radial Teukolsky equation can be transformed to the Regge-Wheeler equation (4.21) via the Detweiler-Chandrasekhar transformation [71, 70]

$$X^{\mathrm{RW}}_{\hat{l}m\omega} = r^3 \left(\frac{d}{dr} - \frac{i\omega}{f_{\mathrm{Schw}}} \right) \left(\frac{d}{dr} + \frac{i\omega}{f_{\mathrm{Schw}}} \right) \frac{{}_{-2}R_{\hat{l}m\omega}}{r}. \tag{4.97}$$

One can similarly make a second transformation to generate a solution of the even-parity Zerilli equation as well

$$X^{\mathrm{Z},\pm}_{\hat{l}m\omega} = \frac{1}{\lambda^{\mathrm{Z}}(\lambda^{\mathrm{Z}}+1) \pm 3i\omega M} \left\{ 3M f_{\mathrm{Schw}} \frac{dX^{\mathrm{RW},\pm}_{\hat{l}m\omega}}{dr} + \left[\lambda^{\mathrm{Z}}(\lambda^{\mathrm{Z}}+1) + \frac{9M^2 f_{\mathrm{Schw}}}{r(r\lambda^{\mathrm{Z}}+3M)} \right] X^{\mathrm{RW},\pm}_{\hat{l}m\omega} \right\}, \tag{4.98}$$

where $\lambda^{\mathrm{Z}} \equiv \frac{1}{2}(l-1)(l+2)$, and ± refers to the asymptotic behavior of the solutions, defined in Eq. (4.83). Thus one can see that the Weyl scalars, in analogy with the master functions of Schwarzschild spacetime, serve as "master" functions for Kerr perturbations. Note that many of the results presented in this section (Sec. 4.4.4) hold for gravitational and scalar sources and thus connects the gravitational and scalar self-force problems. In Chapter 5, I will review how these results are directly applied to the scalar case ($s = 0$).

4.4.5: Metric reconstruction and completion

Upon obtaining the Weyl scalars, one still needs to use this information to reconstruct the metric perturbation $h_{\mu\nu}$. Chrzanowski [72] built on the previous work of Cohen and Kegeles [73] and developed a procedure for reconstructing the metric (in radiation gauge) from homogeneous solutions of the Teukolsky equation. This is known as the CCK procedure. Wald [232] later showed, however, that the reconstructed metric $h^{\mathrm{recon}}_{\mu\nu}$ corresponding to the vacuum gravitational perturbations ψ_0 and ψ_4 is not constructed by applying the CCK procedure to the Weyl scalars themselves but to some intermediate function. Cohen and Kegeles [144] then modified the CCK procedure by identifying a suitable Hertz potential, Ψ^{Hertz}, which is related but not equivalent to the Weyl scalars, and produces the physically desired vacuum metric perturbation $h^{\mathrm{recon}}_{\mu\nu}$. Constructing the Hertz potential from the Weyl scalars requires inverting a fourth-order differential equation. Lousto and Whiting [151] first found a procedure for constructing Ψ^{Hertz} from ψ_0 and ψ_4 in the time domain for vacuum perturbations ($T_{\mu\nu} = 0$) of Schwarzschild spacetime. Following their work, Ori [174] devised a similar procedure for constructing the Hertz potential from ψ_0 and ψ_4 for both vacuum and inhomogeneous perturbations ($T_{\mu\nu} \neq 0$) in Kerr spacetime.

Schematically, the metric reconstruction process can be understood by rewriting the linearized Einstein equations and the Teukolsky equations in operator form

$$\hat{\mathcal{E}}\boldsymbol{h} = \boldsymbol{T}, \qquad \text{(linearized Einstein equation)} \qquad \hat{\mathcal{O}}_\pm \psi_\pm = T'_\pm, \qquad \text{(Teukolsky equation)} \tag{4.99}$$

where $\hat{\mathcal{E}}$ is the linearized Einstein operator, $\hat{\mathcal{O}}_\pm$ is the Teukolsky operator, $\boldsymbol{h}$ represents the metric perturbation, $\boldsymbol{T}$ the stress-energy source, $\psi_\pm$ the Weyl scalars, $T'_\pm$ the Teukolsky source, and all prefactors have been absorbed for convenience. The $\pm$ subscripts refer to the $s = \pm 2$ cases, e.g., $\psi_- \equiv \Psi_{-2} = \rho^{-4}\psi_4$. I will denote operators with a calligraphic font and a hat (e.g., $\hat{\mathcal{A}}$) and tensors with bold italicized font (e.g., $\boldsymbol{g}$). The stress-energy source is related to the Teukolsky source via Eqs. (4.47) and (4.48), which takes the form

$$\hat{\mathcal{S}}_\pm \boldsymbol{T} = T'_\pm, \tag{4.100}$$

while the relationship between the metric perturbation and the Weyl scalars through the Weyl tensor takes the from

$$\hat{\mathcal{W}}_\pm \boldsymbol{h} = \psi_\pm. \tag{4.101}$$

Thus these differential operators are related by combining Eqs. (4.99)-(4.101),

$$\hat{\mathcal{S}}_\pm \hat{\mathcal{E}} \boldsymbol{h} = T'_\pm = \hat{\mathcal{O}}_\pm \hat{\mathcal{W}}_\pm \boldsymbol{h} \tag{4.102}$$

so that [232]

$$\hat{\mathcal{S}}_\pm \hat{\mathcal{E}} = \hat{\mathcal{O}}_\pm \hat{\mathcal{W}}_\pm, \qquad \Longrightarrow \qquad \hat{\mathcal{E}} \hat{\mathcal{S}}^\dagger_\pm = \hat{\mathcal{W}}^\dagger_\pm \hat{\mathcal{O}}^\dagger_\pm, \tag{4.103}$$

where $\hat{\mathcal{A}}^\dagger$ denotes the adjoint of $\hat{\mathcal{A}}$. The linearized Einstein operator is self-adjoint ($\hat{\mathcal{E}} = \hat{\mathcal{E}}^\dagger$).

Consider the case of purely vacuum perturbations, so that $\boldsymbol{T} = 0 = T'_\pm$. One can then use an ansatz for the reconstructed metric perturbation, namely

$$\boldsymbol{h}^{\text{recon}} = \hat{\mathcal{S}}^\dagger_\pm \Psi^{\text{Hertz}}_\pm, \tag{4.104}$$

where $\Psi^{\text{Hertz}}_\pm$ are Hertz potentials that satisfy $\hat{\mathcal{O}}^\dagger_\pm \Psi^{\text{Hertz}}_\pm = 0$. Note that the Hertz potential is also a homogeneous solution to the Teukolsky equation, because the Teukolsky operator, for gravitational perturbations in Kerr spacetime, is related to its adjoint by an overall factor. One can see then, by inserting this ansatz into Eq. (4.99) and using relation (4.103), that

$$\hat{\mathcal{E}} \boldsymbol{h} = \hat{\mathcal{E}} \hat{\mathcal{S}}^\dagger_\pm \Psi^{\text{Hertz}}_\pm = \hat{\mathcal{W}}^\dagger_\pm \hat{\mathcal{O}}^\dagger_\pm \Psi^{\text{Hertz}}_\pm = 0, \tag{4.105}$$

confirming that $\boldsymbol{h}^{\mathrm{recon}}$ is a valid vacuum solution. Through the CCK procedure, one can calculate the metric via Eq. (4.104) using the ingoing and outgoing radiation gauges [232**?**]. In the ingoing radiation gauge, metric perturbations are reconstructed from Hertz potentials that satisfy the $s = -2$ homogeneous Teukolsky equation, so that

$$h^{\mathrm{IRG}}_{\mathtt{nn}} = -(\hat{\delta} + \alpha^*_{\mathrm{NP}} + 3\beta_{\mathrm{NP}} - \tau_{\mathrm{NP}})(\hat{\delta} + 4\beta_{\mathrm{NP}} + 3\tau_{\mathrm{NP}})\Psi^{\mathrm{Hertz}}_{\mathrm{IRG}} + \text{c.c.}, \tag{4.106}$$

$$h^{\mathrm{IRG}}_{\mathtt{m^*m^*}} = -(\hat{D} - \rho_{\mathrm{NP}})(\hat{D} + 3\rho_{\mathrm{NP}})\Psi^{\mathrm{Hertz}}_{\mathrm{IRG}}, \tag{4.107}$$

$$h^{\mathrm{IRG}}_{\mathtt{nm^*}} = -\frac{1}{2}\Big[(\hat{\delta} - \alpha^*_{\mathrm{NP}} + 3\beta_{\mathrm{NP}} - \pi^*_{\mathrm{NP}} - \tau_{\mathrm{NP}})(\hat{D} + 3\rho_{\mathrm{NP}}) \tag{4.108}$$

$$+ (\hat{D} + \rho^*_{\mathrm{NP}} - \rho_{\mathrm{NP}})(\hat{\delta} + 4\beta_{\mathrm{NP}} + 3\tau_{\mathrm{NP}})\Big]\Psi^{\mathrm{Hertz}}_{\mathrm{IRG}}, \tag{4.109}$$

where $\Psi^{\mathrm{Hertz}}_{\mathrm{IRG}} = \Psi^{\mathrm{Hertz}}_{-}$. In outgoing radiation gauge the metric perturbations are reconstructed from the Hertz potentials satisfying the $s = 2$ homogeneous Teukolsky equation,

$$h^{\mathrm{ORG}}_{\mathtt{ll}} = -\rho^{-4}_{\mathrm{NP}}(\hat{\delta}^* - 3\alpha_{\mathrm{NP}} - \beta^*_{\mathrm{NP}} + 5\pi_{\mathrm{NP}})(\delta^*_{\mathrm{NP}} - 4\alpha_{\mathrm{NP}} + \pi_{\mathrm{NP}})\Psi^{\mathrm{Hertz}}_{\mathrm{ORG}} + \text{c.c.}, \tag{4.110}$$

$$h^{\mathrm{ORG}}_{\mathtt{mm}} = -\rho^{-4}_{\mathrm{NP}}(\hat{\Delta} + 5\mu_{\mathrm{NP}} - 3\gamma_{\mathrm{NP}} + \gamma^*_{\mathrm{NP}})(\hat{\Delta} + \mu_{\mathrm{NP}} - 4\gamma_{\mathrm{NP}})\Psi^{\mathrm{Hertz}}_{\mathrm{ORG}}, \tag{4.111}$$

$$h^{\mathrm{ORG}}_{\mathtt{lm}} = -\frac{\rho^{-4}_{\mathrm{NP}}}{2}\Big[(\hat{\delta}^* - 3\alpha_{\mathrm{NP}} + \beta^*_{\mathrm{NP}} + 5\pi_{\mathrm{NP}} + \tau^*_{\mathrm{NP}})(\hat{\Delta} + \mu_{\mathrm{NP}} - 4\gamma_{\mathrm{NP}}) \tag{4.112}$$

$$+ (\hat{\Delta} + 5\mu_{\mathrm{NP}} - \mu^*_{\mathrm{NP}} - 3\gamma_{\mathrm{NP}} - \gamma^*_{\mathrm{NP}})(\hat{\delta}^* - 4\alpha_{\mathrm{NP}} + \pi_{\mathrm{NP}})\Big]\Psi^{\mathrm{Hertz}}_{\mathrm{ORG}}, \tag{4.113}$$

where $\Psi^{\mathrm{Hertz}}_{\mathrm{ORG}} = \Psi^{\mathrm{Hertz}}_{+}$.

The remaining step is to solve for Ψ^{Hertz} by requiring that the reconstructed metric perturbation reproduces the Weyl scalars

$$\hat{\mathcal{W}}_{\pm}\boldsymbol{h}^{\mathrm{recon}} = \hat{\mathcal{W}}_{\pm}\hat{\mathcal{S}}^{\dagger}_{\pm}\Psi^{\mathrm{Hertz}}_{\pm} = \psi_{\pm}. \tag{4.114}$$

In the ingoing radiation, this reduces to the conditions [151]

$$\psi_0 = \hat{D}\hat{D}\hat{D}\hat{D}\Psi^{*\mathrm{Hertz}}_{\mathrm{IRG}}, \qquad \rho^{-4}\psi_4 = \frac{1}{4}\left[\hat{L}^*_{-2}\hat{L}^*_{-2}\hat{L}^*_{-2}\hat{L}^*_{-2}\Psi^{*\mathrm{Hertz}}_{\mathrm{IRG}} - 12M\partial_t\Psi^{\mathrm{Hertz}}_{\mathrm{IRG}}\right], \tag{4.115}$$

while in outgoing radiation gauge

$$\rho^{-4}\psi_4 = \Delta^2\hat{\Delta}\hat{\Delta}\hat{\Delta}\hat{\Delta}\left(\Delta^2\Psi^{*\mathrm{Hertz}}_{\mathrm{ORG}}\right), \qquad \psi_0 = \frac{1}{4}\left[\hat{L}_2\hat{L}_2\hat{L}_2\hat{L}_2\Psi^{*\mathrm{Hertz}}_{\mathrm{ORG}} - 12M\partial_t\Psi^{\mathrm{Hertz}}_{\mathrm{ORG}}\right]. \tag{4.116}$$

Recall that the operator $\hat{L}_s$ was defined in Eq. (4.63). Thus $\Psi_{\pm}^{\text{Hertz}}$ is found by inverting Eq. (4.114)

$$\Psi_{\pm}^{\text{Hertz}} = \left[\hat{\mathcal{W}}_{\pm}\hat{\mathcal{S}}_{\pm}^{\dagger}\right]^{-1}\psi_{\pm}. \tag{4.117}$$

As stated earlier, a procedure for calculating this inversion of $\Psi_{\text{IRG}}^{\text{Hertz}}$ from ψ_0 in Kerr spacetime was first found by Ori [174]. Keidl et. al [146] then found a similar procedure for calculating $\Psi_{\text{ORG}}^{\text{Hertz}}$ from ψ_0, and van de Meent and Shah [225] outlined a procedure for assembling $\Psi_{\text{ORG}}^{\text{Hertz}}$ from ψ_4.

Up to now, these results have all relied on the key assumption that the metric is sourced by vacuum perturbations. For EMRIs, however, the first-order metric perturbation is sourced by a point particle. Away from the particle's wordline the metric perturbation does satisfy the vacuum field equations, allowing one to use the CCK and Ori procedures to reconstruct the metric in these vacuum regions and then take the limit of the field as one approaches the particle. Barack and Ori [38, 174] did observe, though, that this produces "string-like" gauge singularities in the metric that emanate from the particle along null rays towards infinity and the black hole horizon. These singularities were further studied by Pound, Merlin, and Barack [185] and are now well understood.

To avoid these singularities Ori decomposed spacetime into two regions: an outer region extending from the particle to infinity, Σ_+, and an inner region extending from the particle to the horizon, Σ_-. (This decomposition is described more precisely in Refs. [174, 222, 224].) One can then reconstruct the metric through the method of *extended homogeneous solutions* [174, 40]. In this method one calculates two separate homogeneous solutions for the metric perturbation, $h_{\mu\nu}^{\text{recon},+}$ and $h_{\mu\nu}^{\text{recon},-}$, in these vacuum regions so that they are free of these string singularities. The full metric is then formed by stitching together these two solutions, which are only valid in their respective regions, Σ_+ and Σ_-. This provides a solution that is valid in the entire spacetime. These extended homogeneous methods were more fully developed by van de Meent and Shah [225] to calculate the metric perturbations for geodesic orbits in Kerr spacetime. In Chapter 5 I will discuss how this method of extended homogeneous solutions is also used to tame Gibbs ringing that occurs in the time-domain reconstruction of frequency-domain solutions.

These extended homogeneous solutions give a full description of the metric perturbation up to and at the location of the particle, but the reconstructed metric is, consequently, discontinuous in the neighborhood of the particle source. While this complicates the singular structure of the particle, Pound, Merlin, and Barack [185] found that mode-sum regularization can still be applied for a particular subset of radiation gauges and that, by taking the average of the two extended solutions at the source location (leading to a "no-string" radiation gauge), one can calculate the self-force using the well-known Lorenz-gauge mode-sum regularization parameters, i.e.

$$F^{\alpha(\mathrm{rad})}_{\mathrm{GSF}} = \lim_{x\to x_p}\sum_{l=0}^{\infty}\left[\frac{F^{\alpha(+),l}_{\mathrm{GSF}}+F^{\alpha(-),l}_{\mathrm{GSF}}}{2} - B^{\alpha}_{\mathrm{Lor}} - \frac{C^{\alpha}_{\mathrm{Lor}}}{l+1/2} - \sum_{n=1}^{\infty}\frac{D^{\alpha,n}_{\mathrm{Lor}}}{\prod_{k=1}^{n}(2l+1+2k)(2l+1-2k)}\right], \quad (4.118)$$

where $F^{\alpha(\pm)}_{\mathrm{GSF}} = \mu\nabla^{\alpha\mu\nu}h^{\mathrm{recon},\pm}_{\mu\nu}$ and $F^{\alpha(\pm)}_{\mathrm{GSF}}$ are its multipoles, analogous to Eq. (4.4).

As mentioned earlier, this process of metric reconstruction does not provide all of the information about the metric perturbation. In the context of a multipole expansion, the metric reconstruction procedure cannot reconstruct the $l = 0$ and $l = 1$ modes, which are tied to the perturbations of the mass M and angular momentum J of the Kerr spacetime. Thus the full metric perturbation can be separated into its reconstructed and "completion" pieces

$$h^{\pm}_{\mu\nu} = h^{\mathrm{recon},\pm}_{\mu\nu} + h^{\mathrm{compl},\pm}_{\mu\nu}, \quad (4.119)$$

where the metric completion is expressed in terms of the mass and angular momentum perturbations $\delta M^{\pm}$ and $\delta J^{\pm}$

$$h^{\mathrm{compl},\pm}_{\mu\nu} = \delta M^{\pm}\frac{\partial g_{\mu\nu}}{\partial M} + \delta J^{\pm}\frac{\partial g_{\mu\nu}}{\partial J}. \quad (4.120)$$

The derivatives are straightforward to evaluate, making the determination of $\delta M^{\pm}$ and $\delta J^{\pm}$ the final step in completing the metric. Building off the work of Merlin et. al [160], van de Meent [223] found that, for generic bound sources in Kerr spacetime, $\delta M^{-} = \delta J^{-} = 0$, $\delta M^{+} = \mathcal{E}$, and $\delta J^{+} = \mathcal{L}_z$, where $\mathcal{E}$ and $\mathcal{L}_z$ are the specific energy and z-component of the specific angular moment of the bound source, defined in Eq. (2.5).

Together, metric reconstruction and completion, paired with mode-sum regularization, provide a path towards leveraging the separability of the Teukolsky equations to calculate the gravitational self-force. The numerical implementation of these methods was first spearheaded by Friedman and collaborators [145, 146, 207]. Expanding their work, van de Meent then produced the first calculations of the gravitational self-force along eccentric [222] and inclined [224] orbits in Kerr spacetime.

4.4.6: Gravitational fluxes in Kerr spacetime

Much like in Schwarzschild spacetime, in Kerr spacetime the energy and angular momentum fluxes due to gravitational wave emission can be calculated from ψ_4. This avoids the complicated procedure of metric reconstruction if one is merely interested in the leading-order radiative behavior of the system. As discussed in Sec. 3.3.5, the fluxes at infinity can be found by integrating over the Isaacson stress-energy tensor, which is related to the polarization amplitudes h_{+} and $h_{\times}$ of the asymptotic metric perturbation, as given in

Eqs. (3.135), (3.136), and (3.137). The asymptotic form of the Weyl scalar ψ_4 can also be expressed in terms of h_+ and $h_\times$

$$\psi_4(r \to \infty) \sim \frac{1}{2}\left(\ddot{h}_+ - i\ddot{h}_\times\right). \tag{4.121}$$

Because h_+ and $h_\times$ are real, one finds that

$$h_+ = \int^t dt' \int^{t'} dt''(\psi_4 + \psi_4^*), \qquad\qquad h_\times = i\int^t dt' \int^{t'} dt''(\psi_4 - \psi_4^*). \tag{4.122}$$

Recalling the asymptotic behavior of ψ_4 in terms of the Teukolsky amplitudes, given in Eq. (4.96), for non-resonant geodesic orbits Eq. (3.135) simplifies to

$$\langle \dot{E} \rangle^\infty = \sum_{\hat{l}mkn} \frac{1}{4\pi\omega_{mkn}^2}\left|C^+_{-2\hat{l}mkn}\right|^2, \qquad\qquad \langle \dot{L}_z \rangle^\infty = \sum_{\hat{l}mkn} \frac{m}{4\pi\omega_{mkn}^3}\left|C^+_{-2\hat{l}mkn}\right|^2, \tag{4.123}$$

Calculating the fluxes through the black hole horizon is more challenging, because there is no known form for the stress-energy of the gravitational waves at r_+. Instead, using the area of the Kerr horizon, Teukolsky and Press [210] related the fluxes to changes in the horizon area. The evolution of the horizon area depends on perturbations in the shear of the horizon generators, which are, in turn, encoded in ψ_0. As a result, they found that the fluxes on the horizon can also be related to the Teukolsky amplitudes via [210, 93]

$$\langle \dot{E} \rangle^\mathcal{H} = \sum_{\hat{l}mkn} \frac{\alpha_{\hat{l}mkn}}{4\pi\omega_{mkn}^2}\left|C^-_{-2\hat{l}mkn}\right|^2, \qquad\qquad \langle \dot{L}_z \rangle^\mathcal{H} = \sum_{\hat{l}mkn} \frac{m\alpha_{\hat{l}mkn}}{4\pi\omega_{mkn}^3}\left|C^-_{-2\hat{l}mkn}\right|^2, \tag{4.124}$$

where

$$\alpha_{\hat{l}mkn} \equiv \frac{256(2Mr_+)^5\gamma_{mkn}(\gamma_{mkn}^2 + 4\epsilon_\mathrm{T}^2)(\gamma_{mkn}^2 + 16\epsilon_\mathrm{T}^2)\omega_{mkn}^3}{|A_{\hat{l}mkn}|^2}, \tag{4.125}$$

$$\begin{aligned} |A_{\hat{l}mkn}|^2 \equiv {} & \left[\left({}_{-2}\lambda_{\hat{l}mkn} + 2\right)^2 + 4ma\omega_{mkn} - 4a^2\omega_{mkn}^2\right]\left({}_{-2}\lambda_{\hat{l}mkn}^2 + 36ma\omega_{mkn} - 36a^2\omega_{mkn}^2\right) \\ & + \left(2\,{}_{-2}\lambda_{\hat{l}mkn} + 3\right)\left(96a^2\omega_{mkn}^2 - 48ma\omega_{mkn}\right) + 144\omega_{mkn}^2(M^2 - a^2), \end{aligned} \tag{4.126}$$

and where $\epsilon_\mathrm{T} \equiv (r_+ - M)/4Mr_+$ and ${}_s\lambda_{\hat{l}mkn} \equiv {}_s\lambda_{\hat{l}m}^{a\omega_{mkn}}$ is the spin-weighted spheroidal eigenvalue. Note that the amplitudes $A_{\hat{l}mkn}$ are defined such that $C_{2\hat{l}mkn} = A_{\hat{l}mkn}C_{-2\hat{l}mkn}$ and $\mathrm{Im}\,A_{\hat{l}mkn} = 12M\omega_{mkn}$.[3]

Kerr spacetime has a third constant of motion, the Carter constant, which will also evolve due to the radiation of gravitational waves. While no one has yet identified a physical "flux" quantity related to the time evolution of $Q = \mu^2\mathcal{Q}$, one can calculate its time rate-of-change based on radiation-reaction arguments

---

[3] Note that Ref. [93] has a small typo in its definition of $A_{\hat{l}mkn}$. Its factor of $4a\omega_{mkn}$ should read $4ma\omega_{mkn}$.

[162, 91, 202, 101],

$$\langle \dot{Q} \rangle^{\infty} \equiv \sum_{\hat{l}mkn} \frac{\mathcal{M}_{mkn} + k\Upsilon_{\theta}}{2\pi\omega^3_{mkn}} \left| C^{+}_{-2\hat{l}mkn} \right|^2, \qquad \langle \dot{Q} \rangle^{\mathcal{H}} \equiv \sum_{\hat{l}mkn} \frac{\mathcal{M}_{mkn} + k\Upsilon_{\theta}}{2\pi\omega^3_{mkn}} \alpha_{\hat{l}mkn} \left| C^{-}_{-2\hat{l}mkn} \right|^2, \tag{4.127}$$

where

$$\mathcal{M}_{mkn} \equiv m\langle \cot^2\theta_p \rangle L_z - a^2\omega_{mkn}\langle \cos^2\theta_p \rangle E. \tag{4.128}$$

The change in the Carter constant can then be similarly related to the self-force. Taking the proper time derivative of the Carter constant

$$\frac{d\mathcal{Q}}{d\tau} = u^{\mu}u^{\nu}u^{\alpha}\nabla_{\alpha}K_{\mu\nu} + 2u^{\mu}K_{\mu\nu}u^{\alpha}\nabla_{\alpha}u^{\nu} - 2(\mathcal{L}_z - a\mathcal{E})\left(\frac{d\mathcal{L}_z}{d\tau} - a\frac{d\mathcal{E}}{d\tau}\right). \tag{4.129}$$

Using the properties of the Killing tensor $\nabla_{(\alpha}K_{\mu\nu)} = 0$ and recalling the equations of motion, this expression reduces to

$$\mu^2\frac{d\mathcal{Q}}{d\tau} = 2\mu K_{\mu\nu}u^{\mu}F^{\nu}_{\mathrm{GSF},1} - 2(L_z - aE)\left(\frac{dL_z}{d\tau} - a\frac{dE}{d\tau}\right). \tag{4.130}$$

Defining $\mathcal{K} \equiv \left\langle \mu^2 \dot{\mathcal{Q}} \right\rangle$, one then finds that

$$\mathcal{K} = \frac{2}{\Gamma}\left\langle \mu\Sigma K_{\mu\nu}u^{\mu}F^{\nu}_{\mathrm{GSF},1} - \Sigma(L_z - aE)\left(F^{\mathrm{GSF},1}_{\varphi} + aF^{\mathrm{GSF},1}_{t}\right)\right\rangle_{\lambda}, \tag{4.131}$$

$$= -\frac{2}{\Gamma}(L_z - aE)(\mathcal{T} - a\mathcal{W}) + \frac{2\mu}{\Gamma}\int_0^{2\pi}\frac{dq_r}{2\pi}\int_0^{2\pi}\frac{dq_{\theta}}{2\pi}\,\Sigma K_{\mu\nu}u^{\mu}F^{\nu}_{\mathrm{GSF},1}, \tag{4.132}$$

where $\mathcal{W}$ and $\mathcal{T}$ are the average work and torque on the particle. As a result, the gravitational balance formulas are given by

$$\langle \dot{E} \rangle^{\mathcal{H}} + \langle \dot{E} \rangle^{\infty} = -\mathcal{W}, \qquad \langle \dot{L}_z \rangle^{\mathcal{H}} + \langle \dot{L}_z \rangle^{\infty} = -\mathcal{T}, \qquad \langle \dot{Q} \rangle^{\mathcal{H}} + \langle \dot{Q} \rangle^{\infty} = -\mathcal{K} \tag{4.133}$$

Note that Eqs. (4.124) and (4.127) only hold for the case of *non-resonant* geodesic sources. The effects of resonances will be taken into consideration in Chapter 8.

Section 4.5: Connection to scalar perturbations of black holes

In the this chapter, I reviewed current methods for calculating the gravitational self-force in Kerr spacetime. As one can see, the computational roadmap is involved. To date, only one researcher has been able to design a code that computes the gravitational self-force for EMRIs with Kerr primaries [224]. Thus using an analogous scalar model is an attractive alternative for developing and testing new approaches to the gravitational self-force problem. Calculating the scalar self-force involves many of the methods reviewed in this chapter. The perturbing field of the scalar charge obeys the ($s = 0$) Teukolsky master equation, Eq. (4.69). The field, therefore, separates in the frequency-domain (Sec. 4.4.4) and can be constructed from the (scalar) spheroidal harmonics (Eq. (4.79)) and the ($s = 0$) radial Teukolsky functions (Eq. (4.80)). Like the retarded metric perturbation, the retarded scalar field diverges at the location of the small body and, consequently, the SSF is obtained via mode-sum regularization (Sec. 4.2.1). The SSF problem ultimately mirrors the construction of the Weyl scalars and the regularization of the perturbing field, while avoiding the additional procedures of metric reconstruction and completion. In the next chapter, I discuss the specific numerical and analytical methods that I used to approach the SSF problem and discuss how novel procedures developed for the scalar case can be extended to gravitational self-force calculations.

CHAPTER 5: Scalar perturbation model

Section 5.1: Chapter overview

For this dissertation, I consider a developmental scalar model for studying perturbations of Kerr spacetime. In this scalar model the perturbing particle is given a scalar charge and sources a scalar field. Consequently, the particle also radiates scalar waves, which act back on the charge to produce a *scalar self-force* [191]. The scalar self-force, while similar to the gravitational self-force, is mathematically and computationally more tractable. (Scalar calculations do not require the delicate processes of metric reconstruction and metric completion, and the gauge is simply set by the choice of coordinates, reducing further ambiguities.) I built a *Mathematica* code to construct the scalar self-force and use this code for testing and implementing new approaches for calculating self-forces. In the following sections I review the scalar self-force formalism used for this work, highlighting how it mirrors gravitational self-force calculations. I then outline the numerical techniques that I implemented with my *Mathematica* scalar self-force code.

Section 5.2: Review of scalar perturbation formalism

I consider a particle with scalar charge q[1] and bare mass μ_0 moving in Kerr spacetime. The Kerr background is defined by the metric $g_{\mu\nu}$, Kerr mass parameter M, and Kerr spin parameter a. The charge sources a scalar potential field Φ and scalar vector field $\nabla^\alpha \Phi$. Henceforth, I will refer to Φ simply as the scalar field. The scalar-charged body is treated as a point particle with a worldline $x_p^\alpha(\tau)$, four-velocity $u^\alpha = dx_p^\alpha/d\tau$, and proper time τ. For this work, I use the same scalar model proposed by Quinn [191] and used by numerous subsequent researchers [56, 245, 57, 31, 81, 84, 118, 227, 228, 66, 60, 62, 242, 85, 229, 241, 91, 236, 180, 88, 90, 237, 234, 214].[2] The backreaction of the scalar field on the charge results in a scalar self-force (SSF) that drives the particle's motion. For $q^2/\mu M \ll 1$, the SSF acts as a perturbation to the charge's motion. At leading order the charge follows a geodesic in the Kerr spacetime. At higher-orders it undergoes a gradual adiabatic inspiral into the MBH. I assume that the SSF is sourced by the leading-order geodesic motion of the charge. As discussed in Chapter 1, this geodesic approximation is accurate for

---

[1] Note that the charge q is *not* related to the angle variables q_r and q_θ or the resonant variables $\bar{q}$ and $\bar{q}_0$.

[2] This list is not exhaustive.

first-order calculations. A benefit of making this geodesic approximation is that the source motion is bound and periodic, and therefore is naturally represented in the frequency domain. In the following sections I outline the analytical formalism for modeling scalar perturbations and for calculating the *geodesic* SSF in the frequency domain.

5.2.1: Scalar field equations and equations of motion

The scalar system is defined by the action

$$S = -\frac{1}{8\pi}\int g^{\alpha\beta}\nabla_\beta\Phi\nabla_\alpha\Phi\sqrt{-g}\,d^4x - \mu_0\iint \delta^{(4)}(x,x_p)\sqrt{-g}\,d\tau\,d^4x + q\iint \Phi\,\delta^{(4)}(x,x_p)\sqrt{-g}\,d\tau\,d^4x, \tag{5.1}$$

where the first term accounts for the free scalar field, the second term accounts for the free particle with *bare mass* μ_0, the third term accounts for the interaction between the particle and the field, and $g \equiv \det(g)$ is the determinant of $g_{\mu\nu}$. As before, $\delta^{(4)}(x,x') = \delta^{(4)}(x-x')(-g)^{-1/2}$ is the covariant four-dimensional Dirac distribution, and $\delta^{(4)}(x-x') = \delta(x^0-x'^0)\delta(x^1-x'^1)\delta(x^2-x'^2)\delta(x^3-x'^3)$, where $\delta(x)$ is the standard Dirac delta function. The field equations for the scalar potential are obtained by varying the action with respect to Φ,

$$\delta S = \frac{1}{4\pi}\int\left(g^{\alpha\beta}\nabla_\alpha\nabla_\beta\Phi + q\left(\int \delta^{(4)}(x,x_p(\tau))d\tau\right)\right)\delta\Phi\,\sqrt{-g}\,d^4x. \tag{5.2}$$

Demanding that the action is stationary ($\delta S = 0$) leads to the standard Klein-Gordon wave equation in curved spacetime

$$g^{\alpha\beta}\nabla_\alpha\nabla_\beta\Phi = \frac{1}{\sqrt{-g}}\partial_\alpha\left(\sqrt{-g}g^{\alpha\beta}\partial_\beta\Phi\right) = -4\pi\rho_{\text{scalar}}, \tag{5.3}$$

where ρ_{scalar} is the scalar charge density of the point particle

$$\rho_{\text{scalar}} = q\int \delta^{(4)}(x^\alpha, x_p^\beta(\tau))\,d\tau. \tag{5.4}$$

The wave equation (5.3) is equivalent to the spin-weight $s = 0$ Teukolsky equation (Eq. (4.69)) discussed in Sec. 4.4.3. The scalar field, therefore, serves as an analogue to the Weyl scalars, ψ_0 and ψ_4 (which satisfy the $s = +2$ and $s = -2$ Teukolsky equations, respectively).

To obtain the equations of motion, one must vary the action with respect to the worldline. This task is slightly simplified by first evaluating the Dirac delta terms in Eq. (5.1) and then varying with respect to x_p^α

$$\delta S = q \int \nabla_\mu \Phi(x_p)\, \delta x_p^\mu \, d\tau - \int \left(\mu_0 - q\Phi(x_p)\right) \delta \left(\sqrt{-g_{\alpha\beta}(x_p) \frac{dx_p^\alpha}{d\lambda'} \frac{dx_p^\beta}{d\lambda'}} \right) d\lambda', \tag{5.5}$$

where the second term comes from fact that the proper time is related to the wordline of the particle via $d\tau^2 = g_{\mu\nu} dx_p^\mu dx_p^\nu$. Defining, similar to previous authors [91, 180], the *renormalized rest mass* $\mu(\tau) \equiv \mu_0 - q\Phi(x_p(\tau))$, this expression simplifies to

$$= \int \left[q\nabla_\mu \Phi(x_p) - g_{\mu\nu} u^\alpha \left(\partial_\alpha \left(\mu u^\nu\right) + \mu \Gamma^\nu_{\alpha\beta} u^\beta \right) \right] \delta x_p^\mu \, d\tau, \tag{5.6}$$

Once again demanding the action is stationary under these variations, one arrives at the (self-)forced equation of motion for the scalar particle

$$u^\alpha \nabla_\alpha \left(\mu u^\nu\right) = \lim_{x \to x_p} q g^{\mu\nu} \nabla_\mu \Phi. \tag{5.7}$$

A unique feature of the scalar model is that the scalar charge's inertial mass is given by its renormalized mass μ rather than its bare mass μ_0. The renormalized mass, which varies with time, is the observable mass of the scalar charge. This time-varying mass arises because the scalar field has spin-weight $s = 0$ and, therefore, can emit or absorb monopole ($l = 0$) waves [180]. Thus there is an interplay between the energy of the particle and the energy of the field. As the radiation field evolves, so does the particle's mass. Consequently, the forcing term on the righthand side is not orthogonal to the four-velocity, i.e., $u^\alpha \nabla_\alpha \Phi \neq 0$. If $q^2/\mu M \ll 1$, then at leading-order the renormalized mass is constant, i.e., $\mu(\tau) = \mu_0 + O(q^2/M)$.

Just like in the electromagnetic and gravitational cases, Eq. (5.7) is ill-defined along the worldline if Φ is given by the retarded scalar field. Thus, one must find a suitable regular field, Φ^{R}, that is solely responsible for the forced motion of the scalar charge

$$\mu u^\alpha \nabla_\alpha u^\beta = q^2 (g^{\alpha\beta} + u^\alpha u^\beta) F_\alpha, \qquad \frac{d\mu}{d\tau} = -q^2 u^\alpha F_\alpha, \tag{5.8}$$

where $q^2 F_\alpha \equiv q \nabla_\alpha \Phi^{\mathrm{R}}(x_p)$ is the SSF. (F_α, on the other hand, is the SSF per unit charge squared.) Quinn [191], through an axiomatic approach, found that F_α takes the form

$$q^2 F^\alpha = q\nabla^\alpha \Phi^{\mathrm{in}} + q^2 \left[\frac{1}{3} \left(\frac{da^\mu}{d\tau} - g_{\mu\nu} a^\mu a^\nu u^\alpha \right) + \frac{1}{6} \left(R^{\alpha\beta} u_\beta + R_{\mu\nu} u^\mu u^\nu u^\alpha \right) - \frac{1}{12} R u^\alpha \right] + q\nabla^\alpha \Phi_{\mathrm{tail}}, \tag{5.9}$$

where $a^\mu = u^\alpha \nabla_\alpha u^\mu$ is the particle's four-acceleration; Φ^{in} is some incident, external scalar field; and the tail term is found by integrating the retarded Green's function over the entire past history of the charge,

$$\nabla_\alpha \Phi^{\text{tail}} = q \int_{-\infty}^{\tau-} \nabla_\alpha G_+ \left(x_p(\tau), x_p'(\tau') \right) d\tau'. \tag{5.10}$$

In the absence of external fields (and assuming $q^2/\mu M \ll 1$) the acceleration terms a^μ and $da^\mu/d\tau$ can be neglected. Furthermore, for a background Kerr spacetime $R_{\mu\nu} = R = 0$. Therefore, for the system's considered in this work, the tail integral (5.10) is the only contribution the SSF.

5.2.2: Retarded, regular, and singular scalar fields

To construct the regular contribution to the SSF, one can follow the same methods outlined in Chapter 3 for the electromagnetic and gravitational cases. The retarded scalar field takes the integral form

$$\Phi^{\text{ret}}(x) = \int G_+(x, x') \rho_{\text{scalar}}(x') \sqrt{-g(x')} d^4x', \tag{5.11}$$

where ρ_{scalar} is given by Eq. (5.4) and the retarded Green's function satisfies the curved-space wave equation

$$g^{\alpha\beta} \nabla_\alpha \nabla_\beta G_+(x, x') = -4\pi \delta^{(4)}(x, x'). \tag{5.12}$$

The conjugate advanced scalar field solution is similarly formed from the advanced Green's function,

$$\Phi^{\text{adv}}(x) = \int G_-(x, x') \rho_{\text{scalar}}(x') \sqrt{-g(x')} d^4x', \tag{5.13}$$

where $G_-(x, x')$ also satisfies Eq. (5.12). Due to the reciprocity relation $G_+(x, x') = G_-(x', x)$, the advanced field is related to the time-reversed solution of the retarded field. As before, one can remove the singular structure of the retarded field by identifying a symmetric, singular Green's function that is formed from the retarded and advanced Green's functions and a symmetric two-point function $H(x, x')$ that satisfies the conditions (H1)-(H4) provided in Sec. 3.2.3,

$$G_{\text{S}}(x, x') = \frac{1}{2} \left[G_+(x, x') + G_-(x, x') - H(x, x') \right]. \tag{5.14}$$

The singular Green's function $G_{\text{S}}(x, x')$ also satisfies Eq. (5.12), capturing the full divergence of the Dirac delta source. The regular two-point function

$$G_{\text{R}}(x, x') = G_+(x, x') - G_{\text{S}}(x, x') = \frac{1}{2} \left[G_+(x, x') - G_-(x, x') + H(x, x') \right], \tag{5.15}$$

is then used to form the regular field

$$\Phi^{\mathrm{R}}(x) = \int G_{\mathrm{R}}(x,x')\rho_{\mathrm{scalar}}(x')\sqrt{-g(x')}d^4x'. \tag{5.16}$$

Detweiler and Whiting [82] evaluated Eq. (5.16) by expanding the singular Green's function via the Hadamard expansion [119]. As a result, in a generic curved background the regular field takes the form [82, 180]

$$\nabla_\alpha \Phi^{\mathrm{R}} = -\frac{1}{12}qRu_\alpha + q(g_{\alpha\beta}+u_\alpha u_\beta)\left(\frac{1}{3}\frac{da^\beta}{d\tau} + \frac{1}{6}R^\beta{}_\mu u^\mu\right) + \nabla_\alpha\Phi^{\mathrm{tail}}, \tag{5.17}$$

leading to the same result for the SSF as Quinn.

As discussed in Sec. 4.2, it is challenging to numerically evaluate the tail integral (5.10) or the regular Green's function in Eq. (5.16). Instead, researchers typically calculate the self-force through various regularization procedures in which analytic expansions of the singular field are subtracted from retarded solutions to form regular self-force results. For this scalar perturbation model, I will use mode-sum regularization (see Sec. 4.2.1) to evaluate the SSF. This regularization process requires one to first calculate the multipoles of the retarded field, which I outline in the following sections.

5.2.3: Solving for the retarded field

The charge density ρ_{scalar}, which acts as the source of the wave equation (1.20), is that of a point charge following the timelike orbital motion

$$\begin{aligned}\rho_{\mathrm{scalar}}(t,r,\theta,\varphi) &= q\int \delta^{(4)}(x^\alpha - x_p^\alpha(\tau))\,(-g)^{-1/2}\,d\tau, \\ &= q\frac{\delta(r-r_p)\delta(\cos\theta-\cos\theta_p)\delta(\varphi-\varphi_p)}{V_{tr}(r_p)+V_{t\theta}(\theta_p)},\end{aligned} \tag{5.18}$$

where $\sqrt{-g} = \Sigma\sin\theta$, and V_{tr} and $V_{t\theta}$ are given by Eq. (2.18). In Boyer-Lindquist coordinates, the wave equation (5.3) takes the explicit form

$$\begin{aligned}\left(\frac{(r^2+a^2)^2}{\Delta} - a^2\sin^2\theta\right)\frac{\partial^2\Phi}{\partial t^2} + \frac{4Ma\,r}{\Delta}\frac{\partial^2\Phi}{\partial t\partial\varphi} + \left(\frac{a^2}{\Delta} - \frac{1}{\sin^2\theta}\right)\frac{\partial^2\Phi}{\partial\varphi^2} \\ - \frac{\partial}{\partial r}\left(\Delta\frac{\partial\Phi}{\partial r}\right) - \frac{1}{\sin\theta}\frac{\partial}{\partial\theta}\left(\sin\theta\frac{\partial\Phi}{\partial\theta}\right) = 4\pi\Sigma\rho_{\mathrm{scalar}}.\end{aligned} \tag{5.19}$$

Just like in the gravitational case, Eq. (5.19) is amenable to solution via separation of variables [53, 209]

$$\Phi = q \sum_{\hat{l}mkn} R_{\hat{l}mkn}(r)\, S_{\hat{l}mkn}(\theta)\, e^{im\varphi}\, e^{-i\omega_{mkn}t}. \tag{5.20}$$

Matching the notation of Sec. 4.4.4, $R_{\hat{l}mkn}(r) \equiv {}_0R_{\hat{l}mkn}(r)$ is the spin-0 Teukolsky radial function, and $S_{\hat{l}mkn}(\theta) \equiv {}_0S_{\hat{l}mkn}(\theta)$ is the scalar ($s = 0$) spheroidal Legendre function with $\hat{l}$ and m multipole indices and with spheroidicity $\sigma^2 = -a^2\omega_{mkn}^2$ (hence the $\hat{l}mkn$ subscripts). In the above equation and henceforth, the following condensed notion is introduced to represent the sum over modes

$$\sum_{\hat{l}mkn} \equiv \sum_{\hat{l}=0}^{+\infty} \sum_{m=-\hat{l}}^{\hat{l}} \sum_{k=-\infty}^{+\infty} \sum_{n=-\infty}^{+\infty} . \tag{5.21}$$

Following Warburton and Barack [237], I use $\hat{l}$ for the spheroidal harmonic index and reserve l for the spherical harmonic index used in the mode-sum regularization. The frequency domain decomposition in (5.20) assumes bound motion, with a resulting discrete frequency spectrum that allows the field to be represented by a multiple Fourier series.

I follow Refs. [132, 203, 53] in connecting the Teukolsky function, $R_{\hat{l}mkn}(r)$, to a new radial function,

$$X_{\hat{l}mkn}(r) = \sqrt{r^2 + a^2}\, R_{\hat{l}mkn}(r). \tag{5.22}$$

(Warburton and Barack [236, 237, 234] make a different transformation.) Both $R_{\hat{l}mkn}$ and $X_{\hat{l}mkn}$ are used in what follows. Inserting Eqs. (5.20) and (5.22) into Eq. (5.19), one arrives at two ordinary differential equations for $X_{\hat{l}mkn}(r)$ and $S_{\hat{l}mkn}(\theta)$

$$\left[\frac{1}{\sin\theta}\frac{d}{d\theta}\left(\sin\theta\frac{d}{d\theta}\right) - \frac{m^2}{\sin^2\theta} - a^2\omega_{mkn}^2\sin^2\theta - 2am\omega_{mkn} - \lambda_{\hat{l}mkn}\right] S_{\hat{l}mkn}(\theta) = 0, \tag{5.23}$$

$$\left[\frac{d^2}{dr_*^2} - U_{\hat{l}mkn}(r)\right] X_{\hat{l}mkn}(r) = Z_{\hat{l}mkn}(r), \tag{5.24}$$

where $\lambda_{\hat{l}mkn}$ (which is equivalent to ${}_0\lambda_{\hat{l}m}^{a\omega_{mkn}}$ in Sec. 4.4.4) is the angular eigenvalue. In the radial equation, r_* is the tortoise coordinate

$$r_* = r + \frac{2Mr_+}{r_+ - r_-}\ln\frac{r - r_+}{2M} - \frac{2Mr_-}{r_+ - r_-}\ln\frac{r - r_-}{2M}, \tag{5.25}$$

which follows from integrating $dr_*/dr = \varpi^2/\Delta$. Recall that $r_\pm = M \pm \sqrt{M^2 - a^2}$ are the outer and inner horizon radii (roots of $\Delta(r) = 0$). This definition of r_* agrees with e.g., Refs. [91, 204] but differs from

Refs. [236, 237, 234]. The radial potential $U_{\hat{l}mkn}(r)$ in Eq. (5.24) is

$$U_{\hat{l}mkn}(r) = \varpi^{-8}\Big[2am\,\omega_{mkn}\,\varpi^6 - 6Ma^4r - 4Ma^2r^3 + a^2\,\varpi^4(1-m^2) \\ + 8M^2a^2r^2 - \omega_{mkn}^2\,\varpi^8 + \lambda_{\hat{l}mkn}\Delta\,\varpi^4 - 4M^2r^4 + 2Mr^5\Big], \quad (5.26)$$

and $Z_{\hat{l}mkn}(r)$ gives the radial behavior of the source in the frequency domain, which follows from the Fourier transform of $\rho_{\rm scalar}$

$$\rho_{\rm scalar} = -\frac{q\varpi^3}{4\pi\Sigma\Delta}\sum_{\hat{l}mkn} Z_{\hat{l}mkn}(r)\,S_{\hat{l}mkn}(\theta)\,e^{im\varphi}\,e^{-i\omega_{mkn}t}. \quad (5.27)$$

Note that, based on Eq. (4.74), $Z_{\hat{l}mkn}(r) = \Delta\,{}_0T_{\hat{l}mkn}/(q\varpi^3)$.

5.2.4: Extended homogeneous solutions

General solution of Eq. (5.24) requires two independent homogeneous solutions, $X^{h,+}_{\hat{l}mkn}(r)$ and $X^{h,-}_{\hat{l}mkn}(r)$, that hold throughout the region $r_+ \le r \le \infty$ and have respective asymptotic dependences

$$X^{h,+}_{\hat{l}mkn}(r) \simeq e^{+i\omega_{mkn}r_*}, \qquad r \to \infty, \quad (5.28)$$

$$X^{h,-}_{\hat{l}mkn}(r) \simeq e^{-i\gamma_{mkn}r_*}, \qquad r \to r_+. \quad (5.29)$$

Recall that $\gamma_{mkn} \equiv \omega_{mkn} - m\omega_+$ is the wavenumber at the horizon, with $\omega_+ = a/2Mr_+$ denoting the angular velocity of the event horizon. The solution $X^{h,+}_{\hat{l}mkn}$ is "outgoing" (sometimes called the "up" wave), while the solution $X^{h,+}_{\hat{l}mkn}$ is "downgoing" (sometimes called the "in" wave). These two can be combined to construct the causal Green function for the radial equation (5.24), associated ultimately with the retarded solution in the time domain. The solution of the inhomogeneous version of Eq. (5.24) is then found to be

$$X^{\rm inh}_{\hat{l}mkn} = c^+_{\hat{l}mkn}(r)X^{h,+}_{\hat{l}mkn}(r) + c^-_{\hat{l}mkn}(r)X^{h,-}_{\hat{l}mkn}(r), \quad (5.30)$$

$$c^+_{\hat{l}mkn}(r) = \int_{r_{\rm min}}^{r} \frac{\varpi(r')^2X^{h,-}_{\hat{l}mkn}(r')Z_{\hat{l}mkn}(r')}{W_{\hat{l}mkn}\Delta(r')}dr', \quad (5.31)$$

$$c^-_{\hat{l}mkn}(r) = \int_{r}^{r_{\rm max}} \frac{\varpi(r')^2X^{h,+}_{\hat{l}mkn}(r')Z_{\hat{l}mkn}(r')}{W_{\hat{l}mkn}\Delta(r')}dr', \quad (5.32)$$

where

$$W_{\hat{l}mkn} = X^{h,-}_{\hat{l}mkn}\frac{dX^{h,+}_{\hat{l}mkn}}{dr_*} - X^{h,+}_{\hat{l}mkn}\frac{dX^{h,-}_{\hat{l}mkn}}{dr_*}, \quad (5.33)$$

is the (constant) Wronskian.

The (time-domain) Fourier reconstruction of the field using $X^{\rm inh}_{\hat{l}mkn}(r)$ from Eq. (5.30) in the mode series

(5.20) is fraught with difficulty for points within the libration region $r_{\min} < r < r_{\mathrm{rmax}}$ due to Gibbs oscillations caused by the Dirac delta source. In this region, at points away from the worldline, the convergence in k and n is slow, while derivatives (needed for the SSF) may not even converge at the particle. The usual path around this problem, at least in a background spacetime with spherical symmetry, is the method of extended homogeneous solutions (EHS) [40]. (Recall that this method was first introduced in Sec. 4.4.5 as a way to reconstruct the metric from a Hertz potential for non-vacuum sources.) In the case of spherical symmetry, the four-dimensional wave equation separates into two-dimensional wave equations in t and r for each spherical harmonic order l, m. Extended homogeneous solutions are found mode by mode, which are finite at the particle as needed for mode-sum regularization. Unfortunately, in Kerr spacetime the angular decomposition in spheroidal harmonics is inseparably linked to the transformation into the frequency domain. As Warburton and Barack [237] have shown however, it is still possible to define functions on the spherical harmonic basis that can be extended to the particle location and are finite there.

This procedure begins with determining normalization coefficients, $C^{\pm}_{\hat{l}mkn}$, which are found by evaluating $c^{\pm}_{\hat{l}mkn}(r)$ at the limits of the radial libration region

$$C^{\pm}_{\hat{l}mkn} = \int_{r_{\min}}^{r_{\max}} \frac{\varpi^2 X^{h,\mp}_{\hat{l}mkn}(r) Z_{\hat{l}mkn}(r)}{W_{\hat{l}mkn}\Delta} dr, \tag{5.34}$$

and which are used to define the properly normalized extended homogeneous radial modes in the frequency domain

$$X^{\pm}_{\hat{l}mkn}(r) = C^{\pm}_{\hat{l}mkn} X^{h,\pm}_{\hat{l}mkn}(r). \tag{5.35}$$

These solutions in turn may be used in Eq. (5.20) to define extended solutions in the full time and space domain

$$\Phi^{\pm} \equiv \frac{q}{\varpi} \sum_{\hat{l}mkn} X^{\pm}_{\hat{l}mkn}(r)\, S_{\hat{l}mkn}(\theta)\, e^{im\varphi}\, e^{-i\omega_{mkn}t}, \tag{5.36}$$

from which the retarded solution to Eq. (5.19), at least off the worldline, can be given as

$$\Phi^{\mathrm{ret}}(t, r, \theta, \varphi) = \Phi^{-}(t, r, \theta, \varphi)\, \Theta(r_p(t) - r) + \Phi^{+}(t, r, \theta, \varphi)\, \Theta(r - r_p(t)). \tag{5.37}$$

While the functions $\Phi^{\pm}$ (5.36) converge exponentially in k and n and their use eliminates the Gibbs behavior *near* the particle in the libration region, the full reconstruction (5.37) is not of immediate use in calculating the SSF. Time-domain reconstruction of Eq. (5.36) provides spheroidal $\hat{l}$-mode multipoles, but mode-sum regularization is performed on a spherical l-mode basis.

The spheroidal angular harmonics are, therefore, represented in terms of spherical harmonics $Y_{lm}(\theta, \varphi)$

[133]

$$S_{\hat{l}mkn}(\theta)\, e^{im\varphi} = \sum_{l=|m|}^{+\infty} b^{\hat{l}}_{lmkn}\, Y_{lm}(\theta,\varphi). \tag{5.38}$$

While the spheroidal harmonics of order $\hat{l}$ couple to an infinite number of spherical harmonics, the coupling coefficients $b^{\hat{l}}_{lmkn}$ rapidly decay in size as the difference in orders $|\hat{l}-l|$ grows [236], the rate dependent upon the spheroidicity $a^2\omega^2_{mkn}$. In a numerical calculation, the number of spherical harmonics needed for a given accuracy can be determined. The coupling coefficients are determined by a three-term recurrence relation that results from inserting Eq. (5.38) into Eq. (5.23). (See Sec. 5.3.1.)

Substituting Eq. (5.38) into Eq. (5.36), the five-fold summation may be reordered to leave l and m for last. This allows the extended functions $\phi^{\pm}_{lm}(t,r)$ to be defined,

$$\phi^{\pm}_{lm}(t,r) = \frac{1}{\varpi} \sum_{\hat{l}kn} b^{\hat{l}kn}_{lm}\, X^{\pm}_{\hat{l}mkn}(r)\, e^{-i\omega_{mkn}t}, \tag{5.39}$$

where in a practical numerical calculation the sum over $\hat{l}$ will be finite in number, as will the sums over k and n given their exponential convergence. The remaining sums allow $\Phi^{\pm}$ to be recovered

$$\Phi^{\pm}(t,r,\theta,\varphi) = q \sum_{l=0}^{+\infty} \sum_{m=-l}^{l} \phi^{\pm}_{lm}(t,r)\, Y_{lm}(\theta,\varphi). \tag{5.40}$$

The functions $\phi^{\pm}_{lm}(t,r)$ are not modes in the fullest sense, since there are no wave equations in t and r that they satisfy. However, they do derive from linear combinations of extended (homogeneous) radial modes in the frequency domain, they provide a decomposition of $\Phi^{\pm}$, and they are finite at the location of the particle. These properties are all that is essential for employing mode-sum regularization, as shown by Refs. [236, 237, 234] and as outlined in the following section. The generalization that I produced here to eccentric inclined orbits introduces no qualitatively new element in the Kerr SSF regularization, only a further dimension in the mode calculations.

5.2.5: Mode-sum regularization of the scalar field

Sections 5.2.3 and 5.2.4 provide a roadmap for calculating the retarded field, $\Phi^{\rm ret}$, including its decomposition in a spherical harmonic basis, and Sections 1.3.1 and 4.2.1 discuss using the gradient of that field and the singular field (with the vector components also expanded in the same basis) to yield the mode-sum regularized self-force

$$F_\alpha = \sum_{l=0}^{+\infty} \left(F_{\alpha\pm}^{\mathrm{ret},l} - F_{\alpha\pm}^{\mathrm{S},l} \right). \tag{5.41}$$

This equation differs from Eq. (1.23) in making clear that individual l-mode self-force components may differ in value in the limit as $r \to r_p$ depending upon the direction of approach in r. This ± notation aligns with that used in the EHS discussion (i.e., Eq. (5.37)) of mode functions. Using the spherical harmonic decomposition (5.40) of the retarded field, the l-modes of three of the force components are

$$F_{t\pm}^{\mathrm{ret},l} = \lim_{x\to x_p} \sum_{m=-l}^{l} \partial_t \phi_{lm}^{\pm}(t,r)\, Y_{lm}(\theta,\varphi), \tag{5.42}$$

$$F_{r\pm}^{\mathrm{ret},l} = \lim_{x\to x_p} \sum_{m=-l}^{l} \partial_r \phi_{lm}^{\pm}(t,r)\, Y_{lm}(\theta,\varphi), \tag{5.43}$$

$$F_{\varphi\pm}^{\mathrm{ret},l} = \lim_{x\to x_p} \sum_{m=-l}^{l} im\, \phi_{lm}^{\pm}(t,r)\, Y_{lm}(\theta,\varphi). \tag{5.44}$$

The θ component[3] of the self-force is broken down into l-modes, $F_{\theta\pm}^{\mathrm{ret},l}$, only after the derivative $\partial_\theta Y_{lm}$ is re-projected onto the Y_{lm} basis.

To effect this change, I use the window function $f(\theta)$ devised by Warburton [234] (his Eq. 50)

$$f(\theta) = \frac{3\sin^2\theta_p \sin\theta - \sin^3\theta}{2\sin^3\theta_p}. \tag{5.45}$$

This window function $f(\theta)$ satisfies the necessary properties $f\Phi \to \Phi$ and $\partial_\theta\,(f\Phi) \to \partial_\theta \Phi$ as $x^\mu \to x_p^\mu$, ensuring that $F_{\alpha\pm}^{\mathrm{ret}}$ is unaffected by the transformation $\Phi \to f\,\Phi$. Additionally Warburton's window function cleverly avoids wide bandwidth coupling thanks to the compact relationship between $f\,\partial_\theta Y_{jm}$ and Y_{lm}

$$f\,\partial_\theta Y_{jm} = \beta_{jm}^{(-3)} Y_{j-3,m} + \beta_{jm}^{(-1)} Y_{j-1,m} + \beta_{jm}^{(+1)} Y_{j+1,m} + \beta_{jm}^{(+3)} Y_{j+3,m}. \tag{5.46}$$

The coefficients $\beta_{jm}^{(\pm i)}$ are defined as

$$\beta_{lm}^{(\pm1)} \equiv \left(\frac{3\delta_{lm}^{(\pm1)}}{2\sin\theta_p} - \frac{\zeta_{lm}^{(\pm1)}}{2\sin^3\theta_p} \right), \qquad \beta_{lm}^{(\pm3)} \equiv \left(\frac{\zeta_{lm}^{(\pm3)}}{2\sin^3\theta_p} \right), \tag{5.47}$$

---

[3] In the gravitational self-force case it is sufficient to regularize just three of the four force components because the final component is fixed by $u^\alpha F_\alpha = 0$. In the SSF case the force has a tangential component along u^α, leading to variation in mass [192, 191, 58, 91, 180] and requiring calculation and regularization of F_θ.

where δ_{lm} and ζ_{lm} are given in Ref. [43] as

$$\begin{gathered}
\delta^{(+1)}_{lm} \equiv l C_{l+1,m}, \qquad \delta^{(-1)}_{lm} \equiv -(l+1) C_{lm}, \\
\zeta^{(+3)}_{lm} \equiv -l C_{l+1,m} C_{l+2,m} C_{l+3,m}, \qquad \zeta^{(-3)}_{lm} \equiv (l+1) C_{lm} C_{l-1,m} C_{l-2,m}, \\
\zeta^{(+1)}_{lm} \equiv C_{l+1,m}[l(1 - C^2_{l+1,m} - C^2_{l+2,m}) + (l+1) C^2_{lm}], \\
\zeta^{(-1)}_{lm} \equiv -C_{lm}[(l+1)(1 - C^2_{l-1,m} - C^2_{lm}) + l C^2_{l+1,m}], \\
C_{lm} \equiv \left[\frac{l^2 - m^2}{(2l+1)(2l-1)}\right]^{1/2}.
\end{gathered} \tag{5.48}$$

Under these considerations, efficient calculation of $F^{\mathrm{ret},l}_{\theta\pm}$ follows from the replacement $\Phi \to f\,\Phi$

$$\begin{aligned}
F^{\mathrm{ret}}_{\theta\pm} &= \lim_{x^\mu \to x^\mu_p} \sum_{j=0}^{+\infty} \sum_{m=-j}^{j} \phi^{\pm}_{jm}(t,r)\, f(\theta)\, \partial_\theta Y_{jm}(\theta,\varphi), \\
&= \lim_{x^\mu \to x^\mu_p} \sum_{j=0}^{+\infty} \sum_{m=-j}^{j} \phi^{\pm}_{jm}(t,r) \left(\beta^{(-3)}_{jm} Y_{j-3,m} + \beta^{(-1)}_{jm} Y_{j-1,m} + \beta^{(+1)}_{jm} Y_{j+1,m} + \beta^{(+3)}_{jm} Y_{j+3,m}\right).
\end{aligned} \tag{5.49}$$

Refactoring Eq. (5.49), one can define the new functions $\psi^{\pm}_{lm}(t,r)$ such that

$$\psi^{\pm}_{lm}(t,r) = \beta^{(-3)}_{l+3,m}\, \phi^{\pm}_{l+3,m}(t,r) + \beta^{(-1)}_{l+1,m}\, \phi^{\pm}_{l+1,m}(t,r) + \beta^{(+1)}_{l-1,m}\, \phi^{\pm}_{l-1,m}(t,r) + \beta^{(+3)}_{l-3,m}\, \phi^{\pm}_{l-3,m}(t,r). \tag{5.50}$$

This allows the l-modes of the θ-component to be re-expressed as

$$F^{\mathrm{ret},l}_{\theta\pm} = \lim_{x \to x_p} \sum_{m=-l}^{l} \psi^{\pm}_{lm}(t,r)\, Y_{lm}(\theta,\varphi). \tag{5.51}$$

These expressions (5.50) and (5.51) are similar to ones found in Ref. [234] with the exception of minor corrections and the simplification of notation.

To calculate F_α from Eq. (5.41) one requires an expansion of $F^{\mathrm{S},l}_{\alpha\pm}$ in terms of regularization parameters [37, 39, 81]

$$F^{\mathrm{S},l}_{\alpha\pm} = A_{\alpha\pm}(l+1/2) + B_\alpha + \sum_{n=1}^{+\infty} \frac{D_{\alpha,2n}}{\prod_{k=1}^{n}(2l+1-2k)(2l+1+2k)}, \tag{5.52}$$

where the parameters $A_{\alpha\pm}$, B_α, and $D_{\alpha,2n}$ are all independent of l. For each n, the higher-order regularization terms (with coefficients $D_{\alpha,2n}$) have the property that the l-dependent terms sum to zero [81]

$$\sum_{l=0}^{+\infty} \left[\prod_{k=1}^{n}(2l+1-2k)(2l+1+2k)\right]^{-1} = 0. \tag{5.53}$$

As a consequence only the first two regularization parameters, $A_{\alpha\pm}$ and B_α, are necessary to assure a convergent result and the regularized self-force can be calculated from just

$$F_\alpha = \sum_{l=0}^{+\infty} \left(F_{\alpha\pm}^{\mathrm{ret},l} - A_{\alpha\pm} L - B_\alpha \right) \equiv \sum_{l=0}^{+\infty} F_{\alpha\pm}^{\mathrm{alg},l}, \tag{5.54}$$

where I have defined $F_{\alpha\pm}^{\mathrm{alg},l}$ for later convenience. Altogether, Sections 5.2 presents a formal framework for calculating the SSF using extended homogeneous frequency domain solutions of the retarded scalar field and mode-sum regularization.

5.2.6: Conservative and dissipative components of the scalar self-force

It is also convenient to decompose the self-force into its conservative and dissipative components, F_α^{cons} and F_α^{diss}, as described for the electromagnetic and gravitational self-forces. (See Secs. 3.2.3 and 3.3.3, respectively.) Not only do these components impact the evolution of EMRIs in different ways [30, 84, 162, 125], but they also converge at different rates in the mode-sum regularization procedure: F_α^{diss} does not need to be regularized and converges exponentially, while F_α^{cons} does require regularization and converges algebraically. Decomposing the self-force into these components, therefore, provides a helpful diagnostic for checking the consistency of my SSF calculations.

Just as I defined the retarded force F_α^{ret}, I similarly define the advanced force F_α^{adv} from the advanced scalar field solution, along with its l-mode contributions $F_\alpha^{\mathrm{adv},l}$. Using the mode-sum scheme, the dissipative and conservative components to the self-force are constructed from symmetric and antisymmetric combinations of $F_\alpha^{\mathrm{ret/adv},l}$

$$F_\alpha^{\mathrm{diss}} = \sum_{l=0}^{+\infty} \frac{1}{2} \left(F_\alpha^{\mathrm{ret},l} - F_\alpha^{\mathrm{adv},l} \right), \tag{5.55}$$

$$F_\alpha^{\mathrm{cons}} = \sum_{l=0}^{+\infty} \left\{ \frac{1}{2} \left(F_\alpha^{\mathrm{ret},l} + F_\alpha^{\mathrm{adv},l} \right) - F_\alpha^{\mathrm{S},l} \right\}. \tag{5.56}$$

As is well known [162, 125], the advanced and retarded forces may both be obtained from the retarded solution, being related at *reflection point* pairs in the orbital motion—points where the particle passes through the same radial and polar positions (r_p, θ_p) but with opposite radial and polar velocities, $u^r, u^\theta \to -u^r, -u^\theta$. Explicit calculations of the conservative and dissipative components of the self-force have been made by identifying these reflection points along restricted orbits (i.e., circular, equatorial; eccentric, equatorial; or inclined, spherical) [30, 237, 234, 214].

For eccentric, inclined orbits these reflection points can be conveniently identified by mapping the parti-

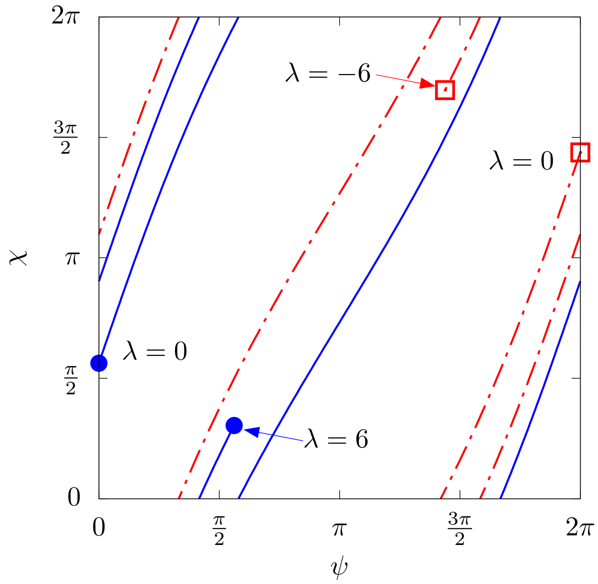

Figure 5.1: Two orbits with the same orbital parameters $(a/M, p, e, \iota) = (0.95, 5, 0.6, 1.04954)$ (see Fig. 2.6) but different initial positions mapped to the two-torus $\mathcal{T}^2_{r\theta}$ now spanned by the rotational coordinates ψ and χ. The blue (solid) line traces an orbit that begins at Mino time $\lambda = 0$ with initial position $(r_p, \theta_p) = (r_{\min}, 1.7409)$ and is terminated at $\lambda = 6$. This orbit follows from choosing $\lambda_0^{(r)} = 0$ and $\lambda_0^{(\theta)} = 0.587813$ in Eqs. (2.68) and (2.69). The red (dot-dashed) line follows an orbit with the reversed parameters, $\lambda_0^{(r)} = 0$ and $\lambda_0^{(\theta)} = -0.587813$, backward in time from $\lambda = 0$ to $\lambda = -6$. The points $\lambda = -6$ and $\lambda = 6$ are example reflection points at which we can relate the advanced force F_α^{adv} to the retarded force F_α^{ret} using Eq. (5.57).

cle's motion to a two-torus, as shown in Fig. 5.1. In this figure I cover the torus using the coordinates ψ and χ, related to the position in the polar (r, θ) plane by Eq. (2.65). (Alternatively, one can use q_r and q_θ to cover the torus, as shown in Figs. 2.4 and 2.5.) The polar motion winds and wraps in this region, either a finite number of times for a resonant orbit or an infinite number of times for a non-resonant orbit. In the latter case, the orbit is ergodic and the motion will eventually pass all points arbitrarily closely. All of the field and self-force information can be projected onto the domain spanned by $\psi, \chi \in [0, 2\pi)$ (or $q_r, q_\theta \in [0, 2\pi)$).

As an example, consider an orbit with geometric parameters $(a/M, p, e, \iota) = (0.95, 5, 0.6, 1.04954)$ and initial position $(r_p, \theta_p) = (r_{\min}, 1.7409)$ set by taking $\lambda_0^{(r)} = 0$ and $\lambda_0^{(\theta)} = 0.587813$. The path of this orbit on the two-torus from $\lambda = 0$ to $\lambda = 6$ is traced out by the solid (blue) line in Fig. 5.1. For any point on this curve, its reflection point is identified by reflecting through the center of the plane at $\psi = \pi$ and $\chi = \pi$ (reflections can be made across any corner of the region equally well). The result of reflecting the entire solid (blue) curve is the dot-dashed (red) curve. This can be verified using Eqs. (2.65)-(2.67). Note that the dot-dashed (red) curve can also be described by an orbit moving backwards in time from $\lambda = 0$ to $\lambda = -6$ with the same geometric parameters as the solid (blue) line, but with opposite offset: $\lambda_0^{(r)} = 0$ but $\lambda_0^{(\theta)} = -0.587813$. This is in line with Eq. (2.46) in Ref. [162].

Therefore (up to a factor of ±1) the advanced force can be calculated by reflecting the retarded force data on the torus. Explicitly, the retarded and advanced forces are related by

$$\check{F}_{\alpha}^{\mathrm{adv},l}(\psi,\chi)=\epsilon_{(\alpha)}\check{F}_{\alpha}^{\mathrm{ret},l}(2\pi-\psi,2\pi-\chi), \tag{5.57}$$

where $\epsilon_{(\alpha)}=(-1,1,1,-1)$ and where there is no summation over α. Eq. (5.57) can be extended to inclined, spherical; eccentric, equatorial; and resonant orbits as well, though the motions on the torus are severely restricted for these special orbits. Parameterizing the self-force with respect to the angle variables, q_r and q_θ, leads to the equivalent relation

$$F_{\alpha}^{\mathrm{adv},l}(q_r,q_\theta)=\epsilon_{(\alpha)}F_{\alpha}^{\mathrm{ret},l}(2\pi-q_r,2\pi-q_\theta), \tag{5.58}$$

where F^α and $\check{F}^\alpha$ are related by the mapping between the Darwin and angle variables,

$$\check{F}_\alpha(\psi,\chi)=F_\alpha\left(\Upsilon_r\lambda^{(r)}(\psi),\Upsilon_\theta\lambda^{(\theta)}(\chi)\right). \tag{5.59}$$

Consequently, F_t^{diss}, F_r^{cons}, F_θ^{cons}, and $F_\varphi^{\mathrm{diss}}$ are symmetric functions on $\mathcal{T}^2_{r\theta}$, while F_t^{cons}, F_r^{diss}, F_θ^{diss}, and $F_\varphi^{\mathrm{cons}}$ are anti-symmetric. While other authors have provided relationships between the advanced and retarded solutions for restricted orbits [237, 234, 214], Eq. 5.58 holds for all geodesic sources.

5.2.7: Scalar wave fluxes and balance laws

The scalar field will not only act back on the charge to produce a SSF, but it will also radiate scalar waves out to infinity and down the black hole horizon. The fluxes of energy and angular momentum carried by this scalar radiation will balance the rate of the local work and torque done on the particle by the SSF, similar to the gravitational case (see Secs. 3.3.5 and 4.4.6.)

$$\mathcal{W}=-q^2\lim_{T\to\infty}\frac{1}{T}\int_0^T\frac{F_t^{\mathrm{diss}}}{u^t}dt, \tag{5.60}$$

$$\mathcal{T}=\quad q^2\lim_{T\to\infty}\frac{1}{T}\int_0^T\frac{F_\varphi^{\mathrm{diss}}}{u^t}dt \tag{5.61}$$

Note that only the dissipative component of the self-force contributes. This is easier to see for fiducial orbits, because both F_t^{cons} and $F_\varphi^{\mathrm{cons}}$ are (time-)antisymmetric, as discussed in Sec. 5.2.6, and thus cancel when averaging over the torus or time. It is convenient to transform these time averages to (non-resonant) orbit averages over the two-torus using the angle variables q_r and q_θ [92]

$$\mathcal{W} = -\frac{q^2}{\Gamma}\int_0^{2\pi}\frac{dq_r}{2\pi}\int_0^{2\pi}\frac{dq_\theta}{2\pi}\,\Sigma_p F_t^{\mathrm{diss}}, \tag{5.62}$$

$$\mathcal{T} = \frac{q^2}{\Gamma}\int_0^{2\pi}\frac{dq_r}{2\pi}\int_0^{2\pi}\frac{dq_\theta}{2\pi}\,\Sigma_p F_\varphi^{\mathrm{diss}}. \tag{5.63}$$

One can similarly define the local evolution of the Carter constant,

$$\mathcal{K} = 2q^2\lim_{T\to\infty}\int_0^T dt\left[\frac{\mu K_{\mu\nu}u^\mu F^\nu}{u^t} - (L_z - aE)\,(F_\varphi + aF_t)\right], \tag{5.64}$$

which, for non-resonant sources, is equivalent to the orbit average

$$\mathcal{K} = -2(L_z - aE)(\mathcal{T} - a\mathcal{W}) + 2\frac{\mu q^2}{\Gamma}\int_0^{2\pi}\frac{dq_r}{2\pi}\int_0^{2\pi}\frac{dq_\theta}{2\pi}\Sigma K_{\mu\nu}u^\mu F^\nu_{\mathrm{diss}}, \tag{5.65}$$

where μ can treated as a constant and pulled outside of the integral, because its variation with time is a higher-order correction. For non-resonant orbits, only the dissipative component of the SSF contributes to $\mathcal{K}$, but it is not yet known whether this is also true for resonant orbits. I will test this open question in more detail later in Chapter 8.

The radiated energy and angular momentum are calculated from Eq. (3.134). Using the stress-energy for a scalar field

$$T_{\mu\nu}^{\mathrm{scalar}} = \frac{1}{4\pi}\left(\partial_\mu\Phi\partial_\nu\Phi - \frac{1}{2}g_{\mu\nu}\partial^\alpha\Phi\partial_\alpha\Phi\right), \tag{5.66}$$

the energy and angular momentum radiated by the field at infinity is given by

$$\dot{E}^\infty = -\lim_{r\to\infty}\frac{r^2}{4\pi}\int\partial_t\Phi^{\mathrm{ret}}\partial_r\Phi^{\mathrm{ret}}\,d\Omega, \qquad \dot{L}_z^\infty = \lim_{r\to\infty}\frac{r^2}{4\pi}\int\partial_\varphi\Phi^{\mathrm{ret}}\partial_r\Phi^{\mathrm{ret}}\,d\Omega. \tag{5.67}$$

Based on Eqs. (5.28) and (5.36), the field at infinity has the form

$$\Phi^{\mathrm{ret}}(r\to\infty) \simeq \frac{q}{r}\sum_{\hat{l}mkn} C^+_{\hat{l}mkn} S_{\hat{l}mkn}(\theta)e^{im\varphi}e^{-i\omega_{mkn}(t-r_*)}. \tag{5.68}$$

Leveraging the orthogonality of the spheroidal harmonics, and the fact that $(\Phi^{\mathrm{ret}})^* = \Phi^{\mathrm{ret}}$, the time-averaged energy and angular momentum fluxes at infinity reduce to

$$\langle\dot{E}\rangle^\infty = \frac{q^2}{4\pi}\sum_{\hat{l}mkn}\omega_{mkn}^2\left|C^+_{\hat{l}mkn}\right|^2, \qquad \langle\dot{L}_z\rangle^\infty = \frac{q^2}{4\pi}\sum_{\hat{l}mkn} m\omega_{mkn}\left|C^+_{\hat{l}mkn}\right|^2, \tag{5.69}$$

assuming that the field is sourced by a non-resonant orbit.

At the horizon, the surface element and accompanying normal vector are instead given by $n^\alpha_{\mathcal{S}} dS = -\delta^\alpha_r \Delta d\Omega$, so that the fluxes through the horizon ($r = r_+$) are given by

$$\dot{E}^{\mathcal{H}} = \lim_{r\to r_+} \frac{\varpi^2}{4\pi}\int \partial_t \Phi^{\mathrm{ret}}\partial_{r_*}\Phi^{\mathrm{ret}}\, d\Omega, \qquad \dot{L}_z^{\mathcal{H}} = -\lim_{r\to r_+}\frac{\varpi^2}{4\pi}\int \partial_\varphi \Phi^{\mathrm{ret}}\partial_{r_*}\Phi^{\mathrm{ret}}\, d\Omega, \tag{5.70}$$

where I have used the fact that $\partial_r = (\varpi^2/\Delta)\partial_{r_*}$. Near the horizon, the asymptotic scalar field takes the form

$$\Phi^{\mathrm{ret}}(r\to r_+) \simeq \frac{q}{\sqrt{r^2+a^2}}\sum_{\hat{l}mkn} C^-_{\hat{l}mkn} S_{\hat{l}mkn}(\theta) e^{im\varphi} e^{-i\omega_{mkn}t} e^{-i\gamma_{mkn}r_*}. \tag{5.71}$$

Consequently, the time-averaged energy and angular momentum fluxes at the horizon reduce to

$$\langle \dot{E}\rangle^{\mathcal{H}} = \frac{q^2}{4\pi}\sum_{\hat{l}mkn} \omega_{mkn}\gamma_{mkn}\left|C^-_{\hat{l}mkn}\right|^2, \qquad \langle \dot{L}_z\rangle^{\mathcal{H}} = \frac{q^2}{4\pi}\sum_{\hat{l}mkn} m\gamma_{mkn}\left|C^-_{\hat{l}mkn}\right|^2, \tag{5.72}$$

where once again I assume that the field is sourced by a non-resonant orbit. The resonant case will be considered in Chapter 8. Altogether, these results lead to the scalar flux-balance formulae

$$\langle \dot{E}\rangle^{\mathrm{tot}} = \langle \dot{E}\rangle^{\mathcal{H}} + \langle \dot{E}\rangle^{\infty} = -\mathcal{W}, \qquad \langle \dot{L}_z\rangle^{\mathrm{tot}} = \langle \dot{L}_z\rangle^{\mathcal{H}} + \langle \dot{L}_z\rangle^{\infty} = -\mathcal{T}. \tag{5.73}$$

Just like in the gravitational case, these fluxes are much more convenient to calculate than constructing the full scalar field and the resulting SSF. The fluxes do not require regularization and the sums converge exponentially. These formulae will be utilized in Chapter 6 to verify SSF results. While $\mathcal{K}$ has not been identified with a physical flux, it does balance with a gauge-invariant quantity $\langle \dot{Q}\rangle^{\mathrm{tot}}$, which only depends on the behavior of the radiative field at infinity and the horizon [91], but I do not calculate $\langle \dot{Q}\rangle^{\mathrm{tot}}$ directly in this work. I will, however, discuss the evolution of the Carter constant in the case of resonances in Chapter 8.

Section 5.3: Numerical methods for calculating the scalar self-force

I wrote a *Mathematica* code to perform frequency-domain calculations of the SSF experienced by a scalar charge on a geodesic in Kerr spacetime. The computational roadmap for this code is as follows:

1. After specifying the parameters a, p, e, and x_{inc} (or ι), I solve for the *fiducial* geodesic motion on Kerr. From the geodesic, I obtain the fundamental frequencies of the orbit Ω_r, Ω_θ, and Ω_φ, and numerical solutions for the geodesic functions $\hat{r}_p$, $\hat{\theta}_p$, $\Delta\hat{t}^{(r)}$, $\Delta\hat{t}^{(\theta)}$, $\Delta\hat{\varphi}^{(r)}$, $\Delta\hat{\varphi}^{(\theta)}$, which are sampled

on equally spaced grids of q_r and q_θ (or ψ and χ). See Sec. 2.7 for more details.

2. I calculate the radial and polar mode functions for each frequency and multipole. The polar mode functions (spheroidal harmonics) $S_{\hat{l}mkn}$ are constructed using Eq. (5.38) and evaluated at the polar positions given by the sampling of $\hat{\theta}_p$. This is discussed in further detail in Sec. 5.3.1.

3. I construct the homogeneous radial mode functions, $X^{h,\pm}_{\hat{l}mkn}$, using the Mano-Suzuki-Takasugi (MST) function expansion formalism [154] and monodromy techniques [68, 69]. The radial functions are sampled at the radial positions given by the sampling of $\hat{r}_p$. This is discussed in further detail in Sec. 5.3.2.

4. I then evaluate the normalization constants $C^{\pm}_{\hat{l}mkn}$, which determine the scalar field via the EHS method. In the scalar case, it proves possible to decompose the scalar source integration of Eq. (5.34) into products of one-dimensional integrals. This is discussed in further detail in Sec. 5.3.3.

5. The multipole contributions of the retarded field to the scalar self-force $F^{\mathrm{ret},l}_{\alpha\pm}$ are constructed from the mode solutions. These self-force contributions are purely functions of q_r and q_θ (or alternatively ψ and χ). I, therefore, numerically sample each self-force mode on a two-dimensional grid of evenly spaced points in q_r and q_θ (ψ and χ). This is discussed in further detail in Sec. 5.3.4.

6. The retarded contributions are then regularized using the known analytic regularization parameters. I fit for higher-order regularization parameters numerically to accelerate the convergence of the mode-sum regularization procedure. The final result is the SSF, sampled along a two-dimensional grid of evenly-spaced points in q_r and q_θ (or ψ and χ). This is discussed in further detail in Sec. 5.3.5.

The resulting code is very accurate and quick to evaluate for moderate eccentricities and inclinations (low-frequencies) but slow for highly-eccentric, strong-field (high-frequency) calculations. In the following sections I outline the numerical implementation of these steps. Because the gravitational self-force may also be constructed from solutions to the Teukolsky equation, I comment on how some of these methods may be implemented in a gravitational self-force code.

5.3.1: Spheroidal harmonics

I build on the numerical routines proposed by Press and Teukolsky [189] and Hughes [132] to construct the spheroidal harmonics (given in Eq. (5.3.1)). Generalizing to an arbitrary spin-weight, Eq. (5.3.1) is replaced by

$$ {}_sS_{\hat{l}m}(\theta;\sigma)e^{im\varphi} = \sum_{l=|m|}^{\infty} {}_sb^{\hat{l}}_{lm}(\sigma)\,{}_sY_{lm}(\theta,\varphi), \tag{5.74}$$

where the ${}_sY_{lm}(\theta,\varphi)$ are the spin-weighted spherical harmonics. Recall that $\sigma^2 = -a^2\omega^2$ is the spheroidicity. Inserting this expansion into the angular Teukolsky equation, one finds that

$$\sum_{l=|m|}^{\infty} {}_sb^{\hat{l}}_{lm}(\sigma)\left[\frac{1}{\sin\theta}\frac{d}{d\theta}\left(\sin\theta\frac{d_sY_{lm}}{d\theta}\right) - \left(\frac{m^2}{\sin^2\theta} + \frac{2ms\cos\theta}{\sin^2\theta} + s^2\cot^2\theta - s\right){}_sY_{lm}\right] = \\ \sum_{l=|m|}^{\infty} {}_sb^{l}_{lm}(\sigma)\left[\left(2\sigma s\cos\theta + \sigma^2\sin^2\theta - 2m\sigma - {}_s\lambda_{\hat{l}m}(\sigma)\right){}_sY_{lm}\right]. \quad (5.75)$$

The lefthand side is the differential equation for ${}_sY_{lm}$ with eigenvalue $l(l+1) - s(s+1)$, leading to

$$\sum_{l=|m|}^{\infty} {}_sb^{\hat{l}}_{lm}(\sigma)\left(\sigma^2\sin^2\theta + 2\sigma s\cos\theta - 2m\sigma - {}_s\lambda_{\hat{l}m}(\sigma) + l(l+1) - s(s+1)\right){}_sY_{lm} = 0. \quad (5.76)$$

Equation (5.76) can be reduced to a five-term recursion relation for the ${}_sb^{\hat{l}}_{lm}$ coefficients by rewriting the trigonometric functions in terms of spin-weighted harmonics and using the triple product relations for angular harmonics. These operations can be efficiently performed in Dirac notation, where the spin-weighted spheroidal harmonics are represented by the kets $|slm\rangle$. Using the relations [189]

$$\langle sjm|\cos\theta\,|slm\rangle = \sqrt{\frac{2l+1}{2j+1}}\,\langle lm;10|jm\rangle\,\langle l,-s;10|j,-s\rangle\,, \quad (5.77)$$

$$\langle sjm|\cos^2\theta\,|slm\rangle = \frac{1}{3}\delta_{lj} + \frac{2}{3}\sqrt{\frac{2l+1}{2j+1}}\,\langle lm;20|jm\rangle\,\langle l,-s;20|j,-s\rangle\,, \quad (5.78)$$

where $\langle j_1m_1;j_2m_2|JM\rangle$ are the Clebsch-Gordon coefficients, Eq. (5.76) reduces to

$$\sum_{l=|m|}^{\infty} {}_sb^{\hat{l}}_{lm}(\sigma)\left(\sigma^2\delta_{lj} - \sigma^2k^l_{jm,2} + 2s\sigma k^l_{jm,1} - {}_s\lambda_{\hat{l}m}(\sigma)\delta_{lj} + l(l+1)\delta_{lj} - s(s+1)\delta_{lj} + 2m\sigma\delta_{lj}\right) = 0, \quad (5.79)$$

where ${}_sk^l_{jm,a} \equiv \langle sjm|\cos^a\theta|slm\rangle$. Because $k^l_{jm,a} = 0$ when $|l-j| > a$, the summation reduces to a five-term recurrence relation, which is given by

$$\left(\sigma^2{}_sk^{l-2}_{lm,2}\right)b^{\hat{l}}_{l-2,m} + \left(\sigma^2{}_sk^{l-1}_{lm,2} - 2s\sigma{}_sk^{l-1}_{lm,1}\right){}_sb^{\hat{l}}_{l-1,m} \\ + \left(\sigma^2{}_sk^{l}_{lm,2} - 2s\sigma{}_sk^{l}_{lm,1} + {}_s\lambda_{\hat{l}m} - l(l+1) + s(s+1) - \sigma^2 + 2m\sigma\right){}_sb^{\hat{l}}_{l,m} \\ + \left(\sigma^2{}_sk^{l+1}_{lm,2} - 2s\sigma{}_sk^{l+1}_{lm,1}\right){}_sb^{\hat{l}}_{l+1,m} + \left(\sigma^2{}_sk^{l+2}_{lm,2}\right){}_sb^{\hat{l}}_{l+2,m} = 0. \quad (5.80)$$

Note that this recurrence relation can be re-expressed as a matrix equation $\mathbb{K}\mathbf{b} = \lambda_{\mathbf{b}}\mathbf{b}$, where the matrix $\mathbb{K}$ represents ${}_sk^l_{jm,a}$, the vector $\mathbf{b}$ represents the coupling coefficients, and the eigenvalue $\lambda_{\mathbf{b}}$ gives ${}_s\lambda_{\hat{l}m}(\sigma) -$

$l(l+1)+s(s+1)-\sigma^2+2m\sigma$. Thus the coupling coefficients and the spheroidal eigenvalue can be calculated through standard numerical routines for evaluating sparse matrix equations.

In the scalar case, the recurrence relation for the coupling coefficients reduces to just three terms,

$$\left(\sigma^2{}_0k^{l-2}_{lm,2}\right){}_0b^{\hat{l}}_{l-2,m} + \left(\sigma^2{}_0k^{l}_{lm,2} + {}_0\lambda_{\hat{l}m} - l(l+1) - \sigma^2 + 2m\sigma\right){}_0b^{\hat{l}}_{l,m} + \left(\sigma^2{}_0k^{l+2}_{lm,2}\right){}_0b^{\hat{l}}_{l+2,m} = 0. \tag{5.81}$$

Due to this simplification, the scalar spheroidal-spherical coupling coefficients can be calculated via a continued fraction method. Defining the coefficients

$$c_l^{(-2)} \equiv \sigma^2{}_0k^{l-2}_{lm,2}, \qquad c_l^{(0)} \equiv {}_0k^{l}_{lm,2} + {}_0\lambda_{\hat{l}m} - l(l+1) - \sigma^2 + 2m\sigma, \qquad c_l^{(+2)} \equiv \sigma^2{}_0k^{l+2}_{lm,2}, \tag{5.82}$$

the recurrence relation simplifies to $c_l^{(-2)}{}_0b^{\hat{l}}_{l-2,m} + c_l^{(0)}{}_0b^{\hat{l}}_{l,m} + c_l^{(+2)}{}_0b^{\hat{l}}_{l+2,m} = 0$ with asymptotic behavior

$$\frac{1}{l^{3/2}}\frac{{}_0b^{\hat{l}}_{l-2,m}}{{}_0b^{\hat{l}}_{lm}} + 1 + \frac{1}{l^{3/2}}\frac{{}_0b^{\hat{l}}_{l+2,m}}{{}_0b^{\hat{l}}_{lm}} \approx 0 \qquad (l \to \infty). \tag{5.83}$$

Thus one can construct raising and lowering operators for the coupling coefficients from the minimal solutions of the recurrence relation

$$D_l^{\hat{l},+} \equiv \frac{{}_0b^{\hat{l}}_{lm}}{{}_0b^{\hat{l}}_{l-2,m}} = -\frac{c_l^{(-2)}}{c_l^{(0)} + c_l^{(+2)}D^{\hat{l},+}_{l+2}}, \tag{5.84}$$

$$D_l^{\hat{l},-} \equiv \frac{{}_0b^{\hat{l}}_{lm}}{{}_0b^{\hat{l}}_{l+2,m}} = -\frac{c_l^{(+2)}}{c_l^{(0)} + c_l^{(-2)}D^{\hat{l},-}_{l-2}}. \tag{5.85}$$

The continued fraction for the lower operator will eventually terminate, with $D_l^{\hat{l},-} = 0$ if $l < |m|$. The raising operator, on the other hand, has a formally infinite continued fraction depth, but converges rapidly. I use Steed's algorithm to evaluate the raising operator. Then starting with the initial point ${}_0b^{\hat{l}}_{\hat{l}m} = 1$, one can apply the raising and lowering operators to construct the nearby coupling coefficients, e.g., ${}_0b^{\hat{l}}_{l+2,m} = D^{\hat{l},+}_{l+2}b^{\hat{l}}_{lm}$. Once all of the coefficients are calculated, within a given accuracy tolerance, one must take the sum of the squares of the coefficients to properly normalize the results. Note that, in the scalar case, the coupling coefficients only depend on σ^2, not σ, and thus are invariant under the interchange $\sigma \to -\sigma$. (Note that the combination ${}_0\lambda_{\hat{l}m} + 2m\sigma$ is also invariant for $\sigma \to -\sigma$.)

For high-precision calculations, this method can be substantially faster to evaluate than solving a large, sparse matrix. However, one must determine the value of the spheroidal eigenvalue ${}_s\lambda_{\hat{l}m}$ prior to calculating the coupling coefficients with this continued fraction method. For this work, I use the `SpinWeightedSpheroidalEigenvalue` function from the Black Hole Perturbation Toolkit's SpinWeighted-

SpheroidalHarmonics package [1] to calculate the eigenvalue separately. This function relies on Leaver's method [149], which also takes advantage of continued fraction relations to evaluate the eigenvalue numerically. I do not make use of the `SpinWeightedSpheroidalHarmonicS` function available through the Toolkit, however, because, at the time of writing my code, my numerical algorithms for calculating the spheroidal harmonics were faster and consistently gave the right normalization (there is an ambiguity in the overall phase factor of the spheroidal harmonics).

5.3.2: Mano-Suzuki-Takasugi expansion of the radial solutions

The function expansion formalism proposed by Mano, Suzuki, and Takasugi (MST) [153, 154] provides a semi-analytic method for obtaining the radial mode function solutions to Eq. (5.24) subject to the boundary conditions (5.28) and (5.29), $X^{h,\pm}_{\hat{l}mkn}$, by yielding the radial Teukolsky functions ${}_sR_{\hat{l}m\omega}$, from which follow $\hat{X}^{\pm}_{\hat{l}mkn}$ (for $s = 0$). A comprehensive review of the MST formalism is given in Ref. [204]. The presentation here primarily focuses on efficient calculation of one set of these solutions. The calculation first starts by determining the separation constant $\lambda_{\hat{l}mkn}$. As mentioned in the previous section, I make use of the Black Hole Perturbation Toolkit's [1] SpinWeightedSpheroidalHarmonics to evaluate $\lambda_{\hat{l}mkn}$.

Specializing to $s = 0$ (spin-weight of the scalar case), the Teukolsky functions ${}_0R^{\mathrm{in}}_{\hat{l}m\omega}$ and ${}_0R^{\mathrm{up}}_{\hat{l}m\omega}$ are the solutions to the (scalar) radial Teukolsky equation with boundary conditions

$$
{}_0R^{\mathrm{in}}_{\hat{l}m\omega}(r \to r_+) \simeq B^{\mathrm{trans}} e^{-i\gamma r_*}, \tag{5.86}
$$

$$
{}_0R^{\mathrm{up}}_{\hat{l}m\omega}(r \to \infty) \simeq C^{\mathrm{trans}} r^{-1} e^{i\omega r_*}, \tag{5.87}
$$

that correspond to the conditions (5.29) and (5.28), respectively, on $X^{h,\pm}_{\hat{l}mkn}$. Here B^{trans} and C^{trans} are asymptotic amplitudes. By introducing the renormalized angular momentum ν and rescaling the radial coordinate in two convenient ways

$$
x \equiv \frac{r_+ - r}{2M\tilde{\kappa}}, \qquad\qquad z \equiv \omega(r - r_-), \tag{5.88}
$$

the functions $R^{\mathrm{in}}_{\hat{l}m\omega}$ and $R^{\mathrm{up}}_{\hat{l}m\omega}$ are expressed as series of hypergeometric functions,

$$
R^{\mathrm{in}}_{\hat{l}m\omega} = e^{i\tilde{\epsilon}\tilde{\kappa}x}(-x)^{-i\tilde{\epsilon}_+}(1-x)^{i\tilde{\epsilon}_-} \sum_{n=-\infty}^{+\infty} a_n^{\nu}\, F\big(n+\nu+1-i\tilde{\tau}, -n-\nu-i\tilde{\tau}; 1-2i\tilde{\epsilon}_+; x\big) \tag{5.89}
$$

$$
R^{\mathrm{up}}_{\hat{l}m\omega} = e^{iz} z^{\nu+i\tilde{\epsilon}_+}(z-\tilde{\epsilon}\tilde{\kappa})^{-i\tilde{\epsilon}_+} \sum_{n=-\infty}^{+\infty} b_n^{\nu}\,(2iz)^n\, \Psi\left(n+\nu+1-i\tilde{\epsilon}, 2n+2\nu+2; -2iz\right), \tag{5.90}
$$

where I have dropped the $s = 0$ prescript and will only consider the scalar case henceforth in this section. Other parameters are given by

$$\tilde{\epsilon} \equiv 2M\omega, \qquad \tilde{\kappa} \equiv \sqrt{1 - \frac{a^2}{M^2}}, \qquad \tilde{\tau} \equiv \frac{1}{\tilde{\kappa}}\left(\tilde{\epsilon} - \frac{ma}{M}\right), \qquad \tilde{\epsilon}_{\pm} \equiv \frac{1}{2}(\tilde{\epsilon} \pm \tilde{\tau}). \tag{5.91}$$

In the expressions above, $F(c_1, c_2; c_3; x)$ is the Gauss hypergeometric function ${}_2F_1(c_1, c_2; c_3; \tilde{x})$ and $\Psi(c_1, c_2; z)$ is the irregular confluent hypergeometric function.

The series coefficients a_n^ν are the minimal solution to a three-term recurrence relation

$$\alpha_n^\nu a_{n+1}^\nu + \beta_n^\nu a_n^\nu + \gamma_n^\nu a_{n-1}^\nu = 0, \tag{5.92}$$

where

$$\alpha_n^\nu \equiv \frac{i\tilde{\epsilon}\tilde{\kappa}(n+\nu+1+i\tilde{\epsilon})(n+\nu+1-i\tilde{\epsilon})(n+\nu+1+i\tilde{\tau})}{(n+\nu+1)(2n+2\nu+3)}, \tag{5.93}$$

$$\beta_n^\nu \equiv -\lambda_{\hat{l}mkn} + (n+\nu)(n+\nu+1) + \tilde{\epsilon}^2 + \tilde{\epsilon}\tilde{\kappa}\tilde{\tau} + \frac{\tilde{\epsilon}^3\tilde{\kappa}\tilde{\tau}}{(n+\nu)(n+\nu+1)}, \tag{5.94}$$

$$\gamma_n^\nu \equiv -\frac{i\tilde{\epsilon}\tilde{\kappa}(n+\nu+i\tilde{\epsilon})(n+\nu-i\tilde{\epsilon})(n+\nu-i\tilde{\tau})}{(n+\nu)(2n+2\nu-1)}. \tag{5.95}$$

The series converges once ν is determined. The second set of coefficients b_n^ν are completely determined by a_n^ν via

$$b_n^\nu = e^{-i\pi(\nu+1-i\tilde{\epsilon})} 2^\nu \frac{(\nu+1-i\tilde{\epsilon})_n}{(\nu+1+i\tilde{\epsilon})_n} a_n^\nu, \tag{5.96}$$

making the "up" series convergent also. Here $(\mu)_n \equiv \Gamma(\mu+n)/\Gamma(\mu)$ is the Pochhammer symbol. For the first three terms in the series, $n = (-1, 0, 1)$, I calculate $F(c_1, c_2; c_3; x)$ and $\Psi(c_1, c_2; z)$ using *Mathematica*'s built-in functions `Hypergeometric2F1` and `HypergeometricU`, respectively. For $|n| > 1$, I construct both types of hypergeometric functions using their respective three-term recursion relations (provided in Ref. [204]).

The eigenvalue ν is often determined by solving for the root of a complex equation formed from Eq. (5.92) with coefficients that are built from continued fractions [204]. An alternative method, employed in this work, relates ν to the eigenvalue of the monodromy matrix defined for the irregular singular point of the Teukolsky equation at $r \to \infty$ [68, 69]. Monodromy matrices describe how a function "runs around" its singular points in the complex plane. The eigenvalues of the monodromy matrix are, therefore, related to the complex phase that a function acquires after circling a point. For example, the function $f(z) = z^\alpha$ will pick-up a phase of $e^{2\pi i\alpha}$ after circling some point z_0, i.e., $f(z_0 e^{2\pi i}) = e^{2\pi i\alpha} z_0^\alpha$. The asymptotic behavior for the Teukolsky radial functions at infinity is given by

$$R(r \to \infty) \sim e^{\pm i\omega r} r^{-1} r^{\pm 2iM\omega}. \tag{5.97}$$

Consequently, the formal monodromy eigenvalues at infinity for the Teukolsky equation are $e^{\pm 4\pi i M\omega}$. However, because this is an irregular singular point, (5.97) is only an asymptotic relation. The formal monodromy does not describe the true monodromy of the Teukolsky function, because the exponential functions of the asymptotic relation (5.97) have a different branching structure from the true Teukolsky solutions.

The true monodromy eigenvalue ν' is determined by numerically calculating Stokes multipliers A_0 and A_1 that connect the formal and true monodromy eigenvalues [198, 69],

$$\frac{1}{2}\left(e^{2\pi i\nu'} + e^{-2\pi i\nu'}\right) = \cos 2\pi\nu' = \cos \pi\left(\lambda_1 - \lambda_2\right) + \frac{1}{2}A_0 A_1, \tag{5.98}$$

where $e^{2\pi i\lambda_1}$ and $e^{2\pi i\lambda_2}$ represent the formal monodromy eigenvalues, e.g., $\lambda_{1,2} = \pm 2M\omega$ for the Teukolsky equation in Boyer-Lindquist coordinates. To the best of my knowledge, there is no formal proof that $\nu' = \nu$, though this equivalence has been found through numerical experimentation. The hypergeometric function $F(c_1, c_2, c_3; x)$ provides a promising route to establishing this connection, since its true monodromy eigenvalues at infinity are simply given by $e^{-2\pi i c_1}$ and $e^{-2\pi i c_2}$. Comparing these eigenvalues with the arguments in Eq. (5.89) leads to the monodromy eigenvalues $e^{\pm 2\pi i\nu}$ for R^{in}. However, this does not constitute a formal proof and Eq. (5.89) does not converge for $|x| = \infty$. Still this behavior alludes to the connection between ν and the true monodromy eigenvalue of the Teukolsky equation. Ultimately, numerical investigations continue to suggest that $\nu = \nu'$, and thus one can determine ν by accurately calculating the Stokes multipliers in Eq. (5.98).

However, rather than directly working with the Teukolsky equation, I found that it is much more convenient to analyze the monodromy eigenvalues and Stokes multipliers using transformed equations, analogous to those presented by Mano, Suzuki, and Takasugi (MST) [154]. Defining the new radial coordinate $\tilde{\epsilon}\tilde{\kappa}y = z = \tilde{\epsilon}\tilde{\kappa}(1-x)$ and transforming to the new radial function $w(y)$ via $R(y) = e^{i\tilde{\epsilon}\tilde{\kappa}(1-y)}(y-1)^{-i\tilde{\epsilon}_-} y^{i\tilde{\epsilon}_+} w(y)$, the Teukolsky equation can be recast in the form of the confluent Heun equation

$$\frac{d^2 w}{dy^2} + \left(\frac{\gamma_{\mathrm{H}}}{y} + \frac{\delta_{\mathrm{H}}}{y-1} + \epsilon_{\mathrm{H}}\right)\frac{dw}{dy} + \frac{\alpha_{\mathrm{H}} y - q_{\mathrm{H}}}{y(y-1)} w = 0, \tag{5.99}$$

where the confluent Heun parameters are related to the MST parameters

$$\gamma_{\mathrm{H}} = 1 + i\tilde{\epsilon} - i\tilde{\tau}, \qquad \delta_{\mathrm{H}} = 1 - i\tilde{\epsilon} - i\tilde{\tau}, \qquad \epsilon_{\mathrm{H}} = -2i\tilde{\epsilon}\tilde{\kappa}, \tag{5.100}$$

$$\alpha_{\mathrm{H}} = -2i\tilde{\epsilon}\tilde{\kappa}\left(1 + i\tilde{\epsilon} - i\tilde{\tau}\right), \tag{5.101}$$

$$q_{\mathrm{H}} = \left[i\tilde{\tau}(1 - i\tilde{\tau}) + \lambda_{\hat{l}mkn}\right] - \tilde{\epsilon}(\tilde{\epsilon} - i\tilde{\kappa}) - 2i\tilde{\epsilon}\tilde{\kappa}\left(1 + i\tilde{\epsilon} - i\tilde{\tau}\right). \tag{5.102}$$

(See Eq. (117) in Ref. [204].) Despite the transformation, w and R share similar monodromy eigenvalues and, thus, one can still use Eq. (5.98) to determine ν. However, now A_0 and A_1 represent the Stokes multipliers for the confluent Heun function, which are constructed from the asymptotic series coefficients of the solutions to Eq. (5.99).

The two solutions to the confluent Heun equation have the asymptotic behavior

$$w_1(y \to \infty) \sim e^{\epsilon_{\mathrm{H}} y} y^{\alpha_{\mathrm{H}}/\epsilon_{\mathrm{H}}} y^{-(\gamma_{\mathrm{H}}+\delta_{\mathrm{H}})}, \qquad w_2(y \to \infty) \sim y^{-\alpha_{\mathrm{H}}/\epsilon_{\mathrm{H}}} \tag{5.103}$$

and therefore admit asymptotic expansions at infinity of the form

$$w_1 = e^{\epsilon_{\mathrm{H}} x} x^{\alpha_{\mathrm{H}}/\epsilon_{\mathrm{H}}} x^{-(\gamma_{\mathrm{H}}+\delta_{\mathrm{H}})} \sum_{n=0}^{\infty} \frac{a_n^{\mathrm{H}}}{(y\epsilon_{\mathrm{H}})^n}, \qquad w_2 = x^{-\alpha_{\mathrm{H}}/\epsilon_{\mathrm{H}}} \sum_{n=0}^{\infty} \frac{b_n^{\mathrm{H}}}{(y\epsilon_{\mathrm{H}})^n}. \tag{5.104}$$

Thus the formal monodromy of the confluent Heun equation is given by $\lambda_1 = \frac{\alpha_{\mathrm{H}}}{\epsilon_{\mathrm{H}}} - \gamma_{\mathrm{H}} - \delta_{\mathrm{H}}$ and $\lambda_2 = -\frac{\alpha_{\mathrm{H}}}{\epsilon_{\mathrm{H}}}$. The series coefficients a_n^{H} and b_n^{H} satisfy the three-term recurrence relations

$$\begin{aligned}
-n\epsilon_{\mathrm{H}}^2\, a_n^{\mathrm{H}} = \Big[&\alpha_{\mathrm{H}}^2 + \alpha_{\mathrm{H}}\epsilon_{\mathrm{H}}(2n - 1 - \gamma_{\mathrm{H}} - \delta_{\mathrm{H}} + \epsilon_{\mathrm{H}}) \\
&+ \epsilon_{\mathrm{H}}^2(n(n - 1 + \gamma_{\mathrm{H}} + \delta_{\mathrm{H}}) - \epsilon_{\mathrm{H}}(n - 1 + \delta_{\mathrm{H}}) - q_{\mathrm{H}})\Big] a_{n-1}^{\mathrm{H}} \qquad (5.105)\\
&- \epsilon_{\mathrm{H}}\Big[\alpha_{\mathrm{H}} - \epsilon_{\mathrm{H}}(n - 1 + \delta_{\mathrm{H}}))(\alpha_{\mathrm{H}} - \epsilon_{\mathrm{H}}(n - 2 + \gamma_{\mathrm{H}} + \delta_{\mathrm{H}})\Big] a_{n-2}^{\mathrm{H}}, \\
-n\epsilon_{\mathrm{H}}^2\, b_n^{\mathrm{H}} = \Big[&\epsilon_{\mathrm{H}}^2 q_{\mathrm{H}} - (\alpha_{\mathrm{H}} + \epsilon_{\mathrm{H}}(n - 1))(\alpha_{\mathrm{H}} + \epsilon_{\mathrm{H}}(n - \gamma_{\mathrm{H}} - \delta_{\mathrm{H}} + \epsilon_{\mathrm{H}})\Big] b_{n-1}^{\mathrm{H}} \qquad (5.106)\\
&+ \epsilon_{\mathrm{H}}\Big[\alpha_{\mathrm{H}} + \epsilon_{\mathrm{H}}(n - 2))(\alpha_{\mathrm{H}} + \epsilon_{\mathrm{H}}(n - 1 - \gamma_{\mathrm{H}})\Big] b_{n-2}^{\mathrm{H}},
\end{aligned}$$

with $a_{-1}^{\mathrm{H}} = b_{-1}^{\mathrm{H}} = 0$ and $a_0^{\mathrm{H}} = b_0^{\mathrm{H}} = 1$. One can then use the series coefficients to numerically calculate the Stokes multipliers A_0 and A_1 which, as described in Ref. [69, 76], are well estimated by

$$A_0 = 2\pi b_N^{\mathrm{H}} \left[\sum_{n=0}^{P-1} a_n^{\mathrm{H}}\, \Gamma\left(N + 2\frac{\alpha_{\mathrm{H}}}{\epsilon_{\mathrm{H}}} - \gamma_{\mathrm{H}} - \delta_{\mathrm{H}} - n\right)\right]^{-1} + O(N^{-P}), \tag{5.107}$$

$$A_1 = 2\pi(-1)^{N-1} a_N^{\mathrm{H}} \left[\sum_{n=0}^{P-1} (-1)^n b_n^{\mathrm{H}}\, \Gamma\left(N - 2\frac{\alpha_{\mathrm{H}}}{\epsilon_{\mathrm{H}}} + \gamma_{\mathrm{H}} - \delta_{\mathrm{H}} - n\right)\right]^{-1} + O(N^{-P}), \tag{5.108}$$

where N and P are integers that are chosen to ensure the numerical convergence of these sums. These results are closely related to those provided in Refs. [198, 69], but I found that the series coefficients are

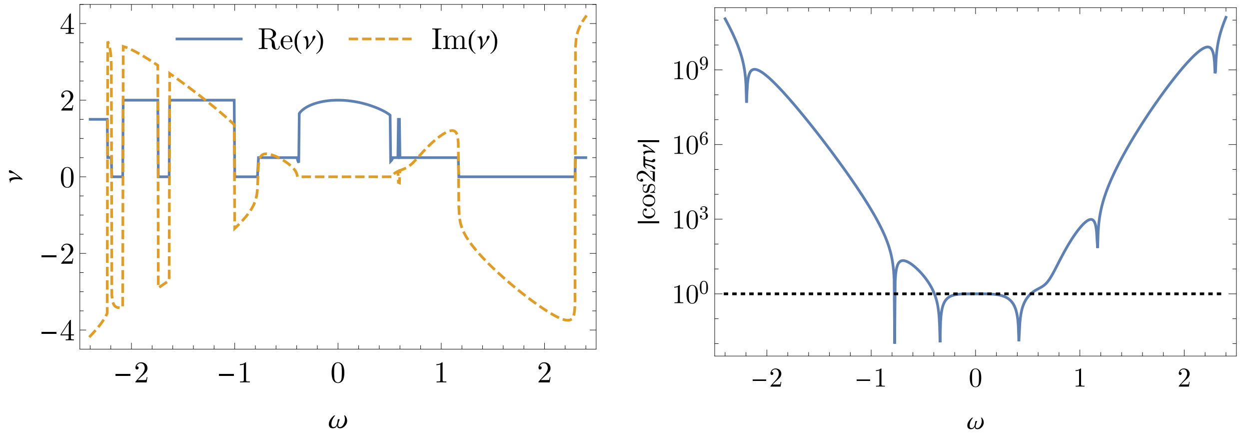

Figure 5.2: Plots of the renormalized angular momentum ν as a function of the frequency ω for the $(s, \hat{l}, m) = (0, 2, 2)$ radial Teukolsky mode (i.e., ${}_0R_{22\omega}$) that describes perturbations of a Kerr spacetime with $a/M = 0.9$. In the left panel, the real part of ν is given by the solid (blue) line, while the imaginary part is given by the dashed (orange) line. For small frequencies ($|\omega| \lesssim 0.3$) ν is purely real, but as $|\omega|$ increases ν becomes complex. The real part of ν assumes an integer or half-integer value as the imaginary part grows. Note, however, that ν is not a smooth function of ω. In the right panel, the absolute value of $\cos 2\pi\nu$ is plotted on a log scale. Though $\cos 2\pi\nu$ rapidly grows with ω, it is a smooth function of the frequency. The dashed (black) line refers to the value of $|\cos 2\pi\nu| = 1$. When the solid (blue) line falls below this threshold, ν is real. Because the absolute value of $\cos 2\pi\nu$ is plotted, the sudden drops represent zero crossings as $\cos 2\pi\nu$ oscillates between positive and negative values.

much faster to evaluate using the transformation to the confluent Heun equation compared to the recurrence relations provided in Ref. [198, 69]. Ottewill and Wardell (private communication) independently knew of this approach and have incorporated a similar method into the Black Hole Perturbation Toolkit's [1] *Mathematica* package TEUKOLSKY, though to the best of my knowledge, these results have not been published.

Interestingly, the magnitude of $\cos 2\pi\nu$ can be greater than one, which is evident from combining Eqs. (5.107) and (5.108) with Eq. (5.98). When this occurs ν will be complex. This was originally observed by Fujita and Tagoshi [111] and is also demonstrated in Fig. 5.2. The left panel plots the real and imaginary parts of ν as a function of ω (in the case that $a/M = 0.9$, $s = 0$, $\hat{l} = 2$, and $m = 2$). For smaller values of $|\omega|$, ν is completely real. However, as $|\omega|$ grows, ν becomes complex with the real component of ν taking on integer or half-integer values and the imaginary component growing in magnitude as the frequency grows in magnitude. These sudden 'jumps' as ν transitions between different real and complex values makes it particularly difficult to determine ν through traditional root-finding methods [111, 218]. The magnitude of $\cos 2\pi\nu$, on the other hand, is a smooth and real function of the frequency, as shown in the right panel of Fig. 5.2. Therefore, the monodromy techniques described above are well-suited for numerically determining ν when it is complex.

After calculating ν numerically, Eqs. (5.89) and (5.90) can be evaluated. An accuracy goal in determining the radial functions is met, in part, by terminating the hypergeometric series at a sufficiently large value of $|n| = n_{\max}$ (where $n_{\max}$ is not necessarily the same for both series). The MST technique provides precise, semi-analytic solutions, but it can be computationally expensive, especially when programmed in *Mathematica*. As the frequency increases, the hypergeometric series expansions must range over an increasing number of terms to meet a pre-defined accuracy goal. Computational costs are exacerbated by roundoff errors from near cancellations in the sums. Roundoff errors are circumvented by making internal *Mathematica* calculations at working precisions significantly higher than desired accuracy in final results.

I found empirically that, for the radial positions considered in this work, the series of confluent hypergeometric functions $\Psi(c_1, c_2; z)$ converges more rapidly than the series of Gauss hypergeometric functions $F(c_1, c_2; c_3; x)$ (used in the "in" solution). Further study showed that computational costs can be mitigated on the horizon side in calculating R^{in} by using an alternative expression given in the MST literature (see Eq. (166) in [204])

$$R^{\text{in}} = K_\nu R_{\text{C}}^{\nu} + K_{-\nu-1} R_{\text{C}}^{-\nu-1}, \tag{5.109}$$

where R_{C}^{ν} is expressed as a series of regular confluent hypergeometric functions $M(c_1, c_2; z)$,

$$R_{\text{C}}^{\nu} = e^{-iz} z^{\nu + i\tilde{\epsilon}_+} \left(z - \tilde{\epsilon}\tilde{\kappa}\right)^{-i\tilde{\epsilon}_+} \sum_{n=-\infty}^{+\infty} f_n^{\nu} \left(-2iz\right)^n M(n + \nu + 1 + i\tilde{\epsilon}, 2n + 2\nu + 2; 2iz). \tag{5.110}$$

Here f_n^{ν} is a new set of series coefficients (given below) and K_ν is a (phase) factor that involves summing over the prior series coefficients a_n^{ν} and b_n^{ν}. The exact form of K_ν in this case is given by

$$K_\nu = e^{i\tilde{\epsilon}\tilde{\kappa}} (\tilde{\epsilon}\tilde{\kappa})^{-\nu}\, \Gamma(1 - 2i\tilde{\epsilon}_+)\, \Gamma(2\nu + 1) \left(\sum_{n=0}^{+\infty} \frac{(-1)^n}{n!} g_n^{\nu}\right) \left(\sum_{n=-\infty}^{0} \frac{(-1)^n}{(-n)!} h_n^{\nu}\right)^{-1}, \tag{5.111}$$

where the new series coefficients f_n^{ν}, g_n^{ν}, and h_n^{ν} can be expressed in terms of the prior coefficients a_n^{ν} and b_n^{ν} by

$$f_n^{\nu} = e^{i\pi(\nu + 1 - i\tilde{\epsilon})} \frac{\Gamma(n + \nu + 1 + i\tilde{\epsilon})}{\Gamma(2n + 2\nu + 2)} b_n^{\nu}, \tag{5.112}$$

$$g_n^{\nu} = (2\nu + 1)_n \frac{(\nu + 1 + i\tilde{\tau})_n}{\Gamma(n + \nu + 1 - i\tilde{\tau})} \frac{(\nu + 1 + i\tilde{\epsilon})_n}{\Gamma(n + \nu + 1 - i\tilde{\epsilon})} a_n^{\nu} \tag{5.113}$$

$$h_n^{\nu} = e^{i\pi(\nu + 1 - i\tilde{\epsilon})} \frac{\Gamma(n + \nu + 1 + i\tilde{\epsilon} - n)}{\Gamma(2n + 2\nu + 2 - n)} b_n^{\nu}. \tag{5.114}$$

The review by Sasaki and Tagoshi [204] discusses Eq. (5.109) as a complement of Eq. (5.89) that provides convergent coverage of the entire domain $[r_+, +\infty]$ but does not mention its computational efficiency. Rapid convergence was my focus in comparing these expressions and settling on use of Eq. (5.109). While developing this code, I sought other MST users' experiences with the potential practical virtues of Eqs. (5.109) and

(5.110). Casals [59] and Wardell (private communication) were aware of the benefits of Eq. (5.109) and make use of it in their work, though have not previously discussed this particular issue in detail. Use of both Eqs. (5.109) and (5.89) are described by Throwe [218], with his observation that both formulae have their own regions in which they are numerically more suitable. Elsewhere [1] Eq. (5.89) is exclusively used. A side benefit in this approach is that the series of regular confluent hypergeometric functions $M(c_1, c_2; z)$ given in Eq. (5.110) converges with similar rapidness as the series of irregular confluent hypergeometric functions $\Psi(c_1, c_2; z)$ given in Eq. (5.90). Thus the same value of $n_{\max}$ can be used to truncate both series.

While use of R_C has benefits, it is not straightforward to construct the underlying functions $M(c_1, c_2; z)$ numerically. The functions $M(c_1, c_2; z)$ satisfy a three-term recurrence relation [204] but evaluating the functions by stepping through the recurrence formula is numerically unstable in the increasing-n direction. There are several ways to circumvent this problem: increase the code's internal precision, calculate $M(c_1, c_2; z)$ directly using *Mathematica*'s built-in function `Hypergeometric1F1`, or translate the three-term recurrence relation into a continued fraction, which does not suffer from the same cancellation errors in the increasing-n direction. Alternatively, since the recurrence relation does not suffer the same instability when moving down in n, one can begin the summation of Eq. (5.110) at $n = n_{\max}$ and evaluate the terms as n decreases down to $n = -n_{\max}$. The value of $n_{\max}$ is conveniently determined by evaluating R^{up} first. A mixture of these strategies is employed to maximize computational efficiency. Ultimately the improved convergence of Eqs. (5.109) and (5.110), compared to Eq. (5.89), offsets the computational cost of summing two series instead of one.

Using these expressions for R^{in} and R^{up}, I construct the unit-normalized functions $X^{h,\pm}$ by comparing Eqs. (5.86) and (5.87) with Eqs. (5.22), (5.28), and (5.29)

$$X^{h,-} = \frac{\varpi}{\varpi_+}\left(\frac{R^{\text{in}}}{B^{\text{trans}}}\right), \qquad X^{h,+} = \varpi\left(\frac{R^{\text{up}}}{C^{\text{trans}}}\right), \tag{5.115}$$

where $\varpi_+ = (r_+^2 + a^2)^{1/2}$. The asymptotic amplitudes can be found by expanding the solutions near the horizon and at large r, respectively

$$B^{\text{trans}} = e^{i\tilde{\kappa}\tilde{\epsilon}_+\left(1+\frac{2\ln\tilde{\kappa}}{1+\tilde{\kappa}}\right)} \sum_{n=-\infty}^{+\infty} a_n^\nu, \tag{5.116}$$

$$C^{\text{trans}} = \omega^{-1} e^{i\left(\tilde{\epsilon}\ln\tilde{\epsilon} - \frac{1-\tilde{\kappa}}{2}\tilde{\epsilon}\right)} A_-^\nu, \tag{5.117}$$

with

$$A_-^\nu = 2^{-(\nu+1-i\tilde{\epsilon})} e^{i\pi(\nu+1-i\tilde{\epsilon})/2} \sum_{n=-\infty}^{+\infty} (-1)^n\, b_n^\nu. \tag{5.118}$$

These normalization choices, ultimately, simplify calculations of the asymptotic energy and angular momentum fluxes at the boundaries (the black hole horizon and infinity).

The MST procedure therefore provides a semi-analytic method for achieving high-precision, numerical values for the homogeneous radial Teukolsky solutions, R^{in} and R^{up}. To construct the SSF, these radial solutions must be evaluated at radial positions along the scalar charge's worldline, i.e. $\hat{r}_p$. However, evaluating series of hypergeometric functions at all of these radial points can be computationally expensive. Therefore, I use the MST method to evaluate R^{in}, R^{up}, and their first derivatives at ~ 16 radial points along the charge's bound orbit. I then construct Taylor expansions around these points using the MST results. The higher-order derivatives of the radial functions (e.g., d^3R/dr^3) are computed by taking derivatives of the Teukolsky equation. The resulting expansions are then used to evaluate the remaining radial points. Once R^{in} and R^{up} are sampled along $\hat{r}_p$, I calculate $X^{h,\pm}$ via Eq. (5.115). This method is similar to the numerical approach employed in Ref. [109]. I found that this method was consistently faster than evaluating all of the radial points with the MST expansions.

5.3.3: Optimized source integration

I now consider the optimized calculation of the normalization coefficients $C^{\pm}_{\hat{l}mkn}$ defined in Eq. (5.34), which was first approached by Osburn [175]. The reduction begins with a review of the derivation of the frequency domain source function $Z_{\hat{l}mkn}(r)$, exploiting the orthogonality of the harmonics in t and φ, and the spheroidal Legendre functions found in Eq. (5.27). Integrating the product of Eq. (5.27) and $e^{-im\varphi}$ over azimuth angle and using the delta function in φ,

$$\sum_{\hat{l}kn} Z_{\hat{l}mkn}(r)\, S_{\hat{l}mkn}(\theta)\, e^{-i\omega_{mkn}t} = -\frac{2\Sigma\Delta\, \delta(r-r_p)\, \delta(\cos\theta - \cos\theta_p)}{\varpi^3\,(V_{tr}+V_{t\theta})}\, e^{-im\varphi_p}. \tag{5.119}$$

Next, one can remove the linear phase factor $e^{-im\Omega_\varphi t}$, which makes the remaining expression

$$\sum_{\hat{l}kn} Z_{\hat{l}mkn}(r)\, S_{\hat{l}mkn}(\theta)\, e^{-i(k\Omega_\theta + n\Omega_r)t} = \\ -2\frac{e^{-im\left(\Delta\varphi^{(r)}+\Delta\varphi^{(\theta)}-\Omega_\varphi(\Delta t^{(r)}+\Delta t^{(\theta)})\right)}}{\varpi_p^3\,(V_{tr}+V_{t\theta})}\Sigma_p\,\Delta_p \delta(r-r_p)\,\delta(\cos\theta-\cos\theta_p), \tag{5.120}$$

bi-periodic with fundamental frequencies Ω_θ and Ω_r, since $\varphi_p - \Omega_\varphi t = \Delta\varphi^{(r)} + \Delta\varphi^{(\theta)} - \Omega_\varphi(\Delta t^{(r)} + \Delta t^{(\theta)})$ up to an irrelevant constant.

Equation (5.120) is reduced to a single sum over $\hat{l}$ by using the orthogonality of the factor $e^{-i(k\Omega_\theta+n\Omega_r)t}$.

To do so, one can convert to Mino time Fourier series, with $e^{-i(k\Upsilon_\theta+n\Upsilon_r)\lambda}$, using results in Ref. [92]

$$\sum_{\hat{l}} Z_{\hat{l}mkn}(r)\, S_{\hat{l}mkn}(\theta) = \frac{1}{\Lambda_\theta\Lambda_r}\int_0^{\Lambda_\theta} d\lambda^{(\theta)} \int_0^{\Lambda_r} d\lambda^{(r)}\, e^{i(k\Upsilon_\theta\lambda^{(\theta)}+n\Upsilon_r\lambda^{(r)})} \times B_{mkn}(r_p,\theta_p)\,\delta(r-r_p)\,\delta(\cos\theta-\cos\theta_p), \quad (5.121)$$

where the function $B_{mkn}(r_p,\theta_p)$ is

$$B_{mkn}(r_p,\theta_p) \equiv -\frac{4\pi\Sigma_p\Delta_p}{\Gamma\varpi_p^3}\, e^{i\omega_{mkn}(\Delta t^{(r)}+\Delta t^{(\theta)})}\, e^{-im(\Delta\varphi^{(r)}+\Delta\varphi^{(\theta)})}, \quad (5.122)$$

which can be thought of as a function of $\lambda^{(r)}$ and $\lambda^{(\theta)}$. The final step in deriving $Z_{\hat{l}mkn}(r)$ is multiplying the above expression by $S_{\hat{l}mkn}(\theta)$ and integrating over θ

$$Z_{\hat{l}mkn}(r) = \frac{1}{\Lambda_\theta\Lambda_r}\int_0^{\Lambda_\theta} d\lambda^{(\theta)} \int_0^{\Lambda_r} d\lambda^{(r)}\, e^{i(k\Upsilon_\theta\lambda^{(\theta)}+n\Upsilon_r\lambda^{(r)})} B_{mkn}(r_p,\theta_p)\, S_{\hat{l}mkn}(\theta_p)\,\delta(r-r_p). \quad (5.123)$$

With the frequency domain source function in hand, one may calculate the normalization constants $C^{\pm}_{\hat{l}mkn}$ by substituting Eq. (5.123) into Eq. (5.34)

$$C^{\pm}_{\hat{l}mkn} = \frac{1}{W_{\hat{l}mkn}}\int_{r_{\min}}^{r_{\max}} dr \frac{\varpi^2 X^{h,\mp}_{\hat{l}mkn}(r)}{\Delta} \times \frac{1}{\Lambda_\theta\Lambda_r}\int_0^{\Lambda_\theta} d\lambda^{(\theta)} \int_0^{\Lambda_r} d\lambda^{(r)}\, e^{i(k\Upsilon_\theta\lambda^{(\theta)}+n\Upsilon_r\lambda^{(r)})} B_{mkn}(r_p,\theta_p)\, S_{\hat{l}mkn}(\theta_p)\,\delta(r-r_p). \quad (5.124)$$

The order of integration is exchanged, allowing the r integral to be evaluated first. Making use of the angle variables q_r and q_θ (see Sec. 2.6.1), one then finds

$$C^{\pm}_{\hat{l}mkn} = \frac{1}{(2\pi)^2}\int_0^{2\pi} dq_\theta \int_0^{2\pi} dq_r\, e^{i(kq_\theta+nq_r)}\, D^{\pm}_{\hat{l}mkn}(r_p,\theta_p), \quad (5.125)$$

where $D^{\pm}_{\hat{l}mkn}(r_p,\theta_p)$, implicitly a function of q_r and q_θ, is given by

$$D^{\pm}_{\hat{l}mkn}(r_p,\theta_p) = -\frac{4\pi\Sigma_p X^{h,\mp}_{\hat{l}mkn}(r_p)\, S_{\hat{l}mkn}(\theta_p)}{\Gamma\, W_{\hat{l}mkn}\,\varpi}\, e^{i\omega_{mkn}(\Delta t^{(r)}+\Delta t^{(\theta)})} e^{-im(\Delta\varphi^{(r)}+\Delta\varphi^{(\theta)})}. \quad (5.126)$$

The double integral in Eq. (5.125) may be computed directly using adaptive-step-size integration [93]. This method is referred to as the “2D-integral” approach. It will deliver numerical results that converge algebraically (i.e., as a power law). Given the number of modes in the Kerr generic-orbit problem, this is a computationally expensive method that compelled a search for more efficient alternatives in evaluating Eq. (5.125).

A first alternative is to exploit the integrand's smoothness and bi-periodicity to make a discrete, evenly-spaced sampling in two dimensions that is analogous to the approach that was taken with the orbit equations (Sec. 2.7). Just as in that case, where an equally-spaced sum over samples of a smooth periodic integrand converged exponentially, one can achieve "spectral" convergence in the two-dimensional integral as well. By discretely sampling q_r and q_θ, one finds

$$q_{r,\imath} \equiv \frac{2\pi\imath}{N_r}, \quad \imath = 0, 1, \dots, N_r - 1, \qquad\qquad q_{\theta,\jmath} \equiv \frac{2\pi\jmath}{N_\theta}, \quad \jmath = 0, 1, \dots, N_\theta - 1, \tag{5.127}$$

$$C^{\pm}_{\hat{l}mkn} \simeq \frac{\Upsilon_r \Upsilon_\theta}{N_r N_\theta} \sum_{\imath=0}^{N_r-1} \sum_{\jmath=0}^{N_\theta-1} e^{inq_{r,\imath}}\, e^{ikq_{\theta,\jmath}} D^{\pm}_{\hat{l}mkn}(r_{p,\imath}, \theta_{p,\jmath}), \tag{5.128}$$

where $r_{p,\imath} \equiv r_p(q_{r,\imath}/\Upsilon_r)$ and $\theta_{p,\jmath} \equiv \theta_p(q_{\theta,\jmath}/\Upsilon_\theta)$. Alternatively, one can also use the discrete sampling locations of Eq. (2.97) and (2.99) to calculate

$$\psi_\imath \equiv \frac{2\pi\imath}{N_r}, \quad \imath = 0, 1, \dots, N_r - 1, \qquad\qquad \chi_\jmath \equiv \frac{2\pi\jmath}{N_\theta}, \quad \jmath = 0, 1, \dots, N_\theta - 1, \tag{5.129}$$

$$C^{\pm}_{\hat{l}mkn} \simeq \frac{\Upsilon_r \Upsilon_\theta}{N_r N_\theta} \sum_{\imath=0}^{N_r-1} \sum_{\jmath=0}^{N_\theta-1} e^{in\Upsilon_r \lambda^{(r)}(\psi_\imath)}\, e^{ik\Upsilon_\theta \lambda^{(\theta)}(\chi_\jmath)} P^{(r)}(\psi_\imath)\, P^{(\theta)}(\chi_\jmath)\, D^{\pm}_{\hat{l}mkn}(\check{r}_{p,\imath}, \check{\theta}_{p,\jmath}), \tag{5.130}$$

where I have changed the integration variables from q_r and q_θ to ψ and χ and adopted $\check{r}_{p,\imath} \equiv \check{r}_p(\psi_\imath)$ and $\check{\theta}_{p,\jmath} \equiv \check{\theta}_p(\chi_\jmath)$. Note that $\check{r}_p$ and $\check{\theta}_p$ are given by Eq. (2.65) and thus differ from the radial and polar functions that are parameterized in terms of q_r and q_θ, i.e., r_p and θ_p.

The integration approach in (5.130) is referred to here as the "2D-SSI" method, i.e., the two-dimensional generalization of the spectral source integration (SSI) technique [130]. Figure 5.3 demonstrates the increased efficiency of the 2D-SSI method compared to the 2D-integral scheme. The 2D-SSI method has been independently adopted by van de Meent [223] in his gravitational self-force frequency-domain calculations on inclined eccentric orbits in Kerr spacetime. The code used in Ref. [93] has also been upgraded to use the 2D-SSI method (Hughes, private communication).

The explicit dependence on r_p and θ_p found in (5.126) allows for further optimization. Because $D^{\pm}_{\hat{l}mkn}(r_p, \theta_p)$ can be written in the following form

$$D^{\pm}_{\hat{l}mkn} = \left(r_p^2 + a^2 \cos^2\theta_p\right) J_{\hat{l}mkn}(\theta_p)\, K^{\pm}_{\hat{l}mkn}(r_p), \tag{5.131}$$

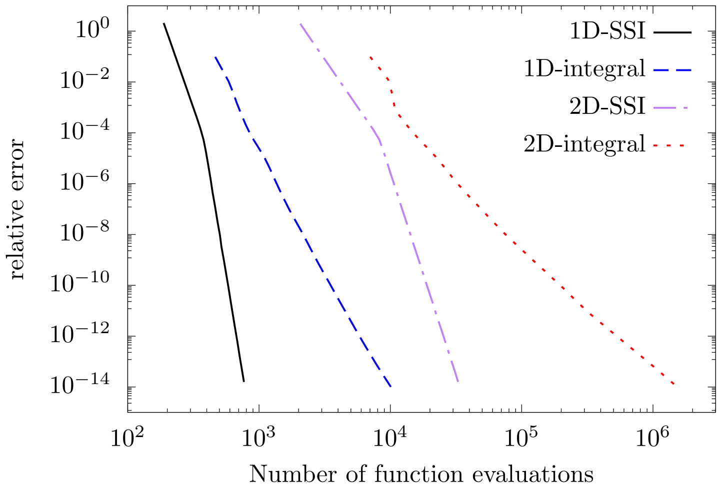

Figure 5.3: Computational efficiency in calculating normalization coefficients. An assessment of computational efficiency is made by measuring the number of integrand evaluations needed to calculate C^{+}_{2222} and C^{-}_{2222} for orbital parameters $(a/M, p, e, \iota) = (0.5, 15, 0.5, \pi/3)$. The lowest efficiency and slowest convergence rate is that of the 2D-integral approach (red dotted curve). The effect of switching to products of 1D integrals is seen in the 1D-integral method (blue dashed curve). The effect of switching from adaptive-step integration to SSI is seen in the 2D-SSI (purple dot-dashed) and 1D-SSI (black solid) scalings. The adaptive step-size integrations (both 2D-integral and 1D-integral) converge algebraically at 8th order.

$$J_{\hat{l}mkn}(\theta_p) \equiv \frac{4\pi}{\Gamma} S_{\hat{l}mkn}(\theta_p) e^{i\omega_{mkn}\Delta t^{(\theta)}} e^{-im\Delta\varphi^{(\theta)}}, \tag{5.132}$$

$$K^{\pm}_{\hat{l}mkn}(r_p) \equiv -\frac{X^{h,\mp}_{\hat{l}mkn}(r_p)}{W_{\hat{l}mkn}\,\varpi}\, e^{i\omega_{mkn}\Delta t^{(r)}} e^{-im\Delta\varphi^{(r)}}, \tag{5.133}$$

the double integral in (5.125) can be calculated from products of one-dimensional integrals

$$C^{\pm}_{\hat{l}mkn} = I^{(1)\pm}_{\hat{l}mkn}\, I^{(2)}_{\hat{l}mkn} + I^{(3)\pm}_{\hat{l}mkn}\, I^{(4)}_{\hat{l}mkn}, \tag{5.134}$$

where

$$I^{(1)\pm}_{\hat{l}mkn} \equiv \frac{1}{2\pi}\int_0^{2\pi} dq_r\, e^{inq_r} r_p^2 K^{\pm}_{\hat{l}mkn}(r_p), \tag{5.135}$$

$$I^{(2)}_{\hat{l}mkn} \equiv \frac{1}{2\pi}\int_0^{2\pi} dq_\theta\, e^{ikq_\theta} J_{\hat{l}mkn}(\theta_p), \tag{5.136}$$

$$I^{(3)\pm}_{\hat{l}mkn} \equiv \frac{1}{2\pi}\int_0^{2\pi} dq_r\, e^{inq_r} K^{\pm}_{\hat{l}mkn}(r_p), \tag{5.137}$$

$$I^{(4)}_{\hat{l}mkn} \equiv \frac{1}{2\pi}\int_0^{2\pi} dq_\theta\, e^{ikq_\theta} \cos^2\theta_p J_{\hat{l}mkn}(\theta_p). \tag{5.138}$$

Computing the integrals (5.135)-(5.138) with a straightforward adaptive integrator leads to an algebraically convergent method that I refer to as the “1D-integral” approach. Despite its algebraic convergence, it is much faster at any required level of accuracy than the 2D-integral approach, by as much as two orders of magnitude at conventional double precision (as seen in Fig. 5.3). At that accuracy level it is also faster than 2D-SSI, though the faster convergence rate of 2D-SSI would ultimately win at higher accuracies.

Finally, the 1D integrals are just as amenable to the SSI method as the double integral in Eqs. (5.128) and (5.130) and it is possible to make an exponentially convergent discrete representation for (5.135)-(5.138). Discretizing the angle variables

$$\begin{aligned} q_{r\imath} &\equiv \frac{2\imath\pi}{N_{1,3}}, &\qquad \imath &\in 0,1,\ldots,N_{1,3}-1, \\ q_{\theta,\jmath} &\equiv \frac{2\jmath\pi}{N_{2,4}}, &\qquad \jmath &\in 0,1,\ldots,N_{2,4}-1, \end{aligned}$$

one can then compute the one-dimensional integrals using discrete, exponentially-convergent sums, given by

$$I^{(1)\pm}_{\hat{l}mkn} \simeq \frac{1}{N_1}\sum_{\imath=0}^{N_1-1} e^{inq_{r,\imath}} r^2_{p,\imath}\, K^{\pm}_{\hat{l}mkn}\left(r_{p,\imath}\right), \tag{5.139}$$

$$I^{(2)}_{\hat{l}mkn} \simeq \frac{1}{N_2}\sum_{\jmath=0}^{N_2-1} e^{ikq_{\theta,\jmath}}\, J_{\hat{l}mkn}\left(\theta_{p,\jmath}\right), \tag{5.140}$$

$$I^{(3)\pm}_{\hat{l}mkn} \simeq \frac{1}{N_3}\sum_{\imath=0}^{N_3-1} e^{inq_{r,\imath}}\, K^{\pm}_{\hat{l}mkn}\left(r_{p,\imath}\right), \tag{5.141}$$

$$I^{(4)}_{\hat{l}mkn} \simeq \frac{1}{N_4}\sum_{\jmath=0}^{N_4-1} e^{ikq_{\theta,\jmath}} a^2\cos^2\theta_{p,\jmath}\, J_{\hat{l}mkn}\left(\theta_{p,\jmath}\right). \tag{5.142}$$

Alternatively, these integrals can be evaluated in terms of the Darwin parameters. Then one must evenly sample ψ and χ

$$\begin{aligned} \psi_\imath &\equiv \frac{2\imath\pi}{N_{1,3}}, &\qquad \imath &\in 0,1,\ldots,N_{1,3}-1, \\ \chi_\jmath &\equiv \frac{2\jmath\pi}{N_{2,4}}, &\qquad \jmath &\in 0,1,\ldots,N_{2,4}-1, \end{aligned}$$

to then compute

$$I^{(1)\pm}_{\hat{l}mkn} \simeq \frac{\Upsilon_r}{N_1}\sum_{\imath=0}^{N_1-1} e^{in\Upsilon_r\lambda^{(r)}(\psi_\imath)} P^{(r)}(\psi_\imath)\check{r}^2_{p,\imath}\, K^{\pm}_{\hat{l}mkn}\big(\check{r}_{p,\imath}\big), \tag{5.143}$$

$$I^{(2)}_{\hat{l}mkn} \simeq \frac{\Upsilon_\theta}{N_2}\sum_{\jmath=0}^{N_2-1} e^{ik\Upsilon_\theta\lambda^{(\theta)}(\chi_\jmath)} P^{(\theta)}(\chi_\jmath)\, J_{\hat{l}mkn}\big(\check{\theta}_{p,\jmath}\big), \tag{5.144}$$

$$I^{(3)\pm}_{\hat{l}mkn} \simeq \frac{\Upsilon_r}{N_3}\sum_{\imath=0}^{N_3-1} e^{in\Upsilon_r\lambda^{(r)}(\psi_\imath)} P^{(r)}(\psi_\imath)\, K^{\pm}_{\hat{l}mkn}\big(\check{r}_{p,\imath}\big), \tag{5.145}$$

$$I^{(4)}_{\hat{l}mkn} \simeq \frac{\Upsilon_\theta}{N_4}\sum_{\jmath=0}^{N_4-1} e^{ik\Upsilon_\theta\lambda^{(\theta)}(\chi_\jmath)} P^{(\theta)}(\chi_\jmath) a^2\cos^2\check{\theta}_{p,\jmath}\, J_{\hat{l}mkn}\big(\check{\theta}_{p,\jmath}\big). \tag{5.146}$$

When Eqs. (5.139)-(5.142) (or (5.143)-(5.146)) are used to evaluate Eq. (5.134), I refer to it as the "1D-SSI" method. Fig. 5.3 shows that the 1D-SSI method is the most efficient and most rapidly convergent technique. Switching to 2D-SSI from 2D adaptive-step integration is nearly two orders of magnitude faster at double precision accuracies. Switching from 2D-SSI to 1D-SSI yields another factor of 30.

The 1D-SSI method is possible because the two-dimensional source integrations decompose as shown in (5.134) into products of 1D integrals. Unfortunately a similar decomposition does not occur in any obvious way for gravitational perturbations in Kerr spacetime due to leading factors of $1/\Sigma$. For small spins or large radial separations, the $1/\Sigma$ factor might be expanded using a binomial series with a modest amount of terms, providing an *approximately* separable source. It is also conceivable that a transformation might exist that would bring the source into a separable form. The benefits of the 1D-SSI method seen in the scalar case are compelling enough to justify a more thorough investigation of the gravitational Teukolsky source integration problem.

As a final note, recall that the transformation from q_r and q_θ to ψ and χ is sensitive to the initial conditions q_{r0} and $q_{\theta 0}$. Thus, Eqs. (5.143)-(5.146) only apply for *fiducial* geodesic sources (i.e., $x_p^\mu(0) = (0, r_{\min}, \theta_{\min}, 0)$). This does not force a loss of generality, though. As noted in Refs. [91, 101], the $C^{\pm}_{\hat{l}mkn}$ for a source with arbitrary initial conditions can be related to the coefficients for a source with *fiducial* initial conditions, $\hat{C}^{\pm}_{\hat{l}mkn}$, which differ by only a phase factor. Transforming to the shifted angle variables $\bar{q}_r \equiv q_r + q_{r0}$ and $\bar{q}_\theta \equiv q_\theta + q_{\theta 0}$, Eq. (5.125) becomes

$$C^{\pm}_{\hat{l}mkn}(q_0^\mu) = \frac{1}{4\pi^2}\int_{q_{r0}}^{2\pi+q_{r0}} d\bar{q}_r \int_{q_{\theta 0}}^{2\pi+q_{\theta 0}} d\bar{q}_\theta \, e^{i(k\bar{q}_\theta + n\bar{q}_r)} D^{\pm}_{\hat{l}mkn}(\bar{q}_r - q_{r0}, \bar{q}_\theta - q_{\theta 0}; q_0^\mu) e^{-i(kq_{\theta 0}+nq_{r0})}, \qquad (5.147)$$

where I have made the dependence on the initial conditions $q_0^\mu = (t_0, q_{r0}, q_{\theta 0}, \varphi_0)$ explicit and where, in a slight abuse of notation, I write

$$D^{\pm}_{\hat{l}mkn}(q_r, q_\theta; q_0^\mu) = D^{\pm}_{\hat{l}mkn}\left(r_p(q_r/\Upsilon_r; q_{r0}), \theta_p(q_\theta/\Upsilon_\theta; q_{\theta 0})\right) e^{i\omega_{mkn}t_0} e^{-im\varphi_0}. \qquad (5.148)$$

First note that, because the integrand is periodic on the intervals q_r, $q_\theta \in [0, 2\pi)$, it is straightforward to shift the limits of integration, e.g.,

$$\int_{q_{r0}}^{2\pi+q_{r0}} = \int_0^{2\pi} + \int_{2\pi}^{2\pi+q_{r0}} - \int_0^{q_{r0}} = \int_0^{2\pi} . \qquad (5.149)$$

Recalling Eq. (5.126), one can see that

$$D^{\pm}_{\hat{l}mkn}(\bar{q}_r - q_{r0}, \bar{q}_\theta - q_{\theta 0}; q_0^\mu) = e^{-i\omega_{mkn}(\Delta t(q_{r0}, q_{\theta 0}) - t_0)} e^{im(\Delta\varphi(q_{r0}, q_{\theta 0}) - \varphi_0)} D^{\pm}_{\hat{l}mkn}(\bar{q}_r, \bar{q}_\theta; 0, 0, 0, 0). \qquad (5.150)$$

Combining these results and defining the phase

$$\xi_{mkn}(q_0^\mu) \equiv -\omega_{mkn}\Delta t(q_{r0}, q_{\theta 0}) + \omega_{mkn} t_0 + m\Delta\varphi(q_{r0}, q_{\theta 0}) - m\varphi_0 - kq_{\theta 0} - nq_{r0}, \tag{5.151}$$

leads to a relationship between the fiducial normalization $\hat{C}^{\pm}_{\hat{l}mkn}$ and the normalization for a source with arbitrary initial phases q_0^μ

$$C^{\pm}_{\hat{l}mkn}(q_0^\mu) = e^{i\xi_{mkn}(q_0^\mu)} \hat{C}^{\pm}_{\hat{l}mkn}. \tag{5.152}$$

I, therefore, construct all normalization coefficients using the fiducial orbit. Arbitrary conditions are then included via Eq. (5.152).

5.3.4: Constructing the scalar self-force

To construct the SSF, I evaluate Eqs. (5.42)-(5.44) and (5.51) along a fiducial geodesic $\hat{x}_p^\alpha = (\hat{t}_p, \hat{r}_p, \hat{\theta}_p, \hat{\varphi}_p)$

$$\hat{F}^{\mathrm{ret},l}_{\alpha\pm}(\lambda) = \sum_{m=-l}^{l} \left[\hat{\mathcal{D}}^{lm}_\alpha \phi^{\pm}_{lm}\right](\hat{t}_p, \hat{r}_p) Y_{lm}(\hat{\theta}_p, \hat{\varphi}_p), \tag{5.153}$$

where the coordinate positions of the particle are understood to be functions of Mino time (e.g., $\hat{t}_p = \hat{t}_p(\lambda)$), and the operator $\hat{\mathcal{D}}^{lm}_\alpha$ performs the following operations on the extended homogeneous solutions

$$\hat{\mathcal{D}}^{lm}_t \phi^{\pm}_{lm} \equiv \partial_t \phi^{\pm}_{lm}, \tag{5.154}$$

$$\hat{\mathcal{D}}^{lm}_r \phi^{\pm}_{lm} \equiv \partial_r \phi^{\pm}_{lm}, \tag{5.155}$$

$$\hat{\mathcal{D}}^{lm}_\theta \phi^{\pm}_{lm} \equiv \beta^{(-3)}_{l+3,m}\phi^{\pm}_{l+3,m} + \beta^{(-1)}_{l+1,m}\phi^{\pm}_{l+1,m} + \beta^{(+1)}_{l-1,m}\phi^{\pm}_{l-1,m} + \beta^{(+3)}_{l-3,m}\phi^{\pm}_{l-3,m}, \tag{5.156}$$

$$\hat{\mathcal{D}}^{lm}_\varphi \phi^{\pm}_{lm} \equiv im\phi^{\pm}_{lm}. \tag{5.157}$$

For generic non-resonant orbits, the SSF is not simply periodic, but varies over the entire interval of $-\infty < \lambda < \infty$. Because one cannot numerically sample the SSF over this infinite domain, I parameterize the SSF in terms of the angle variables introduced in Sec. 2.6.1,

$$\hat{F}^{\mathrm{ret},l}_{\alpha\pm}(q_r, q_\theta) = \sum_{m=-l}^{l} (\hat{\mathcal{D}}^{lm}_\alpha \hat{\phi}^{\pm}_{lm})(q_r, q_\theta) \hat{Y}_{lm}(q_r, q_\theta). \tag{5.158}$$

where

$$\hat{Y}_{lm}(q_r, q_\theta) \equiv Y_{lm}(\hat{\theta}_p(q_\theta), 0) e^{im\Delta\hat{\varphi}(q_r, q_\theta)}, \tag{5.159}$$

$$\hat{\phi}^{\pm}_{lm}(q_r, q_\theta) \equiv \sum_{\hat{l}kn} \hat{\phi}^{\pm}_{l\hat{l}mkn}(q_r) e^{-i\omega_{mkn}\Delta\hat{t}(q_r,q_\theta)} e^{-i(kq_\theta + nq_r)}, \tag{5.160}$$

$$\hat{\phi}^{\pm}_{l\hat{l}mkn}(q_r) \equiv \hat{\varpi}_p^{-1}(q_r) b^{l}_{\hat{l}mkn} \hat{C}^{\pm}_{\hat{l}mkn} \tilde{X}^{\pm}_{\hat{l}mkn}(\hat{r}_p(q_r)), \tag{5.161}$$

and where $\hat{\varpi}_p(q_r) = (\hat{r}_p^2(q_r) + a^2)^{1/2}$, while $\hat{\mathcal{D}}^{lm}_\alpha$ performs the same operations as before. Recall that this mapping in terms of q_r and q_θ results from the ergodic nature of non-resonant geodesic motion in Kerr spacetime. Given an infinite amount of time, the orbit samples every point in the (q_r, q_θ)-plane an equal number of times. Therefore the infinite motion of the scalar charge maps to this finite, two-dimensional domain. Because the regularization parameters only vary with respect to r_p, θ_p, u^r, and u^θ (assuming the orbital constants are fixed), the singular field can also be translated into this angle-variable parameterization, ultimately providing a description of the SSF in terms of q_r and q_θ,

$$\hat{F}_\alpha(q_r, q_\theta) = \sum_{l=0}^{\infty} \left(\hat{F}^{\mathrm{ret},l}_{\alpha\pm}(q_r, q_\theta) - \hat{F}^{\mathrm{S},l}_{\alpha\pm}(q_r, q_\theta) \right). \tag{5.162}$$

As a result, the SSF naturally maps to the two-torus spanned by q_r and q_θ (and visualized in Fig. 2.4). The angle variables also provide convenient parameters for representing the SSF in terms of a Fourier series,

$$\hat{F}_\alpha(q_r, q_\theta) = \sum_{k=-\infty}^{+\infty} \sum_{n=-\infty}^{+\infty} \tilde{f}^{kn}_\alpha e^{-i(kq_\theta + nq_r)}, \tag{5.163}$$

$$\tilde{f}^{kn}_\alpha = \frac{1}{4\pi^2} \int_0^{2\pi} dq_r \int_0^{2\pi} dq_\theta \; \hat{F}_\alpha\left(q_r, q_\theta\right) e^{i(kq_\theta + nq_r)}.$$

By densely sampling the two-torus at the points $q_{r,\imath} = 2\pi\imath/N_r$ and $q_{\theta,\jmath} = 2\pi\jmath/N_\theta$, where $N_r, N_\theta \in \mathbb{Z}$, I construct discrete Fourier representations of the SSF

$$\hat{F}_\alpha(q_r, q_\theta) = \sum_{k=0}^{N_\theta - 1} \sum_{n=0}^{N_r - 1} f^{kn}_\alpha e^{-i(kq_\theta + nq_r)}, \tag{5.164}$$

$$f^{kn}_\alpha = \frac{1}{N_r N_\theta} \sum_{\imath=0}^{N_\theta - 1} \sum_{\jmath=0}^{N_r - 1} \hat{F}_\alpha\left(q_{r,\imath}, q_{\theta,\jmath}\right) e^{i(kq_{\theta,\jmath} + nq_{r,\imath})}.$$

Given that N_r and N_θ are large enough such that $\max|f^{kn}_\alpha - \tilde{f}^{kn}_\alpha| < \epsilon_{\mathrm{FS}}$—where ϵ_{FS} is some pre-defined accuracy goal—the discrete representation will provide an accurate representation of Eq. (5.163) [130, 172]. I found that sample numbers of $N_r = N_\theta = 2^8$ were typically sufficient for constructing a discrete representation that was accurate to about $\epsilon_{\mathrm{FS}} \sim 10^{-6} - 10^{-8}$. This provides an efficient method for storing and interpolating SSF data.

While up to this point I have focused on fiducial geodesic sources, one can easily generalize these results to arbitrary geodesics with initial phases $q_0^\mu = (t_0, q_{r0}, q_{\theta 0}, \varphi_0)$, as provided in Eqs. (2.41)-(2.44). The retarded contributions to the self-force for generic initial conditions then takes the form

$$F^{\mathrm{ret},l}_{\alpha\pm}(q_r, q_\theta) = \sum_{m=-l}^{l} (\hat{\mathcal{D}}^{lm}_\alpha \phi^\pm_{lm})(q_r, q_\theta) Y_{lm}(q_r, q_\theta), \tag{5.165}$$

where

$$Y_{lm}(q_r, q_\theta; q_0^\mu) \equiv \hat{Y}_{lm}(q_r + q_{r0}, q_\theta + q_{\theta 0}) \times e^{-im(\Delta\hat{\varphi}(q_{r0}, q_{\theta 0}) - \varphi_0)}, \tag{5.166}$$

and where

$$\begin{aligned}
\phi^\pm_{lm}(q_r, q_\theta; q_0^\mu) &\equiv \sum_{\hat{l}kn} \hat{\phi}^\pm_{l\hat{l}mkn}(q_r + q_{r0}) e^{-i(kq_\theta + nq_r)} e^{-i\omega_{mkn}\Delta\hat{t}(q_r + q_{r0}, q_\theta + q_{\theta 0})} e^{i\omega_{mkn}(\Delta\hat{t}(q_{r0}, q_{\theta 0}) - t_0)} e^{i\xi_{mkn}(q_0^\mu)}, \\
&= \sum_{\hat{l}kn} \hat{\phi}^\pm_{l\hat{l}mkn}(q_r + q_{r0}) e^{-i(kq_\theta + nq_r)} e^{-i(kq_{\theta 0} + nq_{r0})} e^{im(\Delta\hat{\varphi}(q_{r0}, q_{\theta 0}) - \varphi_0)}, && (5.167) \\
&= \hat{\phi}^\pm_{lm}(q_r + q_{r0}, q_\theta + q_{\theta 0}) e^{im(\Delta\hat{\varphi}(q_{r0}, q_{\theta 0}) - \varphi_0)}. && (5.168)
\end{aligned}$$

The exponential factor of $\xi_{mkn}(q_0^\mu)$ comes from the dependence of the normalization coefficient on initial conditions, Eq. (5.152). This phase is defined in Eq. (5.151). Combining Eqs. (5.166) and (5.167) in Eq. (5.165), the exponential factors cancel, so that I find the following shifting relation

$$F^{\mathrm{ret},l}_{\alpha\pm}(q_r, q_\theta; q_0^\mu) = \hat{F}^{\mathrm{ret},l}_{\alpha\pm}(q_r + q_{r0}, q_\theta + q_{\theta 0}). \tag{5.169}$$

The same result also holds true for $F^{\mathrm{S},l}_\alpha$, so that

$$F_\alpha(q_r, q_\theta; q_0^\mu) = \hat{F}_\alpha(q_r + q_{r0}, q_\theta + q_{\theta 0}). \tag{5.170}$$

Accordingly, the SSF for a source with arbitrary initial conditions can always be related to a source that shares the same constants of motion (e.g., $\mathcal{E}$, $\mathcal{L}_z$, and $\mathcal{Q}$) but fiducial initial conditions.

Using the results presented by van de Meent [224], I find that (5.169) also extends to the gravitational case, at least for the form of the gravitational self-force in the outgoing radiation gauge presented in Ref. [224]. In outgoing radiation gauge, the unregularized l-mode contributions to the gravitational self-force are given by (Eq. 44 in Ref. [224])[4]

---

[4] Correcting for one small typo due to a missing factor of Y_{lm} and reformatting indicies to more closely reflect the notation used in our SSF calculations.

$$
\begin{aligned}
F^{\mu,l\pm}_{\mathrm{Rad}}(q_r, q_\theta; q_{r0}, q_{\theta 0}) = \sum_{\substack{mknsij \\ l_1 l_2 \hat{l}}} & C^{\mu}_{mknsij}(\hat{r}_p(q_r + q_{r0}), \hat{\theta}_p(q_\theta + q_{\theta 0}))\Psi^{\pm}_{\hat{l}mkn}(q_{r0}, q_{\theta 0}) \\
& \times {}_2R^{\pm,(i)}_{\hat{l}mkn}(\hat{r}_p(q_r + q_{r0}))\, {}_2b^{l_1}_{\hat{l}mkn}\, {}^{m}_{s}\mathcal{A}^{l_2}_{l_1}\, {}^{j}_{m}\mathcal{B}^{l}_{l_2} Y_{lm}(\hat{\theta}_p(q_\theta + q_{\theta 0}), 0) e^{im\Delta\varphi(q_r + q_{r0}, q_\theta + q_{\theta 0})} e^{-im\Delta\varphi(q_{r0}, q_{\theta 0})} \\
& \times e^{-i\omega_{mkn}\Delta t(q_r + q_{r0}, q_\theta + q_{\theta 0})} e^{i\omega_{mkn}\Delta t(q_{r0}, q_{\theta 0})} e^{-ikq_\theta} e^{-inq_r} + \text{c.c.}, \qquad (5.171)
\end{aligned}
$$

where the functions and coefficients are defined in Ref. [224] and c.c. denotes complex conjugation of the previous terms. As van de Meent and Shah demonstrated in Ref. [225], the asymptotic amplitudes of the outgoing radiation gauge Hertz potential $\Psi^{\pm}_{\hat{l}mkn}(q_{r0}, q_{\theta 0})$ are proportional to the Teukolsky amplitudes (normalization coefficients) for a gravitational source, $C^{\pm}_{-2\hat{l}mkn}(q_{r0}, q_{\theta 0})$ (what they call $Z^{\pm}_{\hat{l}mkn}$). Because the gravitational Teukolsky amplitudes for generic initial conditions are also related to the amplitudes for fiducial sources according to Eq. (5.152) [101], the $\Delta t(q_{r0}, q_{\theta 0})$ and $\Delta\varphi(q_{r0}, q_{\theta 0})$ terms cancel, and the gravitational self-force in outgoing radiation gauge can be expressed in terms of the fiducial gravitational self-force by

$$
F^{\mu,l\pm}_{\mathrm{Rad}}(q_r, q_\theta; q_{r0}, q_{\theta 0}) = \hat{F}^{\mu,l\pm}_{\mathrm{Rad}}(q_r + q_{r0}, q_\theta + q_{\theta 0}). \qquad (5.172)
$$

In practice, choosing different initial conditions is equivalent to choosing a new starting point for the geodesic flow of $F_\alpha(\lambda)$ on $\mathcal{T}^2_{r\theta}$, as shown in Fig. 2.4. While this result seems almost trivial for the non-resonant case, it is useful for improving the efficiency of SSF calculations for resonant orbits, as I will discuss in Chapter 8.

5.3.5: Regularization with numerical fitting

While the sum in Eq. (5.54) gives a finite result, the higher-order terms drop off at a rate of l^{-2}. When the sum is approximated by being truncated at $l = l_{\max}$, there is a residual error that scales as $l^{-1}_{\max}$. For computational cost reasons, it is typically beneficial to truncate the SSF calculation at $l_{\max} \sim 20$, which means that relying only upon the regularization parameters $A_{\alpha\pm}$ and B_α will determine F_α to just one or two digits of accuracy.

Including the higher-order parameters $D_{\alpha,2n}$ can improve the rate of convergence of the partial sums of Eq. (5.41), which are now written as

$$
F_\alpha = \sum_{l=0}^{l_{\max}} \left(F^{\mathrm{alg},l}_{\alpha\pm} - \sum_{n=1}^{n_{\max}} \frac{D_{\alpha,2n}}{\prod_{k=1}^{n}(2l+1-2k)(2l+1+2k)} \right). \qquad (5.173)
$$

Here there is a two-fold truncation, with $l_{\max}$ determining the number of modes we calculate in the retarded field, Φ, and $n_{\max}$ setting the limit in the number of available higher-order regularization parameters.

Eq. (5.173) converges at a rate of $l^{-2(n_{\max}+1)}$ and therefore the SSF has an error that scales as $l_{\max}^{-2n_{\max}-1}$. Unfortunately, only $A_{\alpha\pm}$ and B_α are known analytically for generic orbits in Kerr [39] (although, terms up to $n_{\max}=2$ are known for equatorial orbits in Kerr [122]).

I overcome the lack of analytically known higher-order regularization parameters by fitting [81] the high-l contributions to the SSF to the assumed form in (5.52), similar to the methods discussed in Sec. IVC of Ref. [236]. At high l, the self-force contributions are primarily determined by the missing regularization parameters

$$F^{\mathrm{alg},l}_{\alpha\pm} \simeq \sum_{n=1}^{N} \frac{D_{\alpha,2n}}{\prod_{k=1}^{n}(2l+1-2k)(2l+1+2k)}. \tag{5.174}$$

The number of regularization parameters N that can be determined is limited by the precision of $F^{\mathrm{alg},l}_{\alpha\pm}$ and $l_{\max}$. I take the last $\bar{n}$ self-force l-mode contributions, $F^{\mathrm{alg},l}_{\alpha\pm}$, and fit these values to N regularization parameters by applying a least-squares algorithm to Eq. (5.174). The value of $\bar{n}$ is varied and a weighted average is taken as described in Ref. [236]. I also vary N and use the standard deviation of the results to estimate the error produced by this fitting scheme. However, I do not use Eq. (47) in Ref. [236], but instead reapply the fitted regularization parameters using Eq. (5.173) to improve the convergence of my SSF results. The estimated errors are also propagated to determine the accuracy of the SSF results. Errors due to fitting typically dominate over the error from terminating the l-mode summation. The validity of these fits and their errors is further discussed in Sec. 6.2, where I compare fitted conservative self-force data (for an inclined Schwarzschild orbit) to conservative self-force data that has been regularized with known higher-order parameters (for an equatorial Schwarzschild orbit).

CHAPTER 6: Scalar self-force for non-resonant motion in Kerr spacetime

Section 6.1: Chapter overview

In this chapter I present numerical results for the SSF, $\hat{F}_\alpha$, experienced by a scalar charge q following fiducial non-resonant geodesics in Kerr spacetime. These results are broken down into three categories:

(a) eccentric, inclined orbits in Schwarzschild spacetime;

(b) spherical, inclined orbits in Kerr spacetime; and

(c) non-resonant, eccentric, inclined (generic) orbits in Kerr spacetime.

The Schwarzschild results provide a diagnostic test for my SSF code and verify the accuracy of the numerical fitting procedure described in Sec. 5.3.5. The spherical orbits in Kerr spacetime provide another check and are compared to previously published spherical, inclined Kerr SSF results [234]. The generic non-resonant Kerr SSF results are novel calculations performed with the numerical algorithms discussed in the previous chapter (Chapter 5) and are key results of this dissertation. These generic SSF results were first developed and reported in collaboration with Osburn and Evans in Ref. [172]. Because we compare our SSF data to previously published results by Warburton and Barack [236, 237, 234], we will follow some of their notation and conventions in this chapter. The inclination of orbits will be specified in terms of ι, while the SSF will be parameterized in terms of either the radial motion of the source or the Darwin phase variables ψ and χ. These parameterizations were discussed earlier in Chapter 2. In a slight abuse of notation, in this chapter we will refer to the SSF as $\hat{F}_\alpha$, regardless of its parameterization, to emphasize that all of the orbits considered here have fiducial initial conditions. Additionally, to simplify notation, we set $M = 1$ for the remainder of this chapter.

Section 6.2: Eccentric, inclined orbits in Schwarzschild spacetime

We first examine eccentric, inclined orbits in the Schwarzschild limit ($a = 0$). These models serve as a strong validation of the SSF code, since all elements of the field and self-force calculation are required, yet they can be compared to much simpler-to-compute eccentric, equatorial models (i.e., ones with vastly fewer computed modes). The one-to-one correspondence results from spherical-symmetry of Schwarzschild

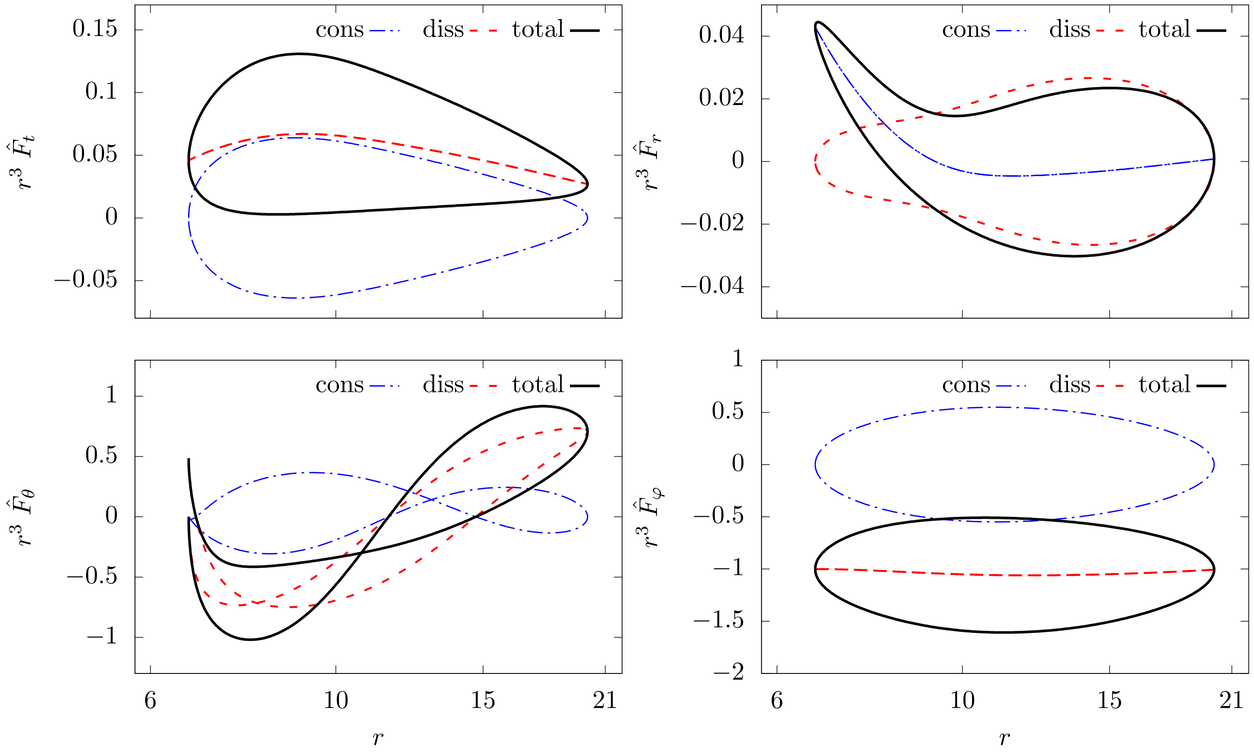

Figure 6.1: Components of the scalar self-force for an inclined eccentric orbit in Schwarzschild spacetime. The orbital parameters are given by $(a, p, e, \iota) = (0, 10, 0.5, \pi/5)$. The red (dashed) lines refer to the dissipative pieces of the self-force components, while the blue (dot-dashed) lines refer to the conservative pieces. The black (solid) lines represent the total values for each self-force component. $\hat{F}_t$ $\hat{F}_r$, $\hat{F}_\varphi$ share the same periodicity as the particle's radial motion. Therefore, plotted as functions of r, these components form closed self-force "loops." However $\hat{F}_\theta$ does not close on itself in this eccentric, inclined case, because $\hat{F}_\theta$ also depends on the longitudinal position of the particle $\hat{\theta}_p$, which librates at a different frequency from the particle's radial position $\hat{r}_p$ $(\Omega_r \neq \Omega_\theta)$.

spacetime, where two geodesics with the same eccentricities but different inclinations are related merely by a rotation.

In spherically-symmetric spacetimes, the self-force for an eccentric inclined orbit F_α can be compared to the force F_α^{rot} that is obtained through rotational transformation of the equatorial plane self-force F_α^{eq}. The transformation is

$$F_t^{\text{rot}} = F_t^{\text{eq}}, \qquad F_\theta^{\text{rot}} = \pm F_\varphi^{\text{eq}} \sqrt{1 - \cos\iota \csc^2\theta_p}, \tag{6.1}$$

$$F_r^{\text{rot}} = F_r^{\text{eq}}, \qquad F_\varphi^{\text{rot}} = F_\varphi^{\text{eq}} \cos\iota, \tag{6.2}$$

where ± depends on the sign of u^θ (+ when $u^\theta > 0$).[1]

The four SSF components for an orbit characterized by $(a, p, e, \iota) = (0, 10, 0.5, \pi/5)$ are plotted in Fig. 6.1.

---

[1] Note that I do not use the hat notation here, because these relations also hold for non-fiducial SSF results.

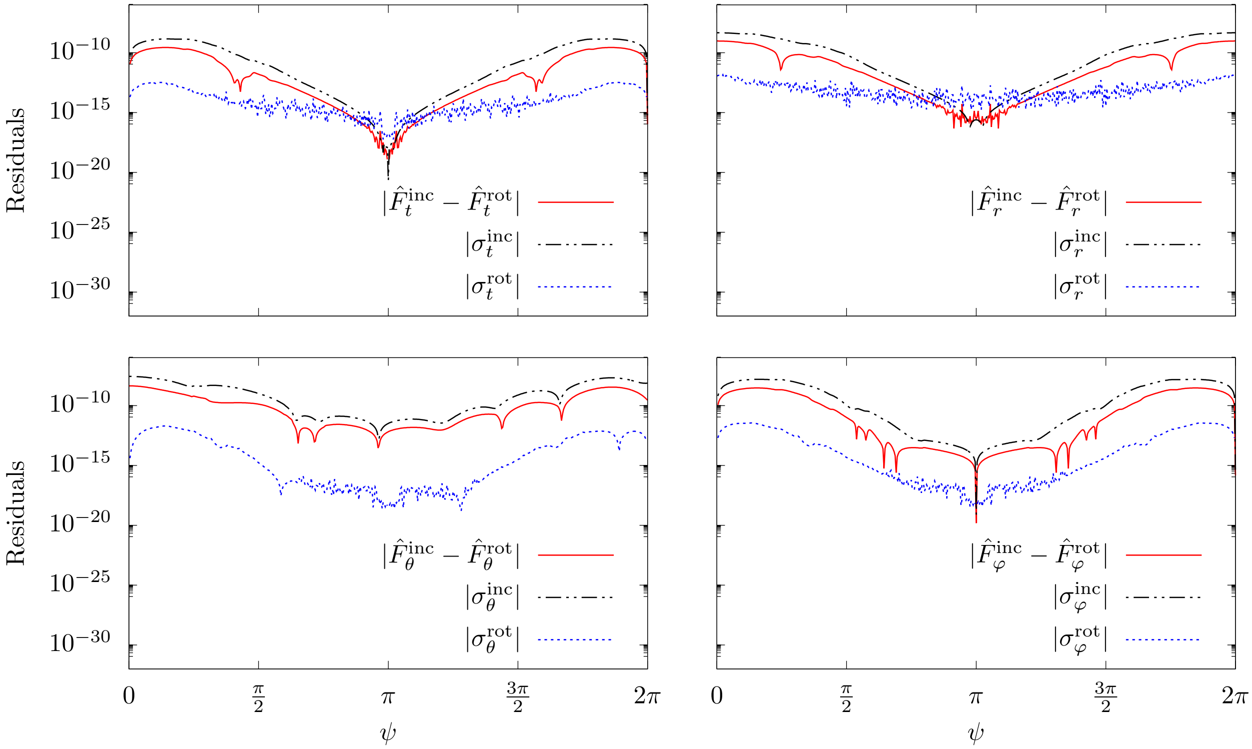

Figure 6.2: Comparison of the scalar self-force calculated from an inclined orbit and a rotated equatorial orbit in Schwarzschild spacetime with $M = 1$ and $a = 0$. The equatorial orbit is described by the orbital parameters $(a, p, e, \iota) = (0, 10, 0.5, 0)$, while the inclined orbit is described by $(a, p, e, \iota) = (0, 10, 0.5, \pi/5)$. Red (solid) lines refer to the absolute residuals between the self-force calculated by rotating the results from an equatorial orbit $\hat{F}_\alpha^{\rm rot}$ and the scalar self-force directly calculated from the inclined orbit $\hat{F}_\alpha^{\rm inc}$. The black (dot-dashed) and blue (dotted) lines refer, respectively, to the errors from calculating the self-force along an inclined orbit and an equatorial orbit. The error for both the rotated equatorial orbit $\sigma_\alpha^{\rm rot}$ and the error for the inclined orbit $\sigma_\alpha^{\rm inc}$ are based on the estimated error from fitting the conservative component of the self-force, as outlined in Sec. 5.3.5.

For equatorial orbits, the self-force is a periodic function of ψ. This periodicity continues to be seen in Fig. 6.1 for the $\hat{F}_t$, $\hat{F}_r$, and $\hat{F}_\varphi$ components in the inclined model as these self-force components "loop" back onto themselves as the particle librates from $r_{\rm min}$ to $r_{\rm max}$ and then back to $r_{\rm min}$. This periodicity is evident in examining $\hat{F}_t^{\rm rot}$, $\hat{F}_r^{\rm rot}$, and $\hat{F}_\varphi^{\rm rot}$ in Eqs. (6.1) and (6.2).

The behavior of $\hat{F}_\theta$ is different. When the orbit is rotated out of the equatorial plane, the $\hat{F}_\varphi^{\rm eq}$ contribution is split between the rotated self-force components $\hat{F}_\varphi^{\rm rot}$ and $\hat{F}_\theta^{\rm rot}$. While $\hat{F}_\varphi^{\rm rot}$ differs from $\hat{F}_\varphi^{\rm eq}$ by a trigonometric factor; the projection of $\hat{F}_\varphi^{\rm eq}$ onto the new inclined basis depends on the polar position of the particle. This causes $\hat{F}_\theta^{\rm rot}$ to also depend upon θ_p (see Eq. (6.1)). The small body librates at different frequencies in r and θ, which demonstrates why the inclined force component $\hat{F}_\theta$ does not form a closed loop when plotted versus r.

These inclined SSF results can be compared in quantitative detail, again via Eqs. (6.1) and (6.2), to results computed from an equivalent equatorial orbit $(a, p, e, \iota) = (0, 10, 0.5, 0)$. We refer to the self-force calculated directly using an inclined orbit as $\hat{F}_\alpha^{\text{inc}}$ (previously we referred to the inclined SSF results more generally as $\hat{F}_\alpha$), while the force computed by rotating the equatorial-orbit self-force remains being denoted by $\hat{F}_\alpha^{\text{rot}}$. The absolute residuals from comparing these orbits are plotted in Fig. 6.2. We also plot the estimated numerical errors $\sigma_\alpha^{\text{inc}}$ and $\sigma_\alpha^{\text{rot}}$ for both self-force calculations. The primary source of error comes from fitting the conservative component of the self-force. In Fig. 6.2 the residual errors between the two calculations consistently fall below the errors that are estimated by the fitting procedure. This provides additional confidence in the validity of our error estimation, which is outlined in Sec. 5.3.5, and makes a strong case for having summed over all the required modes and correctly computed the regularization in the inclined model.

Additionally, we compare specific numerical values of $\hat{F}_\alpha^{\text{inc}}$ to previously and independently computed equatorial results published in Ref. [237], by again using Eqs. (6.1) and (6.2) to transform the equatorial plane SSF. We compare both the conservative and dissipative parts of the self-force in Table 6.1. The fractional errors between the independently computed conservative parts typically fall below the estimated errors in the conservative parts themselves that owe to the high-l fitting procedure. The dissipative part of the inclined SSF typically agrees with the transformed dissipative part from Ref. [237] to 6 or more decimal places.

		Conservative		Dissipative	
		$\psi = 0$	$\psi = \frac{\pi}{2}$	$\psi = 0$	$\psi = \frac{\pi}{2}$
$\hat{F}_t \times 10^4$	This paper	0	$0.568\,263\,3(2)$	$1.551\,695\,9$	$0.657\,753\,715\,363$
	Rotated [237]	0	$0.568\,25(3)$	$1.551\,696\,2$	$0.657\,754\,26$
$\hat{F}_r \times 10^4$	This paper	$1.446\,26(5)$	$-0.030\,666\,1(7)$	0	$0.176\,664\,399\,73$
	Rotated [237]	$1.446(2)$	$-0.030\,671\,7(7)$	0	$0.176\,664\,37$
$\hat{F}_\theta \times 10^4$	This paper	0	$-1.912\,00(1)$	0	$-3.726\,015\,695$
	Rotated [237]	0	$-1.9119(2)$	0	$-3.726\,015\,6$
$\hat{F}_\varphi \times 10^3$	This paper	0	$-0.539\,248\,9(1)$	$-3.377\,102\,3$	$-1.050\,859\,941\,917$
	Rotated [237]	0	$-0.539\,23(6)$	$-3.377\,101\,9$	$-1.050\,859\,9$

Table 6.1: A comparison between the scalar self-force (SSF) data produced by our code for an eccentric, inclined orbit $(a, p, e, \iota) = (0, 10, 0.5, \pi/5)$ and equatorial SSF results from Ref. [237]. We rotate the results of Ref. [237] using Eqs. (6.1) and (6.2) to directly compare with our inclined values. Conservative values include error estimates due to fitting the large-l contribution as discussed in Sec. 5.3.5. Note that our fitting procedure, outlined in Sec. 5.3.5, is partially motivated by but not equivalent to the fitting procedure in Ref. [237]. Numbers in parentheses describe the estimated error in the last reported digit, i.e. $1.44626(5) = 1.446(2) \pm 0.002$. Dissipative values are truncated based on the value of the last computed self-force l-mode l_{max}.

Section 6.3: Spherical, inclined orbits in Kerr spacetime

We next examine inclined orbits in the Kerr background by calculating the SSF along spherical, inclined orbits. (In Kerr spacetime, spherical orbits are inclined orbits that maintain a fixed Boyer-Lindquist distance from the black hole, but are not ‘circular’ because precession makes these orbits non-planar.) Similar to other restricted orbits, spherical, inclined orbits are bi-periodic in their frequency spectrum, $\omega_{mk0} = m\Omega_\varphi + k\Omega_\theta$, rather than tri-periodic like eccentric, inclined orbits. Additionally, while the number of summed radial-frequency modes in Eq. (5.39) rapidly grows with increasing eccentricities, the number of summed polar-frequency modes is not as dramatically affected by increasing the inclination. Furthermore, the radial mode functions only need to be evaluated at a single radial point for spherical orbits. This is beneficial, because calculating the radial mode functions is one of the primary computational bottlenecks of my code. Altogether these factors significantly reduce computational costs, allowing us to compute the SSF along spherical orbits at large inclinations with high precision.

These orbits serve as a code test, since the SSF along spherical orbits was previously investigated by

ψ		$\psi = 0$	$\psi = \pi/3$	$\psi = \pi/2$
$\hat{F}_t^{\mathrm{cons}} \times 10^4$	This paper	0	1.077 533(4)	0
	[234]	0	1.077 40(5)	0
$\hat{F}_t^{\mathrm{diss}} \times 10^3$	This paper	1.683 771 018 273 96	1.623 585 013 78	1.668 641 421 01
	[234]	1.683 771	1.623 585	1.668 641 4
$\hat{F}_r^{\mathrm{cons}} \times 10^4$	This paper	4.050 372 7(9)	−3.901 868(4)	−7.719 77(2)
	[234]	4.050 36(4)	−3.901 90(8)	−7.720 01(4)
$\hat{F}_r^{\mathrm{diss}} \times 10^4$	This paper	0	−1.280 407 14	0
	[234]	0	−1.280 407 1	0
$\hat{F}_\theta^{\mathrm{cons}} \times 10^3$	This paper	3.552 535 1(2)	2.254 85(3)	0
	[234]	3.552 43(9)	2.254 95(4)	0
$\hat{F}_\theta^{\mathrm{diss}} \times 10^2$	This paper	0	−1.185 212 479	−1.146 202 895 87
	[234]	0	−1.185 212 5	−1.146 202 9
$\hat{F}_\varphi^{\mathrm{cons}} \times 10^4$	This paper	0	−2.979 84(2)	0
	[234]	0	−2.9793(5)	0
$\hat{F}_\varphi^{\mathrm{diss}} \times 10^3$	This paper	−4.960 869 925 391 37	−7.246 295 971 2	−8.304 515 578 0
	[234]	−4.960 869 9	−7.246 296 0	−8.304 515 6

Table 6.2: A comparison between the scalar self-force data produced by our code for a spherical, inclined orbit $(a, p, e, \mathcal{L}_z) = (0.998, 4, 0, 1)$ and the SSF results for the same orbit reported in Tables II and III of Ref. [234]. Conservative values include error estimates due to fitting the large-l contribution as discussed in Sec. 5.3.5. Numbers in parentheses describe the estimated error in the last reported digit, i.e. $-2.9793(5) = -2.9793 \pm 0.0005$. Dissipative values are truncated based on the value of the last computed dissipative self-force l-mode $l_{\max}$.

model	p	e	ι	a
base	10	0.1	$\pi/5$	0.5
large e	10	0.3	$\pi/5$	0.5
large ι	10	0.1	$\pi/3$	0.5
large a	10	0.1	$\pi/5$	0.9

Table 6.3: Orbital parameters for generic orbits presented in Fig. 6.4.

Warburton [234]. We reproduced the results from Ref. [234] for the orbit with parameters $(a, p, e, \mathcal{L}_z) = (0.998, 4, 0, 1)$. To match the conventions of Ref. [234], the orbit is parameterized by the z-component of angular momentum, $\mathcal{L}_z$, instead of the inclination ι. The self-force data produced by my code are in good agreement with those of Ref. [234]. The conservative components agree to ~ 4 digits and dissipative components to 7 or more digits. Comparative SSF values are provided in Table 6.2.

Section 6.4: Eccentric, inclined orbits in Kerr spacetime

The truly unique capability of my code is its ability to model the SSF on generic (bound) eccentric, inclined orbits. We investigate the SSF on four different orbits of this type, with their characteristic parameters specified in Table 6.3. We refer to these orbits by their reference names: 'base', 'large e', 'large ι', and 'large a.' We use the orbit $(a, p, e, \iota) = (0.5, 10, 0.1, \pi/5)$ as a reference case and then vary either the orbital eccentricity, the orbital inclination, or the black hole spin to get a sense of how the self-force depends on these orbital and spin parameters. This also provides tests of my code's ability to probe more challenging regions of parameter space.

The 'large e' orbit is also used in Fig. 6.3 to demonstrate improved convergence of the mode-sum through incorporating additional numerically-extracted regularization parameters. In Fig. 6.3, we plot the l-mode contributions to the polar component of the SSF, $\hat{F}^l_\theta$, at the point $(\psi = \pi/8, \chi = 3\pi/4)$. The (black) squares represent the value of the retarded SSF contributions, $\hat{F}^{\text{ret},l}_\theta$, prior to applying mode-sum regularization. The dashed (black) line demonstrates the asymptotic $1/l^0$ behavior of the retarded l-mode contributions at large l. It is clear that summing over these unregularized l-modes leads to a divergent result. Subtracting the analytically-known regularization parameter B_θ produces the (red) triangles in Fig. 6.3, which fall-off as $1/l^2$ at large l, as demonstrated by the dotted (red) line. (Note that $A_\theta = 0$.) We then fit for the higher-order regularization parameters, $D_{\theta,n}$, using the numerical fitting procedures described in Sec. 5.3.5. Successively subtracting our numerically-obtained values for $D_{\theta,2}$, $D_{\theta,4}$, and $D_{\theta,6}$ leads to the (blue) diamonds, the (purple) circles, and the (orange) inverted triangles, respectively. The residual l-modes fall-off at increasing

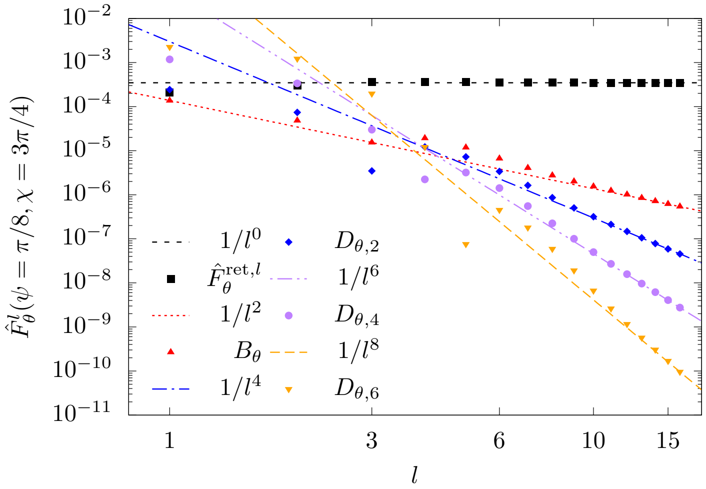

Figure 6.3: Convergence of the scalar self-force l-modes for an eccentric, inclined orbit in Kerr spacetime. Orbital parameters are taken to be $(a, p, e, \iota) = (0.5, 10, 0.3, \pi/5)$. The dashed and dotted lines depict the increasing rate of convergence for $\hat{F}_\theta(\psi = \pi/8, \chi = 3\pi/4)$ as additional regularization parameters are incorporated. The (black) squares represent individual l-modes of the SSF prior to regularization, which diverge as expected. The (red) triangles show the effect of subtracting the known analytic regularization parameters A_θ and B_θ. The (blue) diamonds include the next regularization parameter $D_{\theta,2}$, estimated numerically (Sec. 5.3.5). The (purple) circles and the (orange) inverted triangles represent including additional numerically-fitted regularization parameters. Mode-sum convergence improves through inclusion of successively more regularization parameters.

rates of $1/l^{2n+2}$, just as expected, validating our numerical fits of the higher-order regularization parameters.

While in restricted cases the self-force can be periodic, for generic orbits the self-force is instead bi-periodic. (Even though inclined, eccentric orbits are tri-periodic due to the radial, polar, and azimuthal motion of the particle, the SSF only depends on the radial and polar motion due to the rotational invariance of Kerr spacetime. Therefore, the SSF is only bi-periodic.) As such, it is less practical to plot the self-force as a function of time or radial position as in Fig. 6.1. Instead, one can map the self-force as contour levels on the torus spanned by the coordinates ψ and χ, similar to the use of the torus in the discussion surrounding Figs. 2.4, 2.5, and 2.6 of Sec. 2.6. The ergodic nature of the particle's motion implies that the SSF is a smooth continuous field over ψ and χ, with any given point eventually sampled by the motion (see also Ref. [223]). This representation of the SSF for the generic (non-resonant) orbits listed in Table 6.3 is shown in Fig. 6.4. (In these plots I use ψ and χ as coordinates rather than q_r and q_θ.)

For the orbits presented in Fig. 6.4, the largest variations in the SSF occur in the radial direction, with the exception of the $\hat{F}_\theta$ component. Consequently, despite the low eccentricities considered, $\hat{F}_t$, $\hat{F}_r$, and $\hat{F}_\varphi$ are most dependent on ψ, i.e., the radial motion of the small body. Additionally, the maxima and minima of each self-force component are shifted away from the turning points of the particle's motion ($\psi = 0, \pi, 2\pi; \chi = 0, \pi, 2\pi$) and the particle's passage through the equatorial plane ($\chi = \pi/2, 3\pi/2$), as a result of conservative effects. These shifts are most easily recognized in $\hat{F}_r$.

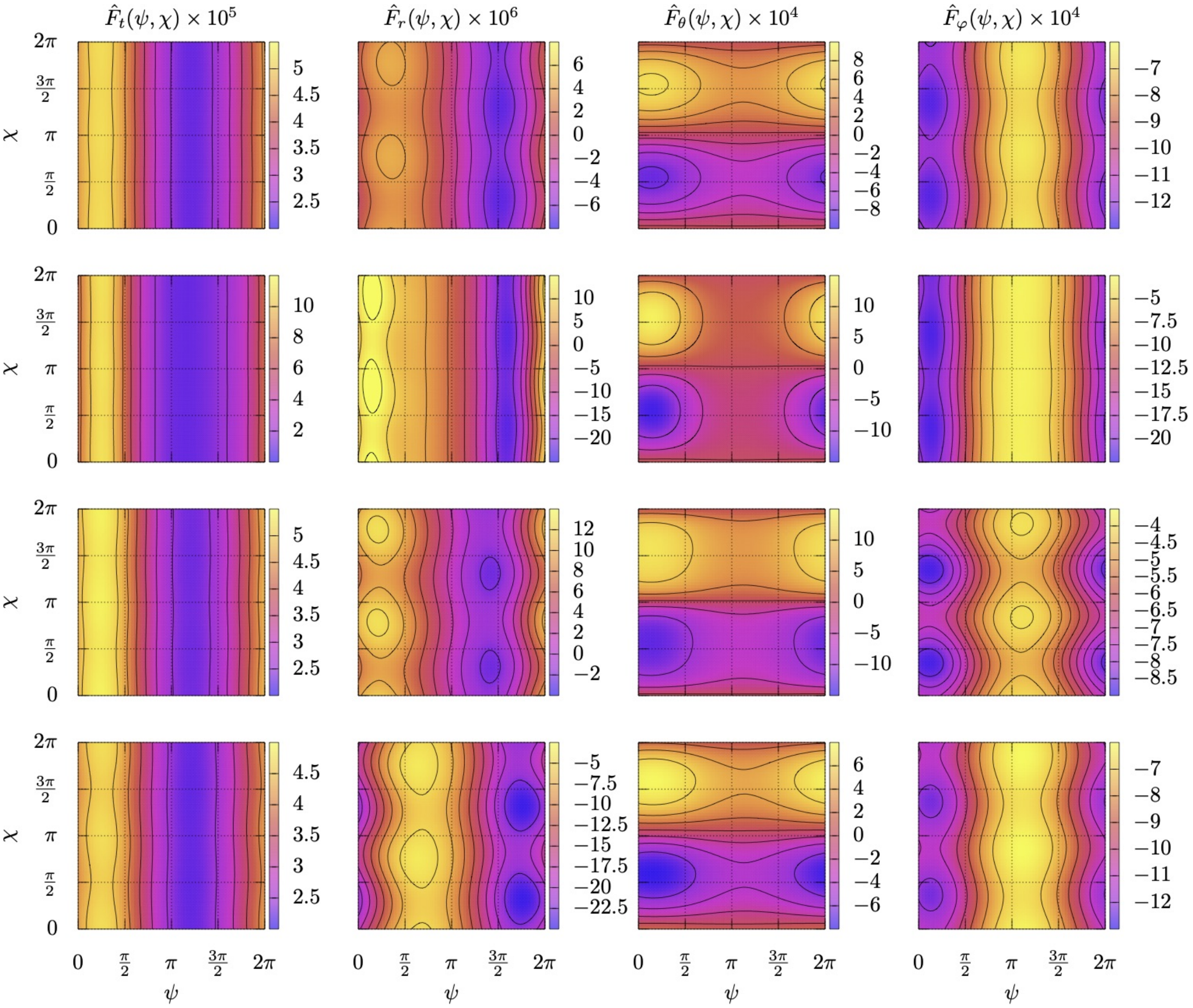

Figure 6.4: The scalar self-force components, $\hat{F}_\alpha(\psi,\chi)$, for the four orbits listed in Table 6.3 is depicted through sampling on the torus. Each row of plots directly corresponds to the orbit in the same row of Table 6.3. (The first, second, third, and fourth rows correspond to the orbits 'base,' 'large e,' 'large ι,' and 'large a' respectively.) The vertical axis is correlated with the θ-dependence of the self-force components, while the horizontal axis is related to the r-dependence. Colors correspond to different values of the self-force, with the values denoted in the colorbar to the right side of each plot. The self-force is constant along each contour line. The tic labels in each colorbar correspond to the values of the contour lines. Therefore, in the top left plot, $\hat{F}_t = 5\times 10^{-5}$ along the leftmost contour line.

Taking the 'base' orbit for comparison, one can also examine how the self-force changes as the orbital parameters e and ι or the spin parameter a are varied. With the 'high e' orbit, the eccentricity is increased from $e = 0.1$ to $e = 0.3$. The radial dependence of the self-force becomes further accentuated due to the orbit's increased eccentricity. Additionally, the maximum magnitude of the SSF increases in every self-force component, most likely due to the particle's smaller pericentric distance at the higher eccentricity.

For the 'high ι' orbit, the inclination is increased from $\iota = \pi/5$ to $\iota = \pi/3$. The dependence of the

SSF on the particle's polar (χ) motion becomes more pronounced, as the particle sweeps out a larger region above and below the equatorial plane. Additionally, the radial component of the SSF shifts to become predominantly positive. A similar behavior is seen for inclined, spherical orbits, where the average value of F_r grows monotonically with inclination, as it ranges from $\iota = 0$ to $\iota = \pi$ [234]. (Retrograde orbits are parameterized with $a < 0$ in our code.)

For the 'high a' orbit, the black hole spin parameter is increased from $a = 0.5$ to $a = 0.9$. One can observe a stronger dependence of the scalar self-force on the polar position of the particle when a is increased. Also, the radial component of the SSF becomes attractive ($\hat{F}_r < 0$) along the entire orbit in this case. This is consistent with previous work on circular, equatorial orbits, where $\hat{F}_r$ decreases with increasing spin a [236].

Section 6.5: Scalar flux balance

As a final self-consistency check, we analyze the balance between the asymptotic fluxes with the local dissipative self-force effects [162, 164, 163, 202, 237]. As discussed in Sec. 5.2.7, the average work done on the particle by the SSF should be balanced by the rate of radiative energy loss. Likewise there should be a balance between the local torque on the particle due to the SSF and the angular momentum radiated away by the scalar field.

As described earlier in Sec. 5.2.7, the asymptotic energy and angular momentum fluxes can be calculated by analyzing the scalar field at $r \simeq \infty$ and $r \simeq r_+$

$$\langle \dot{E} \rangle^{\text{tot}} = \frac{q^2}{4\pi} \sum_{\hat{l}mkn} \omega_{mkn} \left(\gamma_{mkn} |C^-_{\hat{l}mkn}|^2 + \omega_{mkn} |C^+_{\hat{l}mkn}|^2 \right), \tag{6.3}$$

$$\langle \dot{L}_z \rangle^{\text{tot}} = \frac{q^2}{4\pi} \sum_{\hat{l}mkn} m \left(\gamma_{mkn} |C^-_{\hat{l}mkn}|^2 + \omega_{mkn} |C^+_{\hat{l}mkn}|^2 \right), \tag{6.4}$$

Recall that $\gamma_{mkn} \equiv \omega_{mkn} - ma/2Mr_+$. The flux balance formulae then take the form

$$\langle \dot{E} \rangle^{\text{tot}} = -\mathcal{W}, \tag{6.5}$$

$$\langle \dot{L}_z \rangle^{\text{tot}} = -\mathcal{T}. \tag{6.6}$$

The fluxes and self-force are calculated independently from one another. Consequently, comparing SSF results with flux calculations provides a self-consistency check for my code. Flux balance comparisons are included in Table 6.4. One can see that they are in good agreement with fractional errors $\lesssim 10^{-10}$.

p	e	ι	a	$\langle \dot{E} \rangle^{\text{tot}} \times q^{-2}$	$\vert 1 + \langle \dot{E} \rangle^{\text{tot}} / \mathcal{W} \vert$	$\langle \dot{L}_z \rangle^{\text{tot}} \times q^{-2}$	$\vert 1 + \langle \dot{L}_z \rangle^{\text{tot}} / \mathcal{T} \vert$
10	0.5	$\pi/5$	0	$3.329\,332\,97 \times 10^{-5}$	1×10^{-11}	$6.346\,485\,50 \times 10^{-4}$	3×10^{-10}
10	0.5	0	0	$3.329\,332\,97 \times 10^{-5}$	3×10^{-11}	$7.844\,687\,49 \times 10^{-4}$	2×10^{-11}
10	0.3	$\pi/5$	0.5	$2.961\,026\,3 \times 10^{-5}$	9×10^{-14}	$6.984\,021\,2 \times 10^{-4}$	4×10^{-14}
10	0.1	$\pi/3$	0.5	$2.994\,475\,370 \times 10^{-5}$	0×10^{-11}	$4.938\,962\,06 \times 10^{-4}$	0×10^{-12}
10	0.1	$\pi/5$	0.9	$2.745\,901\,231 \times 10^{-5}$	7×10^{-12}	$7.281\,232\,718 \times 10^{-4}$	0×10^{-11}
10	0.1	$\pi/5$	0.5	$2.917\,529\,922 \times 10^{-5}$	5×10^{-14}	$7.567\,560\,34 \times 10^{-4}$	6×10^{-15}
8	0.8	0	0.99	3.1363×10^{-5}	7×10^{-8}	4.2122×10^{-4}	7×10^{-9}
4	0	1.22	0.998	$9.642\,339\,9 \times 10^{-4}$	7×10^{-10}	$3.787\,652\,4 \times 10^{-3}$	8×10^{-10}

Table 6.4: Energy and angular momentum fluxes for various orbits, along with their comparisons to the local work and torque done by the SSF on the particle. The plus signs in columns six and eight are due to the negative signs in Eqs. (6.5) and (6.6). Flux expressions are truncated two digits prior to the order of the last calculated SSF l-mode, l_{max}. If the energy flux for l_{max} is on the order of 10^{-14}, then the flux is reported to an accuracy of 10^{-12}. The fluxes typically agree with the local work and angular momentum beyond the level of reported accuracy (the relative errors are greater than the reported accuracy of the results). Note that the inclination for the last orbit is irrational and only reported with three significant digits. In this case the inclination value corresponds to an angular momentum value of $\mathcal{L}_z = 1$.

Section 6.6: Significance of results

In this chapter, we presented the first SSF results for (non-resonant) eccentric, inclined orbits in Kerr spacetime. These results extend previous work by Warburton and Barack [236, 237, 234], in which they calculated the SSF along equatorial and spherical orbits in Kerr spacetime with their own frequency-domain code. Our SSF results are also complementary to recent gravitational self-force calculations performed by van de Meent [224] along eccentric, inclined orbits in Kerr, though his results are limited to orbits with eccentricities of $e = 0.1$ due to the computational rigor of the gravitational self-force problem. My code, on the other hand, can more rapidly evaluate higher-eccentricity orbits, as demonstrated in Sec. 6.4. These SSF results, therefore, validate the efficacy of my SSF code and provide an important stepping stone for surveying unexplored regions of the physical EMRI parameter space. In the following chapters, I use my SSF code to explore two particularly interesting phenomena: the presence of high-frequency oscillations in the waveforms of highly-eccentric EMRIs, known as quasinormal bursts, and the impact of eccentric, inclined $r\theta$-resonant orbits on the self-force and the ensuing evolution of the energy, angular momentum, and the Carter constant that characterize the small body's motion.

CHAPTER 7: Quasinormal bursts

Section 7.1: Chapter overview

An advantage of my SSF code is that it can more rapidly explore interesting areas of physical parameter space that are less accessible to current Kerr gravitational self-force codes. This capability led to a primary physical result of this dissertation: the discovery of faint periodic signals in the EMRI waveform, which we term *quasinormal bursts*. This discovery was precipitated by the work of Thornburg and Wardell [214], who first found the existence of quasinormal mode excitation in the self-force itself for time-domain SSF simulations of highly-eccentric Kerr orbits. That finding was discussed in a series of talks [212, 213, 215] by Thornburg and reported in a paper by Thornburg and Wardell [214]. Oscillations were observed in the self-force during the outbound portion of certain highly-eccentric orbits following periastron passage near a rapidly-rotating black hole. These oscillations were confirmed to fit the least-damped overtone of the $\hat{l} = m = 1$ quasinormal mode. I confirmed this phenomenon with my frequency-domain SSF calculations of a similar highly-eccentric ($e = 0.8$) equatorial orbit about a rapidly-rotating ($a/M = 0.99$) primary.

More interestingly, my collaborators[1] and I decided to take a look at the waveform in this same model to see if the excitation is imprinted in an asymptotically-accessible signal. Confirming our expectation, it is indeed possible to discern repeated (albeit faint) quasinormal bursts (QNBs) in the waveform following each periastron passage. This work was originally published in Ref. [172]. Since its publication, the presence of QNBs has also been confirmed by gravitational self-force codes [216] and motivated follow-on research [197] to better understand their behavior, particularly for near-extremal black hole spins $a/M \geq 0.999$.

In the following sections, I give a brief review of Kerr black hole quasinormal modes and present frequency-domain SSF results that match the quasinormal ringing observed by the time-domain SSF calculations of Thornburg and Wardell [214]. I then present evidence for the presence of periodic quasinormal ringing in the EMRI (scalar) waveform, showing that these QNBs are in fact a superposition of (at least) four least-damped quasinormal modes, with $\hat{l} = m = 1$ through $\hat{l} = m = 4$. I conclude with some comments on the detectability and observational implications of QNBs. I refer the reader to Ref. [49] for a detailed review of black hole quasinormal modes.

---

[1] This work was also done in collaboration with Osburn and Evans [172].

Section 7.2: Quasinormal modes of black holes

Quasinormal modes (QNMs) are the natural frequency modes of black holes. Unlike normal modes, QNMs are represented by complex frequencies and therefore decay with time. For black hole spacetimes, this decay arises due to the emission of gravitational waves [49]. Quasinormal modes also appear to be deeply tied to the "no-hair theorem" of black holes [65, 168, 49]. The "no-hair theorem" proposes that axisymmetric, stationary, vacuum spacetimes are characterized by just two observable quantities: the mass M of the black hole and the angular momentum J of the black hole (or its spin $a = J/M$) [65]. (A third parameter, the charge Q of a black hole, is less astrophysically significant.) In other words, the Kerr metric is *the metric* that describes isolated, rotating black holes in general relativity. Perturbations to a Kerr black hole (or "hair" added to the black hole), therefore, correspond to quasinormal excitations that dissipate to the surrounding spacetime as the the black hole "rings down" back to its stationary (Kerr) state. Moreover, the frequencies of the quasinormal modes are dictated only by the properties of the black hole and the particular angular harmonic numbers of the perturbation.

The quasinormal ringing of black holes was originally investigated by Vishveshwara [230] by 'pinging' Schwarzschild black holes with Gaussian wave packets through numerical simulations. Today this ringing appears as a characteristic feature of the gravitational wave signals produced by stellar-mass compact-object binaries (and seen by LIGO and Virgo) due to the quasinormal ringdown of the merged system as it settles into a newly-formed, single black hole. Because the QNM frequencies only depend on a black hole's mass and angular momentum, identifying this quasinormal ringing in gravitational waveforms is an important tool for parameter estimation.

Black hole QNMs are defined by the eigenfrequencies ω_{QNM} of a field Ψ_s that perturbs the black hole. These eigenfrequencies satisfy the boundary conditions of downgoing waves at the horizon and outgoing waves at infinity [49],

$$\Psi_s(r_* \to -\infty) \sim e^{-i\omega_{\mathrm{QNM}}(t+r_*)}, \qquad \Psi_s(r_* \to \infty) \sim e^{-i\omega_{\mathrm{QNM}}(t-r_*)}, \tag{7.1}$$

where ω_{QNM} will be complex. Here s is the spin-weight of the field that excites the black hole's QNMs. For Kerr black holes, Ψ_s is governed by the Teukolsky equation, as described in Secs. 4.4.3 and 4.4.4. Alternatively, QNM frequencies are given by the poles of the retarded Green's function that defines the behavior of the perturbing field [49, 67].

A black hole has an infinite QNM spectrum. Furthermore, for Kerr black holes, the QNM spectrum exhibits Zeeman-like splitting that arises from the breaking of spherical symmetry by the black hole's rotation

[49]. The QNM spectrum of a Kerr black hole is labeled by three principal mode numbers: the overtone p, the spheroidal harmonic index $\hat{l}$, and the azimuthal index m, i.e., $\omega_{\text{QNM}} = \omega_{p\hat{l}m}$. The $\hat{l}$ and m mode numbers refer to the angular dependence of the perturbation. (In Kerr spacetime, the QNM frequencies are intimately tied to the spheroidal harmonics and their angular eigenvalues [148, 49].) For a given $\hat{l}$ and m, the $p = 0$ (or fundamental) frequency (i.e, $\omega_{0\hat{l}m}$) is always found to be the least damped QNM frequency and typically the easiest to excite and observe, while the higher overtones ($p > 0$) are subdominant. However, for near-extremal Kerr black holes ($M - a \ll M$), several excited overtones can "stack together" to create unique frequency responses [197]. Another unique feature of Kerr QNMs is that their decay rates (imaginary components of the QNM frequencies) are tied to the normalized spin of the black hole a/M. As the spin increases, the decay rate decreases. Thus perturbations for more rapidly-spinning black holes will dissipate more slowly. This leads to "zero-damping modes" (purely real QNM frequencies) in the extremal limit [246, 248].

Section 7.3: Scalar self-force for highly-eccentric orbits around rapidly-rotating black holes

Thornburg and Wardell [212, 213, 215, 214] were the first to demonstrate that for highly-eccentric orbits ($e \gtrsim 0.7$) about rapidly-rotating black holes ($a/M \gtrsim 0.8$) interesting "wiggles" arise in the SSF. They further showed that these high-frequency oscillations were attributable to the excitation of a QNM, the least-damped $\hat{l} = m = 1$ mode, produced by periastron passage of the scalar-charged small body. Thornburg and Wardell observed these excitations for a number of orbital configurations. The most pronounced excitations were present in orbits with $e \geq 0.9$, though weak oscillations arise for the orbit $(a/M, p, e, x_{\text{inc}}) = (0.8, 8, 0.8, 1)$ (see Fig. 16 in Ref. [214]).

Thornburg and Wardell utilize a time-domain code, which can be well-suited for computing highly-eccentric orbits. However, time-domain codes involve solving partial differential equations and have potential numerical issues with initial-value transients, boundary conditions, and source modeling. Our code works in the frequency domain, where the numerical problem involves solving ordinary differential equations for large numbers of Fourier-harmonic modes. In general it is easier to attain higher accuracy with a frequency-domain code. However, a countering factor is that the required number of modes and computational demand in a frequency-domain code grows rapidly at high eccentricities. Accordingly, we have so far restricted ourselves to orbits with $e \leq 0.8$. On the positive side, a frequency-domain code only captures periodic behavior and is not subject to initial-value transients. Given the many differences between the two approaches, a comparison between results seemed desirable.

Having said that, we have not made an exact comparison. We have so far not tried to make a very time-

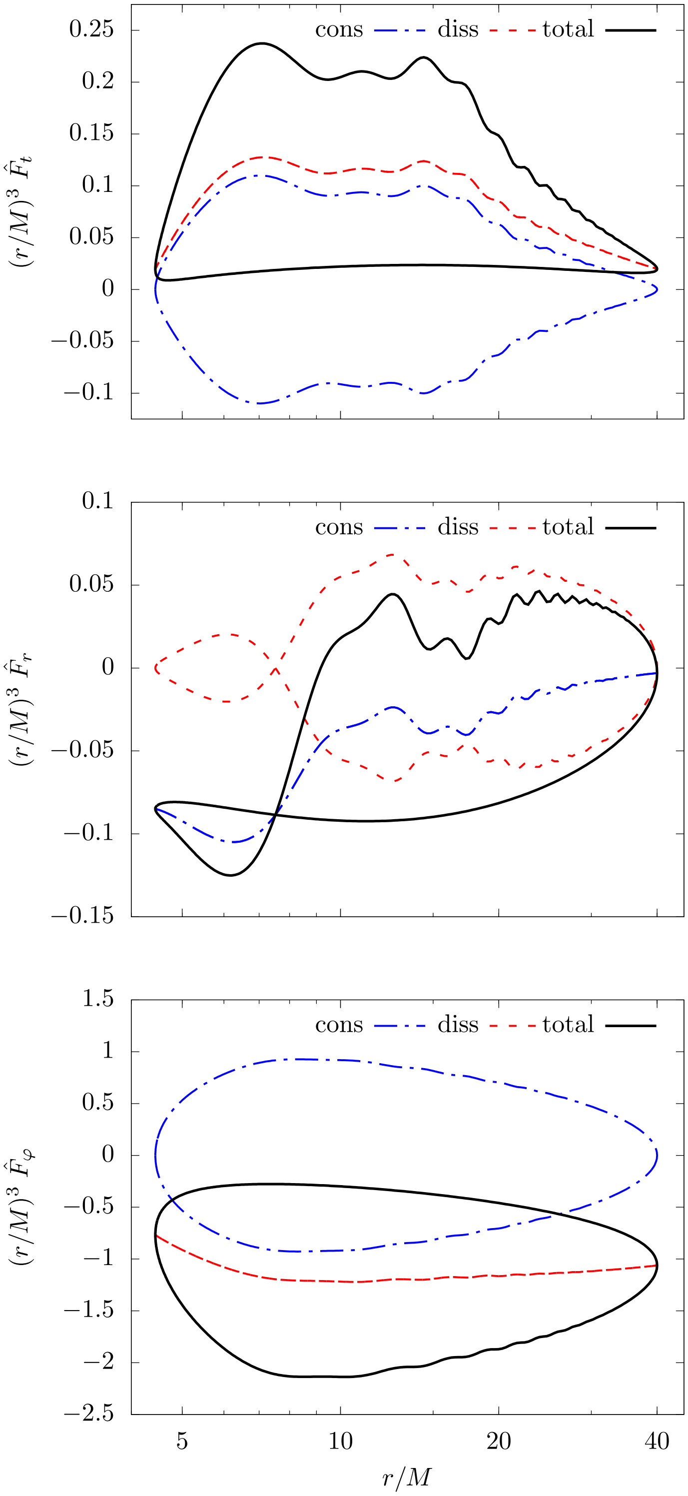

Figure 7.1: The three non-zero components of the scalar self-force for a particle orbiting in a Kerr background with orbital parameters $(a/M, p, e, x_{\text{inc}}) = (0.99, 8, 0.8, 1)$. The red (dashed) lines refer to the dissipative pieces of the self-force components, while the blue (dot-dashed) lines refer to the conservative pieces. The black (solid) lines represent the total values for each respective self-force component.

consuming calculation with $e = 0.9$ to duplicate one of the results in Ref. [214]. At the same time, rather than replicating the $e = 0.8$ results of Thornburg and Wardell, with $a/M = 0.8$, we decided to calculate the SSF and fluxes for the same orbital parameters but with a higher black hole spin: $(a/M, p, e, x_{\mathrm{inc}}) = (0.99, 8, 0.8, 1)$. The expectation was that we might see more pronounced ringing in the $e = 0.8$ orbit if the QNM damping is lessened with a higher a/M.

We also chose to model an orbit in the equatorial plane, which substantially offsets the computational cost of high-eccentricity orbits by restricting the mode spectrum $\omega_{m0n} = m\Omega_\varphi + n\Omega_r$ to be bi-periodic and not tri-periodic. Additionally, higher-order regularization parameters are known for equatorial orbits [122] and we were able to circumvent the fitting schemes discussed in Sec. 5.3.5 in this case, improving convergence and reducing the estimated error.

Our frequency-domain SSF results for this model are plotted in Fig. 7.1. The closed loops in the force components are split out into conservative part, dissipative part, and total. We see the same oscillatory features in our self-force results as Thornburg and Wardell found, with the oscillations most prominent in the t and r self-force components. After the point charge's periastron approach ($r \simeq 4.4M$), the ringing in the scalar field sweeps past the small body driving oscillations in the self-force, with the oscillations then decaying as the system approaches apastron. As expected, by increasing the black hole spin, we observe a more persistent ringing compared to that seen in the Thornburg and Wardell $e = 0.8$ model. Note that in the plots the SSF is weighted by the cube of the radial position of the particle. This compensates for the leading $1/r^3$ behavior of the SSF, accentuating the presence of QNM excitations even as the charge approaches apastron.

Section 7.4: Quasinormal bursts in the waveforms of extreme-mass-ratio inspirals

As we mentioned at the beginning of the chapter, we decided to look at the waveform in this model to see if the excitations were present in the asymptotic field. The left panel of Fig. 7.2 shows the asymptotic waveform over a period of two radial librations at several observer angles. The waveform appears devoid of ringing for all three observer angles: $(\theta_{\mathrm{obs}}, \varphi_{\mathrm{obs}}) = (\pi/2, 0)$, $(\theta_{\mathrm{obs}}, \varphi_{\mathrm{obs}}) = (\pi/4, 0)$, and $(\theta_{\mathrm{obs}}, \varphi_{\mathrm{obs}}) = (0, 0)$. However, by high-pass filtering or otherwise enhancing high frequencies in the signal, we can make the low-level QNBs evident. One particular way of enhancing high frequencies is shown in the right panel of Fig. 7.2 where the log (base 10) of the absolute value of the second time derivative of the waveform measured by the observer at $(\theta_{\mathrm{obs}}, \varphi_{\mathrm{obs}}) = (\pi/2, 0)$ is plotted. (Computing the second derivative is reminiscent of some numerical relativity codes where, to extract gravitational radiation, ψ_4 is first obtained, from which the waveforms are derived by integrating twice or by Fourier processing, as given by Eq. (4.121).) Now the

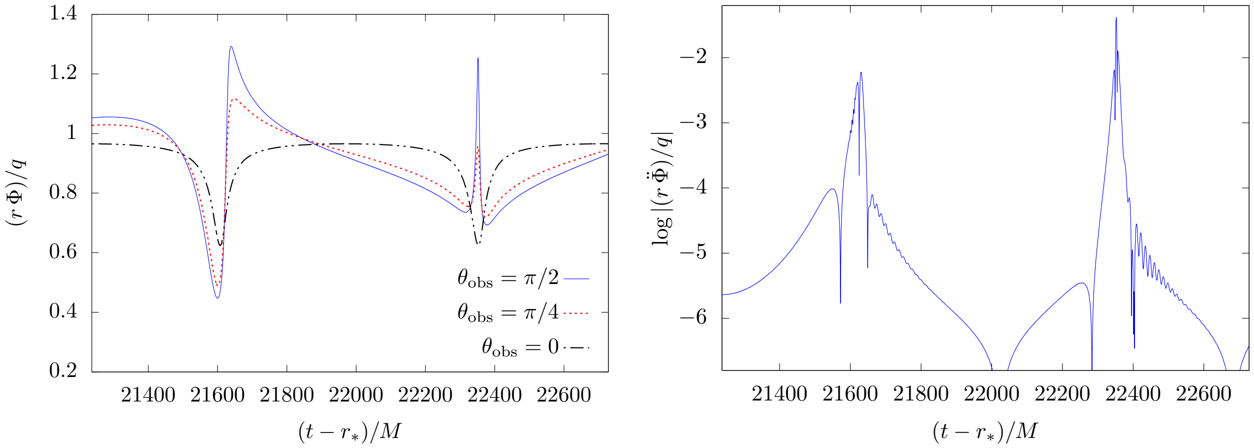

Figure 7.2: The left panel depicts the asymptotic waveform $r\Phi/q$ visible to observers at several polar angles: $\theta_{\rm obs} = \pi/2$ (blue solid line), $\theta_{\rm obs} = \pi/4$ (red dashed line), $\theta_{\rm obs} = 0$ (black dot dashed line). The plot window covers two radial librations. Computed from an eccentric equatorial orbit (with associated apsidal advance), the waveform is bi-periodic. Sharp transitions roughly correspond to the retarded time of successive periastron passages. The right panel plots the log (base 10) of the absolute value of the second time derivative of the waveform in Fig. 7.2 (for the observer at $\theta_{\rm obs} = \pi/2$). The second time derivative enhances higher frequencies, making the faint QNBs visible in the aftermath of each periastron passage.

QNBs are revealed, superimposed on the lower frequency waveform components. Similar excitation is visible to an observer at $(\theta_{\rm obs}, \varphi_{\rm obs}) = (\pi/4, 0)$, but the QNBs are not present for an observer at position $\theta_{\rm obs} = 0$ (i.e., along the polar axis). As we show below, this is consistent with the ringing being due to (prograde) axial $\hat{l} = m$ perturbations of the field in the Kerr geometry.

Rather than emphasizing high frequencies by taking time derivatives of the signal, one can instead apply a high-pass filter to attenuate the lower frequency "background." We construct a high-pass Butterworth filter using *Mathematica*'s `ButterworthFilterModel`, `ToDiscreteTimeModel`, and `RecurrenceFilter`. We choose the filter's parameters by inspecting the power spectrum of the waveform.

After applying the high-pass filter and observing the presence of QNBs, we attempted to extract a complex frequency $\omega = \omega' + i\omega''$ for the excitation by (1) selecting a time window during which the excitation dominates the filtered signal and (2) then performing a least-squares fit of a burst template to the filtered data, as demonstrated in Fig. 7.3. The data was fitted to a real function of the form $Ae^{+\omega'' t}\sin\omega'(t+t_0)$ using MATHEMATICA's `FindFit`. Fitted complex frequencies have negative imaginary parts ($\omega'' < 0$), consistent with damped bursts. The data in Fig. 7.3 was found to be best fit by the complex frequency $\omega_{\rm fit} = 0.4937 - 0.0367i$ (in units with $M = 1$; henceforth assumed in this section).

We can compare this value to the spectrum of known QNM frequencies ω_{plm} due to scalar perturbations of Kerr spacetimes published by Berti [49]. The QNMs depend on a and are indexed by the spheroidal harmonic mode numbers $(\hat{l}, m)$ and the overtone p. Assuming $M = 1$ but without assuming a value for a, we find that the extracted complex frequency $\omega_{\rm fit}$ above most closely matches the QNM frequency $\omega_{011} = 0.4933 - 0.0368i$

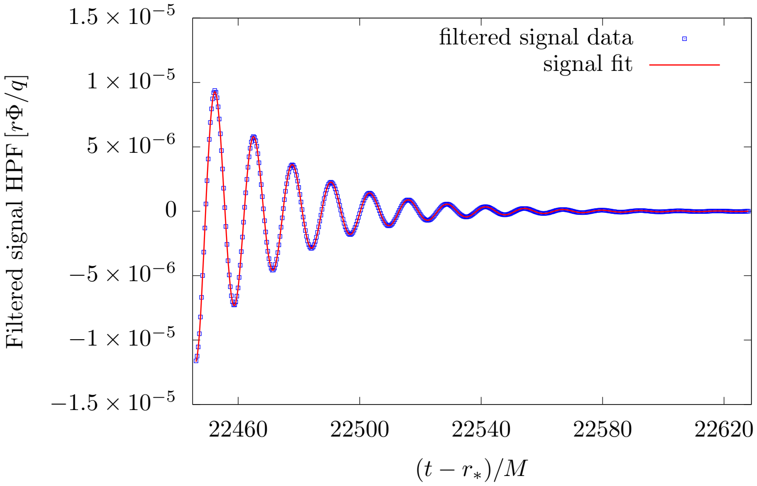

Figure 7.3: Plot of a segment of the scalar field signal presented in Fig. 7.2 after applying a high-pass filter (blue squares), along with a least-squares fit of the filtered signal (red line) to a model template. The high-pass filter and fit were constructed as outlined in Sec. 7.4. The data are best fit by a decaying sinusoid with a complex frequency of $M\omega = 0.4933 - 0.0368i$.

for a spin of $a = 0.9899$. In other words, by assuming that this complex frequency should be represented by a QNM, the extracted frequency accurately recovers the spin of the primary black hole to three digits. This result is consistent with those presented by Thornburg [212, 213, 215], who found that, across several orbital configurations and spin parameters, the QNM frequencies in his self-force data were best fit by the least-damped (smallest $|\omega''|$) $\hat{l} = m = 1$ QNMs.

Surprisingly perhaps, our frequency domain numerical results actually allow us to extract additional QNMs. To do so, we obtain the residuals between the high-frequency signal and its fit in Fig. 7.3 and apply the high-pass filter a second time to remove a remaining background (i.e., "flat-fielding" the signal). We fit and obtain the complex frequency of a second damped oscillation. By iterating this process, we managed to extract three additional QNM excitations in the filtered waveform. These are shown in Fig. 7.4. The numerical values of the frequencies of all extracted QNMs are presented in Table 7.1 and compared to the closest published QNMs for scalar perturbations of a Kerr spacetime with $a = 0.99$.

However, we can instead try to remain agnostic to the black hole spin and mode numbers and compare the extracted frequencies to all known QNM frequencies across Berti's densely sampled set of Kerr spacetimes. Consulting Table 7.1, our second extracted frequency best fits a QNM in Berti's table with frequency $\omega_{022} = 0.9269 - 0.0314i$ for $a = 0.9897$. Our third extracted frequency best fits one with $\omega_{033} = 1.3680 - 0.0304i$ for $a = 0.9899$ and the fourth best fits Berti's mode $\omega_{044} = 1.8084 - 0.0304i$ for $a = 0.9897$. By simply looking for the best fit to known QNMs, we obtain multiple estimates of the black hole spin parameter. Multiple parameter estimates all yield values for the black hole spin that are surprisingly close to $a = 0.99$ (with approximately three digits of agreement). If QNBs can be observed in highly-eccentric EMRIs, it

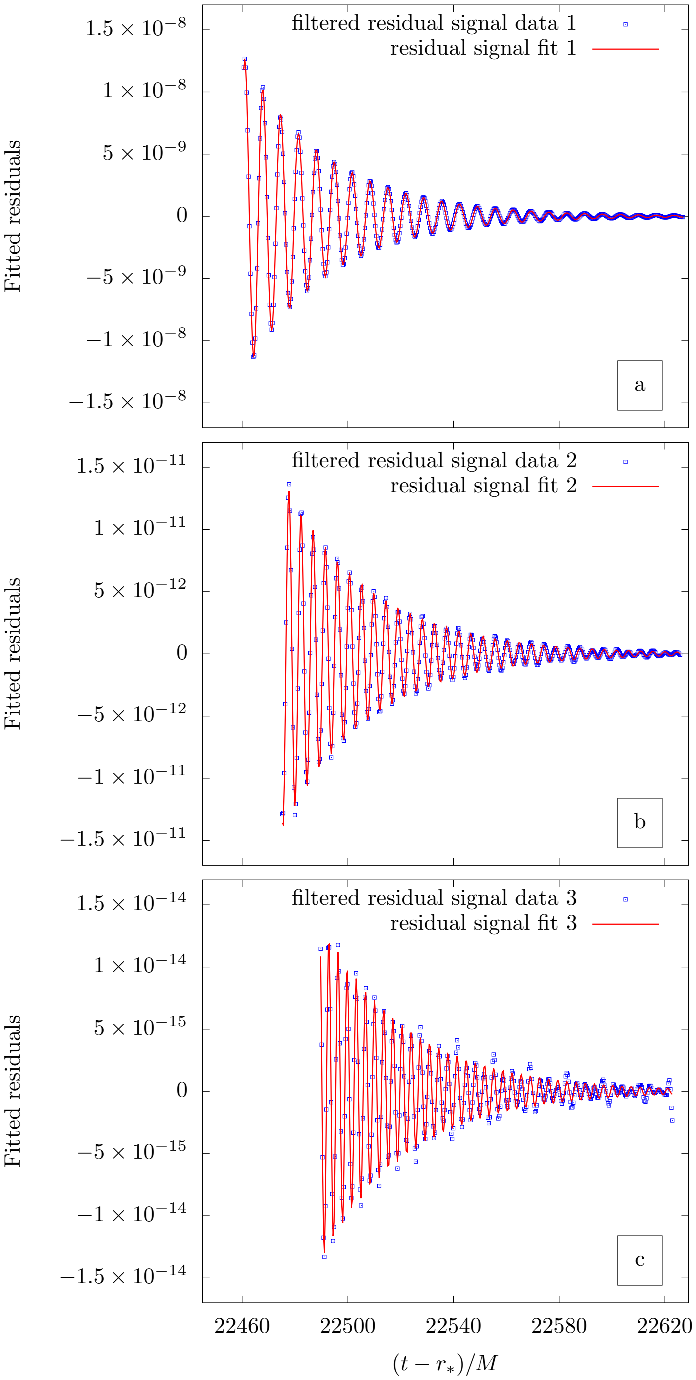

Figure 7.4: Short window on the waveform showing successive sets of residuals (blue squares) after subtracting successively determined modes via fitting. Also shown are the least-squares determined fits of the residual signal data (red lines) at each stage in the subtraction. The top plot (a) depicts the residual signal from subtracting the fit in Fig. 7.3 from the waveform and high-pass filtering a second time. The residuals in the top panel are then fit by a damped sinusoid with $M\omega = 0.9277 - 0.0314i$. The middle panel (b) depicts the residuals after subtracting the first two QNMs and high-pass filtering. The result is fit by a mode with $M\omega = 1.3682 - 0.0304i$. The bottom panel (c) shows residuals after subtracting the first three determined QNMs and filtering, yielding a final mode with $M\omega = 1.8115 - 0.0304i$. We found it necessary to slightly shift forward the time window after each fit.

Figure	p	l	m	Extracted QNM	Known QNM
Fig. 7.3	0	1	1	$0.4933 - 0.0368i$	$0.4934 - 0.0367i$
Fig. 7.4a	0	2	2	$0.9277 - 0.0314i$	$0.9280 - 0.0311i$
Fig. 7.4b	0	3	3	$1.3682 - 0.0304i$	$1.3686 - 0.0302i$
Fig. 7.4c	0	4	4	$1.8115 - 0.0304i$	$1.8111 - 0.0300i$

Table 7.1: A comparison of the QNM frequencies extracted from filtering and fitting the waveform, as shown in Figs. 7.3 and 7.4, and the QNM frequencies calculated by Berti for scalar perturbations of Kerr spacetime with spin parameter $a/M = 0.99$ [49]. The value of a is based on the spin parameter chosen for this highly-eccentric SSF investigation.

may well be possible to get repeated snapshot determinations of the mass and spin of the primary black hole. Furthermore, while the "orbital parts" of the EMRI waveform will evolve and move through the LISA passband, the frequencies of the QNB component of the waveform will remain invariant, as these depend upon the (essentially unchanging) primary mass and spin.

Section 7.5: Observational implications

By reproducing Thornburg and Wardell's "wiggles," we affirm that these are integral components of the SSF. The finding of related QNBs in the scalar waveform suggests the strong likelihood that QNBs exist in the gravitational waveforms of (some) EMRIs. A gauge invariant signal of this type, from repeatedly "tickling" the primary black hole, might have important observational consequences in sufficiently high signal-to-noise ratio EMRIs. These bursts are faint and might be fainter still in the gravitational case where $\hat{l} = m = 2$ will be the first mode excited. On the other hand, we have not yet conducted a thorough parameter survey to find where the excitation is maximized. Furthermore, it is entirely possible that even faint QNBs might be detected and measured using template matching. QNBs in EMRIs provide the exciting possibility of measuring black hole properties by repeatedly "tickling the dragon's tail," as opposed to settling for the single final excitation of quasinormal modes seen in LIGO/Virgo mergers. Finally, QNBs might reveal the presence of EMRIs in systems with heavy $M \gtrsim 10^7 M_\odot$ primaries, where the usual, low-frequency parts of the signal would be difficult to detect but the periodic, higher-frequency QNBs would lie in LISA's area of best sensitivity. Ultimately, the presence of QNBs in EMRI waveforms has sparked a flurry of research, with its presence in gravitational waveforms just recently being confirmed [216]. The QNB response for near-extremal black holes is also revealing new insights into the cumulative behavior of superimposed quasinormal frequency overtones [197]. QNBs, therefore, are another tool for exploring the rich physical features of Kerr black holes and EMRIs with Kerr primaries.

CHAPTER 8: Scalar self-force for resonant motion in Kerr spacetime

Section 8.1: Chapter overview

In this chapter, I use my SSF code to explore another important class of physical phenomena in EMRIs: *transient orbital $r\theta$-resonances.* An orbital resonance occurs when two frequencies of orbital motion, ω_1 and ω_2, form a rational ratio, i.e., $\omega_2/\omega_1 = \beta_2/\beta_1$ with $\beta_1, \beta_2 \in \mathbb{Z}$. The smaller the relatively prime integers, β_1 and β_2, the stronger the resonance. In the solar system, orbital resonances occur among satellites sharing the same primary, such as the 2:3 ($\beta_1 = 2$ and $\beta_2 = 3$) resonance of the solar satellites Neptune and Pluto and the 1:2 ($\beta_1 = 1$ and $\beta_2 = 2$) resonance of the Galilean satellites Io and Europa. Resonances can also occur between orbital periods and periods of rotation, like the 3:2 spin-orbit resonance of Mercury.

For an EMRI with a Kerr primary, a resonance can form between any of the three orbital frequencies, Ω_r, Ω_θ, and Ω_φ. Previous authors have studied the effects of $r\varphi$- [221] and $\theta\varphi$-resonances [126]. These resonances can lead to the anisotropic radiation of gravitational waves, resulting in resonant 'kicks' to the velocity of the EMRI's center of mass. Such effects are expected to contribute to an EMRI's phase evolution and waveform at $O(\epsilon)$ and, therefore, are presumably safe to neglect [221]. On the other hand, during $r\theta$-resonances, an EMRI can instead experience 'kicks' to the energy and angular momentum radiated away by gravitational waves and to the evolution of the Carter constant [100, 101, 48]. Not only can these resonant kicks significantly alter the inspiral of the EMRI, but they are particularly difficult to incorporate in certain evolutionary models. It may also be possible for an EMRI to be caught in an $r\theta$-resonance, which would lead to a dramatic change in the EMRI's dynamics. Recent analysis by van de Meent [220] suggests that the conditions required for achieving these *sustained resonances* are fairly stringent (if even possible), making it unlikely that LISA will measure an astrophysical EMRI that is trapped in a sustained resonant state. Investigating such effects requires calculation of the gravitational self-force during resonances, which has not yet been performed.

On the other hand, almost all EMRIs are expected to pass through at least one *transient* $r\theta$-resonance, as they evolve in the LISA passband [200]. Transient resonances, unlike sustained resonances, persist for a resonant period $T_{\text{res}} \sim M\epsilon^{-1/2}$ [100]. This leads to an $O(\epsilon^{-1/2})$ shift in the cumulative phase evolution of the system, as expressed in Eq. (1.17). Flanagan and Hinderer [100] provided the first evidence of resonant kicks to an EMRI's orbital evolution using weak-field post-Newtonian approximations of the gravitational self-force. Berry, Cole, Cañizares, and Gair [48] then used this same model to demonstrate how unmodeled resonances may impact LISA's ability to detect EMRI signals. They found that resonances should not significantly decrease LISA detection rates of EMRIs with low spins and eccentricities, though resonances will likely hamper accurate parameter estimation for observed EMRI gravitational wave sources [48]. The impact of resonances on the detection of EMRIs with higher spins and eccentricities is still unknown. Flanagan, Hughes, and Ruangsri [101] provided some of the first strong-field results for EMRI $r\theta$-resonances, demonstrating how gravitational fluxes vary with the orbital phase at which an EMRI enters resonance. Hughes and Ruangsri [200] followed-up on this work, driving evolutions using flux results and finding that nearly all EMRIs will encounter either a 1:3, 1:2, or 2:3 $r\theta$-resonance as they emit gravitational wave signals in the LISA passband. Due to the computational demand of calculating the local strong-field gravitational self-force in Kerr spacetime, self-force effects have not yet been calculated for EMRIs as they encounter $r\theta$-resonances. As a first step in exploring the local radiation-reaction effects driven by $r\theta$-resonances, I use my scalar code to calculate the SSF experienced by scalar-charged particles on $r\theta$-resonant geodesics.

Section 8.2: Impact of resonances on radiation-reaction

As discussed in Sec. 2.5, $r\theta$-resonant geodesics have two distinguishing features: their radial and polar frequencies are commensurate and they are sensitive to initial conditions. Due to these unique characteristics, EMRI inspirals that encounter strong $r\theta$-resonances will significantly differ from inspirals that do not. To further understand this impact, consider the radiated energy flux and its relation to the self-force

$$\langle \dot{E} \rangle^{\mathrm{tot}} = \frac{1}{\Gamma} \int_0^{2\pi} \frac{dq_r}{2\pi} \int_0^{2\pi} \frac{dq_\theta}{2\pi}\, \Sigma F_t^{\mathrm{GSF},1}. \tag{8.1}$$

As described in Sec. 5.3.4, the self-force is only a function of the radial and polar motions of the source. Therefore, the integrand of Eq. (8.1), $\dot{E} \equiv \Sigma F_t^{\mathrm{GSF}} \Gamma^{-1}$, can be represented by a double Fourier series,

$$\dot{E} = \sum_{kn} \dot{E}_{kn} e^{-iq_{kn}}, \tag{8.2}$$

where the exponential phase is defined in terms of the angle variables, $q_{kn} \equiv kq_\theta + nq_r$, and the angle variables depend on the orbital frequencies Υ_r and Υ_θ, i.e., $q_{r,\theta} = \Upsilon_{r,\theta}\lambda$. For most of this work, I have approximated the source motion as a geodesic and ignored changes to the motion due to the self-force. Thus, the frequencies Υ_r and Υ_θ have been treated as constants. As the EMRI evolves, however, the backreaction of the self-force will not only lead to the orbital 'constants' evolving, but the orbital frequencies will evolve, as well. To capture this evolution, consider an arbitrary point in Mino time, λ_0. On orbital timescales ($T_{\mathrm{orb}} \sim M$), the trajectory of the small compact object is tangent to a geodesic with frequencies Υ_r^0 and Υ_θ^0. The phase in Eq. (8.2) then takes the expanded form

$$q_{kn}(\lambda) \simeq q_{kn}^0 + \left(k\Upsilon_\theta^0 + n\Upsilon_\theta^0\right)(\lambda - \lambda_0) + \left(k\Upsilon_\theta'(0) + n\Upsilon_r'(0)\right)(\lambda - \lambda_0)^2 + O(\Delta\lambda^3), \tag{8.3}$$

where q_{kn}^0 is the initial phase at $\lambda = \lambda_0$ and $\Upsilon_r' \equiv d\Upsilon_r/d\lambda$. Because the evolution of the frequencies is sourced by the self-force, their Mino time derivatives go like $\Upsilon_r' \sim M^2\epsilon$. Away from resonances the first term in Eq. (8.3) dominates, provided $M(\lambda - \lambda_0) \lesssim \epsilon^{-1}$. Phases with mode numbers $k, n \neq 0$ rapidly oscillate, and these modes average away. Thus, the leading-order motion is set by the single zero-frequency mode, i.e., the fluxes ($\langle \dot{E} \rangle^{\text{tot}} = \dot{E}_{00}$). On the radiation-reaction timescale ($T_{\text{rr}} \sim M\epsilon^{-1}$), the expansion breaks down as the frequencies substantially shift away from Υ_r^0 and Υ_θ^0. The EMRI is no longer well approximated by the original geodesic due to its adiabatic evolution. This accounts for the first term in Eq. (1.17).

On the other hand, if the EMRI enters a resonance at $\lambda = \lambda_0$, the first term in Eq. (8.3) will vanish for certain k, n when $k\beta_\theta + n\beta_r = 0$. Because the second term is $O(\epsilon)$, these modes will oscillate slowly and form nearly stationary phases. These modes will also contribute to the leading-order dynamics, e.g.,

$$\langle \dot{E} \rangle^{\text{tot}} = \sum_{(k,n)_{N=0}} \dot{E}_{kn} e^{i q_{kn}^0}, \tag{8.4}$$

where $(k, n)_N$ represents all k and n values that satisfy the relation $k\beta_\theta + n\beta_r = N$, including $n = k = 0$.[1] As $M(\lambda - \lambda_0) \to \epsilon^{1/2}$, the expansion breaks down. The frequencies no longer remain commensurate, the EMRI leaves the resonance, and the phases shift away from these stationary states so that, once again, only the $k = n = 0$ mode contributes at leading order. This sets the timescale of the resonance, $T_{\text{res}} \sim M\epsilon^{-1/2}$, which accounts for the second term in Eq. (1.17).

An important consequence of Eq. (8.4) is that the presence of the higher modes results in fluxes that are sensitive to the initial phase of the EMRI as it enters resonance. This is problematic for EMRI models. An error in this phase will consequently lead to an error in the fluxes. Neglecting the phases may only lead to a flux error $\varepsilon_{\text{flux}}$ of $O(\epsilon)$, but this error will accumulate over the course of the resonance so that it grows to $\varepsilon_{\text{res}} \sim \varepsilon_{\text{flux}} T_{\text{res}} \sim \epsilon^{1/2}$. As the EMRI leaves resonance, this error will continue to propagate through the rest of the EMRI inspiral, leading to a final error in the waveform $\varepsilon_{\text{waveform}} \sim \varepsilon_{\text{res}} T_{\text{rr}} \sim \epsilon^{-1/2}$. If the EMRI passes through another strong resonance, this error could be magnified by another factor of $\epsilon^{-1/2}$. Thus, it is particularly important to understand the behavior of the local self-force and global fluxes as an EMRI

---

[1] For smaller integer-values of β_r and β_θ, lower, more dominant modes will contribute to the leading-order evolution. As β_r and β_θ increase, only higher, less dominant modes will contribute, leading to a weaker effect. This is why low-integer ratios are referred to as strong resonances, and higher ratios as weak resonances.

approaches and transitions through a resonance.

A key difference between the resonant and non-resonant SSF problems is that in the case of resonances one must take into account the initial conditions of the source, as discussed in Sec. 2.5. While most resonances cannot be mapped to a fiducial geodesic (Eqs. (2.34)-(2.37)), they can be mapped to geodesics that are parameterized by Mino time and the resonant offset λ_0 (Eqs. (2.51)-(2.54)). As a result, for resonant sources, the SSF is naturally parameterized by the resonant angle variables $\bar{q}$ and $\bar{q}_0$ (see Sec. 2.6.1). In the following sections, I outline various methods for constructing the SSF during $r\theta$-resonances.

8.2.1: Scalar field for resonant sources

Once again I consider a point particle with scalar charge q orbiting a Kerr MBH. In the previous chapters, I assumed that the charge followed a fiducial geodesic $\hat{x}_p^\mu$ (Eqs. (2.34)-(2.37)). Now I consider the case where the charge follows a resonant geodesic. Therefore, I use $\bar{x}_p^\mu(\bar{q}_0)$, defined by Eqs. (2.51)-(2.54), as the wordline of the scalar source. I leave the initial phase $\bar{q}_0$ as a free-parameter. The charge's scalar field can be constructed using the same methods outlined in Chapter 5,

$$\Phi^{\pm}(t,r,\theta,\varphi) = \frac{q}{\varpi}\sum_{l\hat{l}mkn} C^{\pm}_{\hat{l}mkn} X^{\pm}_{\hat{l}mkn}(r) S_{\hat{l}mkn}(\theta) e^{im\varphi} e^{-i\omega_{mkn}t}, \tag{8.5}$$

$$= \frac{q}{\varpi}\sum_{l\hat{l}mkn} b^{\hat{l}}_{lmkn} C^{\pm}_{\hat{l}mkn} X^{\pm}_{\hat{l}mkn}(r) Y_{lm}(\theta,\varphi) e^{-i\omega_{mkn}t}, \tag{8.6}$$

Alternatively, one can use the reduced frequency spectrum $\omega_{mN} = m\Omega_\varphi + N\Omega$ (see Sec. 2.5) to decrease the number of modes that contribute to the mode-summed field,

$$\Phi^{\pm}(t,r,\theta,\varphi) = \frac{q}{\varpi}\sum_{l\hat{l}mN} \bar{C}^{\pm}_{\hat{l}mN} X^{\pm}_{\hat{l}mN}(r) S_{\hat{l}mN}(\theta) e^{im\varphi} e^{-i\omega_{mN}t}, \tag{8.7}$$

$$= \frac{q}{\varpi}\sum_{l\hat{l}mN} b^{\hat{l}}_{lmN} \bar{C}^{\pm}_{\hat{l}mN} X^{\pm}_{\hat{l}mN}(r) Y_{lm}(\theta,\varphi) e^{-i\omega_{mN}t}. \tag{8.8}$$

The mode functions $X^{\pm}_{\hat{l}mN}$ and $S_{\hat{l}mN}$ satisfy the same differential equations as $X^{\pm}_{\hat{l}mkn}$ and $S_{\hat{l}mkn}$, Eq. (5.23) and (5.24), but with the frequencies replaced by ω_{mN} rather than ω_{mkn}. As a result, most of the mode functions and constants are equivalent to their $\hat{l}mkn$-mode counterparts, $\omega_{mN} = \omega_{m(k,n)_N}$, $b^{\hat{l}}_{lmN} = b^{\hat{l}}_{lm(k,n)_N}$, $X^{\pm}_{\hat{l}mN} = X^{\pm}_{\hat{l}m(k,n)_N}$, and $S_{\hat{l}mN} = S_{\hat{l}m(k,n)_N}$.

The resonant normalization coefficients $\bar{C}^{\pm}_{\hat{l}mN}$ are the exception. They are defined by the integrals

$$\bar{C}^{\pm}_{\hat{l}mN} = \int_{r_{\min}}^{r_{\max}} \frac{\varpi^2 X^{h,\mp}_{\hat{l}mN}(r) \bar{Z}_{\hat{l}mN}(r)}{W_{\hat{l}mN}\Delta} dr, \tag{8.9}$$

where $\bar{Z}_{\hat{l}mN}$ is the radial decomposition of the resonant source in the frequency domain

$$\rho_{\text{scalar}} = -\frac{q\varpi^3}{4\pi\Sigma\Delta}\sum_{\hat{l}mN} \bar{Z}_{\hat{l}mN}(r) S_{\hat{l}mN}(\theta) e^{im\varphi} e^{-i\omega_{mN}t}, \tag{8.10}$$

and $W_{\hat{l}mN}$ is the Wronskian, defined similarly to Eq. (5.33). The radial dependence $\bar{Z}_{\hat{l}mN}$ of the resonant source, unlike $Z_{\hat{l}mkn}$ in Eqs. (5.27) and (5.123), is naturally parameterized in terms of the resonant angle variable $\bar{q}$ and the controllable phase parameter $\bar{q}_0$. Therefore it can be constructed from the single integral

$$\bar{Z}_{\hat{l}mN}(r;\bar{q}_0) = \frac{1}{2\pi}\int_0^{2\pi} d\bar{q}\, e^{iN\bar{q}} \bar{B}_{mN}(\bar{q},\bar{q}_0) S_{\hat{l}mN}(\bar{\theta}_p)\delta(r-\bar{r}_p), \tag{8.11}$$

where

$$\bar{B}_{mN}(\bar{q};\bar{q}_0) \equiv -\frac{4\pi}{\Gamma}\frac{\bar{\Sigma}_p\bar{\Delta}_p}{\bar{\varpi}_p^3} e^{i\omega_{mN}\Delta\bar{t}} e^{-im\Delta\bar{\varphi}}. \tag{8.12}$$

Recall from Secs. 2.5 and 2.6.1 that the resonant geodesic functions $\Delta\bar{t}$, $\bar{r}_p$, $\bar{\theta}_p$, and $\Delta\bar{\varphi}$ are understood to be functions of $\bar{q}$ and the parameter $\bar{q}_0$, i.e.,

$$\Delta\bar{t} \equiv \Delta\hat{t}^{(r)}(\bar{q}) + \Delta\hat{t}^{(\theta)}(\bar{q}+\bar{q}_0) - \Delta\hat{t}^{(\theta)}(\bar{q}_0), \tag{8.13}$$

$$\bar{r}_p \equiv \hat{r}_p(\bar{q}), \tag{8.14}$$

$$\bar{\theta}_p \equiv \hat{\theta}_p(\bar{q}+\bar{q}_0). \tag{8.15}$$

$$\Delta\bar{\varphi} \equiv \Delta\hat{\varphi}^{(r)}(\bar{q}) + \Delta\hat{\varphi}^{(\theta)}(\bar{q}+\bar{q}_0) - \Delta\hat{\varphi}^{(\theta)}(\bar{q}_0). \tag{8.16}$$

Using Eq. (8.11), Eq. (8.9) simplifies to

$$\bar{C}^{\pm}_{\hat{l}mN}(\bar{q}_0) = \frac{1}{2\pi}\int_0^{2\pi} d\bar{q}\, \bar{D}^{\pm}_{\hat{l}mN}(\bar{q},\bar{q}_0) e^{iN\bar{q}}, \tag{8.17}$$

where

$$\bar{D}^{\pm}_{\hat{l}mkn}(\bar{q};\bar{q}_0) \equiv -\frac{4\pi}{\Gamma} X^{h,\mp}_{\hat{l}mN}(\bar{r}_p) S_{\hat{l}mN}(\bar{\theta}_p)\frac{\bar{\Sigma}_p}{\bar{\varpi}_p W_{\hat{l}mN}} e^{i\omega_{mN}\Delta\bar{t}} e^{-im\Delta\bar{\varphi}}. \tag{8.18}$$

Equation (8.17), like Eq. (5.125) for $C^{\pm}_{\hat{l}mkn}$, is amenable to spectral integration,

$$\bar{q}_\jmath = \frac{2\pi\jmath}{N_{\text{res}}}, \qquad \jmath = 0, 1, \ldots, N_{\text{res}}-1 \tag{8.19}$$

$$\bar{C}^{\pm}_{\hat{l}mN}(\bar{q}_0) \simeq \frac{1}{N_{\text{res}}}\sum_{\jmath=0}^{N_{\text{res}}-1} \bar{D}^{\pm}_{\hat{l}mN}(\bar{q}_\jmath;\bar{q}_0) e^{iN\bar{q}_\jmath}, \tag{8.20}$$

One can also see that, much like $C^{\pm}_{\hat{l}mkn}$, $\bar{C}^{\pm}_{\hat{l}mN}$ depends on the initial conditions of the source. For non-resonant sources, I ignored this dependence and assumed fiducial initial conditions without loss of generality. This same assumption cannot be made for resonances. Consequently, I will express $\bar{C}_{\hat{l}mN}(\bar{q}_0)$ as an explicit function of the initial resonant phase parameter $\bar{q}_0$ from now on.

While $\bar{C}_{\hat{l}mN}(\bar{q}_0)$ and $C_{\hat{l}mkn}$ are not equivalent, they are related by a coherent sum over all of the modes that share the same frequency

$$\bar{C}^{\pm}_{\hat{l}mN}(\bar{q}_0) = \sum_{(k,n)_N} C^{\pm}_{\hat{l}mkn}(\bar{q}_0) = \sum_{(k,n)_N} e^{i\xi_{mkn}(0,0,\beta_\theta q_0,0)}\hat{C}^{\pm}_{\hat{l}mkn}, \tag{8.21}$$

as demonstrated in Appendix A of Ref. [101] and Sec. IIID of Ref. [117]. Recall that ξ_{mkn} is defined in Eq. (5.151). Combining all of these relations, one can see that Eqs. (8.5) and (8.7) are equivalent. This leads to two methods for calculating the SSF: one using the ω_{mN} spectrum and the other using ω_{mkn}. I present both methods in the following sections, outlining the advantages and disadvantages of both approaches.

8.2.2: Constructing the self-force on the reduced mode-sum basis

In the preceding chapters, I parameterized the SSF using the angle variables q_r and q_θ (Eq. (5.158)). For non-resonant sources, this parameterization allows one to map the infinite time evolution of the SSF to a finite domain, as discussed in Secs. 2.6.1 and 5.3.4. For resonant sources—which are periodic with respect to coordinate time but depend on initial conditions—I will make use of the resonant angle variable $\bar{q}$ and the relative phase parameter $\bar{q}_0$, which were introduced in Sec. 2.6.1. For an individual resonant source, $\bar{q}_0$ is constant and only $\bar{q}$ varies with time. By treating $\bar{q}_0$ as a free parameter, however, one can capture the dependence of the SSF on the initial conditions. Therefore, while resonant geodesics are singly periodic, they still have two degrees of freedom, just like non-resonant sources. To distinguish between these two parameterizations, the SSF constructed from fiducial geodesic functions is denoted by $\hat{F}_\alpha(q_r, q_\theta)$, while the SSF constructed from resonant geodesic functions is denoted by $\bar{F}^{\text{res}}_\alpha(\bar{q};\bar{q}_0)$. Other quantities that also depend on the resonant source will be symbolized with an overbar, e.g., $\bar{r}_p$ and $\bar{C}^{\pm}_{\hat{l}mN}(\bar{q}_0)$.

The retarded contribution to the resonant SSF, when parameterized in terms of the resonant angle variable and parameter, takes a similar form to Eq. (5.158),

$$\bar{F}^{\text{ret},l}_{\alpha\pm}(\bar{q},\bar{q}_0) = \sum_{m=-l}^{l} (\mathcal{D}^{lm}_\alpha \bar{\phi}^{\pm}_{lm})(\bar{q};\bar{q}_0)\bar{Y}_{lm}(\bar{q};\bar{q}_0), \tag{8.22}$$

where, like Eqs. (5.159) and (5.160),

$$\bar{Y}_{lm}(\bar{q};\bar{q}_0) \equiv Y_{lm}(\bar{\theta}_p(\bar{q}+\bar{q}_0),0)e^{im(\Delta\bar{\varphi}(\bar{q},\bar{q}+\bar{q}_0)-\Delta\bar{\varphi}(0,\bar{q}_0))}, \tag{8.23}$$

$$\bar{\phi}^{\pm}_{lm}(\bar{q};\bar{q}_0) \equiv \sum_{\hat{l}=|m|}^{+\infty} \sum_{N=-\infty}^{+\infty} \bar{\phi}^{\pm}_{l\hat{l}mN}(\bar{q};\bar{q}_0) e^{-i\omega_{mN}(\Delta\hat{t}(\bar{q},\bar{q}+\bar{q}_0)-\Delta\bar{t}(0,\bar{q}_0))} e^{-iN\bar{q}}, \tag{8.24}$$

$$\bar{\phi}^{\pm}_{l\hat{l}mN}(\bar{q};\bar{q}_0) \equiv \varpi_p^{-1}(\bar{q}) b^{l}_{\hat{l}mN} \bar{C}^{\pm}_{\hat{l}mN}(\bar{q}_0) X^{h,\pm}_{\hat{l}mN}(\bar{r}_p(\bar{q})). \tag{8.25}$$

Each resonant geodesic with a new value of $\bar{q}_0$ leads to a different source integral. Thus, a trade-off of using the reduced mode-spectrum is that one must repeatedly integrate over different resonant sources with different initial phases, $\bar{q}_0$.

In this approach, the regularized SSF is then obtained through mode-sum regularization

$$\bar{F}^{\mathrm{res}}_{\alpha}(\bar{q};\bar{q}_0) = \sum_{l=0}^{\infty} \left(\bar{F}^{\mathrm{ret},l}_{\alpha\pm}(\bar{q};\bar{q}_0) - \bar{F}^{\mathrm{S},l}_{\alpha\pm}(\bar{q};\bar{q}_0) \right), \tag{8.26}$$

where the singular contributions, $\bar{F}^{\mathrm{S},l}_{\alpha\pm}(\bar{q};\bar{q}_0)$, are constructed using the analytic regularization parameters and numerical fitting procedure presented in Sec. 5.3.5. However, the resonant SSF, $\bar{F}^{\mathrm{res}}_{\alpha}$, does not describe the SSF for just a single geodesic. Instead it describes an entire family of resonant geodesics that share the same orbital parameters, (p, e, x_{inc}), but different initial phases, $\bar{q}_0$. The behavior of the SSF along a single resonant orbit is found by choosing a particular value of $\bar{q}_0$ and then varying $\bar{q}$.

Much like the fiducial SSF, the resonant SSF is periodic with respect to $\bar{q}$ and $\bar{q}_0$, and therefore can be expressed as a multiple Fourier series

$$\bar{F}^{\mathrm{res}}_{\alpha}(\bar{q};\bar{q}_0) = \sum_{KN} \bar{g}^{KN}_{\alpha} e^{-iN\bar{q}} e^{-iK\bar{q}_0}, \qquad \bar{g}^{KN}_{\alpha} = \int_0^{2\pi} \frac{d\bar{q}}{2\pi} \int_0^{2\pi} \frac{d\bar{q}_0}{2\pi} \bar{F}^{\mathrm{res}}_{\alpha}(\bar{q};\bar{q}_0) e^{iN\bar{q}} e^{iK\bar{q}_0}. \tag{8.27}$$

By sampling the resonant SSF on an evenly-spaced two-dimensional grid in $\bar{q}$ and $\bar{q}_0$, I construct discrete Fourier representations of $\bar{F}^{\mathrm{res}}_{\alpha}$,

$$\bar{q}_{\imath} = \frac{2\pi\imath}{N_{\mathrm{res}}}, \qquad \imath = 0, 1, \ldots, N_{\mathrm{res}} - 1, \qquad \bar{q}_{0\jmath} = \frac{2\pi\jmath}{N_0}, \qquad \jmath = 0, 1, \ldots, N_0 - 1, \tag{8.28}$$

$$\bar{g}^{KN}_{\alpha} \simeq \frac{1}{N_0 N_{\mathrm{res}}} \sum_{\jmath=0}^{N_0-1} \sum_{\imath=0}^{N_{\mathrm{res}}-1} \bar{F}^{\mathrm{res}}_{\alpha}(\bar{q}_{\imath};\bar{q}_{0\jmath}) e^{iN\bar{q}_{\imath}} e^{iK\bar{q}_{0\jmath}}, \tag{8.29}$$

$$\bar{F}^{\mathrm{res}}_{\alpha}(\bar{q};\bar{q}_0) \simeq \sum_{K=0}^{N_0-1} \sum_{N=0}^{N_{\mathrm{res}}-1} \bar{g}^{KN}_{\alpha} e^{-iN\bar{q}} e^{-iK\bar{q}_0}. \tag{8.30}$$

This provides an efficient way of storing resonant SSF data and interpolating results to obtain the SSF at arbitrary times and initial phases.[2]

---

[2] One can further simplify the form of Eq. (8.29) by making use of the crossing relations, because $\bar{F}^{\mathrm{res}}_{\alpha}$ is real, though I do not demonstrate the simplification here.

8.2.3: Constructing the self-force on the full mode-sum basis

Alternatively, one can construct $\bar{F}^{\mathrm{res}}_\alpha(\bar{q};\bar{q}_0)$ from $\hat{F}_\alpha(q_r,q_\theta)$. As described in Sec. 5.3.4, $\hat{F}_\alpha(q_r,q_\theta)$—the SSF evaluated along a fiducial orbit—is related to the SSF evaluated along an orbit with arbitrary initial conditions via Eq. (5.170),

$$\bar{F}^{\mathrm{res}}_\alpha(\bar{q};\bar{q}_0) = \hat{F}_\alpha(\beta_r\bar{q}, \beta_\theta\bar{q} + \beta_\theta\bar{q}_0). \tag{8.31}$$

This is equivalent to constructing the resonant SSF using the full mode-sum representation of the scalar field given in Eq. (8.5). While this connection is relatively simple, it demonstrates that one can calculate the resonant SSF for any given initial phase using only fiducial geodesic functions. By summing over an additional mode index, one avoids integrating over multiple sources. On the one hand, there appears at first to be no computational savings from this approach. On the other hand, if one has already built a code to calculate the SSF for non-resonant orbits, then that code can be easily optimized to calculate the SSF along resonant orbits. This avoids the time-consuming process of constructing of an entirely new code just to handle resonances.

In reality, it is somewhat more efficient to construct $\hat{F}_\alpha$ than $\bar{F}^{\mathrm{res}}_\alpha$. As mentioned in Sec. 5.3.4, to numerically calculate $\hat{F}_\alpha$, I sample the fiducial SSF on a two-dimensional grid in q_r and q_θ and then represent $\hat{F}_\alpha$ as a discrete Fourier series

$$q_{r,\imath} = \frac{2\pi\imath}{N_r}, \qquad \imath = 0,1,\dots,N_r-1, \qquad\qquad q_{\theta,\jmath} = \frac{2\pi\jmath}{N_\theta}, \qquad \jmath = 0,1,\dots,N_\theta-1, \tag{8.32}$$

$$\hat{f}^{kn}_\alpha = \frac{1}{N_r N_\theta}\sum_{\jmath=0}^{N_\theta-1}\sum_{\imath=0}^{N_r-1}\hat{F}_\alpha\left(q_{r,\imath},q_{\theta,\jmath}\right)e^{i(kq_{\theta,\jmath}+nq_{r,\imath})}, \tag{8.33}$$

$$\hat{F}_\alpha(q_r,q_\theta) = \sum_{k=0}^{N_\theta-1}\sum_{n=0}^{N_r-1}\hat{f}^{kn}_\alpha e^{-i(kq_\theta+nq_r)}, \tag{8.34}$$

For resonant orbits, the Fourier coefficients $\hat{f}^{kn}_\alpha$ are related to the Fourier coefficients of the resonant SSF $\bar{g}^{KN}_\alpha$ because

$$\begin{aligned}
\hat{F}_\alpha(\beta_r\bar{q}, \beta_\theta\bar{q} + \beta_\theta\bar{q}_0) &= \sum_{kn}\hat{f}^{kn}_\alpha e^{-i\beta_\theta k(\bar{q}+\bar{q}_0)}e^{-i\beta_r n\bar{q}}, && (8.35)\\
&= \sum_{kn}\hat{f}^{kn}_\alpha e^{-i(\beta_\theta k+\beta_r n)\bar{q}}e^{-i\beta_\theta k\bar{q}_0}, && (8.36)\\
&= \sum_{KN}\hat{f}^{K/\beta_\theta,(N-K)/\beta_r}_\alpha e^{-iN\bar{q}}e^{-iK\bar{q}_0}, && (8.37)\\
&= \bar{F}^{\mathrm{res}}_\alpha(\bar{q};\bar{q}_0). && (8.38)
\end{aligned}$$

Comparing to Eq. (8.29), we see that

$$\bar{g}_\alpha^{KN} = \hat{f}_\alpha^{K/\beta_\theta,(N-K)/\beta_r}. \tag{8.39}$$

This relation between the Fourier coefficients demonstrates that $\hat{F}_\alpha$ captures the behavior of the resonant SSF with fewer Fourier modes than $\bar{F}_\alpha^{\mathrm{res}}$. For example, consider a resonance defined by $\beta_r = 2$ and $\beta_\theta = 3$. Based on Eq. (8.39), $\bar{g}_\alpha^{KN} = 0$ unless K is a multiple of 3 and $N - K$ is a multiple of 2. Thus the Fourier representation of $\bar{F}_\alpha^{\mathrm{res}}$, given by Eq. (8.29), will be full of (K, N)-modes that are equivalent to 0, and $\bar{F}_\alpha^{\mathrm{res}}$ will require more modes (higher values of K and N) to encode the same amount of information as $\hat{F}_\alpha$. Calculating these higher modes requires a denser sampling of $\bar{q}$ and $\bar{q}_0$ and, consequently, will require more computational time. Therefore, to efficiently construct the SSF for resonant sources, one can first construct the SSF using fiducial geodesics as outlined in Sec. 5.3.4, then relate $\hat{f}_\alpha^{kn}$ to $\bar{g}_\alpha^{KN}$ to calculate $\bar{F}_\alpha^{\mathrm{res}}$. However, as a consistency check, I still use both methods to construct the SSF results reported in the following section.

8.2.4: Constructing resonant fluxes

In Secs. 4.4.6 and 5.2.7 I outlined the calculation of the gravitational and scalar wave fluxes using the normalization constants $C^{\pm}_{s\hat{l}mkn}$. However, Eqs. (4.123), (4.124), (5.69), and (5.72) only hold for non-resonant orbits. For resonant sources, the fluxes must be modified due to the reduced frequency spectrum ω_{mN}. The essential point here is that for non-resonant orbits the fluxes calculated from Eqs. (5.69) and (5.72) reflect an incoherent sum over the modes. When the orbit has a resonance, there are various interference terms which averaged to zero in the non-resonant case, but no longer do so when Ω_r and Ω_θ are rationally related. Then the (scalar) energy and angular momentum fluxes at the horizon take the form

$$\langle \dot{E} \rangle^{\mathcal{H}} = \frac{q^2}{4\pi} \sum_{\hat{l}mN} \omega_{mN}\gamma_{mN} \left| C^-_{\hat{l}mN}(\bar{q}_0) \right|^2, \qquad \langle \dot{L}_z \rangle^{\mathcal{H}} = \frac{q^2}{4\pi} \sum_{\hat{l}mN} m\gamma_{mN} \left| C^-_{\hat{l}mN}(\bar{q}_0) \right|^2, \tag{8.40}$$

while the fluxes at infinity are given by

$$\langle \dot{E} \rangle^{\infty} = \frac{q^2}{4\pi} \sum_{\hat{l}mN} \omega^2_{mN} \left| C^+_{\hat{l}mN}(\bar{q}_0) \right|^2, \qquad \langle \dot{L}_z \rangle^{\infty} = \frac{q^2}{4\pi} \sum_{\hat{l}mN} m\omega_{mN} \left| C^+_{\hat{l}mN}(\bar{q}_0) \right|^2. \tag{8.41}$$

(The gravitational fluxes in Sec. (4.4.6) would similarly be rewritten in terms of the reduced-mode Teukolsky amplitudes $C^{\pm}_{-2\hat{l}mN}$.) As emphasized at the beginning of this section, resonances are sensitive to the phase at which an EMRI enters resonance. Equations (8.40) and (8.41) demonstrate that this dependence is captured by the normalization constants, which depend on the resonant phase $\bar{q}_0$. Thus, unlike in Chapter 6, the

$\langle \dot{E} \rangle^{\mathrm{tot}}$ and $\langle \dot{L}_z \rangle^{\mathrm{tot}}$ are no longer constant for a given set of (resonant) orbital parameters (p, e, x_{inc}) but also depend on $\bar{q}_0$. A similar behavior appears in the local work and torque done on the particle, along with the time-rate-of-change of the Carter constant. While Eqs. (5.60) (5.61), (5.64) still hold true for resonances, the orbital averages in Eqs. (5.62) (5.63), and (8.44) reduce to

$$\mathcal{W} = -\frac{q^2}{\Gamma} \int_0^{2\pi} \frac{d\bar{q}}{2\pi} \, \bar{\Sigma}(\bar{q}; \bar{q}_0) \bar{F}_t^{\mathrm{res,diss}}(\bar{q}; \bar{q}_0). \tag{8.42}$$

$$\mathcal{T} = \frac{q^2}{\Gamma} \int_0^{2\pi} \frac{d\bar{q}}{2\pi} \, \bar{\Sigma}(\bar{q}; \bar{q}_0) \bar{F}_\varphi^{\mathrm{res,diss}}(\bar{q}; \bar{q}_0), \tag{8.43}$$

$$\mathcal{K} = -2(L_z - aE)(\mathcal{T} - a\mathcal{W}) + 2\frac{\mu q^2}{\Gamma} \int_0^{2\pi} \frac{d\bar{q}}{2\pi} \bar{\Sigma}(\bar{q}; \bar{q}_0) \bar{K}_{\mu\nu}(\bar{q}; \bar{q}_0) \bar{u}^\mu(\bar{q}; \bar{q}_0) \bar{f}^\nu_{\mathrm{res}}(\bar{q}; \bar{q}_0), \tag{8.44}$$

where $f^\mu \equiv (g^{\mu\nu} + u^\mu u^\nu) F_\nu$ is the component of the self-force that is orthogonal to u^α, while $\bar{\Sigma}$, $\bar{K}_{\mu\nu}$ and $\bar{u}^\alpha$ are all evaluated along a resonant worldline $\bar{x}_p^\mu$. For $\bar{q}_0 \neq 0$, the conservative SSF components $\bar{F}_t^{\mathrm{cons}}$ and $\bar{F}_\varphi^{\mathrm{cons}}$ are no longer antisymmetric with respect to $\bar{q}$, and $\bar{F}_t^{\mathrm{cons}}$ and $\bar{F}_\varphi^{\mathrm{cons}}$ are no longer symmetric. Therefore, the conservative components are not guaranteed to vanish in Eqs. (8.42)-(8.44) as they do with non-resonant sources. For the local work and torque, the conservative components are discarded, because the global energy and angular momentum fluxes, which balance the work and torque, are purely dissipative effects.

However, it is still unclear whether the conservative component of the self-force should contribute to $\mathcal{K}$, since the evolution of the Carter constant, $\langle \dot{Q} \rangle^{\mathrm{tot}}$, is not tied to a physical flux like the energy or angular momentum. Flanagan and Hinderer [100] conjectured, because the conservative dynamics of the system is integrable, that conservative effects cannot drive resonances nor will the conservative self-force contribute to $\mathcal{W}$, $\mathcal{T}$, or $\mathcal{K}$. While this "integrability conjecture" has been assumed in other work [101, 200], it has not yet been confirmed by strong-field calculations of the conservative self-force. Accordingly, Isoyama et. al [139, 140] included potential contributions from the conservative sector in their derivations of $\langle \dot{Q} \rangle^{\mathrm{tot}}$ based on a Hamiltonian approach. Since I was able to make the first self-force calculation of $r\theta$-resonances, it was possible to test this conjecture. Later, in Sec. 8.5, I demonstrate that the conservative contribution of the SSF to $\mathcal{K}$ is consistent with zero within the numerical tolerances of my results.

Section 8.3: Scalar self-force for resonant orbits

I present, for the first time, the SSF for six different resonant orbits, which are listed in Table 8.1. To simplify notation, I once again set $M = 1$ for the remainder of this chapter. Each of these sources follows an $r\theta$-resonant geodesic in a Kerr spacetime with spin $a = 0.9$. I consider a spin of $a = 0.9$, because the measured spins of massive black holes tend to be relatively high ($a \gtrsim 0.6$) with many approaching the extremal limit

label	p	e	x_{inc}	β_r:β_θ
$e02.13$	3.622	0.2	$\cos(\pi/4)$	1:3
$e02.12$	4.508	0.2	$\cos(\pi/4)$	1:2
$e02.23$	6.643	0.2	$\cos(\pi/4)$	2:3
$e05.13$	3.804	0.5	$\cos(\pi/4)$	1:3
$e05.12$	4.607	0.5	$\cos(\pi/4)$	1:2
$e05.23$	6.707	0.5	$\cos(\pi/4)$	2:3

Table 8.1: A table summarizing the SSF sources presented in Sec. 8.3. All sources follow a $r\theta$-resonant geodesic in a Kerr spacetime with $a = 0.9$. The values of the semi-latus rectum for these resonant orbits are all irrational. Therefore I report p with four significant digits for brevity.

$(a \to 1)$ [195]. I focus on 1:3, 1:2, and 2:3 $r\theta$-resonances, which are the three resonances an EMRI is most likely to encounter during its final years of evolution [200, 48]. To pick orbital parameters (p, e, x_{inc}) that produce resonant frequencies, I follow the work of Brink, Geyer, and Hinderer [55, 54]: I first specify values for e and x_{inc}, then numerically calculate p using the root-finding method described in Sec. V E of Ref. [54]. For this work, all of the orbits share the same inclination, $x_{\mathrm{inc}} = \cos(\pi/4)$, but I evaluate each resonance at two different eccentricities, $e = 0.2$ and $e = 0.5$. The resulting values of p for each resonant configuration are listed in Table 8.1.

As discussed in Sec. 5.3.4, the SSF produced by resonant sources can be conveniently expressed as a function of the resonant angle variable $\bar{q}$ and the initial resonant phase $\bar{q}_0$, i.e., $\bar{F}^{\mathrm{res}}_\alpha(\bar{q}; \bar{q}_0)$, or the more general angle variables q_r and q_θ and the initial phases q_{r0} and $q_{\theta 0}$, i.e., $\hat{F}_\alpha(\beta_r \bar{q}, \beta_\theta \bar{q} + \beta_\theta \bar{q}_0) = \hat{F}_\alpha(q_r, q_\theta + q_{\theta 0})$. I use both descriptions to express these SSF results. Plotting the SSF as a function of $\bar{q}$, as shown in Sec. 8.3.2, highlights the periodicity of the SSF during resonances and more clearly demonstrates the evolution of the SSF with time. On the other hand, plotting the SSF as a function of q_r and q_θ, as shown in Sec. 8.3.3, separates the dependence of the SSF on the radial and polar motion of the source. It also mirrors the parameterizations used for non-resonant orbits, as seen in Chapter 6 and Refs. [224, 172]. To better analyze the impact of different orbital parameters and resonances on the SSF, I present each self-force component separately.

8.3.1: Regularization and convergence of results

The regularized SSF is constructed via mode-sum regularization and the numerical fitting procedures outlined in Sec. 5.3.5. As discussed earlier, the convergence of the mode-sum regularization procedure is well understood. For example, subtracting the analytically-known regularization parameters, A_α and B_α, produces residuals that fall off $\sim l^{-2}$ at large l. This provides an important validation test for these new SSF results, because inaccurate results will not converge at these expected rates. In Fig. 8.1 I plot the

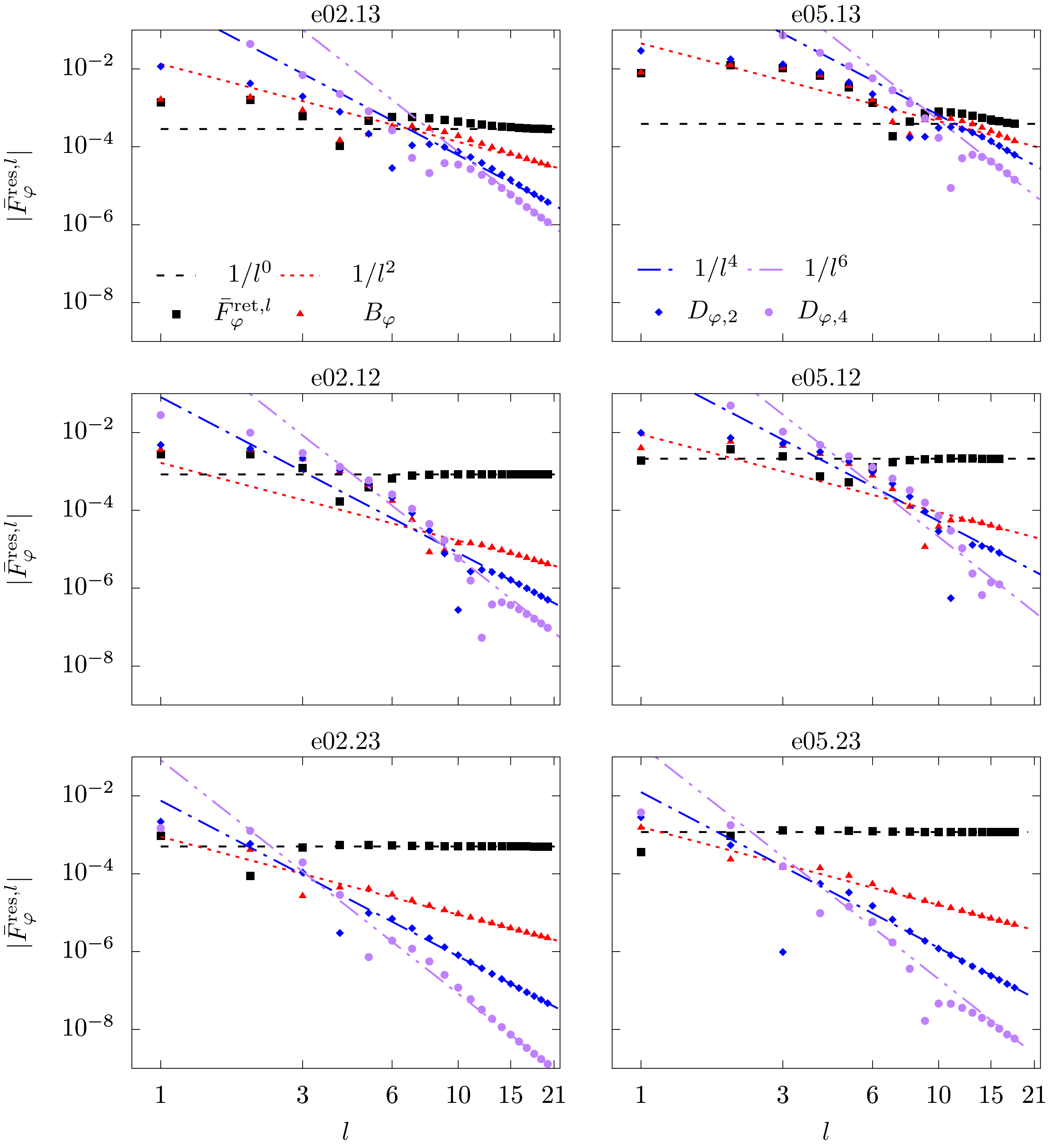

Figure 8.1: Convergence of the SSF l-modes for the resonant sources listed in Table 8.1. The dashed and dotted lines depict the increasing rate of convergence for $\bar{F}_\varphi^{\mathrm{res}}(\bar{q} = 5\pi/16; \bar{q}_0 = 5\pi/32/\beta_\theta)$ as additional regularization parameters are incorporated. The (black) squares represent individual l-modes of the unregularized SSF, which clearly diverge. The (red) triangles are the residuals from subtracting A_φ and B_φ. The (blue) diamonds represent the residuals after subtracting $D_{\varphi,2}$, which I obtain numerically as discussed in Sec. 5.3.5. The (purple) circles represent the inclusion of $D_{\varphi,4}$, which is also numerically approximated.

mode-sum convergence of $\bar{F}_\varphi^{\mathrm{res}}$ at the point ($\bar{q} = 5\pi/16, \beta_\theta\bar{q}_0 = 5\pi/32$) for all six resonant configurations. Points refer to the l-mode residuals that result from subtracting the analytically-known and numerically-fitted regularization parameters, while the lines refer to the expected convergence rate of these residuals at large l. Across all six sources, the residuals approach their expected asymptotic rates of convergence.

While all of the sources have the same asymptotic behavior at large l, Fig. 8.1 demonstrates that for low l-modes the $e = 0.2$ sources converge faster than $e = 0.5$, the 2:3 resonances converge faster than the 1:2 resonances, and the 1:2 resonances faster than the 1:3, as expected. Higher eccentricities require a broader frequency spectrum to capture the radial motion. Additionally, sources that orbit farther into the strong-field (closer to the MBH) will excite stronger perturbations and require more frequency modes to construct the behavior of the self-force. The 1:3 resonances have the smallest separation, the 1:2 resonances the next smallest, and the 2:3 resonances have the largest, reflecting the varying rates of convergence at low l.

This behavior poses a problem for the $e05.13$ orbits. For this source, it takes thousands of additional modes to capture the behavior of the SSF compared to other resonant configurations. Because of the slow convergence at low multipoles, truncating mode summations at a similar value of l as the other orbits will introduce larger numerical errors in the retarded SSF contributions. While these numerical errors are still relatively small, they are significant enough that they make it much more difficult to fit for higher-order regularization parameters. The accuracy of the conservative component of the SSF suffers because of this. Therefore, the conservative SSF is only known to $\sim 1 - 2$ digits of accuracy for the $e05.13$ orbit. This numerical error becomes particularly noticeable when the F_θ component of the SSF is close to zero, as can be seen in Fig. 8.8. Fortunately, the dissipative component typically dominates over the conservative contribution in regions of the orbit where the conservative contribution is known less accurately. Therefore, the overall results still capture most of the quantitative behavior of the SSF during resonances, though the $e05.13$ model will need to be recalculated with additional numerical precision in order to extract sufficiently accurate numerical results for the conservative SSF.

8.3.2: Scalar self-force as a function of $\bar{q}$

As a first step, I present the SSF as a function of the resonant variable $\bar{q}$ in Figs. 8.2, 8.3, 8.4, and 8.5. The SSF results are weighted by the cube of the minimum radial position of the particle (i.e., $r_{\text{min}}^3 \bar{F}_\alpha^{\text{res}}$). This weighting normalizes the SSF results, facilitating comparisons across different scalar sources without distorting the dependence of the SSF on the radial and polar motion of the different orbits. For each resonant source I plot the SSF produced by two geodesics with different initial conditions. The dot-dashed (black) lines illustrate how the SSF varies along a resonant geodesic with initial polar phase $\beta_\theta \bar{q}_0 = q_{\theta 0} = 0$ (i.e., initial conditions $x_p^\mu(\lambda = 0) = (0, r_{\text{min}}, \theta_{\text{min}}, 0)$ and $u^r(0) = u^\theta(0) = 0$), while the solid (red) lines illustrate how the SSF varies along a resonant geodesic with $\beta_\theta \bar{q}_0 = q_{\theta 0} = -\pi/2$ (i.e., initial conditions

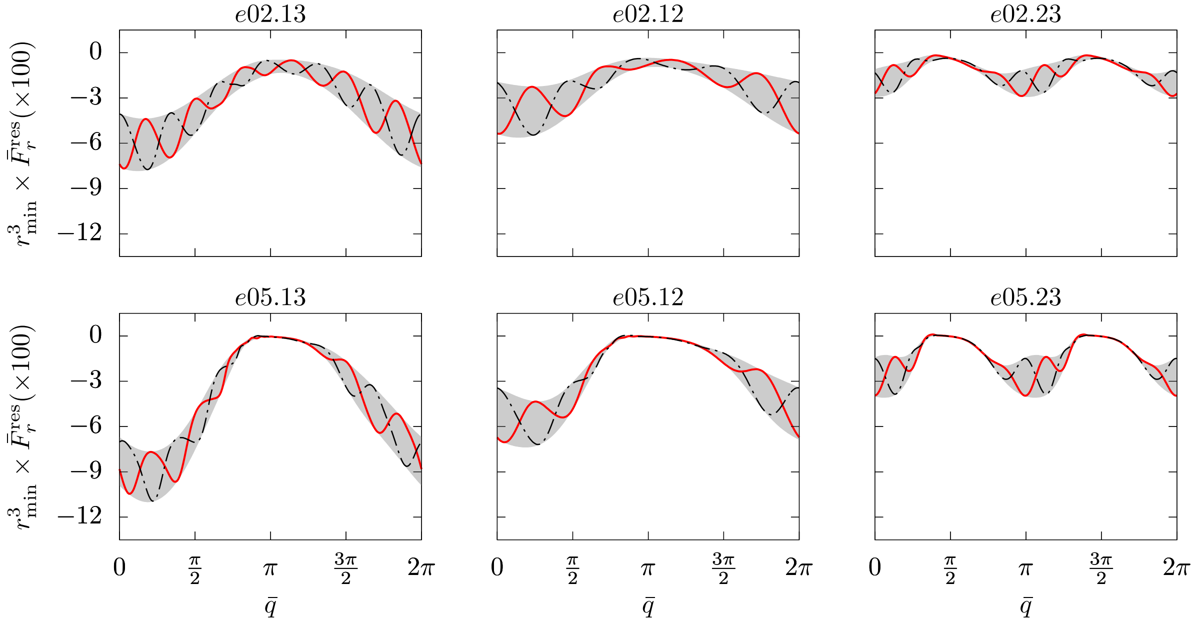

Figure 8.2: The radial-component of the SSF as a function of the resonant angle variable $\bar{q}$, i.e., $\bar{F}^{\rm res}_r(\bar{q};\bar{q}_0)$, for the six resonant geodesics presented in Table 8.1. The SSF is weighted by the cube of the pericenter radius, $r^3_{\rm min}$, so that all six orbits are of comparable magnitude. The dot dashed (black) line represents the SSF for a resonant geodesic with an initial resonant phase of $\beta_\theta \bar{q}_0 = q_{\theta 0} = 0$, while the solid (red) line represents the SSF for a resonance with the same orbital parameters, but an initial resonant phase of $\beta_\theta \bar{q}_0 = q_{\theta 0} = -\pi/2$. The shaded grey region represents all of the SSF values produced by varying the initial phase $\bar{q}_0$ from 0 to 2π.

$x^\mu_p(\lambda = 0) = (0, r_{\rm min}, \pi/2, 0)$, $u^r(0) = 0$, and $u^\theta(0) < 0$).[3] The shaded grey regions refer to the full range of SSF values that result from varying the initial phases—either $q_{\theta 0}$ or $\bar{q}_0$—of the resonant orbit.

Figures 8.2, 8.3, 8.4, and 8.5 illustrate that the SSF is periodic with respect to $\bar{q}$. Interestingly, for the 2:3 resonances, $\bar{F}^{\rm res}_t$, $\bar{F}^{\rm res}_r$, and $\bar{F}^{\rm res}_\varphi$ are periodic on the interval of $[0, \pi]$ rather than $[0, 2\pi]$. This behavior arises, because (in Kerr spacetime) the time-, radial-, and azimuthal-components of the SSF are invariant under parity transformations of the radial and polar motion (i.e., reflections through the equatorial plane, $r_p \to r_p$ and $\theta_p \to \pi - \theta_p$), while the polar-component changes sign [234]. This is also observed for the gravitational self-force [224]. For a 2:3 resonance, the radial motion of the source is identical on the intervals $[0, \pi]$ and $[\pi, 2\pi]$, while the polar motion is related by a parity transformation. This explains the repetition in $\bar{F}^{\rm res}_t$, $\bar{F}^{\rm res}_r$, and $\bar{F}^{\rm res}_\varphi$, while also highlighting that $\bar{F}^{\rm res}_\theta(\bar{q};\bar{q}_0) = -\bar{F}^{\rm res}_\theta(\bar{q}+\pi;\bar{q}_0)$.

These symmetries also manifest themselves in the number of low-frequency "oscillations" that arise in the SSF components, particularly for the low-eccentricity orbits. Focusing on $\bar{F}^{\rm res}_r$ in Fig. 8.2, the SSF peaks six times for the $e02.13$ and $e02.23$ sources and four times for the $e02.12$ source, with the peaks closely aligning

---

[3] Note that we keep our choice of $q_{\theta 0}$ constant rather than $\bar{q}_0$, because the same value of $\bar{q}_0$ can actually generate different initial conditions for resonances with different values of β_θ.

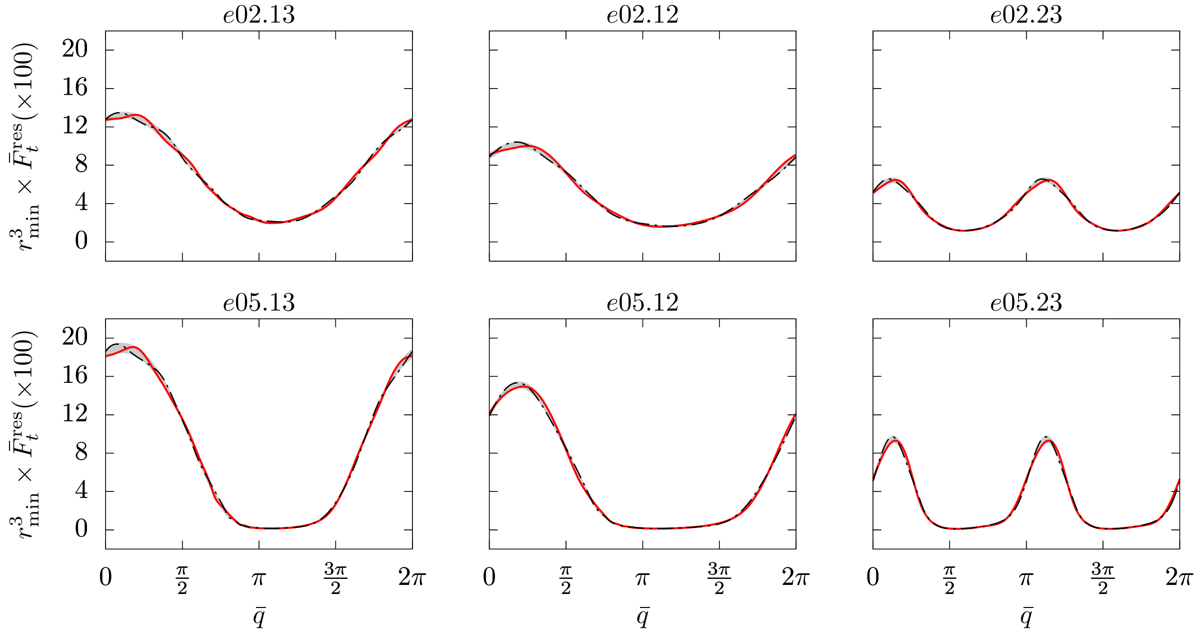

Figure 8.3: The time-component of the SSF as a function of the resonant angle variable $\bar{q}$, i.e., $\bar{F}^{\rm res}_t(\bar{q};\bar{q}_0)$, for the six resonant geodesics presented in Table 8.1.

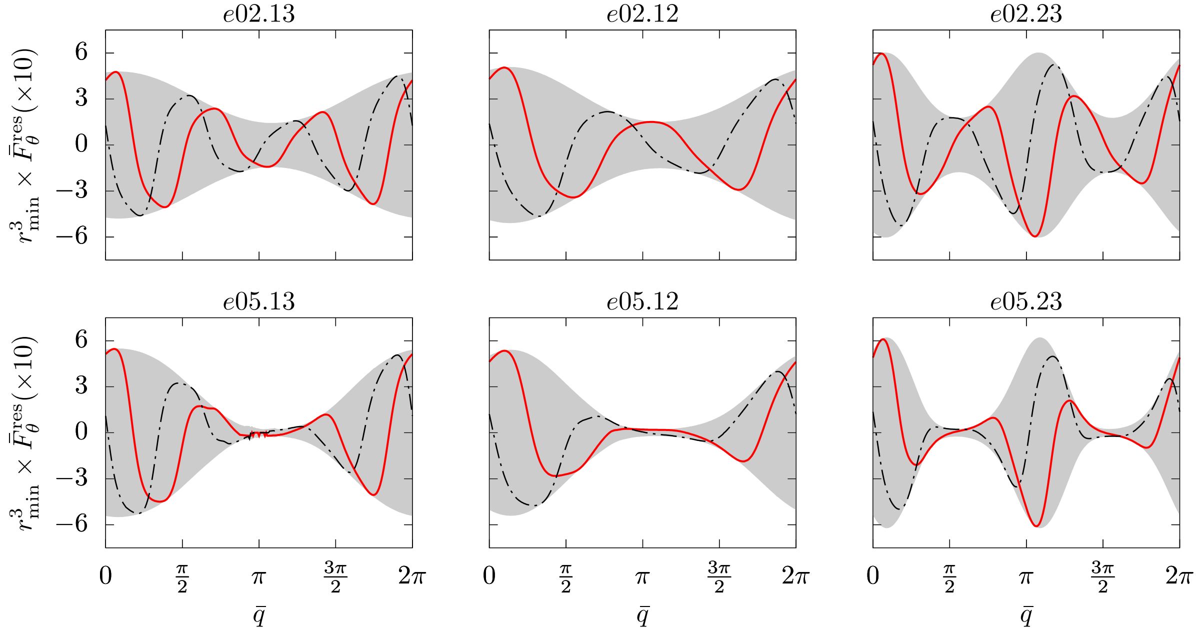

Figure 8.4: The polar-component of the SSF as a function of the resonant angle variable $\bar{q}$, i.e., $\bar{F}^{\rm res}_\theta(\bar{q};\bar{q}_0)$, for the six resonant geodesics presented in Table 8.1.

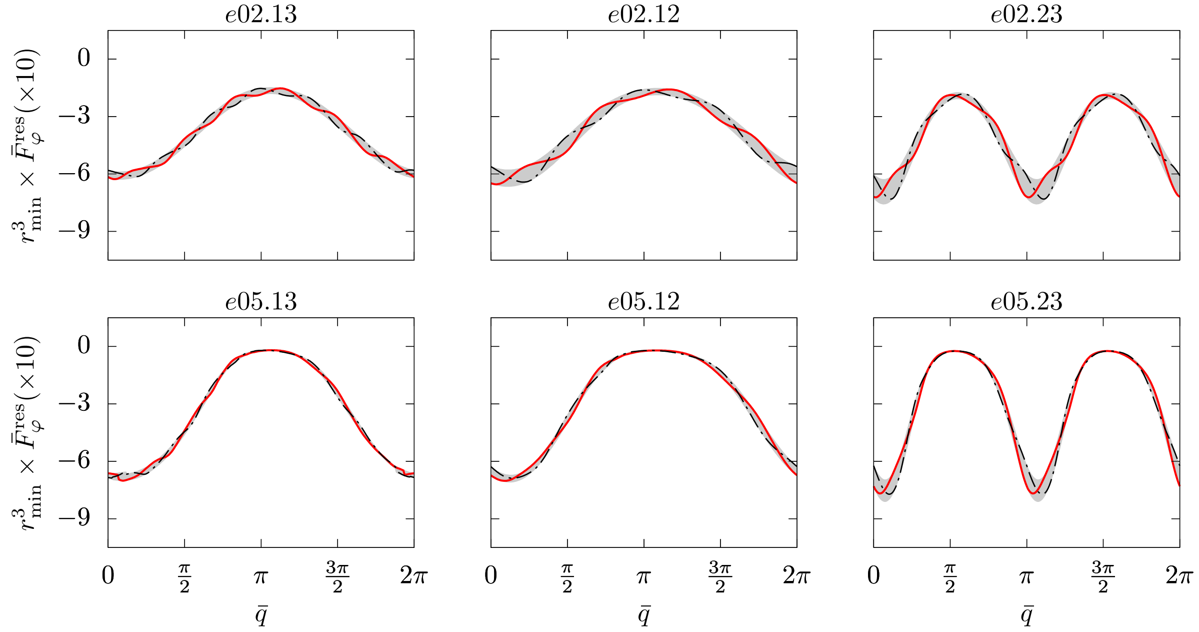

Figure 8.5: The azimuthal-component of the SSF as a function of the resonant angle variable $\bar{q}$, i.e., $\bar{F}^{\rm res}_\varphi(\bar{q};\bar{q}_0)$, for the six resonant geodesics presented in Table 8.1.

with the points at which each orbit passes through its polar extrema. Additionally the troughs tend to align with the passage of the source through the equatorial plane. A similar behavior is also seen for $\bar{F}^{\rm res}_t$, $\bar{F}^{\rm res}_\varphi$, and the higher eccentricity sources, though for the $e = 0.5$ orbits it is more difficult to identify local peaks, particularly as the small body approaches apocenter. For $\bar{F}^{\rm res}_\theta$ in Fig. 8.4, the peaks align with the passage of the source through $\theta_{\rm min}$, while the troughs align with its passages through $\pi - \theta_{\rm min}$.

I also find that initial conditions have varying effects on different SSF components. For $\bar{F}^{\rm res}_t$ in Fig. 8.3 the initial conditions have a minimal impact on the SSF. For $\bar{F}^{\rm res}_r$ in Fig. 8.2 and $\bar{F}^{\rm res}_\varphi$ in Fig. 8.5 there are greater variation due to initial conditions. Likewise, for $\bar{F}^{\rm res}_\theta$ in Fig. 8.4, there is significant variation. To understand the source of this variance, recall that the radial and polar position of the resonant source, $\bar{r}_p$ and $\bar{\theta}_p$, depend on the angle variables according to

$$\bar{r}_p = \hat{r}_p(q_r) = \hat{r}(\beta_r \bar{q}), \tag{8.45}$$

$$\bar{\theta}_p = \hat{\theta}_p(q_\theta + q_{\theta 0}) = \hat{\theta}(\beta_\theta \bar{q} + \beta_\theta \bar{q}_0). \tag{8.46}$$

Consequently, broader grey bands indicate a stronger dependence on the polar motion of the source. Thus, $\bar{F}^{\rm res}_t$ primarily depends on the radial motion of the source. In contrast, $\bar{F}^{\rm res}_r$ is sensitive to the both the polar and radial motion of the source, though at apocenter the polar motion has a smaller impact. In behavior opposite of $\bar{F}^{\rm res}_t$, $\bar{F}^{\rm res}_\theta$ is primarily dependent on the polar motion of the source. Finally, $\bar{F}^{\rm res}_\varphi$ depends mostly

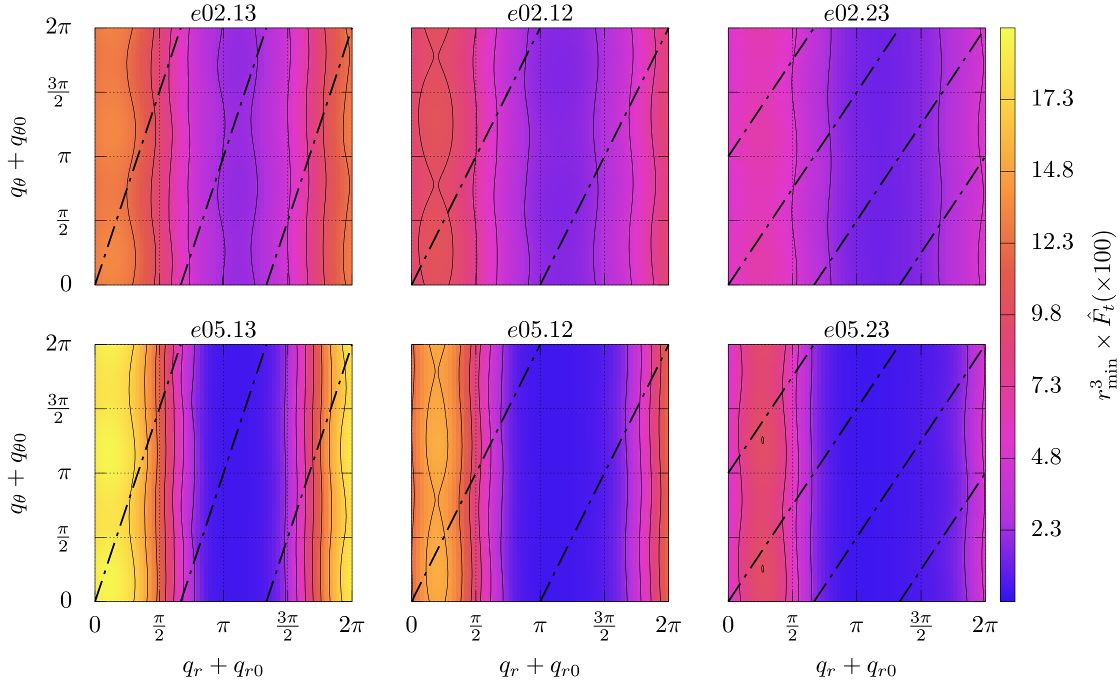

Figure 8.6: The time-component of the SSF, $\hat{F}_t$, is depicted through sampling on the torus for the six sources listed in Table 8.1. The SSF is normalized by the cube of each source's pericenter distance. The vertical axis is correlated with the θ-dependence of the self-force, while the horizontal axis is related to the r-dependence. Colors correspond to different values of the self-force, with the values denoted in the colorbar on the right. The self-force is constant along each (solid) contour line. The tic labels in the colorbar correspond to the values of the contour lines (e.g., in the top left plot, $r^3_{\rm min} \times \hat{F}_t = -0.118$ along the leftmost contour line). The dot-dashed lines trace over the SSF values that are sampled by a resonant source with fiducial initial conditions ($\bar{q}_0 = 0$).

on the radial motion of the source, though the polar position becomes more important near pericenter.

8.3.3: Scalar self-force as a function of q_r and q_θ

To better visualize the dependence of the SSF on the radial and polar motion of resonant orbits, I project the SSF components onto the two-torus spanned by $q_r + q_{r0}$ and $q_\theta + q_{\theta 0}$ in Figs. 8.6, 8.7, 8.8, and 8.9. While I set $q_{r0} = 0$ in my earlier discussions, those results hold for arbitrary values of q_{r0} as well. As before, I weight the force components by the cube of the minimum radial position of the source. The dot-dashed (black) lines trace the geodesic motion of a source with initial conditions $\beta_\theta \bar{q}_0 = q_{\theta 0} = 0$. Sampling the SSF as the source evolves along these tracks reproduces the black dot-dashed curves in Figs. 8.2, 8.3, 8.4, and 8.5. Maintaining previous notation, I will refer to the SSF parameterized by $q_r + q_{r0}$ and $q_\theta + q_{\theta 0}$ as $\hat{F}_\alpha$.

As observed in Sec. 8.3.2, $\hat{F}_t$ (shown in Fig. 8.6) primarily depends on the radial motion of the source, with little variation as one moves along the q_θ-axis. The radial and azimuthal components, $\hat{F}_r$ and $\hat{F}_\varphi$ (shown in Figs. 8.7 and 8.9, respectively) are sensitive to both the radial and polar motion of the scalar

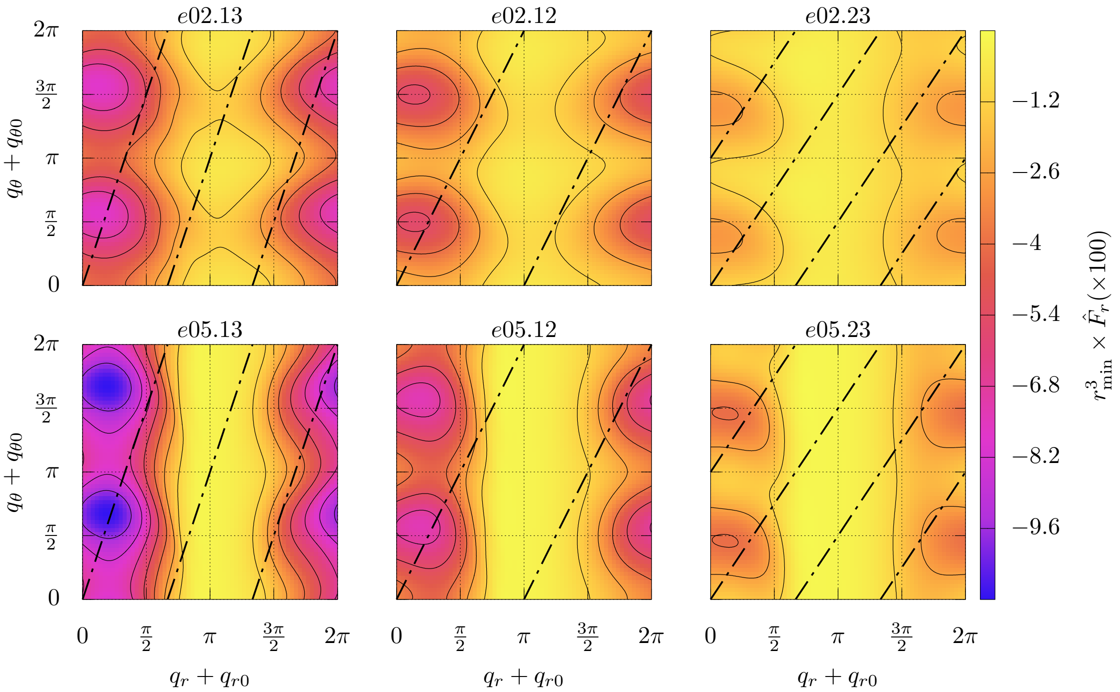

Figure 8.7: The radial-component of the scalar self-force, $\hat{F}_r$, for the six orbits listed in Table 8.1.

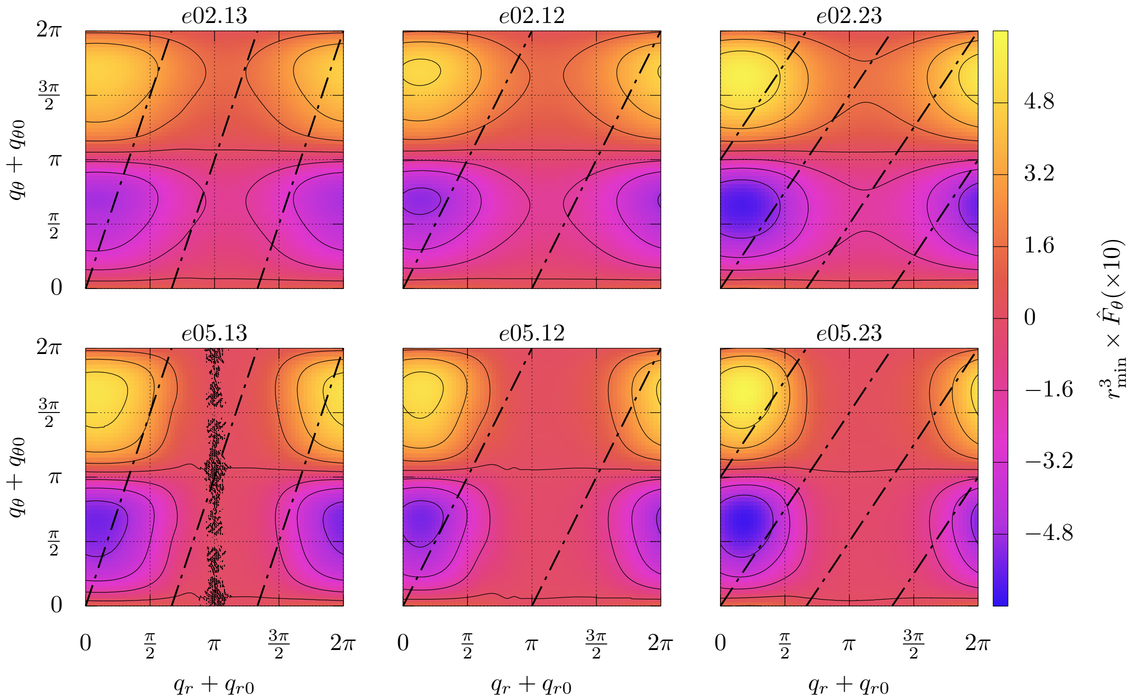

Figure 8.8: The polar-component of the scalar self-force, $\hat{F}_\theta$, for the six orbits listed in Table 8.1. Note that the disjointed lines centered around $q_r + q_{r0} = \pi$ are due to numerical noise dominating the value of $\hat{F}_\theta$ as its value approaches zero, as discussed in Sec. 8.3.1.

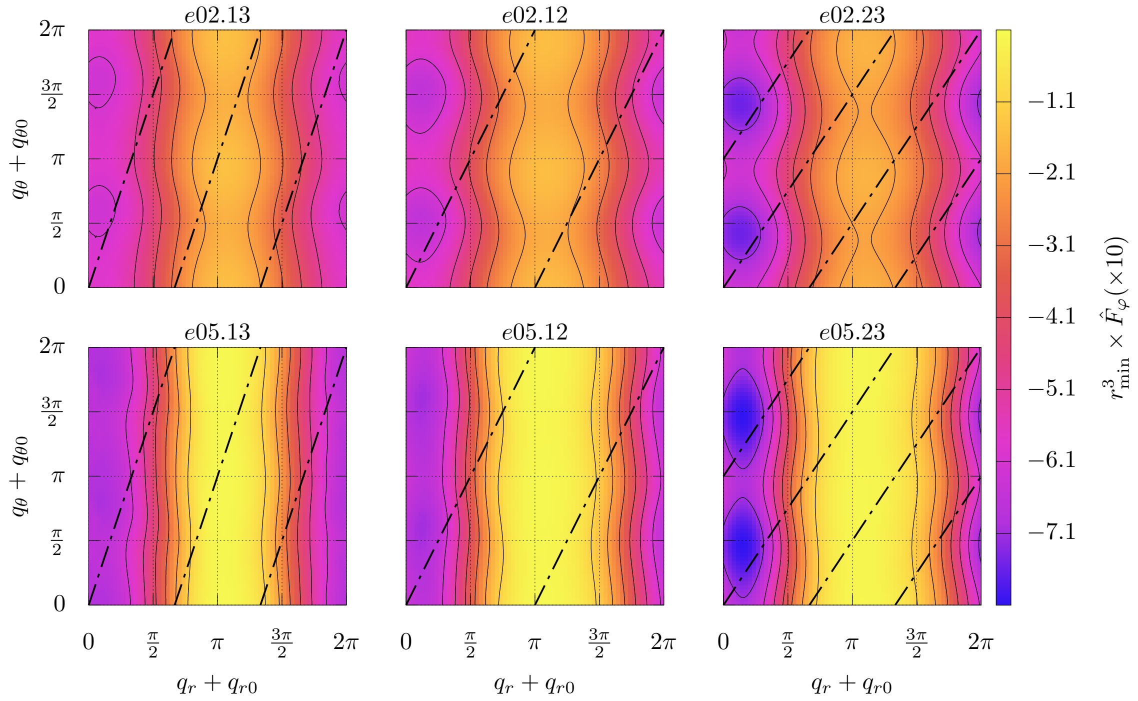

Figure 8.9: The azimuthal-component of the scalar self-force, $\hat{F}_\varphi$, for the six orbits listed in Table 8.1.

charge, especially near pericenter, though $\hat{F}_r$ appears to have a stronger dependence on the polar motion. Figure 8.7 clearly demonstrates the parity antisymmetry of $\hat{F}_\theta$ discussed in the previous section.

In agreement with previous investigations [236, 237, 234, 172] of the SSF, I find that $\hat{F}_t$ is strictly positive, in contrast to the gravitational self-force case, where the time-component can become negative in both radiation and Lorenz gauge [222, 224].[4] On the other hand, $\hat{F}_r$ is predominantly negative across the entire torus, though it becomes slightly positive near apocenter. This behavior is consistent with higher spins leading to attractive radial SSF results [236]. Large inclinations, on the other hand, lead to predominantly positive values of the SSF, as seen in SSF results for spherical orbits [234], however this requires inclinations $x \gtrsim 0.5$, which I do not consider here. Interestingly, while all of the SSF components peak in magnitude following the pericenter passage of the source, the magnitude of these peaks grows for $\hat{F}_t$ and $\hat{F}_r$ as r_{min} decreases, while the peaks grow for $\hat{F}_\theta$ and $\hat{F}_\varphi$ as r_{min} increases. The latter behavior is actually due to the factor of r^3_{min}. If one removes this weighting, then closer pericenter passages excite larger peaks in the SSF for all components. This suggests that the leading-order behavior of $\hat{F}_\theta$ and $\hat{F}_\varphi$ is closer to $1/r^2$, which one might expect based on dimensional analysis ($[F_{\theta,\varphi}/F_{t,r}]_{\mathrm{dim}} \sim [M]_{\mathrm{dim}}$).

While these results provide the first insights into the behavior of the strong-field SSF during $r\theta$-resonances,

---

[4] I do not try to draw any physical interpretation from this behavior, because the SSF and gravitational self-force are both gauge-dependent results (though in the SSF case the gauge is simply set by the overall spacetime coordinates).

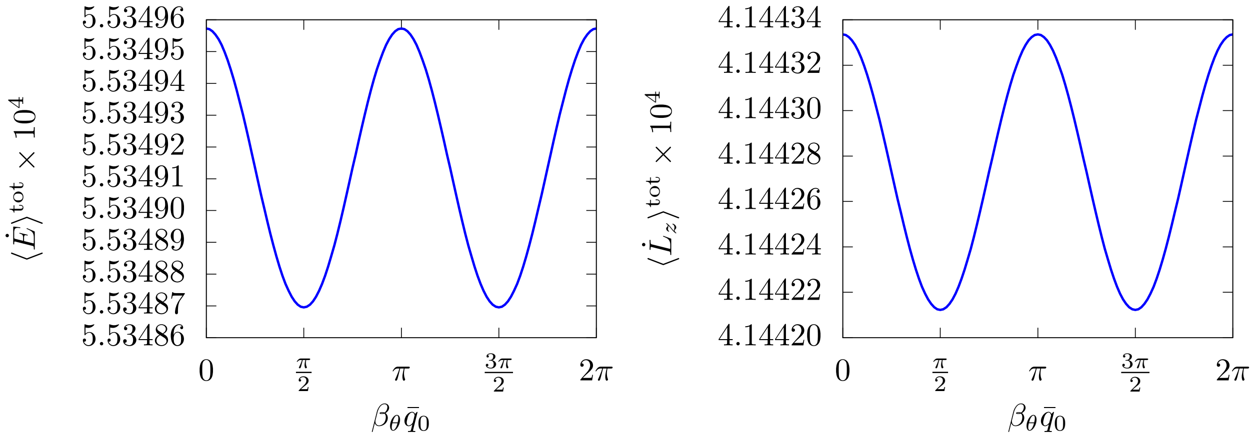

Figure 8.10: The total energy and angular momentum fluxes, $\langle \dot{E} \rangle^{\mathrm{tot}}$ and $\langle \dot{L}_z \rangle^{\mathrm{tot}}$ for a resonant scalar source with orbital parameters $(a, p, e, x_{\mathrm{inc}}) = (0.9, 4.607, 0.5, \cos\pi/4)$ ($e05.12$ in Table 8.1). The fluxes vary with respect to the initial phase $\bar{q}_0$, though these variations are small.

the SSF data for the highly-eccentric ($e = 0.5$) sources are only accurate to a few digits, as discussed in Sec. 8.3.1. A limited ability to numerically extract higher-order regularization parameters ultimately limits the accuracy of the $e = 0.5$ SSF values. This is particularly apparent in Fig. 8.8 for the $e05.13$ source. The numerical noise that is introduced by fitting for the higher-order regularization parameters eventually dominates $\hat{F}_\theta$ as its values pass close to and through zero. This leads to disjointed variations in $\hat{F}_\theta$ centered around $q_r + q_{r0} = \pi$ in the bottom left plot of Fig. 8.8. Therefore, to extract numerical values of $\hat{F}_\theta$ around $q_r + q_{r0} = \pi$, I will need to rerun this calculation with additional numerical precision. However, in the rest of the plot, the numerical noise is subdominant to the physical variation in the SSF.

Section 8.4: Resonant fluxes

Using Eqs. (8.40) and (8.41), I calculate the scalar wave fluxes $\langle \dot{E} \rangle^{\mathrm{tot}}$ and $\langle \dot{L}_z \rangle^{\mathrm{tot}}$. As discussed earlier, the fluxes, like the SSF, vary with respect to the initial phase $\bar{q}_0$. Figure 8.10 illustrates this variation for the $e05.12$ resonant orbit. While both fluxes certainly oscillate with the initial phase, their fractional variations are small, i.e., $\Delta \dot{E}^{\mathrm{tot}} = 0.036\%$ and $\Delta \dot{L}_z^{\mathrm{tot}} = 0.085\%$, where [101]

$$\Delta X \equiv 2 \left| \frac{\max\left[\langle X \rangle\right] - \min\left[\langle X \rangle\right]}{\max\left[\langle X \rangle\right] + \min\left[\langle X \rangle\right]} \right| . \tag{8.47}$$

The skeptical reader may be concerned that these variations are not physical but the result of numerical error. However, flux calculations are exponentially convergent and do not require regularization. These fluxes, therefore, are much more accurate than the previously discussed SSF results, with fractional errors that I found to be $\sim 10^{-8}$. The small fractional variations seen in Fig. 8.10 are therefore accurate to many

source	$\langle \dot{E} \rangle^{\mathcal{H}} \times 10^5$	$\langle \dot{L}_z \rangle^{\mathcal{H}} \times 10^4$	$\langle \dot{E} \rangle^{\infty} \times 10^3$	$\langle \dot{L}_z \rangle^{\infty} \times 10^3$	$\left\lvert 1 + \frac{\langle \dot{E} \rangle^{\mathrm{tot}}}{\mathcal{W}} \right\rvert$	$\left\lvert 1 + \frac{\langle \dot{L}_z \rangle^{\mathrm{tot}}}{\mathcal{T}} \right\rvert$
$e02.13$	-4.411457095	-7.017966266	1.301535	7.677846	9×10^{-7}	8×10^{-7}
$e02.12$	-2.021123696	-3.395925026	0.5737075	4.843929	2×10^{-8}	2×10^{-8}
$e02.23$	-0.324830139	-0.877896699	0.134964247	1.762343845	6×10^{-9}	3×10^{-11}
$e05.13$	-0.482340196	-6.445882073	1.45739	7.28846	9×10^{-5}	8×10^{-5}
$e05.12$	-0.364726314	-2.915401042	0.590229	3.85672	3×10^{-5}	2×10^{-5}
$e05.23$	0.092800200	-0.713304108	0.12832694	1.3990094	3×10^{-7}	2×10^{-7}

Table 8.2: The resonant energy and angular momentum fluxes for the scalar sources listed in Table 8.1. Fluxes through the horizon, $\langle \dot{E} \rangle^{\mathcal{H}}$ and $\langle \dot{L}_z \rangle^{\mathcal{H}}$, and infinity, $\langle \dot{E} \rangle^{\infty}$ and $\langle \dot{L}_z \rangle^{\infty}$, are included. All quantities are evaluated along orbits with an initial phase $\bar{q}_0 = 0$ and are normalized by q^{-2}. The reported precision is limited by the accuracy of each calculation, though I truncate high-precision results at nine decimal places for brevity. The total fluxes are also compared to the local work and torque performed by the SSF, $\mathcal{W}$ and $\mathcal{T}$ via the flux balance relations. The fractional errors between the fluxes and orbit-averaged SSF range from $\sim 10^{-5} - 10^{-11}$ and reflect the numerical accuracy of the dissipative SSF results.

source	$\langle \dot{E} \rangle^{\mathcal{H}} \times 10^5$	$\langle \dot{L}_z \rangle^{\mathcal{H}} \times 10^4$	$\langle \dot{E} \rangle^{\infty} \times 10^3$	$\langle \dot{L}_z \rangle^{\infty} \times 10^3$	$\left\lvert 1 + \frac{\langle \dot{E} \rangle^{\mathrm{tot}}}{\mathcal{W}} \right\rvert$	$\left\lvert 1 + \frac{\langle \dot{L}_z \rangle^{\mathrm{tot}}}{\mathcal{T}} \right\rvert$
$e02.13$	-4.411497781	-7.017992874	1.301534	7.677831	7×10^{-7}	6×10^{-7}
$e02.12$	-2.021127357	-3.396083610	0.5736988	4.843824	2×10^{-8}	2×10^{-8}
$e02.23$	-0.325170299	-0.877675562	0.134984611	1.762586419	6×10^{-9}	3×10^{-11}
$e05.13$	-0.480744834	-6.448440589	1.45724	7.28681	9×10^{-5}	8×10^{-5}
$e05.12$	-0.361475840	-2.919310921	0.589990	3.85408	3×10^{-5}	2×10^{-5}
$e05.23$	0.090053088	-0.710893569	0.12855813	1.4017751	3×10^{-7}	2×10^{-7}

Table 8.3: The same as Table 8.2, but now all quantities are evaluated along orbits with an initial phase $\beta_\theta \bar{q}_0 = -\pi/2$.

source	$\Delta \dot{E}^{\mathcal{H}}$	$\Delta \dot{L}_z^{\mathcal{H}}$	$\Delta \dot{E}^{\infty}$	$\Delta \dot{L}_z^{\infty}$	$\Delta \dot{E}^{\mathrm{tot}}$	$\Delta \dot{L}_z^{\mathrm{tot}}$
$e02.13$	0.0011%	0.0004%	0.0001%	0.0002%	0.0001%	0.0003%
$e02.12$	0.0204%	0.0047%	0.0017%	0.0023%	0.0016%	0.0029%
$e02.23$	0.2008%	0.0252%	0.0156%	0.0138%	0.0129%	0.0158%
$e05.13$	1.1214%	0.0400%	0.0109%	0.0227%	0.0092%	0.0287%
$e05.12$	2.3850%	0.1352%	0.0427%	0.0684%	0.0352%	0.0849%
$e05.23$	5.8510%	0.3400%	0.1835%	0.1975%	0.1575%	0.2262%

Table 8.4: The fractional variation in the resonant fluxes for the scalar sources listed in Table 8.1. Fractional variations are reported to four decimal places for brevity.

digits and are physical and consistent with observations of the resonant fluxes in the gravitational case [101]. In Table 8.2 I present the value of the fluxes at $\bar{q}_0 = 0$, while in Table 8.3 I report their values at $\beta_\theta \bar{q}_0 = -\pi/2$. In Table 8.4 I give the fractional variations of the fluxes as defined by Eq. (8.47). For the 1:2 and 1:3 resonances, the fluxes reach their maximum at $\bar{q}_0$ (see Fig. 8.10). On the other hand, the fluxes of the 2:3 sources are minimized at $\bar{q}_0 = 0$.

As shown in Tables 8.2 and 8.3, most of the horizon fluxes are negative due to superradiant scattering [167]. Orbits with smaller pericenter values r_{min} tend to produce larger fluxes, while the eccentricity of an orbit has a much smaller impact. I also compare these flux values to the average work and torque done by the SSF. The fractional errors from this comparison are given in the last two columns of Tables 8.2 and 8.3. I find good agreement between the fluxes and my SSF results, with fractional errors of $\sim 10^{-6}$. Recalling the numerical convergence of the SSF reported in Fig. 8.1, these fractional errors are indicative of the numerical accuracy of my results.

Table 8.4 demonstrates that the variations in the fluxes tend to increase as p and e increase. In fact, the flux variations for the e02.13 source are negligible compared to the other sources. This suggests that this variation is dampened as a source moves closer to the MBH. While e05.13 has a smaller pericenter value than e02.13, the larger variation in the radial motion could then be responsible for the larger variation in the fluxes with respect to the phase $\bar{q}_0$.

Section 8.5: Impact of conservative self-force and the integrability conjecture

While the conservative component of the SSF is often ignored when computing fluxes and time-averaged quantities, researchers are still uncertain whether or not the conservative self-force will contribute to the evolution of the Carter constant during resonances [100, 140]. Therefore, I investigated this open problem with my resonant SSF results. Figure 8.11 plots $\langle \dot{Q} \rangle^{\mathrm{tot}}$, the average time-rate-of-change of the Carter constant, for the resonant source e02.23. I calculate $\langle \dot{Q} \rangle^{\mathrm{tot}}$ using the balance formula

$$\langle \dot{Q} \rangle^{\mathrm{tot}} = -\mathcal{K}, \tag{8.48}$$

where $\mathcal{K}$ is given in Eq. (8.44). In the left plot of Fig. 8.11, the solid (red) line gives the value of $\langle \dot{Q} \rangle^{\mathrm{tot}}$ when it is evaluated using the full SSF (dissipative plus conservative), while the dashed (black) line plots the value of $\langle \dot{Q} \rangle^{\mathrm{tot}}$ when it is evaluated using only the dissipative component of the SSF. In the right plot, $\langle \dot{Q} \rangle^{\mathrm{tot}}$ is evaluated using only the conservative SSF.

Comparing these two plots, the contribution from the dissipative component clearly dominates that of

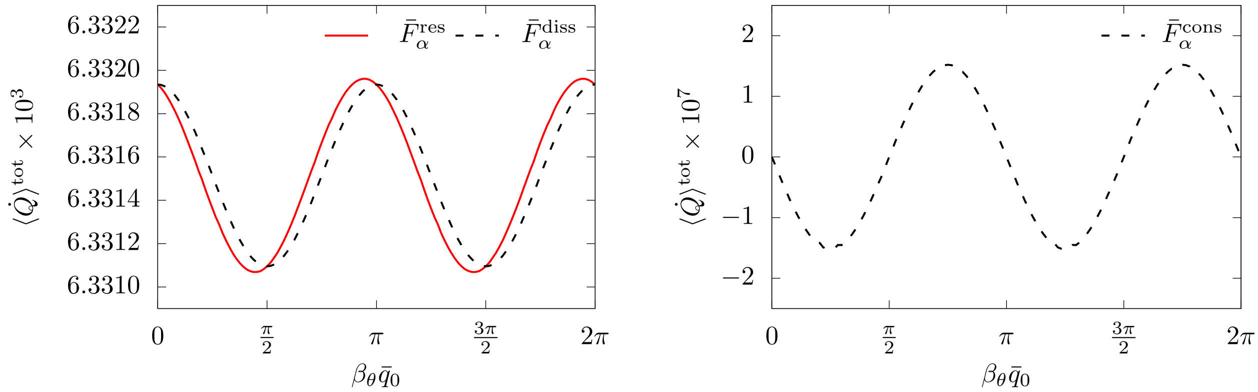

Figure 8.11: The average time-rate-of-change of the Carter constant $\langle \dot{Q} \rangle^{\rm tot}$ for the resonant source $(a, p, e, x_{\rm inc}) = (0.9, 6.643, 0.2, \cos \pi/4)$. In the left panel, the solid (red) line represents the value of $\langle \dot{Q} \rangle^{\rm tot}$ when it is constructed using the full SSF, $\hat{F}_\alpha^{\rm res}$, in Eq. (8.44). The dashed (black) line represents the value of $\langle \dot{Q} \rangle^{\rm tot}$ when it is constructed using just the dissipative component of the SSF $\hat{F}_\alpha^{\rm diss}$. As seen with the energy and angular momentum fluxes, $\langle \dot{Q} \rangle^{\rm tot}$ varies with the initial phase of the source $\bar{q}_0$. In the right planel, the black (dashed) line represents the value of $\langle \dot{Q} \rangle^{\rm tot}$ when it is calculated using only the conservative SSF components $\hat{F}_\alpha^{\rm cons}$. Note that the left plot is scaled by 10^3, while the right plot is scaled by 10^7. Thus, the conservative contribution is about four orders of magnitude weaker than the dissipative contribution.

the conservative component. However, the conservative contribution does not vanish and produces a small shift and change in the magnitude of the variations of $\langle \dot{Q} \rangle^{\rm tot}$. This initially suggests that the conservative SSF *does* contribute to the evolution of $\mathcal{Q}$. Further analysis shows, however, that the residual conservative contribution is smaller than my estimated numerical error due to the mode-sum regularization procedure and the attendant numerical fitting of the higher-order regularization parameters. This estimated error is $\sim 5 \times 10^{-7}$. Therefore, within the numerical tolerances of this code, the conservative contribution is consistent with zero.

However, the conservative contribution in the right plot of Fig. 8.11 has a much smoother behavior than what one might expect for numerical noise. To understand this behavior, consider that for a non-resonant orbit one can calculate $\mathcal{W}$, $\mathcal{T}$, and $\mathcal{K}$ without regularizing the SSF, because the singular field averages away when integrated over the course of the orbit. However, this is not the case for resonant orbits. Figure 8.12 demonstrates the effect of neglecting regularization when calculating $\langle \dot{Q} \rangle^{\rm tot}$. As one sums over additional l-modes the singular contribution to $\langle \dot{Q} \rangle^{\rm tot}$ does not average away, but instead diverges (for $\beta_\theta \bar{q}_0 \neq 0, \pi/2, \pi, 3\pi/2$). The growing singular contribution also varies in the exact same manner as the conservative contribution in Fig. 8.11. Subtracting the analytically-known regularization parameters, A_α and B_α, leads to a convergent result, but unless one sums over an infinite number of modes this does not completely remove the presence of the singular field.

Therefore, I argue that the (fully regularized) conservative component of the SSF is not responsible for the non-vanishing variations in the right plot of Fig. 8.11. Instead, this "conservative contribution" results

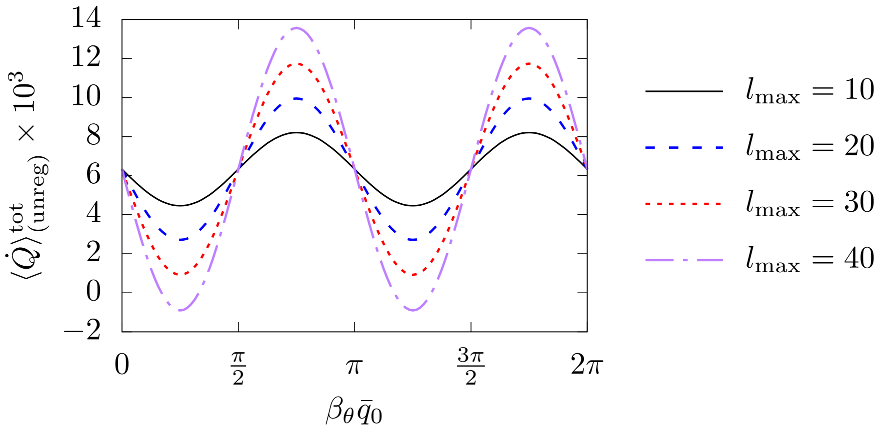

Figure 8.12: The average time-rate-of-change of the Carter constant $\langle\dot{Q}\rangle^{\rm tot}_{\rm (unreg)}$ calculated from the unregularized SSF results for the resonant source $(a, p, e, x_{\rm inc}) = (0.9, 6.643, 0.2, \cos\pi/4)$. The solid (black) line refers to the value of $\langle\dot{Q}\rangle^{\rm tot}_{\rm (unreg)}$ if one truncates the calculation of the unregularized SSF at $l_{\rm max} = 10$. Likewise, the dashed (blue) line refers to result after truncating calculations at $l_{\rm max} = 20$, the dotted (red) line for truncating at $l_{\rm max} = 30$, and the dot dashed (purple) line for $l_{\rm max} = 40$. While these results are diverging, if one averages over the initial phase, the singular contributions vanishes.

from the residual singular field that has not been completely removed through mode-sum regularization. In effect, any residual contributions from the conservative SSF in $\mathcal{W}$, $\mathcal{T}$, and $\mathcal{K}$ most likely result from my numerically-fitted higher-order regularization parameters, which are not fully capturing (and then removing) the singular field. This suggests, based on Fig. 8.11, that my numerical fitting procedure regularized the SSF data of e02.23 down to an accuracy of $\sim 1 \times 10^{-7}$, which is slightly better than the estimated error of 5×10^{-7}.

Section 8.6: Significance of results

In this chapter I presented the first numerical calculations of the strong-field (scalar) self-force for $r\theta$-resonant orbits in Kerr spacetime. This serves as a first step in understanding the still unquantified behavior of the gravitational self-force during transient resonances. While constructing these results, I found that a simple mapping exists between self-force calculations for fiducial, non-resonant orbits and self-force calculations for non-fiducial, resonant orbits. This mapping provides an efficient method for analyzing the self-force as a function of the initial phase at which a system enters resonance.

With my novel self-force calculations I also analyzed the impact of the conservative self-force on the orbit-averaged time-rate-of-change of the Carter constant, $\langle\dot{Q}\rangle^{\rm tot}$, to test the "integrability conjecture" proposed by Flanagan and Hinderer [100]. While the conservative SSF makes a small contribution to $\langle\dot{Q}\rangle^{\rm tot}$, it appears that this contribution results from errors in the mode-sum regularization procedure, rather than being connected to a physical effect. Ultimately, these results do demonstrate that any possible conservative contribution is subdominant to that of the dissipative self-force. Understanding the source of this residual conservative contribution, however, will require alternative, improved regularization schemes or access to analytic expressions for the higher-order regularization parameters. For now, the validity of the “integrability conjecture” remains an open question.

CHAPTER 9: Conclusion

Section 9.1: Summary of dissertation research

For this dissertation, I used a developmental scalar field model to investigate numerical and analytical techniques for calculating self-force effects in EMRIs with a Kerr primary. In this scalar problem, a point scalar charge follows a generic bound geodesic in Kerr spacetime and experiences a backreaction to its motion from a scalar self-force (SSF). Thus the scalar problem is similar to but mathematically more tractable than the gravitational self-force problem, making it a powerful tool for developing new computational algorithms. A *Mathematica* code was designed to perform these calculations in the frequency domain, mirroring current methods for calculating the gravitational self-force in Kerr spacetime [222, 224]. A novel feature of this code is the use of fast spectral source integration techniques to reduce expensive two-dimensional source integrals to successive one-dimensional Fourier sums (Sec. 5.3.3). These methods prove to be three orders of magnitude more efficient than traditional adaptive-step-size methods [175, 172]. These same techniques were also used to numerically integrate Kerr geodesics (Sec. 2.7). I have incorporated these methods in the openly-available KerrGeodesics *Mathematica* package of the Black Hole Perturbation Toolkit [1].

Several other key optimizations were also found to improve the calculation of scalar perturbations in the frequency domain. When implementing the Mano-Suzuki-Takasugi (MST) [154] function expansion method, Eq. (5.110) was found, empirically, to improve the convergence of the inner (scalar) Teukolsky radial solutions (Sec. 5.3.2). When determining the renormalized angular momentum parameter ν via monodromy techniques [68, 69], transforming to the confluent Heun equation improved the numerical calculation of the monodromy eigenvalue at infinity via Stokes multipliers (Sec. 5.3.2). Furthermore, when calculating the scalar spheroidal harmonics, the three-term recurrence relation for the coupling coefficients was recast in terms of continued fractions, which proved to be much faster to evaluate at higher-precisions compared to solving the recurrence relation with standard matrix methods (Sec. 5.3.1). I also outlined optimized procedures for constructing the SSF for both resonant (Sec. 8.2) and non-resonant sources (Sec. 5.3.4). A key result is that, by parameterizing the SSF in terms of the angle variables q_r and q_θ, the SSF due to a source with fiducial initial conditions, $\hat{x}_p^\mu(0) = (0, r_\mathrm{min}, \theta_\mathrm{min}, 0)$, can be directly related to the SSF due to a source with arbitrary initial conditions via Eq. (5.170). This provides an efficient method for evaluating the SSF along resonant orbits (Eq. (8.31)), which are sensitive to the initial phase at which the system enters resonance. This result also generalizes to the gravitational self-force case.

Using my SSF code, Osburn, Evans, and I [172] produced novel results for the SSF experienced by a scalar charge on inclined, eccentric geodesics in Kerr spacetime (Sec. 6.4). In the process of computing the SSF for highly-eccentric ($e = 0.8$), equatorial orbits around a rapidly-rotating ($a/M = 0.99$) Kerr primary, we verified the existence of previously observed [214] quasinormal excitations in the SSF (Sec. 7.3). We then further searched for and observed quasinormal bursts (QNBs)—periodic bursts of quasinormal ringing—in the asymptotically observed (scalar) waveform itself (Sec. 7.4) [172]. I then produced the first calculation of the SSF due to $r\theta$-resonant orbits (Sec. 8.3). Using these resonant results, I demonstrated that the conservative component of the SSF makes a negligible, if not vanishing, contribution to the time-rate-of-change of the Carter constant $\langle \dot{Q} \rangle^{\mathrm{tot}}$ during resonances. This provides the first calculation of strong-field conservative effects during EMRI resonances, and is thus a key result of this dissertation.

Section 9.2: Future prospects

In future work, Evans and I hope to make a thorough survey of QNB strengths, including moving beyond equatorial orbits. Eccentric, inclined orbits may source stronger QNB excitations and will likely excite non-axial modes ($\hat{l} \neq m$). Part of this work will also focus on possible strategies for processing EMRI waveforms, such as matching templates or co-adding waveform segments, to try and draw QNBs out of the detector noise. I also plan on extending my investigation of EMRI $r\theta$-resonances by collaborating with other researchers to evolve scalar-charged EMRIs through resonances using my SSF results. This will provide a new step in understanding the currently unquantified long term radiation-reaction effects that arise during resonances.

Moving forward, I will also explore the overlap between post-Newtonian (PN) theory and black hole perturbation theory (BHPT). Analytic PN approximations can describe EMRIs in weak-field, low-frequency regimes. Consequently, researchers have produced analytic PN expressions for the time-averaged gravitational wave fluxes of EMRIs and expansions of conservative quantities, such as the generalized redshift invariant [80, 107, 50, 143, 105, 131, 171]. Looking to extend this work, I am building a *Mathematica* code to produce purely analytic PN expansions of scalar and gravitational self-force quantities for EMRIs with Kerr MBH primaries to first-order in the mass-ratio. These PN expansions can then be incorporated in numerical calculations to rapidly evaluate low-frequency solutions to the Teukolsky equation. Future work also aims to incorporate PN results in the mode-sum regularization procedure to improve the convergence of self-force results [124].

Lastly, I plan on generalizing many of the methods and techniques developed in this work to design a new code that calculates gravitational wave fluxes and the gravitational self-force. Much of my SSF code is already set up to calculate gravitational as well as scalar perturbations using the Teukolsky formalism, providing a firm foundation for this future work.

REFERENCES

[1] Black Hole Perturbation Toolkit. `bhptoolkit.org`.

[2] Einstein Toolkit homepage. `https://einsteintoolkit.org/`.

[3] KAGRA homepage. `http://gwcenter.icrr.u-tokyo.ac.jp/en/`.

[4] LIGO homepage. `http://www.ligo.caltech.edu/`.

[5] LISA homepage. `http://sci.esa.int/lisa/`.

[6] NASA LISA Project Office homepage. `http://lisa.nasa.gov`.

[7] Spectral Einstein Code homepage. `http://www.black-holes.org/SpEC.html`.

[8] Virgo homepage. `https://www.virgo-gw.eu/`.

[9] ESA: Next steps for LISA, 2019. `http://sci.esa.int/science-e/www/object/index.cfm?fobjectid=48728`.

[10] B. P. Abbott et al., (The LIGO Scientific Collaboration, and the Virgo Collaboration). Astrophysical Implications of the Binary Black-hole Merger GW150914. *The Astrophysical Journal Letters*, 818:L22, February 2016.

[11] B. P. Abbott et al., (The LIGO Scientific Collaboration, and the Virgo Collaboration). GW150914: First results from the search for binary black hole coalescence with Advanced LIGO. *Phys. Rev. D*, 93:122003, Jun 2016.

[12] B. P. Abbott et al., (The LIGO Scientific Collaboration, and the Virgo Collaboration). GW151226: Observation of Gravitational Waves from a 22-Solar-Mass Binary Black Hole Coalescence. *Physical Review Letters*, 116:241103, Jun 2016.

[13] B. P. Abbott et al., (The LIGO Scientific Collaboration, and the Virgo Collaboration). Tests of General Relativity with GW150914. *Physical Review Letters*, 116:221101, May 2016.

[14] B. P. Abbott et al., (The LIGO Scientific Collaboration, and the Virgo Collaboration). A gravitational-wave standard siren measurement of the Hubble constant. *Nature*, 551(7678):85–88, November 2017.

[15] B. P. Abbott et al., (The LIGO Scientific Collaboration, and the Virgo Collaboration). Gravitational Waves and Gamma-Rays from a Binary Neutron Star Merger: GW170817 and GRB 170817A. *The Astrophysical Journal Letters*, 848:L13, October 2017.

[16] B. P. Abbott et al., (The LIGO Scientific Collaboration, and the Virgo Collaboration). GW170104: Observation of a 50-Solar-Mass Binary Black Hole Coalescence at Redshift 0.2. *Physical Review Letters*, 118:221101, Jun 2017.

[17] B. P. Abbott et al., (The LIGO Scientific Collaboration, and the Virgo Collaboration). GW170608: Observation of a 19 Solar-mass Binary Black Hole Coalescence. *The Astrophysical Journal Letters*, 851:L35, December 2017.

[18] B. P. Abbott et al., (The LIGO Scientific Collaboration, and the Virgo Collaboration). GW170814: A Three-Detector Observation of Gravitational Waves from a Binary Black Hole Coalescence. *Physical Review Letters*, 119(14):141101, October 2017.

[19] B. P. Abbott et al., (The LIGO Scientific Collaboration, and the Virgo Collaboration). GW170817: Observation of Gravitational Waves from a Binary Neutron Star Inspiral. *Physical Review Letters*,

119:161101, Oct 2017.

[20] B. P. Abbott et al., (The LIGO Scientific Collaboration, and the Virgo Collaboration). Multi-messenger Observations of a Binary Neutron Star Merger. *The Astrophysical Journal Letters*, 848:L12, October 2017.

[21] B. P. Abbott et al., (The LIGO Scientific Collaboration, and the Virgo Collaboration). GW170817: Measurements of Neutron Star Radii and Equation of State. *APhysical Review Letters*, 121(16):161101, October 2018.

[22] B. P. Abbott et al., (The LIGO Scientific Collaboration, and the Virgo Collaboration). GWTC-1: A Gravitational-Wave Transient Catalog of Compact Binary Mergers Observed by LIGO and Virgo during the First and Second Observing Runs. *Phys. Rev. X*, 9:031040, Sep 2019.

[23] B. P. Abbott et al., (The LIGO Scientific Collaboration, and the Virgo Collaboration). GW190425: Observation of a Compact Binary Coalescence with Total Mass $\sim 3.4\ M_{\odot}$. *The Astrophysical Journal*, 892(1):L3, Mar 2020.

[24] M. Alcubierre. *Introduction to 3+1 Numerical Relativity.* Oxford University Press, UK, 2008.

[25] P. Amaro-Seoane, S. Aoudia, S. Babak, P. Binétruy, E. Berti, A. Bohé, C. Caprini, M. Colpi, N. J. Cornish, K. Danzmann, J.-F. Dufaux, J. Gair, I. Hinder, O. Jennrich, P. Jetzer, A. Klein, R. N. Lang, A. Lobo, T. Littenberg, S. T. McWilliams, G. Nelemans, A. Petiteau, E. K. Porter, B. F. Schutz, A. Sesana, R. Stebbins, T. Sumner, M. Vallisneri, S. Vitale, M. Volonteri, H. Ward, and B. Wardell. eLISA: Astrophysics and cosmology in the millihertz regime. *GW Notes, Vol. 6, p. 4-110*, 6:4–110, May 2013.

[26] P. Amaro-Seoane, J. R. Gair, A. Pound, S. A. Hughes, and C. F. Sopuerta. Research Update on Extreme-Mass-Ratio Inspirals. In *Journal of Physics Conference Series*, volume 610 of *Journal of Physics Conference Series*, page 012002, May 2015.

[27] S. Babak, J. Gair, A. Sesana, E. Barausse, C. F. Sopuerta, C. P. L. Berry, E. Berti, P. Amaro-Seoane, A. Petiteau, and A. Klein. Science with the space-based interferometer LISA. V. Extreme mass-ratio inspirals. *Phys. Rev. D*, 95(10):103012, May 2017.

[28] J. Baker, J. Bellovary, P. L. Bender, E. Berti, R. Caldwell, J. Camp, J. W. Conklin, N. Cornish, C. Cutler, R. DeRosa, M. Eracleous, E. C. Ferrara, S. Francis, M. Hewitson, K. Holley-Bockelmann, A. Hornschemeier, C. Hogan, B. Kamai, B. J. Kelly, J. Shapiro Key, S. L. Larson, J. Livas, S. Manthripragada, K. McKenzie, S. T. McWilliams, G. Mueller, P. Natarajan, K. Numata, N. Rioux, S. R. Sankar, J. Schnittman, D. Shoemaker, D. Shoemaker, J. Slutsky, R. Spero, R. Stebbins, I. Thorpe, M. Vallisneri, B. Ware, P. Wass, A. Yu, and J. Ziemer. The Laser Interferometer Space Antenna: Unveiling the Millihertz Gravitational Wave Sky. *arXiv e-prints*, page arXiv:1907.06482, July 2019.

[29] J. G. Baker, J. Centrella, D. Choi, M. Koppitz, and J. van Meter. Gravitational wave extraction from an inspiraling configuration of merging black holes. *Physical Review Letters*, 96:111102, 2006.

[30] L. Barack. Gravitational self force in extreme mass-ratio inspirals. *Class. Quant. Grav.*, 26:213001, 2009.

[31] L. Barack and L. M. Burko. Radiation-reaction force on a particle plunging into a black hole. *Phys. Rev. D*, 62:084040, 2000.

[32] L. Barack and C. Cutler. Using LISA EMRI sources to test off-Kerr deviations in the geometry of massive black holes. *Phys. Rev. D*, 75:042003, 2007.

[33] L. Barack and P. Giudice. Time-domain metric reconstruction for self-force applications. *Phys. Rev.*

D, 95(10):104033, May 2017.

[34] L. Barack and D. A. Golbourn. Scalar-field perturbations from a particle orbiting a black hole using numerical evolution in 2+1 dimensions. *Physical Review D*, 76(4):044020, August 2007.

[35] L. Barack, D. A. Golbourn, and N. Sago. m-mode regularization scheme for the self-force in Kerr spacetime. *Phys. Rev. D*, 76(12):124036, December 2007.

[36] L. Barack and C. O. Lousto. Perturbations of Schwarzschild black holes in the Lorenz gauge: Formulation and numerical implementation. *Phys. Rev. D*, 72:104026, 2005.

[37] L. Barack and A. Ori. Mode sum regularization approach for the self force in black hole spacetime. *Phys. Rev. D*, 61:061502(R), 2000.

[38] L. Barack and A. Ori. Gravitational self force and gauge transformations. *Phys. Rev. D*, 64:124003, 2001.

[39] L. Barack and A. Ori. Gravitational self-force on a particle orbiting a Kerr black hole. *Physical Review Letters*, 90:111101, 2003.

[40] L. Barack, A. Ori, and N. Sago. Frequency-domain calculation of the self-force: The high-frequency problem and its resolution. *Phys. Rev. D*, 78(8):084021, October 2008.

[41] L. Barack and A. Pound. Self-force and radiation reaction in general relativity. *Reports on Progress in Physics*, 82(1):016904, January 2019.

[42] L. Barack and N. Sago. Gravitational self force on a particle in circular orbit around a Schwarzschild black hole. *Phys. Rev. D*, 75:064021, 2007.

[43] L. Barack and N. Sago. Gravitational self-force on a particle in eccentric orbit around a Schwarzschild black hole. *Phys. Rev. D*, 81(8):084021, April 2010.

[44] T. W. Baumgarte and S. L. Shapiro. *Numerical Relativity: Solving Einstein's Equations on the Computer*. Cambridge University Press, June 2010.

[45] P. G. Bergmann. Summary of the Chapel Hill Conference. *Rev. Mod. Phys.*, 29:352–354, Jul 1957.

[46] L. Bernard, L. Blanchet, A. Bohé, G. Faye, and S. Marsat. Fokker action of nonspinning compact binaries at the fourth post-Newtonian approximation. *Phys. Rev. D*, 93(8):084037, April 2016.

[47] C. Berry, S. Hughes, C. Sopuerta, A. Chua, A. Heffernan, K. Holley-Bockelmann, D. Mihaylov, C. Miller, and A. Sesana. The unique potential of extreme mass-ratio inspirals for gravitational-wave astronomy. *Bull. Am. Astron. Soc.*, 51(3):42, May 2019.

[48] C. P. L. Berry, R. H. Cole, P. Cañizares, and J. R. Gair. Importance of transient resonances in extreme-mass-ratio inspirals. *Phys. Rev. D*, 94:124042, Dec 2016.

[49] E. Berti, V. Cardoso, and A. O. Starinets. Quasinormal modes of black holes and black branes. *Classical and Quantum Gravity*, 26(16):163001, jul 2009.

[50] D. Bini and T. Damour. High-order post-Newtonian contributions to the two-body gravitational interaction potential from analytical gravitational self-force calculations. *Phys. Rev. D*, 89(6):064063, March 2014.

[51] D. Bini, T. Damour, and A. Geralico. Novel approach to binary dynamics: application to the fifth post-Newtonian level. *Phys. Rev. Lett.*, 123(23):231104, Dec 2019.

[52] L. Blanchet. Gravitational Radiation from Post-Newtonian Sources and Inspiralling Compact Binaries. *Living Reviews in Relativity*, 17:2, February 2014.

[53] D. R. Brill, P. L. Chrzanowski, C. M. Pereira, E. D. Fackerell, and J. R. Ipser. Solution of the Scalar Wave Equation in a Kerr Background by Separation of Variables. *Phys. Rev. D*, 5:1913–1915, April 1972.

[54] J. Brink, M. Geyer, and T. Hinderer. Astrophysics of resonant orbits in the Kerr metric. *Phys. Rev. D*, 91(8):083001, Apr 2015.

[55] J. Brink, M. Geyer, and T. Hinderer. Orbital Resonances Around Black Holes. *APhysical Review Letters*, 114(8):081102, Feb 2015.

[56] L. M. Burko. Self force on particle in orbit around a black hole. *Physical Review Letters*, 84:4529, 2000.

[57] L. M. Burko. Self-force on static charges in Schwarzschild spacetime. *Classical and Quantum Gravity*, 17:227–250, January 2000.

[58] L. M. Burko, A. I. Harte, and E. Poisson. Mass loss by a scalar charge in an expanding universe. *Phys. Rev. D*, 65(12):124006, June 2002.

[59] C. Buss and M. Casals. Quantum correlator outside a Schwarzschild black hole. *Physics Letters B*, 776:168–173, January 2018.

[60] P. Cañizares and C. F. Sopuerta. Efficient pseudospectral method for the computation of the self-force on a charged particle: Circular geodesics around a Schwarzschild black hole. *Phys. Rev. D*, 79(8):084020, April 2009.

[61] M. Campanelli, C. O. Lousto, P. Marronetti, and Y. Zlochower. Accurate evolutions of orbiting black-hole binaries without excision. *Physical Review Letters*, 96:111101, Mar 2006.

[62] P. Canizares, C. F. Sopuerta, and J. L. Jaramillo. Pseudospectral collocation methods for the computation of the self-force on a charged particle: Generic orbits around a Schwarzschild black hole. *Phys. Rev. D*, 82(4):044023, August 2010.

[63] S. M. Carroll. *Spacetime and Geometry: An Introduction to General Relativity.* Cambridge University Press, 2019.

[64] B. Carter. Global structure of the kerr family of gravitational fields. *Phys. Rev.*, 174:1559–1571, Oct 1968.

[65] B. Carter. Axisymmetric Black Hole Has Only Two Degrees of Freedom. *APhysical Review Letters*, 26(6):331–333, February 1971.

[66] M. Casals, S. Dolan, A. C. Ottewill, and B. Wardell. Self-force calculations with matched expansions and quasinormal mode sums. *Phys. Rev. D*, 79(12):124043, June 2009.

[67] M. Casals, S. Dolan, A. C. Ottewill, and B. Wardell. Self-force and Green function in Schwarzschild spacetime via quasinormal modes and branch cut. *Phys. Rev. D*, 88(4):044022, August 2013.

[68] A. Castro, J. M. Lapan, A. Maloney, and M. J. Rodriguez. Black hole monodromy and conformal field theory. *Phys. Rev. D*, 88(4):044003, August 2013.

[69] A. Castro, J. M. Lapan, A. Maloney, and M. J. Rodriguez. Black hole scattering from monodromy. *Classical and Quantum Gravity*, 30(16):165005, August 2013.

[70] S. Chandrasekhar. On the Equations Governing the Perturbations of the Schwarzschild Black Hole. *Royal Society of London Proceedings Series A*, 343:289–298, May 1975.

[71] S. Chandrasekhar and S. Detweiler. On the equations governing the axisymmetric perturbations of the Kerr black hole. *Royal Society of London Proceedings Series A*, 345:145–167, August 1975.

[72] P. L. Chrzanowski. Vector potential and metric perturbations of a rotating black hole. *Phys. Rev. D*, 11:2042–2062, 1975.

[73] J. M. Cohen and L. S. Kegeles. Electromagnetic fields in curved spaces - a constructive procedure. *Phys. Rev. D*, 10:1070–1084, 1974.

[74] G. Compère, K. Fransen, T. Hertog, and Y. Liu. Scalar self-force for high spin black holes. *Phys. Rev. D*, 101(6):064006, March 2020.

[75] C. T. Cunningham, R. H. Price, and V. Moncrief. Radiation from collapsing relativistic stars. I. Linearized odd-parity radiation. *Astrophys. J.*, 224:643–667, 1978.

[76] A. B. Olde Daalhuis and F. W. J. Olver. On the calculation of stokes multipliers for linear differential equations of the second order. *Methods Appl. Anal.*, pages 348–67, 1995.

[77] T. Damour, P. Jaranowski, and G. Schäfer. Nonlocal-in-time action for the fourth post-newtonian conservative dynamics of two-body systems. *Phys. Rev. D*, 89:064058, Mar 2014.

[78] T. Damour, P. Jaranowski, and G. Schäfer. Conservative dynamics of two-body systems at the fourth post-Newtonian approximation of general relativity. *Phys. Rev. D*, 93(8):084014, April 2016.

[79] C. Darwin. The Gravity Field of a Particle. II. *Proceedings of the Royal Society of London Series A*, 263:39–50, August 1961.

[80] S. Detweiler. A consequence of the gravitational self-force for circular orbits of the Schwarzschild geometry. *Phys. Rev. D*, 77:124026, 2008.

[81] S. Detweiler, E. Messaritaki, and B. F. Whiting. Self-force of a scalar field for circular orbits about a Schwarzschild black hole. *Phys. Rev. D*, 67:104016, 2003.

[82] S. L. Detweiler and B. F. Whiting. Self-force via a Green's function decomposition. *Phys. Rev. D*, 67:024025, 2003.

[83] B. S. DeWitt and R. W. Brehme. Radiation damping in a gravitational field. *Annals of Physics*, 9:220–259, February 1960.

[84] L. M. Diaz-Rivera, E. Messaritaki, B. F. Whiting, and S. Detweiler. Scalar field self-force effects on orbits about a Schwarzschild black hole. *Phys. Rev. D*, 70(12):124018, December 2004.

[85] P. Diener, I. Vega, B. Wardell, and S. Detweiler. Self-Consistent Orbital Evolution of a Particle around a Schwarzschild Black Hole. *Physical Review Letters*, 108(19):191102, May 2012.

[86] P. A. M. Dirac. Classical theory of radiating electrons. *Proc. R. Soc. London, Ser. A*, 167:148, 1938.

[87] S. R. Dolan. Electromagnetic fields on Kerr spacetime, Hertz potentials, and Lorenz gauge. *Phys. Rev. D*, 100(4):044044, August 2019.

[88] S. R. Dolan and L. Barack. Self-force via m-mode regularization and 2+1D evolution: Foundations and a scalar-field implementation on Schwarzschild spacetime. *Phys. Rev. D*, 83(2):024019, January 2011.

[89] S. R. Dolan and L. Barack. Self-force via m-mode regularization and 2+1 evolution. iii. gravitational field on schwarzschild spacetime. *Phys. Rev. D*, 87:084066, Apr 2013.

[90] S. R. Dolan, L. Barack, and B. Wardell. Self-force via m-mode regularization and 2+1D evolution. II. Scalar-field implementation on Kerr spacetime. *Phys. Rev. D*, 84(8):084001, October 2011.

[91] S. Drasco, É. É. Flanagan, and S. A. Hughes. Computing inspirals in Kerr in the adiabatic regime: I. The scalar case. *Classical and Quantum Gravity*, 22:S801–S846, August 2005.

[92] S. Drasco and S. A. Hughes. Rotating black hole orbit functionals in the frequency domain. *Phys. Rev. D*, 69:044015, Feb 2004.

[93] S. Drasco and S. A. Hughes. Gravitational wave snapshots of generic extreme mass ratio inspirals. *Phys. Rev. D*, 73(2):024027, January 2006.

[94] A. S. Eddington. The propagation of gravitational waves. *Proceedings of the Royal Society of London. Series A, Containing Papers of a Mathematical and Physical Character*, 102(716):268–282, 1922.

[95] A. Einstein. Näherungsweise Integration der Feldgleichungen der Gravitation. *Sitzungsberichte der Königlich Preußischen Akademie der Wissenschaften (Berlin*, pages 688–696, January 1916.

[96] A. Einstein. Über Gravitationswellen. *Sitzungsberichte der Königlich Preußischen Akademie der Wissenschaften (Berlin), Seite 154-167.*, 1918. `http://echo.mpiwg-berlin.mpg.de/MPIWG:8HSP60BU`.

[97] A. Einstein, L. Infeld, and B. Hoffmann. The gravitational equations and the problem of motion. *Annals of Mathematics*, 39(1):65–100, 1938.

[98] A. Einstein and N. Rosen. On Gravitational Waves. *Journal of The Franklin Institute*, 223:43–54, January 1937.

[99] J. A. Faber and F. A. Rasio. Binary Neutron Star Mergers. *Living Reviews in Relativity*, 15(1):8, July 2012.

[100] É. É. Flanagan and T. Hinderer. Transient resonances in the inspirals of point particles into black holes. *Physical Review Letters*, 109:071102, Aug 2012.

[101] É. É Flanagan, S. A. Hughes, and U. Ruangsri. Resonantly enhanced and diminished strong-field gravitational-wave fluxes. *Phys. Rev. D*, 89(8):084028, Apr 2014.

[102] V. A. Fock. On motion of finite masses in general relativity. *J. Phys. (Moscow)*, 1(2):81–116, 1939.

[103] S. Foffa, R. A. Porto, I. Rothstein, and R. Sturani. Conservative dynamics of binary systems to fourth post-Newtonian order in the EFT approach. II. Renormalized Lagrangian. *Phys. Rev. D*, 100(2):024048, July 2019.

[104] S. Foffa and R. Sturani. Conservative dynamics of binary systems to fourth post-Newtonian order in the EFT approach. I. Regularized Lagrangian. *Phys. Rev. D*, 100(2):024047, July 2019.

[105] E. Forseth, C. R. Evans, and S. Hopper. Eccentric-orbit extreme-mass-ratio inspiral gravitational wave energy fluxes to 7PN order. *Phys. Rev. D*, 93:064058, Mar 2016.

[106] V. P. Frolov and I. D. Novikov. *Black hole physics : basic concepts and new developments.* Springer, Dordrecht, 1998.

[107] R. Fujita. Gravitational Waves from a Particle in Circular Orbits around a Schwarzschild Black Hole to the 22nd Post-Newtonian Order. *Progress of Theoretical Physics*, 128:971–992, November 2012.

[108] R. Fujita and W. Hikida. Analytical solutions of bound timelike geodesic orbits in Kerr spacetime. *Classical and Quantum Gravity*, 26(13):135002, July 2009.

[109] R. Fujita, W. Hikida, and H. Tagoshi. An efficient numerical method for computing gravitational waves induced by a particle moving on eccentric inclined orbits around a Kerr black hole. *Prog. Theor. Phys.*, 121:843–874, 2009.

[110] R. Fujita, S. Isoyama, A. Le Tiec, H. Nakano, N. Sago, and T. Tanaka. Hamiltonian formulation of the conservative self-force dynamics in the Kerr geometry. *Classical and Quantum Gravity*, 34(13):134001, July 2017.

[111] R. Fujita and H. Tagoshi. New Numerical Methods to Evaluate Homogeneous Solutions of the Teukolsky Equation. II —Solutions of the Continued Fraction Equation —. *Progress of Theoretical Physics*, 113:1165–1182, June 2005.

[112] J. R. Gair, É. É. Flanagan, S. Drasco, T. Hinderer, and S. Babak. Forced motion near black holes. *Phys. Rev. D*, 83(4):044037, February 2011.

[113] D. V. Gal'tsov. Radiation reaction in the Kerr gravitational field. *Journal of Physics A: Mathematical and General*, 15(12):3737–3749, 1982.

[114] R. Geroch and J. Traschen. Strings and other distributional sources in general relativity. *Phys. Rev. D*, 36:1017–1031, 1987.

[115] S. E. Gralla, A. I. Harte, and R. M. Wald. Rigorous derivation of electromagnetic self-force. *Phys. Rev. D*, 80(2):024031, July 2009.

[116] P. Grandclément and J. Novak. Spectral Methods for Numerical Relativity. *Living Reviews in Relativity*, 12(1):1, January 2009.

[117] R. Grossman, J. Levin, and G. Perez-Giz. Faster computation of adiabatic extreme mass-ratio inspirals using resonances. *Phys. Rev. D*, 88:023002, Jul 2013.

[118] R. Haas. Scalar self-force on eccentric geodesics in Schwarzschild spacetime: A time-domain computation. *Phys. Rev. D*, 75:124011, 2007.

[119] J. Hadamard. *Lectures on Cauchy's problem in linear partial differential equations.* New Haven Yale University Press, 1923.

[120] S. G. Hahn and R. W. Lindquist. The two-body problem in geometrodynamics. *Annals of Physics*, 29(2):304–331, September 1964.

[121] A. Heffernan, A. Ottewill, and B. Wardell. High-order expansions of the Detweiler-Whiting singular field in Schwarzschild spacetime. *Phys. Rev. D*, 86:104023, Nov 2012.

[122] A. Heffernan, A. Ottewill, and B. Wardell. High-order expansions of the Detweiler-Whiting singular field in Kerr spacetime. *Phys. Rev. D*, 89:024030, Jan 2014.

[123] A. Heffernan, A. C. Ottewill, N. Warburton, B. Wardell, and P. Diener. Accelerated motion and the self-force in Schwarzschild spacetime. *Classical and Quantum Gravity*, 35(19):194001, October 2018.

[124] W. Hikida, S. Jhingan, H. Nakano, N. Sago, M. Sasaki, and T. Tanaka. A New Analytical Method for Self-Force Regularization. I —Charged Scalar Particles in Schwarzschild Spacetime —. *Progress of Theoretical Physics*, 111(6):821–840, June 2004.

[125] T. Hinderer and É. É. Flanagan. Two timescale analysis of extreme mass ratio inspirals in Kerr. I. Orbital Motion. *Phys. Rev. D*, 78:064028, 2008.

[126] C. M. Hirata. Resonant recoil in extreme mass ratio binary black hole mergers. *Phys. Rev. D*, 83(10):104024, May 2011.

[127] J. M. Hobbs. A vierbein formalism of radiation damping. *Annals of Physics*, 47(1):141 – 165, 1968.

[128] S. Hopper and C. R. Evans. Gravitational perturbations and metric reconstruction: Method of extended homogeneous solutions applied to eccentric orbits on a Schwarzschild black hole. *Phys. Rev. D*, 82(8):084010, Oct 2010.

[129] S. Hopper and C. R. Evans. Metric perturbations from eccentric orbits on a Schwarzschild black hole. I. Odd-parity Regge-Wheeler to Lorenz gauge transformation and two new methods to circumvent the Gibbs phenomenon. *Phys. Rev. D*, 87(6):064008, March 2013.

[130] S. Hopper, E. Forseth, T. Osburn, and C. R. Evans. Fast spectral source integration in black hole perturbation calculations. *Phys. Rev. D*, 92(4):044048, August 2015.

[131] S. Hopper, C. Kavanagh, and A. C. Ottewill. Analytic self-force calculations in the post-Newtonian regime: eccentric orbits on a Schwarzschild background. *Phys. Rev. D*, 93(4):044010, February 2016.

[132] S. A. Hughes. Computing radiation from Kerr black holes: Generalization of the Sasaki-Nakamura equation. *Phys. Rev. D*, 62(4):044029, August 2000.

[133] S. A. Hughes. Evolution of circular, nonequatorial orbits of Kerr black holes due to gravitational-wave emission. *Phys. Rev. D*, 61(8):084004, April 2000.

[134] S. A. Hughes. Evolution of circular, nonequatorial orbits of kerr black holes due to gravitational-wave emission. ii. inspiral trajectories and gravitational waveforms. *Phys. Rev. D*, 64:064004, Aug 2001.

[135] S. A. Hughes, S. Drasco, É. É. Flanagan, and J. Franklin. Gravitational radiation reaction and inspiral waveforms in the adiabatic limit. *Physical Review Letters*, 94:221101, 2005.

[136] R. A. Hulse and J. H. Taylor. Discovery of a pulsar in a binary system. *The Astrophysical Journal*, 195(2):L51–L53, 1975.

[137] R. A. Isaacson. Gravitational radiation in the limit of high frequency. i. the linear approximation and geometrical optics. *Phys. Rev.*, 166:1263–1271, Feb 1968.

[138] S. Isoyama, L. Barack, S. R. Dolan, A. Le Tiec, H. Nakano, A. G. Shah, T. Tanaka, and N. Warburton. Gravitational Self-Force Correction to the Innermost Stable Circular Equatorial Orbit of a Kerr Black Hole. *Physical Review Letters*, 113(16):161101, October 2014.

[139] S. Isoyama, R. Fujita, H. Nakano, N. Sago, and T. Tanaka. Evolution of the Carter constant for resonant inspirals into a Kerr black hole: I. The scalar case. *Progress of Theoretical and Experimental Physics*, 2013(6):063E01, June 2013.

[140] S. Isoyama, R. Fujita, H. Nakano, N. Sago, and T. Tanaka. Flux-balance formulae for extreme mass-ratio inspirals. *Progress of Theoretical and Experimental Physics*, 2019(1), 01 2019. 013E01.

[141] J. D. Jackson. *Classical electrodynamics; 3rd ed.* Wiley, New York, NY, 1999.

[142] R. E. Kates. Motion of a small body through an external field in general relativity calculated by matched asymptotic expansions. *Phys. Rev. D*, 22(8):1853–1870, October 1980.

[143] C. Kavanagh, A. C. Ottewill, and B. Wardell. Analytical high-order post-Newtonian expansions for extreme mass ratio binaries. *Phys. Rev. D*, 92(8):084025, 2015.

[144] L. S. Kegeles and J. M. Cohen. Constructive procedure for perturbations of space-times. *Phys. Rev.*

D, 19:1641–1664, 1979.

[145] T. S. Keidl, J. L. Friedman, and A. G. Wiseman. Finding fields and self-force in a gauge appropriate to separable wave equations. *Phys. Rev. D*, 75(12):124009, June 2007.

[146] T. S. Keidl, A. G. Shah, J. L. Friedman, D. Kim, and L. R. Price. Gravitational self-force in a radiation gauge. *Phys. Rev. D*, 82:124012, Dec 2010.

[147] W. Kinnersley. Type D Vacuum Metrics. *Journal of Mathematical Physics*, 10:1195–1203, July 1969.

[148] E. W. Leaver. An analytic representation for the quasi-normal modes of Kerr black holes. *Proceedings of the Royal Society of London Series A*, 402:285–298, December 1985.

[149] E. W. Leaver. Solutions to a generalized spheroidal wave equation: Teukolsky's equations in general relativity, and the two-center problem in molecular quantum mechanics. *Journal of Mathematical Physics*, 27:1238–1265, May 1986.

[150] H. A. Lorentz and J. Droste. *Collected Papers: Volume V.* Springer Netherlands, Dordrecht, 1937.

[151] C. O. Lousto and B. F. Whiting. Reconstruction of black hole metric perturbations from Weyl curvature. *Phys. Rev. D*, 66:024026, 2002.

[152] M. Maggiore. *Gravitational Waves: Volume 1: Theory and Experiments.* Gravitational Waves. OUP Oxford, 2008.

[153] S. Mano, H. Suzuki, and E. Takasugi. Analytic Solutions of the Regge-Wheeler Equation and the Post-Minkowskian Expansion. *Progress of Theoretical Physics*, 96:549–565, September 1996.

[154] S. Mano, H. Suzuki, and E. Takasugi. Analytic Solutions of the Teukolsky Equation and Their Low Frequency Expansions. *Progress of Theoretical Physics*, 95:1079–1096, June 1996.

[155] T. Marchand, L. Bernard, L. Blanchet, and G. Faye. Ambiguity-free completion of the equations of motion of compact binary systems at the fourth post-newtonian order. *Phys. Rev. D*, 97:044023, Feb 2018.

[156] K. Martel. *Particles and black holes: Time-domain integration of the equations of black-hole perturbation theory.* PhD thesis, The University of Guelph, 2003.

[157] K. Martel. Gravitational waveforms from a point particle orbiting a Schwarzschild black hole. *Phys. Rev. D*, 69:044025, 2004.

[158] K. Martel and E. Poisson. Gravitational perturbations of the Schwarzschild spacetime: A practical covariant and gauge-invariant formalism. *Phys. Rev. D*, 71(10):104003–+, May 2005.

[159] J. C. Maxwell. Viii. a dynamical theory of the electromagnetic field. *Philosophical Transactions of the Royal Society of London*, 155:459–512, 1865.

[160] C. Merlin, A. Ori, L. Barack, A. Pound, and M. van de Meent. Completion of metric reconstruction for a particle orbiting a Kerr black hole. *Phys. Rev. D*, 94(10):104066, November 2016.

[161] J. Miller, B. Wardell, and A. Pound. Second-order perturbation theory: The problem of infinite mode coupling. *Phys. Rev. D*, 94(10):104018, November 2016.

[162] Y. Mino. Perturbative approach to an orbital evolution around a supermassive black hole. *Phys. Rev. D*, 67:084027, 2003.

[163] Y. Mino. From the self-force problem to the radiation reaction formula. *Classical and Quantum*

Gravity, 22:S717–S738, August 2005.

[164] Y. Mino. Self-Force in Radiation Reaction Formula —Adiabatic Approximation of the Metric Perturbation and the Orbit—. *Progress of Theoretical Physics*, 113:733–761, April 2005.

[165] Y. Mino, M. Sasaki, and T. Tanaka. Chapter 7. Gravitational Radiation Reaction. *Progress of Theoretical Physics Supplement*, 128:373–406, January 1997.

[166] Y. Mino, M. Sasaki, and T. Tanaka. Gravitational radiation reaction to a particle motion. *Phys. Rev. D*, 55:3457–3476, 1997.

[167] C. W. Misner. Interpretation of gravitational-wave observations. *Phys. Rev. Lett.*, 28:994–997, Apr 1972.

[168] C. W. Misner, K. S. Thorne, and J. A. Wheeler. *Gravitation.* Freeman, San Francisco, CA, U.S.A., 1973.

[169] V. Moncrief. Gravitational perturbations of spherically symmetric systems. I. The exterior problem. *Ann. Phys.*, 88:323–342, 1974.

[170] J. Moxon and É. Flanagan. Radiation-reaction force on a small charged body to second order. *Phys. Rev. D*, 97(10):105001, May 2018.

[171] C. Munna and C. R. Evans. Eccentric-orbit extreme-mass-ratio-inspiral radiation: Analytic forms of leading-logarithm and subleading-logarithm flux terms at high PN orders. *Phys. Rev. D*, 100(10):104060, Nov 2019.

[172] Z. Nasipak, T. Osburn, and C. R. Evans. Repeated faint quasinormal bursts in extreme-mass-ratio inspiral waveforms: Evidence from frequency-domain scalar self-force calculations on generic Kerr orbits. *Phys. Rev. D*, 100(6):064008, September 2019.

[173] E. Newman and R. Penrose. An Approach to Gravitational Radiation by a Method of Spin Coefficients. *Journal of Mathematical Physics*, 3:566–578, May 1962.

[174] Amos Ori. Reconstruction of inhomogeneous metric perturbations and electromagnetic four-potential in Kerr spacetime. *Phys. Rev. D*, 67:124010, 2003.

[175] T. Osburn. *Extreme-mass-ratio inspirals into a black hole.* PhD thesis, The University of North Carolina at Chapel Hill, 2016.

[176] T. Osburn, E. Forseth, C. R. Evans, and S. Hopper. Lorenz gauge gravitational self-force calculations of eccentric binaries using a frequency domain procedure. *Phys. Rev. D*, 90:104031, Nov 2014.

[177] T. Osburn, N. Warburton, and C. R. Evans. Highly eccentric inspirals into a black hole. *Phys. Rev. D*, 93:064024, Mar 2016.

[178] E. Poisson. Absorption of mass and angular momentum by a black hole: Time-domain formalisms for gravitational perturbations, and the small-hole or slow-motion approximation. *Phys. Rev. D*, 70(8):084044, October 2004.

[179] E. Poisson. *A Relativist's Toolkit: The Mathematics of Black-Hole Mechanics.* Cambridge University Press, 2004.

[180] E. Poisson, A. Pound, and I. Vega. The motion of point particles in curved spacetime. *Living Rev. Rel.*, 14:7, 2011.

[181] E. Poisson and C. M. Will. *Gravity: Newtonian, Post-Newtonian, Relativistic.* Cambridge University

Press, Cambridge, UK, 1st edition, 2014.

[182] A. Pound. Nonlinear gravitational self-force. I. Field outside a small body. *Phys. Rev. D*, 86:084019, 2012.

[183] A. Pound. Second-order gravitational self-force. *Physical Review Letters*, 109:051101, 2012.

[184] A. Pound. Nonlinear gravitational self-force: Second-order equation of motion. *Phys. Rev. D*, 95(10):104056, May 2017.

[185] A. Pound, C. Merlin, and L. Barack. Gravitational self-force from radiation-gauge metric perturbations. *ArXiv e-prints*, October 2013.

[186] A. Pound and J. Miller. Practical, covariant puncture for second-order self-force calculations. *Phys. Rev. D*, 89(10):104020, May 2014.

[187] A. Pound and E. Poisson. Osculating orbits in Schwarzschild spacetime, with an application to extreme mass-ratio inspirals. *Phys. Rev. D*, 77:044013, 2008.

[188] A. Pound, B. Wardell, N. Warburton, and J. Miller. Second-Order Self-Force Calculation of Gravitational Binding Energy in Compact Binaries. *APhysical Review Letters*, 124(2):021101, January 2020.

[189] W. H. Press and S. A. Teukolsky. Perturbations of a Rotating Black Hole. II. Dynamical Stability of the Kerr Metric. *Astrophys. J.*, 185:649–674, October 1973.

[190] F. Pretorius. Evolution of Binary Black Hole Spacetimes. *Physical Review Letters*, 95:121101, 2005.

[191] T. C. Quinn. Axiomatic approach to radiation reaction of scalar point particles in curved spacetime. *Phys. Rev. D*, 62(6):064029, September 2000.

[192] T. C. Quinn and R. M. Wald. Axiomatic approach to electromagnetic and gravitational radiation reaction of particles in curved spacetime. *Phys. Rev. D*, 56(6):3381–3394, Sep 1997.

[193] T. C. Quinn and R. M. Wald. Energy conservation for point particles undergoing radiation reaction. *Phys. Rev. D*, 60(6):064009, September 1999.

[194] T. Regge and J. A. Wheeler. Stability of a Schwarzschild singularity. *Phys. Rev.*, 108:1063–1069, 1957.

[195] C. S. Reynolds. The spin of supermassive black holes. *Classical and Quantum Gravity*, 30(24):244004, Dec 2013.

[196] D. Rickles and C. M. DeWitt. The Role of Gravitation in Physics: Report from the 1957 Chapel Hill Conference. The Role of Gravitation in Physics: Report from the 1957 Chapel Hill Conference, February 2011.

[197] N. E. M. Rifat, G. Khanna, and L. M. Burko. Repeated ringing of black holes: Quasinormal bursts from highly eccentric, extreme mass-ratio binaries. *Physical Review Research*, 1(3):033150, December 2019.

[198] M. J. Rodriguez. `sites.google.com/site/justblackholes/techy-zone`.

[199] E. Rosenthal. Regularization of the second-order gravitational perturbations produced by a compact object. *Phys. Rev. D*, 72:121503, 2005.

[200] U. Ruangsri and S. A. Hughes. Census of transient orbital resonances encountered during binary inspiral. *Phys. Rev. D*, 89(8):084036, Apr 2014.

[201] N. Sago, H. Nakano, and M. Sasaki. Gauge problem in the gravitational self-force. I: Harmonic gauge approach in the Schwarzschild background. *Phys. Rev. D*, 67:104017, 2003.

[202] N. Sago, T. Tanaka, W. Hikida, K. Ganz, and H. Nakano. The adiabatic evolution of orbital parameters in the Kerr spacetime. *Prog. Theor. Phys.*, 115:873–907, 2006.

[203] M. Sasaki and T. Nakamura. A class of new perturbation equations for the kerr geometry. *Physics Letters A*, 89(2):68 – 70, 1982.

[204] M. Sasaki and H. Tagoshi. Analytic Black Hole Perturbation Approach to Gravitational Radiation. *Living Reviews in Relativity*, 6:6, November 2003.

[205] W. Schmidt. Celestial mechanics in Kerr spacetime. *Class. Quant. Grav.*, 19:2743, 2002.

[206] A. G. Shah, J. L. Friedman, and T. S. Keidl. Extreme-mass-ratio inspiral corrections to the angular velocity and redshift factor of a mass in circular orbit about a Kerr black hole. *Phys. Rev. D*, 86(8):084059, October 2012.

[207] A. G. Shah, T. S. Keidl, J. L. Friedman, D.-H. Kim, and L. R. Price. Conservative, gravitational self-force for a particle in circular orbit around a Schwarzschild black hole in a radiation gauge. *Phys. Rev. D*, 83(6):064018, March 2011.

[208] J. H. Taylor and J. M. Weisberg. A new test of general relativity - Gravitational radiation and the binary pulsar PSR 1913+16. *Astrophys. J.*, 253:908–920, February 1982.

[209] S. A. Teukolsky. Perturbations of a rotating black hole. I. Fundamental equations for gravitational, electromagnetic, and neutrino-field perturbations. *Astrophys. J.*, 185:635–647, 1973.

[210] S. A. Teukolsky and W. H. Press. Perturbations of a rotating black hole. III. Interaction of the hole with gravitational and electromagnetic radiation. *Astrophys. J.*, 193:443–461, October 1974.

[211] The LIGO Scientific Collaboration and the Virgo Collaboration. GW190412: Observation of a Binary-Black-Hole Coalescence with Asymmetric Masses. *arXiv e-prints*, page arXiv:2004.08342, April 2020.

[212] J. Thornburg and B. Wardell. Scalar self-force for highly eccentric orbits in Kerr spacetime. 2014. 17th Capra Meeting on Radiation Reaction in General Relativity, Caltech, California, USA.

[213] J. Thornburg and B. Wardell. Scalar self-force for highly eccentric orbits in Kerr spacetime. 2016. 19th Capra Meeting on Radiation Reaction in General Relativity, Paris Observatory, France.

[214] J. Thornburg and B. Wardell. Scalar self-force for highly eccentric equatorial orbits in Kerr spacetime. *Phys. Rev. D*, 95(8):084043, April 2017.

[215] J. Thornburg and B. Wardell. Scalar self-force for highly eccentric orbits in Kerr spacetime. 2017. 20th Capra Meeting on Radiation Reaction in General Relativity, University of North Carolina at Chapel Hill, USA.

[216] J. Thornburg, B. Wardell, and M. van de Meent. Excitation of kerr quasinormal modes in extreme-mass-ratio inspirals. *Phys. Rev. Research*, 2:013365, Mar 2020.

[217] K. S. Thorne. Multipole expansions of gravitational radiation. *Rev. Mod. Phys.*, 52(2):299–339, Apr 1980.

[218] W. Throwe. High precision calculation of generic extreme mass ratio inspirals, 2010. http://hdl.handle.net/1721.1/61270.

[219] C. S. Unnikrishnan. IndIGO and Ligo-India Scope and Plans for Gravitational Wave Research and

Precision Metrology in India. *International Journal of Modern Physics D*, 22:1341010, January 2013.

[220] M. van de Meent. Conditions for sustained orbital resonances in extreme mass ratio inspirals. *Phys. Rev. D*, 89(8):084033, April 2014.

[221] M. van de Meent. Resonantly enhanced kicks from equatorial small mass-ratio inspirals. *Phys. Rev. D*, 90(4):044027, Aug 2014.

[222] M. van de Meent. Gravitational self-force on eccentric equatorial orbits around a kerr black hole. *Phys. Rev. D*, 94:044034, Aug 2016.

[223] M. van de Meent. The mass and angular momentum of reconstructed metric perturbations. *Classical and Quantum Gravity*, 34(12):124003, June 2017.

[224] M. van de Meent. Gravitational self-force on generic bound geodesics in Kerr spacetime. *Phys. Rev. D*, 97, May 2018.

[225] M. van de Meent and A. G. Shah. Metric perturbations produced by eccentric equatorial orbits around a Kerr black hole. *Phys. Rev. D*, 92(6):064025, September 2015.

[226] M. van de Meent and N. Warburton. Fast self-forced inspirals. *Classical and Quantum Gravity*, 35(14):144003, July 2018.

[227] I. Vega and S. Detweiler. Regularization of fields for self-force problems in curved spacetime: Foundations and a time-domain application. *Phys. Rev. D*, 77(8):084008, April 2008.

[228] I. Vega, P. Diener, W. Tichy, and S. Detweiler. Self-force with (3+1) codes: A primer for numerical relativists. *Phys. Rev. D*, 80(8):084021, October 2009.

[229] I. Vega, B. Wardell, P. Diener, S. Cupp, and R. Haas. Scalar self-force for eccentric orbits around a Schwarzschild black hole. *Phys. Rev. D*, 88(8):084021, October 2013.

[230] C. V. Vishveshwara. Stability of the Schwarzschild metric. *Phys. Rev. D*, 1:2870–2879, 1970.

[231] R. M. Wald. On perturbations of a Kerr black hole. *J. Math. Phys.*, 14:1453, 1973.

[232] R. M. Wald. Construction of solutions of gravitational, electromagnetic, or other perturbation equations from solutions of decoupled equations. *Physical Review Letters*, 41:203–206, 1978.

[233] M. Walker and R. Penrose. On quadratic first integrals of the geodesic equations for type {22} spacetimes. *Communications in Mathematical Physics*, 18:265–274, December 1970.

[234] N. Warburton. Self-force on a scalar charge in Kerr spacetime: Inclined circular orbits. *Phys. Rev. D*, 91(2):024045, January 2015.

[235] N. Warburton, S. Akcay, L. Barack, J. R. Gair, and N. Sago. Evolution of inspiral orbits around a schwarzschild black hole. *Phys. Rev. D*, 85:061501(R), Mar 2012.

[236] N. Warburton and L. Barack. Self-force on a scalar charge in Kerr spacetime: Circular equatorial orbits. *Phys. Rev. D*, 81(8):084039, April 2010.

[237] N. Warburton and L. Barack. Self-force on a scalar charge in Kerr spacetime: Eccentric equatorial orbits. *Phys. Rev. D*, 83(12):124038, June 2011.

[238] N. Warburton, L. Barack, and N. Sago. Isofrequency pairing of geodesic orbits in Kerr geometry. *Phys. Rev. D*, 87(8):084012, Apr 2013.

[239] N. Warburton, T. Osburn, and C. R. Evans. Evolution of small-mass-ratio binaries with a spinning secondary. *Phys. Rev. D*, 96(8):084057, October 2017.

[240] N. Warburton and B. Wardell. Applying the effective-source approach to frequency-domain self-force calculations. *Phys. Rev. D*, 89(4):044046, February 2014.

[241] B. Wardell, C. R. Galley, A. Zenginoğlu, M. Casals, S. R. Dolan, and A. C. Ottewill. Self-force via Green functions and worldline integration. *Phys. Rev. D*, 89(8):084021, April 2014.

[242] B. Wardell, I. Vega, J. Thornburg, and P. Diener. Generic effective source for scalar self-force calculations. *Phys. Rev. D*, 85(10):104044, May 2012.

[243] B. Wardell and N. Warburton. Applying the effective-source approach to frequency-domain self-force calculations: Lorenz-gauge gravitational perturbations. *Phys. Rev. D*, 92(8):084019, October 2015.

[244] J. M. Weisberg and J. H. Taylor. *The Relativistic Binary Pulsar B1913+16: Thirty Years of Observations and Analysis*, volume 328 of *Astronomical Society of the Pacific Conference Series*, page 25. 2005.

[245] A. G. Wiseman. Self-force on a static scalar test charge outside a Schwarzschild black hole. *Phys. Rev. D*, 61(8):084014, April 2000.

[246] H. Yang, A. Zimmerman, A. Zenginoğlu, F. Zhang, E. Berti, and Y. Chen. Quasinormal modes of nearly extremal Kerr spacetimes: Spectrum bifurcation and power-law ringdown. *Phys. Rev. D*, 88(4):044047, August 2013.

[247] F. J. Zerilli. Gravitational field of a particle falling in a Schwarzschild geometry analyzed in tensor harmonics. *Phys. Rev. D*, 2:2141–2160, 1970.

[248] A. Zimmerman and Z. Mark. Damped and zero-damped quasinormal modes of charged, nearly extremal black holes. *Phys. Rev. D*, 93(4):044033, February 2016.